Faculté des Sciences
Département de Géographie
Laboratoire de Climatologie et Topoclimatologie

Climate change in Belgium: recent and future evolution of global radiation and hydro-climatic conditions favouring floods using the regional climate model MAR

A thesis submitted for the partial fulfilment
of the requirements for the academic degree of

Philosophiae Doctor in Sciences
at the University of Liège (College of Geography)
by

Coraline Wyard

Academic year 2018–2019

Jury members:

Bernard Tychon	President	Professor, ULiège
Xavier Fettweis	Supervisor	Research Associate FRS-FNRS, ULiège
Louis François	Co-supervisor	Professor, ULiège
Charlotte Lang	Secretary	Postdoctoral Researcher FRS-FNRS, ULiège
Michel Erpicum		Professor emeritus, ULiège
Hubert Gallée		Senior Researcher CNRS, Université Grenoble-Alpes
Rafiq Hamdi		Researcher, Royal Meteorological Institute of Belgium

This research was funded by the Fonds pour la Formation à la Recherche dans l'Industrie et l'Agriculture.

Remerciements

Au moment de clôturer ce chapitre de ma vie, mes premières pensées vont au Professeur Michel Erpicum, à mon promoteur Xavier Fettwies et à mon co-promoteur Louis François, sans qui cette aventure n'aurait jamais pu débuter. Ils ont été les premiers à m'encourager et à m'aider à bâtir ce projet. Je remercie plus particulièrement mon promoteur principal, le Dr. Xavier Fettweis. Sans son génie, sa disponibilité, sa patience et son enthousiasme à toute épreuve, je n'aurais probablement jamais pu mener cette thèse à son terme.

J'aurais également vécu cette expérience moins sereinement sans le soutien financier du Fonds pour la Formation à la Recherche dans l'Industrie et l'Agriculture qui a cru dès le départ en la pertinence de mon projet.

Je tiens également à remercier le Professeur Bernard Tychon, Charlotte Lang, Hubert Gallée et Rafiq Hamdi d'avoir accepté de consacrer du temps à cette thèse en tant que membres de mon jury de thèse.

Ces quatre années passées au Laboratoire de Climatologie n'auraient pas été les mêmes sans la présence au quotidien de mes chers collègues. Je les remercie vivement pour leur générosité, leur aide et leurs encouragements. Je remercie plus particulièrement les membres du Tea Time et les Girls pour tous les moments de détente que nous avons passés ensemble.

Enfin, je tiens à remercier très chaleureusement ma famille, mes proches, et surtout ma maman et Loïc qui ont toujours plus cru en moi que moi en moi-même.

Summary

In Belgium, the future response of the climate to increasing greenhouse gas concentration is not clear, especially with regard to the perturbations of the precipitation regime, snow cover, and global radiation. On the one hand, existing studies show results which differ strongly either according to the future scenario, or from one model to another. On the other hand, there is even an absence of studies focussing on Belgium regarding future changes in snow cover and global radiation. Given their potential impacts on the society (water management, energy supply, biodiversity, tourism), future changes in precipitation, snow cover, and global radiation require further research. As the orography, the exposition to the dominant winds, and the proximity of the North Sea determine a large spatial variability in the Belgian climate, the latter requires a fine representation of these features to be properly simulated. Compared to global climate models (GCM), regional climate models (RCM) are recognized for their ability to represent climatic phenomena with higher spatial resolutions.

In the framework of this doctoral thesis, the RCM MAR (for "Modèle Atmosphérique Régional" in French), which is developed at the Laboratory of Climatology and Topoclimatology of the University of Liège, was applied for the first time to Belgium. The aim was first to assess the performances of MAR over Belgium and then to study the current and future evolution of hydroclimatic conditions favouring floods, and also the current and future evolution of global radiation. For this purpose, historical simulations were performed over 1959–2014. Future projections (2006–2100) were then performed under the most pessimist IPCC future scenario (RCP8.5). The horizontal resolution used for both historical and future simulations is 5 km.

By comparing the MAR outputs to ground-based measurements from 20 weather stations over 2008–2014, the results show that MAR successfully simulates the spatial and temporal variability of the Belgian climate. In fact, the biases

found in the MAR results are non-significant and the correlation coefficients are satisfying with regard to temperature, precipitation, snow height, global radiation and cloudiness. The MAR results are particularly satisfying during the winter months and in High Belgium where the climate is the coldest.

Regarding hydroclimatic conditions favouring floods, we focused on the Ourthe catchment. In this river, about 70 % of floods occur during the winter months and result from either the rapid melting of the snow pack covering the Ardennes eventually combined with rainfall or abundant rainfall alone. The current evolution of hydroclimatic conditions favouring floods was first assessed for the period 1959–2010. Conditions favouring floods in the Ourthe River present a negative trend over 1959–2010 as a result of a decrease in snow accumulation and a shortening of the snow season. Regarding the impact of the evolution of extreme precipitation events on hydroclimatic conditions favouring floods, the signal is less clear because the trends depend on the data used to force the MAR model. By the end of the 21^{st} century, under the most pessimist scenario, the results show an acceleration of the snow cover depletion resulting in a decrease in conditions favouring floods. Further, the impact of the evolution of extreme precipitation events on hydroclimatic conditions favouring floods, no significant change was found although these trends are subject to uncertainties due to the deficiencies of the convective scheme of MAR.

Regarding global radiation, its current evolution was first assessed for the period 1959–2010. In addition, we consider two distinct periods in our analysis: 1959–1979 (dimming) and 1980–2010 (brightening). For both the dimming and the brightening periods, our results show that the annual global radiation trends are mainly driven by global radiation changes in spring and summer. The increase in global radiation observed in Belgium since the 1980s and especially since the 2000s could mainly be explained by a decrease in low and medium cloud cover. This would strengthen the effect of the decrease in aerosol load on global radiation that has been observed in Europe since the 1980s. The origin of these changes in cloudiness is not clear and could result from changes in both aerosol-cloud interactions and atmospheric-circulation, such as more frequent tropical air advections and more frequent anticyclonic conditions over Western Europe due to the poleward shift of extratropical storm tracks. These changes in the atmospheric circulation may result from global warming and may persist in the future. In fact, by the end of the 21^{st} century, under the most pessimist scenario, the models simulate an increase in the blocking regime frequency in summer

over Europe. For Belgium, this implies more frequent anticyclonic conditions favouring cloudless conditions. The future projections performed with MAR exhibit significant decreasing total cloud cover, and particularly decreasing low and medium cloud cover. However, this declining cloud cover leads to contrasting changes in global radiation depending on the data used to force MAR.

Résumé

En Belgique, les impacts de l'augmentation des concentrations en gaz à effet de serre dans l'atmosphère sur le climat futur ne sont pas clairs, surtout en ce qui concerne le régime de précipitation, l'enneigement ou encore le rayonnement solaire reçu à la surface de la Terre. D'un côté, les études montrent des résultats qui varient fortement selon le scénario futur utilisé ou selon le modèle utilisé. D'un autre côté, aucune étude récente ne s'est intéressée aux changements futurs de l'enneigement et du rayonnement solaire en Belgique. Étant donné les impacts sociétaux (gestion de l'eau, approvisionnement en énergie, biodiversité, tourisme) que des changements dans ces variables pourraient provoquer, il apparaît nécessaire d'étudier le sujet plus en détails. Comme l'orographie, l'exposition aux vents dominants et la proximité avec la Mer du Nord entraînent une grande variabilité spatiale du climat de la Belgique, il est important que ces éléments soient finement représentés pour modéliser correctement le climat en Belgique. Par rapport aux modèles climatiques globaux (GCM), les modèles climatiques régionaux (RCM) permettent de modéliser à haute résolution spatiale ces éléments.

Dans le cadre de cette thèse de doctorat, le RCM MAR (Modèle Atmosphérique Régional), développé au Laboratoire de Climatologie de l'Université de Liège, a été utilisé pour la première fois sur la Belgique. Le but était tout d'abord, d'évaluer les performances du MAR sur la Belgique, ensuite, d'étudier l'évolution actuelle et future des conditions climatiques favorisant les inondations, de même que celles affectant le rayonnement solaire. Dans cette optique, le climat a d'abord été reconstitué sur la période historique (1959–2014). Des projections futures ont ensuite été réalisées en considérant le scénario le plus pessimiste du GIEC (le RCP8.5). Il faut signaler que ces simulations ont été réalisées à 5 km de résolution.

La comparaison des résultats du MAR avec des mesures issues de 20 stations météorologiques réalisées entre 2008 et 2014 a montré que MAR parvenait à simuler la variabilité spatiale et temporelle du climat de la Belgique. Les biais

sont en effet non-significatifs et les coefficients de corrélation sont satisfaisants en ce qui concerne la température de l'air, les précipitations, la hauteur de neige, le rayonnement solaire et la couverture nuageuse. Les résultats du MAR sont particulièrement satisfaisants en hiver et en Haute Belgique où le climat est le plus froid.

En ce qui concerne les conditions climatiques favorisant les inondations, nous nous sommes concentrés sur le bassin versant de l'Ourthe. Dans cette rivière, environs 70 % des inondations se produisent en hiver et sont générées soit par la fonte rapide du manteau de neige qui recouvre l'Ardenne, éventuellement combinée à des précipitations, soit par des précipitations abondantes seules. L'évolution actuelle des conditions climatiques favorisant les inondations a d'abord été évaluée sur la période 1959–2010. Durant cette période, les conditions climatiques favorisant les inondations dans l'Ourthe présentent une tendance négative en raison d'une diminution des accumulations de neige au sol et d'un raccourcissement de la saison d'enneigement. L'impact de l'évolution des précipitations extrêmes sur les conditions favorables aux inondations n'est cependant pas clair car les tendances diffèrent selon le set de données utilisé pour forcer MAR. D'ici la fin du 21^e siècle, sous le scénario le plus pessimiste, les résultats montrent une accélération de la diminution de l'enneigement provoquant une diminution des conditions climatiques favorables aux inondations. Par ailleurs, en ce qui concerne l'impact de l'évolution future des précipitations extrêmes sur les conditions favorables aux inondations, aucune tendance significative n'a été mise en évidence. Il faut toutefois signaler que cette tendance est sujette à de grandes incertitudes en raison des déficiences du MAR pour la simulation des précipitations convectives.

En ce qui concerne le rayonnement solaire reçu en surface, son évolution actuelle a tout d'abord été étudiée sur la période 1959–2010. En outre, nous avons considéré deux périodes distinctes dans notre analyse : la période 1959–1979 caractérisée par une diminution du rayonnement solaire, et la période 1980–2010 caractérisée par une ré-augmentation. Quelle que soit la période étudiée, les résultats montrent que les tendances dans le rayonnement solaire moyen annuel sont dirigées par les changements survenus au printemps et en été. L'augmentation du rayonnement solaire observée en Belgique depuis les années 1980 et surtout depuis les années 2000 proviendrait principalement d'une diminution de la couverture de nuages bas et moyens. Il en résulterait un renforcement de l'effet de la diminution des concentrations en aérosols dans l'atmosphère sur le rayonnement solaire qui est observée en Europe depuis les années 1980. L'origine de la diminution de la

nébulosité n'est toutefois pas claire. Ces changements pourraient résulter à la fois de changements dans les interactions entre les aérosols et les nuages mais aussi de changements survenus dans le circulation atmosphérique, comme par exemple des advections plus fréquentes d'air tropical ou des conditions anticycloniques plus fréquentes, provoquées par un déplacement vers le nord des trajectoires suivies par les tempêtes extra-tropicales. Ces changements dans la circulation atmosphérique pourraient eux-mêmes être générés par le réchauffement du climat et pourraient ainsi persister dans le futur. En effet, d'ici la fin du 21^e siècle, sous le scénario le plus pessimiste, les modèles prévoient une augmentation de la fréquence des blocages atmosphériques en été sur l'Europe. Pour la Belgique, cela implique des conditions anticycloniques plus fréquentes favorisant les conditions sans nuage. D'ici la fin du siècle, les projections réalisées avec MAR montrent en effet une diminution significative de la couverture nuageuse, et surtout celle des nuages bas et moyens. Cependant, ce déclin de la couverture nuageuse génère des changements de rayonnement solaire contrastés suivant les données utilisées pour forcer MAR.

List of publications

Wyard C., Doutreloup S., Fettweis X. (2018) Future projections of global radiation and cloudiness in Belgium. To be submitted to *Bulletin de la Société Géographique de Liège*.

Wyard C., Scholzen C., DoutreloupS., Fettweis X. (2018) Future projections of hydroclimatic conditions favouring floods in Belgium. In review in *International Journal of Climatology*

Doutreloup S., Wyard C., Amory C., Kittel C., Erpicum M., and Fettweis X. (2018) Sensitivity to convective schemes on precipitation simulated by the regional climate model MAR over Belgium (1987-2017). In review in *Atmosphere*.

Kittel C., Amory C., Agosta C., Delhasse A., Doutreloup S., Huot P.-V., Wyard C., Fichefet T., Fettweis X. (2018). Sensitivity of the current Antarctic surface mass balance to sea surface conditions using MAR. *The Cryosphere*, **12**, 3827–3839, doi : 10.5194/tc-12-3827-2018.

Termonia P., Schaeybroeck B. V., Cruz L. D., Troch R. D., Caluwaerts S., Giot O., Hamdi R., Willems P., Tabari H., Uytven E. V., Hosseinzadehtalaei P., Lipzig N. V., Wouters H., Broucke S. V., Ypersele J.-p. V., Marbaix P., Villanueva-birriel C., Fettweis X., Wyard C., Ridder K. D., Gobin A., Lauwaet D., Stavrakou T., Bauwens M., Luyten P., Eynde D. V. D., and Pottiaux E. (2018) The CORDEX.be initiative as a foundation for climate services in Belgium. *Climate Services*, **7**, 49–61, doi: https://doi.org/10.1016/j.cliser.2018.05.001

Wyard C., Doutreloup S., Belleflamme A., Wild M., and Fettweis X. (2018) Global Radiative Flux and Cloudiness Variability for the Period 1959–2010 in Belgium: A Comparison between Reanalyses and the Regional Climate Model MAR. *Atmosphere*, **9 (7)**, 262, doi: 10.3390/atmos9070262

Le Clec'h S., Fettweis X., Quiquet A., Kageyama M., Dumas C., Charbit S., Wyard C., and Ritz C. (2017) Assessment of the Greenland ice sheet–atmosphere

feedbacks for the next century with a regional atmospheric model fully coupled to an ice sheet model. *The Cryosphere Discussions*, doi: 10.5194/tc-2017-230

Fettweis X., Wyard C., Doutreloup S., and Belleflamme A. (2017) Noël 2010 En Belgique : Neige En Flandre Et Pluie En Haute-Ardenne. *Bulletin de la Société Géographique de Liège*, 68 (1), 97–107

Wyard C., Scholzen C., Fettweis X., Van Campenhout J., and François L. (2017) Decrease in climatic conditions favouring floods in the south-east of Belgium over 1959-2010 using the regional climate model MAR. *International Journal of Climatology*, **37 (5)**, 2782–2796, doi: 10.1002/joc.4879

List of abbreviations

$\boldsymbol{\sigma}$ or **STD**	Standard deviation
AR5	5^{th} assessment report of the IPCC
CEN	Centre d'Étude de la Neige
CMIP5	Coupled Model Intercomparison Project Phase 5
COD	Cloud optical depth
CORDEX	Coordinated Regional Climate Downscaling Experiments
CPPN or **CP**	Convective precipitation
CRMSE	Centred root mean square error
DJF	December–January–February
ECMWF	European Centre for Medium-Range Weather Forecasts
$\mathbf{E}_{g\downarrow}$	Global radiation
FE	Flood event
GCM	Global climate model
GLF	Green leaf fraction
HCC	High cloud cover
HUR500	Relative humidity at the 500 hPa pressure level
HUR700	Relative humidity at the 700 hPa pressure level
HUS500	Specific humidity at the 500 hPa pressure level
HUS700	Specific humidity at the 700 hPa pressure level
IPCC	Intergovernmental Panel on Climate Change
IWC	Ice water content

JJA	June–July–August
LAI	Leaf area index
LCC	Low cloud cover
LWC	Liquid water content
MAM	March–April–May
MAR	Modèle Atmosphérique Régional
MAR-20CRV2C	MAR forced by 20CRV2C
MAR-ERA	MAR forced ERA40/ERA-interim
MAR-ERA-20C	MAR forced by ERA-20C
MAR-MIR-histo	MAR forced by MIROC5 (present)
MAR-MIR-rcp85	MAR forced by MIROC5 (future)
MAR-NCEP1	MAR forced by NCEP/NCAR-v1
MAR-NOR-histo	MAR forced by NorESM1-M (present)
MAR-NOR-rcp85	MAR forced by NorESM1-M (future)
MB	Mean biases
MCC	Medium cloud cover
MIROC5	Japanese research community's Model for Interdisciplinary Research On Climate Version Five
NAO	North Atlantic Oscillation
NCEP/NCAR	National Centers for Environmental Prediction–National Center for Atmospheric Research
NOAA	National Oceanic and Atmospheric Administration
NorESM1-M	Norwegian Climate Center's Earth System Model
P95	95^{th} percentile
PFD	Precipitation flood days
PPN or **PPNtot**	Total precipitation amount
PPN95	Extreme precipitation intensity
PPNF95	Extreme precipitation frequency
R	Correlation coefficient
RCM	Regional climate model

RCP	Representative concentration pathway
RF	Rainfall amount
RMIB	Royal Meteorological Institute of Belgium
RMS	Root mean square
RMSE	Root mean square error
RU	Run-off
RU2	2-day averaged run-off
RU2$_e$	Effective 2-day averaged run-off
SD5 or **SD**	Snow day
Sf	Last day of the snow season
SF	Snowfall amount
SFD	Snow melting flood days
SH	Snow height
SHAVE	Mean snow height
SHMAX	Maximum snow height
Si	First day of the snow season
SON	September–October–November
SP	Surface pressure
SPPN	Stratiform precipitation
TA500	Air temperature at the 500 hPa pressure level
TA700	Air temperature at the 700 hPa pressure level
Tave	Mean temperature
TCC	Total cloud cover
TFD	Total flood days
T$_{JF}$**850**	Mean winter temperature at the 850 hPa level
T$_{JJA}$**850**	Mean summer temperature at the 850 hPa level
TMAX95	Extreme maximum temperature
TMIN5	Extreme minimum temperature
UV500	Windspeed at the 500 hPa level

UV700	Windspeed at the 700 hPa level
Z500	Geopotential height at the 500 hPa level
Z700	Geopotential height at the 700 hPa level
WMO	World Meteorological Organization

Contents

1 General introduction to current and future climate changes in Belgium **1**

1.1 Belgium and its mean climate 2

1.2 Belgium under climate change 8

1.2.1 Observed climate changes 8

1.2.2 Future climate changes 12

1.3 Regional versus global climate models 15

1.4 Objectives 17

1.5 Thesis outline 18

2 Data and methods **21**

2.1 The MAR model 22

2.1.1 Description and experimental set-up 22

2.1.2 MARv3.6 versus MARv3.8 24

2.2 Reanalyses 27

2.3 GCM outputs 28

2.4 Evaluation datasets 31

2.4.1 Temperature, precipitation and surface pressure 32

2.4.2 Snow height 33

2.4.3 Global radiation 33

2.4.4 Total cloud cover 34

2.4.5 Flow rate 35

2.5 Evaluation of linear trends significance using the uncertainty range for the 95% confidence interval of Snedecor 35

3 Current evolution of hydroclimatic conditions favouring floods in the south-east of Belgium over 1959–2010 37

3.1 Context 38

3.2 Additional methodological aspects 39

3.3 Evaluation of MAR 39

3.3.1 Daily mean temperature 40

3.3.2 Daily precipitation amount 41

3.3.3 Snow height 41

3.3.4 Climatic conditions favouring floods 43

3.3.5 Origin of biases in MAR 45

3.4 Changes in the winter climate over 1959-2010 46

3.4.1 Temperature 47

3.4.2 Precipitation 48

3.4.3 Snow cover 50

3.4.4 Origin of trends in the winter climate of Belgium 50

3.5 Changes in conditions favouring winter floods over the period 1959-2010 54

3.6 Chapter conclusion 56

4 Future evolution of hydroclimatic conditions favouring floods in the south-east of Belgium by 2100 61

4.1 Context 62

4.2 Additional methodological aspects 65

4.3 Evaluation over the current climate 65

4.3.1 Temperature 66

4.3.2 Precipitation 67

4.3.3 Snow 70

4.3.4 Conditions favouring floods . . . 70
4.3.5 Origin of biases . . . 73
4.4 Future changes in the Belgian winter climate . . . 74
4.4.1 Temperature . . . 75
4.4.2 Precipitation . . . 76
4.4.3 Snow cover . . . 79
4.4.4 Conditions favouring floods . . . 80
4.4.5 Origin of discrepancies and uncertainties in future projections 82
4.5 Chapter conclusion . . . 83

5 Current evolution of global radiation and cloudiness over 1959-2010 87

5.1 Context . . . 88
5.2 Additional methodological aspects . . . 90
5.3 Evaluation of MAR . . . 91
5.3.1 Global radiation . . . 91
5.3.2 Total cloud cover . . . 95
5.3.3 Origin of biases in MAR . . . 97
5.4 Changes over the dimming (1959–1979) and the brightening (1980–2010) periods . . . 99
5.4.1 Trends in annual global radiation and total cloud cover . . . 99
5.4.2 Trends in seasonal global radiation and total cloud cover . . 101
5.4.3 Origin of changes in cloudiness . . . 105
5.5 Chapter conclusion . . . 110

6 Future evolution of global radiation and cloudiness by 2100 113

6.1 Context . . . 114
6.2 Additional methodological aspects . . . 115
6.3 Evaluation over the current climate . . . 115
6.3.1 Global radiation . . . 116

6.3.2 Cloud cover 119
6.3.3 Discussion 121
6.4 Future changes in Belgium 124
6.4.1 Global radiation 125
6.4.2 Cloud cover 125
6.4.3 Discussion 127
6.5 Chapter conclusion 132

7 General conclusions and perspectives 135

7.1 Conclusions 136
7.1.1 On the added value of MAR and the sources of uncertainty in the simulations 137
7.1.2 On the current and future evolution of hydroclimatic conditions favouring floods 139
7.1.3 On the current and future evolution of global radiation and cloudiness 141
7.2 Potential improvements in the MAR physics 143
7.2.1 Improvement of convection parameterization in MAR 143
7.2.2 Improvement of cloud microphysics in MAR 144
7.2.3 Improvement of the surface and soil properties in MAR . . . 145
7.3 Perpectives 146
7.3.1 Using the same methodology for other catchments 146
7.3.2 Using a hydrological model to simulate river discharge . . . 146
7.3.3 Studying the impact of snow cover changes on the ecosystem of the High Fens 147
7.3.4 Using MAR for the evaluation of photovoltaic system yield . 147

References 149

Appendix **173**

A Additional figures for Chapter 3 174

B Additional figures for Chapter 4 183

C Additional figures for Chapter 5 184

CHAPTER 1

General introduction to past and projected future climate changes in Belgium

1.1 Belgium and its mean climate

In Western Europe, between 49° 30' and 51° 30' N, and 2° 30' and 6° 30' E, lies the Kingdom of Belgium, a small, low-lying, and densely populated country (Figure 1.1). In fact, its 11 millions inhabitants live together on a 30,528 km^2 area entirely situated within the 0–700 m elevation range. A 66 km-long coast meets the North Sea in north-western Belgium while maximum elevations are found on the high plateaus of the Ardennes massif located in south-eastern Belgium (maximum elevation = 694 m above sea level on the High Fens plateau) (Erpicum *et al.*, 2018). On the basis of its elevation, Belgium is usually divided into three regions: Low Belgium lies between 0 and 100 m, Middle Belgium lies between 100 and 200 m while High Belgium includes regions above 200 m.

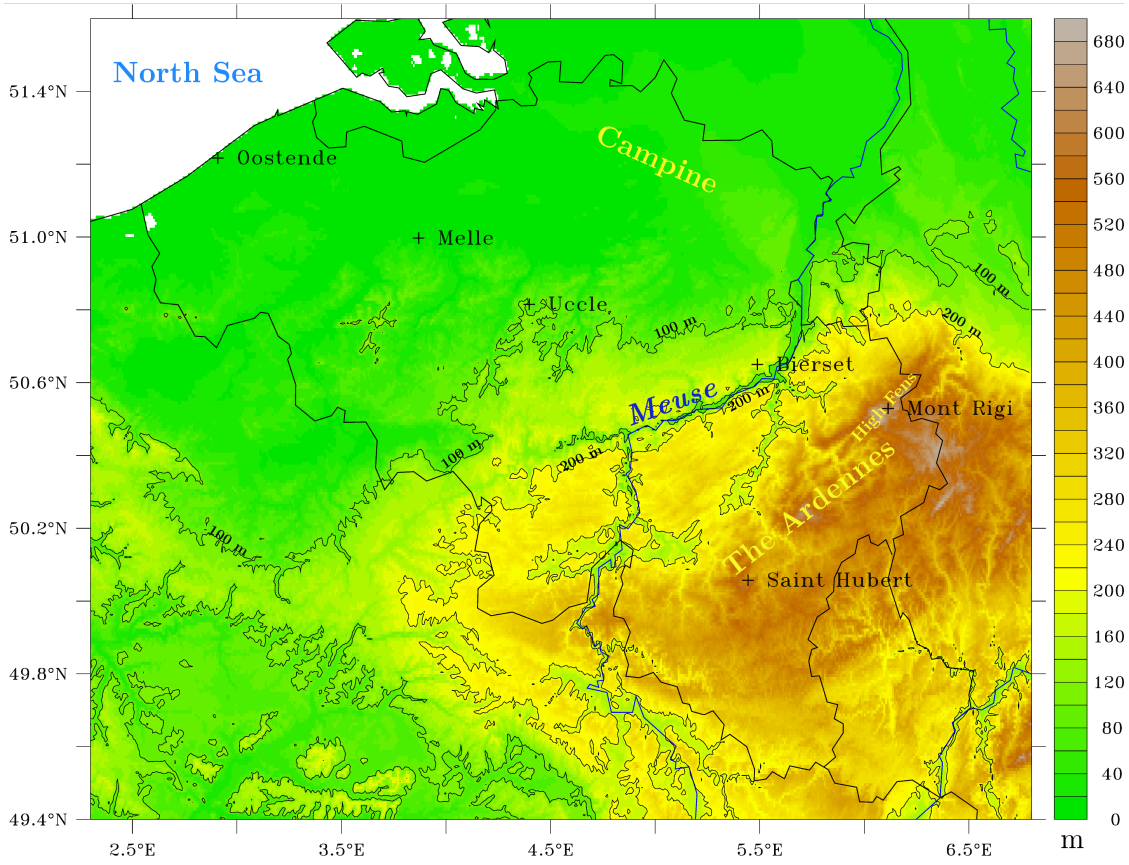

Figure 1.1: Physical map of Belgium. Data: Global Land One-kilometre Base Elevation (GLOBE) Digital Elevation Model.

Given its mid-latitude position and its proximity to the North Atlantic Ocean, Belgium has a temperate oceanic climate, a *Cfb* climate according to the updated classification of Köppen-Geiger (Peel *et al.*, 2007). The following

description of the climate of Belgium is mainly based on the work of Alexandre *et al.* (1992), Erpicum *et al.* (2018) and RMIB (2018). The mean annual temperature at 2 m ranges from 7.5 °C on the Ardennes high plateaus to 11 °C in Low Belgium (Figure 1.2(a)). In summer, the mean temperature is the warmest in Campine (north-eastern Belgium) reaching 18 °C (Figure 1.2(d)). In winter, the mean temperature is positive but hovers near zero in the highest parts of the Ardennes (Figure 1.2(b)). Elevation is the main cause of spatial variations in temperature although the nature of the soil, a Foëhn effect in the Ardennes, the distance to the North Sea and also site effects related to densely urbanized areas locally alter this temperature pattern. For instance, sandy soils cause above-average mean summer temperature and above-average temperature amplitudes in Campine (Figure 1.2(d)). The proximity of the North Sea allows mild winter and summer temperatures in coastal regions (Figure 1.2(b)-(d)). The mean temperature is also slightly warmer on the rain shadow side of the Ardennes than on its windward side which has intercepted rainfall and dried out westerlies. Temperature is higher in densely urbanized areas than in the surrounding rural areas as a result of a lack of evapotranspiration and the absorption of solar radiation by dark surfaces such as asphalt and concrete. This effect is called the urban heat island and causes a mean summer bias of about +0.8 °C in Brussels, for instance (Hamdi and Van de Vyver, 2011).

Westerlies bring precipitation throughout the year although Belgium experiences a fair minimum during the spring months (MAM for March-April-May) and a maximum during the winter months (DJF for December-January-February) (Figure 1.3(b)-(c)). On average, Belgium receives a total of 800 mm year^{-1} (Figure 1.3(a)). Elevation, and exposure to the dominant winds (south-western winds) are the main causes of the spatial variations of the precipitation amount and extremes (Sneyers *et al.*, 1989; Journée *et al.*, 2015). Mean annual precipitation amount ranges from 740 mm in western Belgium and in downwind areas of east-central Belgium, to 1300–1400 mm on the High Fens plateau (Erpicum *et al.*, 2018; RMIB, 2018).

Precipitation mainly falls as rain but snowfall events are frequent in winter especially in the Ardennes (Figure 1.4) where these events can generate a seasonal snow cover. On the high plateaus of the Ardennes, this seasonal snow cover can last from one to two months per year on average, and can reach up to 70-80 cm thick for the most snowy winters with consequences on water management, biodiversity and tourism activities:

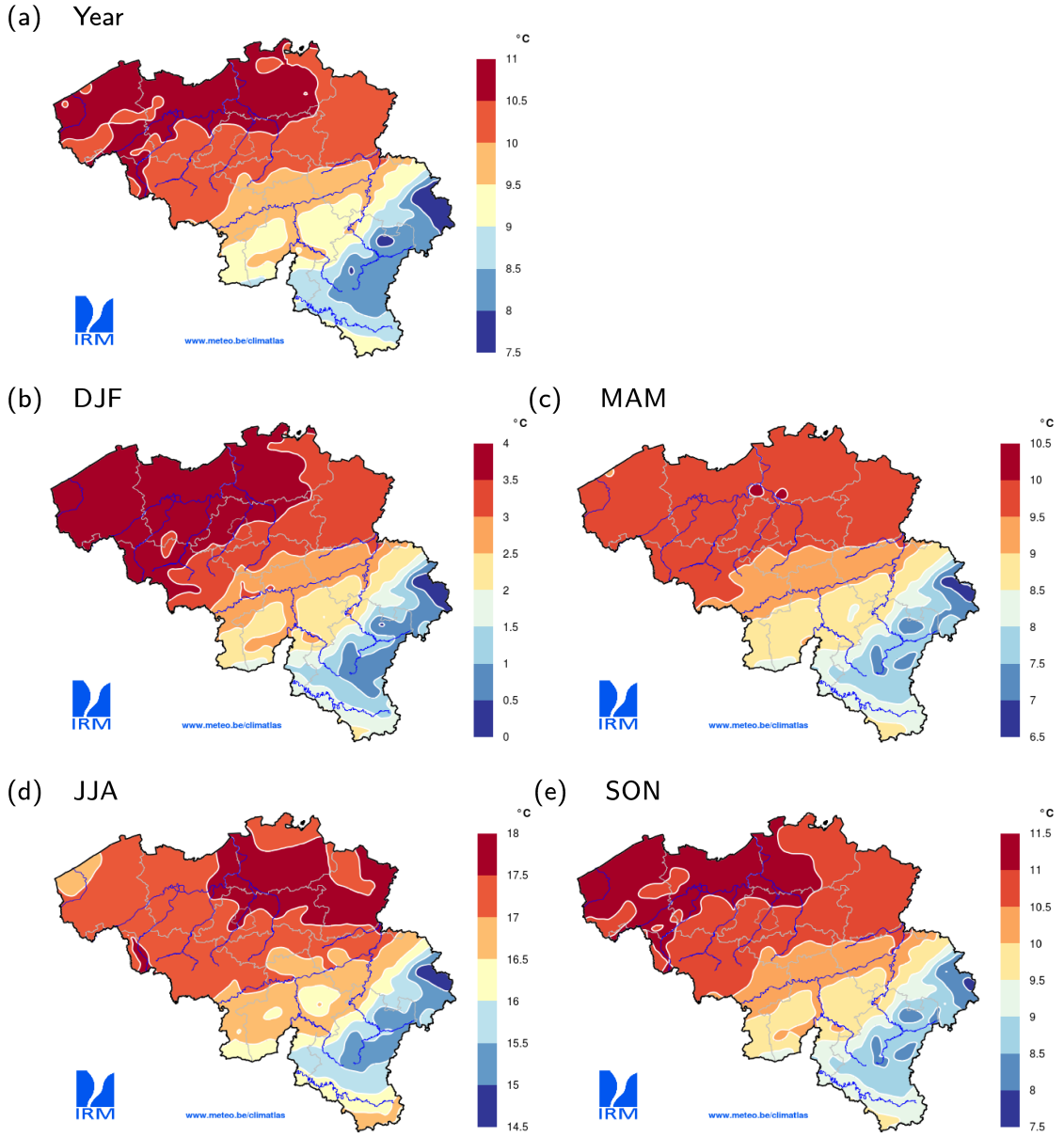

Figure 1.2: Annual and seasonal mean temperature at 2 m measured in Belgium over 1981–2010: **(a)** annual, **(b)** winter (DJF), **(c)** spring (MAM), **(d)** summer (JJA), and (e) autumn (SON). This figure has been modified from RMIB (2018).

– Although snow is a minor component of the Belgian climate, the rapid melting of the snow cover combined with rainfall during a sudden return to milder conditions is responsible for 50% of the floods recorded in the Ardennes valleys such as the major floods in the lower part of the Ourthe River in February 1984, March 1988, December 1991 or, more recently, in January 2002 and January 2011 (Pauquet and Petit, 1993; de Wit *et al.*, 2007; Erpicum *et al.*, 2018).

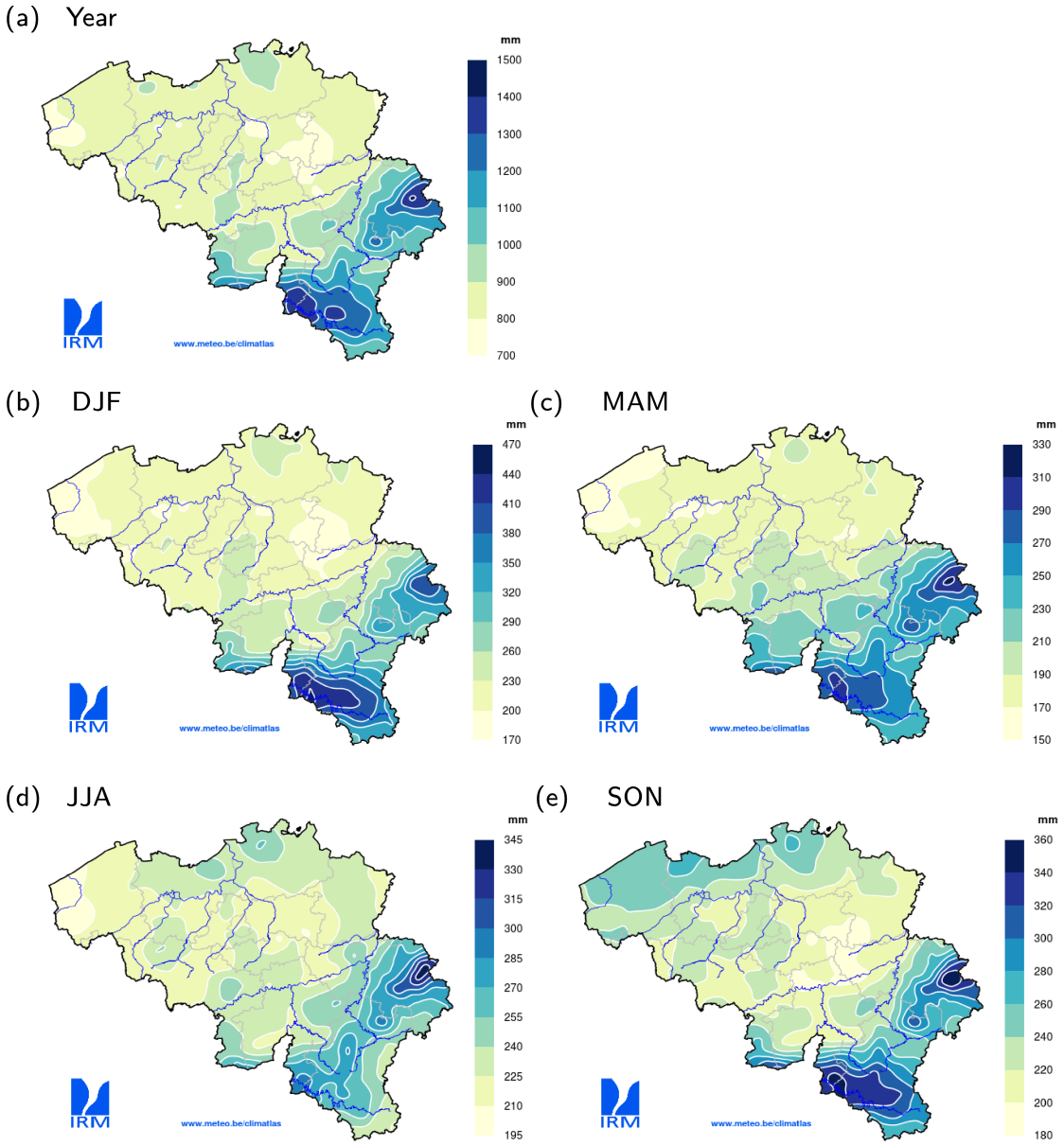

Figure 1.3: Annual and seasonal mean precipitation amount measured in Belgium over 1981–2010: **(a)** annual, **(b)** winter (DJF), **(c)** spring (MAM), **(d)** summer (JJA), and **(e)** autumn (SON). This figure has been modified from RMIB (2018)

— The seasonal snow cover of the Ardennes allows the existence of a remarkable ecosystem at this range of altitude (between 500 and 700 meters a.s.l.) and latitude (between 49 °N and 51 °N), with subarctic animal and plant species surviving to extreme cold temperatures in the winter months thanks to the protective snow cover that acts as a thermal insulator. These parts of the country are therefore subject to nature protection and restoration projects such as LIFE projects mainly funded by the European Union (Plunus *et al.*,

2012).

– Both the peculiar climate and ecosystem of the Belgian high plateaus also generate tourism activities, especially in winter (skiing, hiking, educative walks).

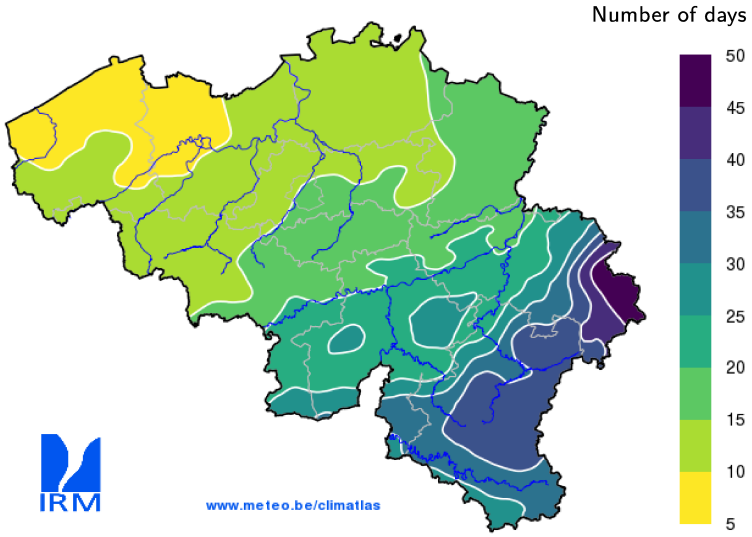

Figure 1.4: Annual mean number of days with snowfall observed in Belgium over 1985–2014. This figure has been modified from RMIB (2018)

A main characteristic of the Belgian climate is the high number of overcast days (60–75% from November to March) and days with cumuliform clouds (80% on average from April to October) (Erpicum *et al.*, 2018). Daily mean sunshine duration is as low as 4 hours day^{-1} on the Haute Fagnes Plateau whereas coastal regions experience 5 hours day^{-1} on average depending on cloudiness (Figure 1.5(a)). Seasonal variations are large as a result of the evolution of the day length throughout the year. Hence, sunshine duration reaches maximum values in spring (5.5 hours day^{-1} on average) and summer (6.5 hours day^{-1} on average) (Figure 1.5(c)-(d)). Regarding global radiation (the total amount of solar radiation received at the surface), Belgium receives on average 110 W m^{-2}. Global radiation is subject to large seasonal variations from about 35 W m^{-2} in winter to about 200 W m^{-2} in summer on average. Spring has values around 150 W m^{-2} while autumn has values around 80 W m^{-2}. The yield of photovoltaic systems is therefore the greater in spring and in summer.

As for the rest of Europe, the climate of Belgium undergoes a large natural variability driven by the variations of the North Atlantic circulation especially

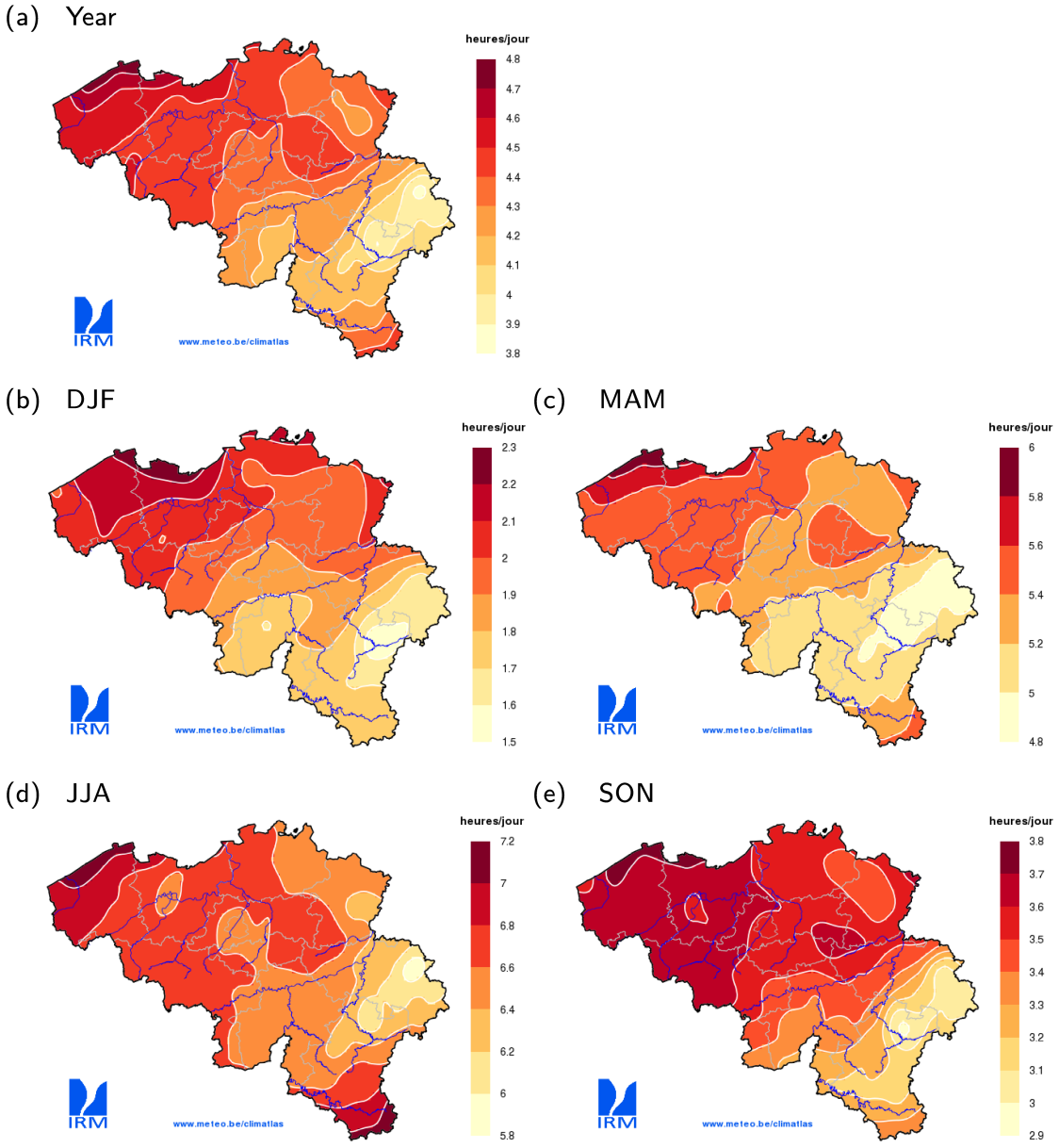

Figure 1.5: Annual and seasonal daily mean sunshine duration in Belgium over 1984–2013: **(a)** annual, **(b)** winter (DJF), **(c)** spring (MAM), **(d)** summer (JJA), and **(e)** autumn (SON). This figure has been modified from RMIB (2018).

in winter. In fact, the European wintertime climate is known to be strongly constrained by the occurrence and the persistence of quasi-stationary circulation patterns of larger scale also referred to as "weather regimes" (Reinhold and Pierrehumbert, 1982; Legras and Ghil, 1985; Vautard, 1990; Philipp *et al.*, 2007). Its day-to-day and year-to-year variability is usually assessed using the North Atlantic Oscillation (NAO) index (Hurrell, 1995; Slonosky and Yiou, 2001; Philipp *et al.*, 2007). The NAO index is defined as the difference in atmospheric surface pres-

sure between the Azores High and the Icelandic Low, which corresponds to the normalized difference of sea level surface pressure measured in Lisbon (Portugal) and in Stykkisholmur/Reykjavik (Iceland). Studies usually classify the wintertime atmospheric circulation patterns into four categories (Figure 1.6) (Cassou, 2008; Cattiaux *et al.*, 2010, 2013):

- The negative phase of NAO (NAO-) is associated to a weak pressure difference between the Icelandic Low and the Azores High causing the air flow and the jet stream to weaken, which often brings cold, dry, and snow conditions over Belgium (Figure 1.6(a)).
- A high barometric difference between the Icelandic Low and the Azores High is associated to the positive phase of NAO (NAO+). Westerlies and jet stream are strong, bringing mild and wet weather to Belgium (Figure 1.6(b)).
- The persistence of a high-pressure system over the North Atlantic Ocean, also referred to as "Atlantic ridge", allows inflow of Arctic maritime air and is associated with cold and snowy conditions (Figure 1.6(c)).
- The persistence of a high-pressure system over Northern Europe or the British Isles, often referred to as "Scandinavian blocking" conditions, leads to cold and dry weather over Western Europe (Figure 1.6(d)).

For instance, the persistence of the NAO- regime is responsible for the 2009–2010 cold and snowy winter in Belgium (Cattiaux *et al.*, 2010).

1.2 Belgium under climate change

1.2.1 Observed climate changes

Despite its large interannual variability, significant changes have already been recorded in the climate of Belgium. Between 1850 and 2013, Belgium annual average **temperature** has increased faster than world and even Europe annual average temperature with values of +2 °C, +0.8 °C and +1.30 °C respectively (Brouwers *et al.*, 2015). Spring exhibits the largest increase in temperature with values around +3 °C. On the contrary, winter shows the lowest temperature increase (+2 °C) but this increase is significant according to Brouwers *et al.* (2015) despite the strongest interannual variability and the influence of NAO observed in

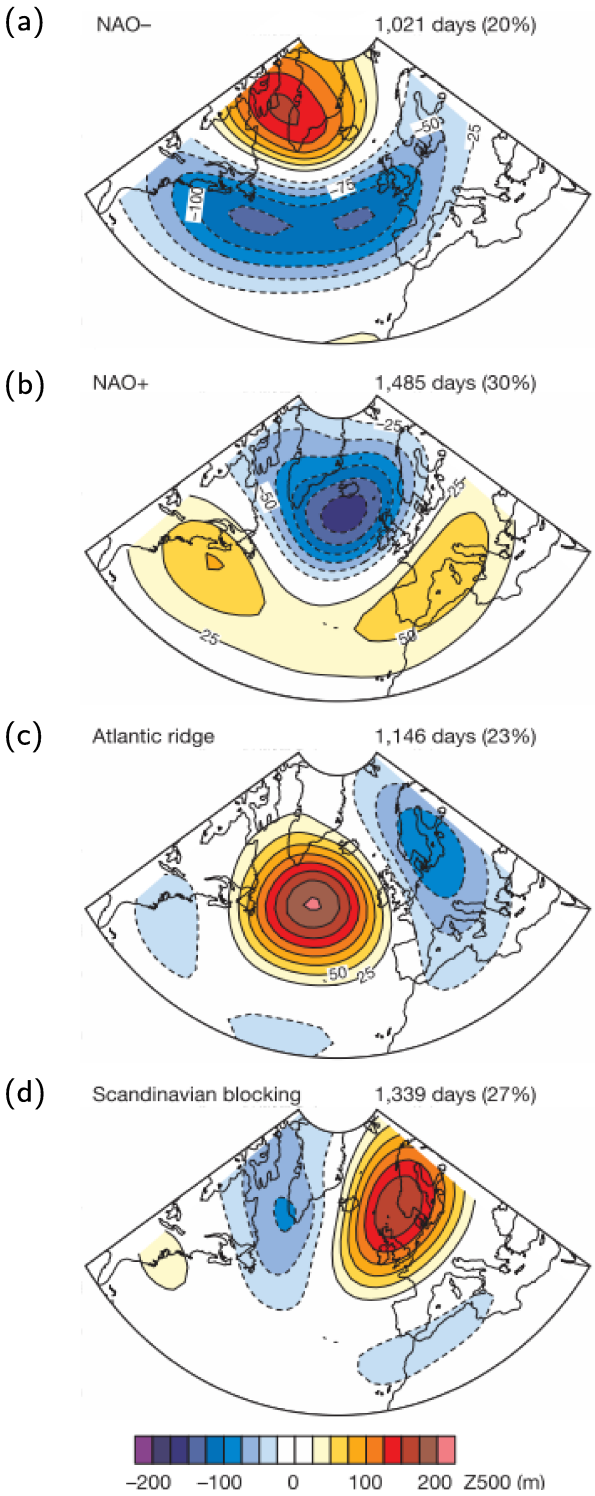

Figure 1.6: Wintertime North Atlantic weather regimes. Centroids of the four regimes obtained from daily anomalies of the geopotential height at the 500-hPa altitude (Z500) from the NCEP/NCAR-v1 reanalysis. Each percentage corresponds to the stated number of days and represents the mean frequency of occurence of the regime computed over 1974–2007 1 November to 31 March. Countour intervals are 25 m. This figure has been taken from Cassou (2008).

winter (Section 1.1). Temperature has not steadily increased over time. RMIB (2015) highlight a first abrupt increase between the 1910s and the beginning of the 1950s followed by a second abrupt increase since the end of the 1980s. Regarding temperature extremes, Van de Vyver (2012) found that both extreme minimum and maximum temperature (Tmin and Tmax) have increased since 1952 for nine weather stations spread over the Belgian territory. Over 1952-2012, extreme daily Tmin (5^{th} percentile of the daily Tmin) has increased by 0.5 °C decade^{-1}. Extreme daily Tmax (95^{th} percentile of the daily Tmax) has increased by 0.5 °C decade^{-1}. The frequency of heat waves has increased since the beginning of the 1990s (RMIB, 2015). On the contrary, the frequency of cold spells has decreased since the beginning of the 1970s as a result of a decrease in the frequency of frost days (Tmin $<$ 0 °C).

Trends in **precipitation** amount and extremes have been widely investigated in the literature. Studies based on observations (Gellens, 2000; Vaes G, Willems P, 2002; De Jongh *et al.*, 2006; Ntegeka and Willems, 2008; Willems, 2013a,b) found no significant long-term trend over the last century in any part of the Belgian territory. Despite the absence of significant long-term trend, these studies identify multidecadal oscillations characterized by drier periods in the 1900s, around 1920, and in the mid-1970s (De Jongh *et al.*, 2006; Willems, 2013a,b) alternating with wetter periods in the 1910–1920s, the 1950–1960s, and in the 1990–2000s (Ntegeka and Willems, 2008; Willems, 2013a,b) along with the decadal variations of NAO. However, by analysing the entire time-series of Uccle, Brouwers *et al.* (2015) and RMIB (2015) stated that the annual precipitation amount has increased by +10 % since the beginning of the measurements (1833) as a result of increasing temperature and increasing evapotranspiration. Precipitation amount has only significantly increased in winter while no significant trend has been observed in the other seasons. These trend go along with the increase in precipitation observed in Northern Europe during winter whereas Southern Europe has undergone a decrease in precipitation in summer. Regarding drought, no clear trend was found in Belgium.

Regarding **wind**, the average inland wind speed has decreased from -10 to -15 % since 1960s. The number of days with wind surges above 70 km/h exhibits no clear trend, nor do the highest measured wind speeds (Brouwers *et al.*, 2015).

As a consequent of increasing temperature, significant reductions in snowfall amount, annual average **snow** cover extent, snow depth and earlier snowmelt have been observed in various European regions such as the Alps (Durand *et al.*,

2009; Valt and Cianfarra, 2010; Beniston, 2012a), Britain (Kay, 2016), Norway (Skaugen *et al.*, 2012; Dyrrdal *et al.*, 2013), or Eastern Europe (Falarz, 2004; Brown and Petkova, 2007; Birsan and Dumitrescu, 2014). This declining snow cover is responsible for a decrease in the intensity and in the frequency of the floods dominated by snowmelt which is predicted to accelerate in the future (Madsen *et al.*, 2014; Bell *et al.*, 2016; Vormoor *et al.*, 2016). In Belgium, despite its implications for water management, biodiversity and economy of High Belgium (Section 1.1), very few studies about the recent evolution of seasonal snow cover have been carried out. Moreover, these studies, which do not cover the last two decades (1990–2015), have been conducted either over much shorter periods (Sneyers, 1967a,b; Erpicum *et al.*, 1991), or on a more limited number of weather stations (Sneyers, 1965) to build robust statistics. The report written by RMIB (2015) investigates the recent evolution of snowfall and snow accumulation using the few existing measurements. In fact, RMIB (2015) stated that snow cover records over the Belgian territory are patchy, discontinuous or made with techniques that change over time. For instance, the number of days with snowfall events is recorded since 1901 but for Uccle only which is located in Middle Belgium while snow is a important parameter especially for High Belgium. Nevertheless, the Uccle time-series is characterized by a large interannual variability and by a decrease in the frequency of snowfall events which is first observed in the 1920s and later in the 1980s. These decreases coincide with the abrupt warming observed during these periods. Regarding snow cover, only two long time-series exist in Belgium. Snow height is measured at Uccle since the end of the 19th century. This time series shows again the strong interannual variability which characterized the Belgian winter climate but no long-term significant trend. Snow height was also measured at Saint-Hubert (High Belgium) since 1948 but measurements stopped in 2008. A decrease in the maximum snow height was observed between 1990 and 2008. A snow depth laser sensor was installed at the Mont Rigi weather station (High Belgium, High Fens plateau) in 2001 and provides continuous snow depth measurements. However, the Mont Rigi time-series is too short to be exploited for trend study. **Given the scarcity of snow observations in Belgium, the validity of these trends is therefore questionable. In addition, given the trends observed over other European massifs and the importance of snow for the hydrology, the ecology and the economy of High Belgium, we are therefore wondering if global warming is already influencing snow processes in the country.**

Global radiation, for its part, has been measured at Uccle since 1951, at Saint-Hubert since 1962, at Melle since 1967 and at Oostende since 1975. Uccle and Saint-Hubert exhibit a significant decrease during 1950–1980 followed by a partial recovery since the 1980s measured for all stations (De Bock *et al.*, 2014). In fact these trends have been observed worldwide. The 1950–1980 decrease in global radiation is known as the "global dimming" and was caused by massive aerosol emissions in the atmosphere and to the subsequent increase in cloud cover (De Bock *et al.*, 2014). On the one hand, aerosols such as sulphate particles directly modify global radiation by scattering and/or absorbing solar radiation (aerosol-radiation interactions) (Marmer *et al.*, 2007; Schulz *et al.*, 2006; Cherian *et al.*, 2014; Yang *et al.*, 2016a,b). In addition, aerosols modify cloud properties (aerosol-cloud interactions) by changing the amount of cloud condensation nuclei which also changes the albedo (Twomey, 1977) and the lifetime of clouds (Lohmann and Feichter, 2005). On the other hand, low to medium clouds reflect solar radiation towards space, which affects variations on monthly to decadal time scales (cloud-radiation interactions) (Chiacchio and Wild, 2010; Norris and Wild, 2007). The partial recovery which has followed the dimming period is referred to as "brightening" in the litterature. The brightening only concerns Northern America and Western Europe which cut their emissions of air pollutants, including sulphates, following the ratification the 1979 Convention on Long-range Transboundary Air Pollution (Sliggers and Kakebeeke, 2004). The resulting decrease in the aerosol load in the atmosphere also impacts cloud properties. A decrease in cloud cover was observed since 1979 in Western Europe. However, despite a stabilisation of the aerosol concentration since the 2000s which has also been recorded at Uccle, cloud cover is still decreasing (De Bock *et al.*, 2014). Changes in the large-scale circulation are suspected to be responsible for this declining cloud cover. **The origin of the recent decrease in cloud cover and therefore the recent increase in global radiation observed since the 2000s is unclear and requires further investigation.**

1.2.2 Future climate changes

The assessment of future climate changes is made by using climate models constrained by greenhouse gas concentration scenarios or by the corresponding radiative forcing. The most recent scenarios are the "Representative Concentration Pathway" (RCP) which were developed by IPCC for AR5 (Moss *et al.*, 2010). Four RCPs were designed depending on how much greenhouse gases are emitted in the

years to come. RCP2.6, RCP4.5, RCP6.0 and RCP8.5 are labelled after a possible range of radiative forcing values in the year 2100 relative to pre-industrial values (+2.6, +4.5, +6.0, and +8.5 W m^{-2}, respectively). The most optimist scenario is RCP2.6 (low climate change scenario) while the most pessimist is the RCP8.5 (high climate change scenario). Table 1.1 provides an overview of three possible future climates in Belgium using the RCP2.6, RCP4.5 and RCP8.5 scenarios.

Regarding future changes in **temperature** by 2100, Brouwers *et al.* (2015) show increasing trends in annual average temperature and in frequency of extremely hot days (with daily average temperature above 25 °C). The magnitude if these trends depends on the scenario: the higher the scenario, the larger is the increase. Annual average temperature is predicted to increase by +0.7 °C by 2100 under RCP2.6 while the increase would reach +7.2 °C under RCP8.5 in central Belgium (Table 1.1). The frequency of extremely cold days (with daily average temperature below 0 °C), for its part, is predicted to decrease from -1 to -33 days $year^{-1}$.

Regading future changes in **precipitation** by 2100, the trends are much less clear because the pattern and the sign of the trends depend on the future scenario and the model used (Baguis *et al.*, 2010; Brouwers *et al.*, 2015; Tabari *et al.*, 2015; Saeed *et al.*, 2017; Vanden Broucke *et al.*, 2018). For instance, by using two regional climate models Brouwers *et al.* (2015) show that total winter and summer precipitation is predicted to decrease by -1 and -52 % respectively under RCP2.6 while it is predicted to increase by +38 and +18 % respectively under RCP8.5 (Table 1.1). By analysing 30 global climate models, (Tabari *et al.*, 2015) brought to light contrasting trends which depend on the model used. Nevertheless, whatever the future scenario, the ensemble mean suggests an increase in the total winter precipitation and a decrease in summer (Tabari *et al.*, 2015) which contrasts with the results presented in Brouwers *et al.* (2015).

The trends in the **wind** speed are unclear as well. By 2100, daily average wind speed is predicted to decrease from -28 % and -1 % under RCP2.6 and RCP4.5 respectively while an increase of about +11 % is found under RCP8.5 (Table 1.1).

Regarding future changes in **global radiation**, there is no studies focussing on Belgium as shown in Table 1.1). A limited number of papers describe the scenarios of $E_{g\downarrow}$ changes for Europe based on global climate simulations (Crook *et al.*, 2011; Gaetani *et al.*, 2014; Wild *et al.*, 2015), regional climate simulations (Pašičko *et al.*, 2012; Panagea *et al.*, 2014; Jerez *et al.*, 2015) or both (Bartók

Table 1.1: Overview of possible climate change for Belgium according to the low (RCP2.6), medium (RCP4.5), and high (RCP8.5) climate scenario, over 30 (2030), 50 (2050) and 100 (2100) years. This table has been taken from Brouwers *et al.* (2015).

change for	over number of years	climate scenario			additional info
		low	medium	high	
annual average temperature	30	+0.2 °C	+1.1 °C	+2.2 °C	The coast has a mitigating effect on warming, but the effect is small with respect to the expected climate change.
	50	+0.3 °C	+1.8 °C	+3.6 °C	
	100	+0.7 °C	+3.7 °C	+7.2 °C	
average number of extremely hot days per year	30	0	+5	+19	The number of extremely hot days increases the most in the centre of Belgium.
	50	0	+8	+32	
	100	0	+16	+64	
average number of extremely cold days per year	30	0	-2	-10	The number of extremely cold days decreases the most in the Ardennes.
	50	-1	-4	-17	
	100	-1	-7	-33	
total winter precipitation	30	-0.4 %	+3 %	+11 %	Winter precipitation increases more along the coast.
	50	-0.6 %	+6 %	+19 %	
	100	-1 %	+12 %	+38 %	
total summer precipitation	30	-16 %	-4 %	+5 %	Extreme summer precipitation intensities may increase significantly. Spatially, a north-south pattern is emerging with greater desiccation in the south of the country.
	50	-26 %	-7 %	+9 %	
	100	-52 %	-15 %	+18 %	
number of wet days in winter	30	-1 %	+0.5 %	+2 %	
	50	-2 %	+0.8 %	+4 %	
	100	-5 %	+1.5 %	+8 %	
number of wet days in summer	30	-12 %	-5 %	+1 %	
	50	-21 %	-8 %	+2 %	
	100	-41 %	-15 %	+4 %	
total potential evapotranspiration in winter	30	+0.5 %	+3 %	+11 %	
	50	+1 %	+6 %	+18 %	
	100	+2 %	+12 %	+35 %	
total potential evapotranspiration in summer	30	+0.5 %	+5 %	+14 %	
	50	+1 %	+8 %	+23 %	
	100	+2 %	+17 %	+47 %	
daily average wind speed in winter	30	-8 %	0 %	+3 %	
	50	-14 %	-0.5 %	+6 %	
	100	-28 %	-1 %	+11 %	

et al., 2017). The results show contrasting trends depending on the type of model used. Global climate models simulate an increase in global radiation over our regions while regional climate models simulate a decrease in global radiation by 2100 under RCP8.5 (Bartók *et al.*, 2017).

As global radiation, the assessment of future changes in **snow** cover is characterized by an absence of studies focussing on Belgium as illustrated in Table 1.1).

In the end, the future response of the climate to increasing greenhouse gas concentration is not clear in Belgium, especially with regard to the perturbations of the precipitation regime, snow cover, and global radiation. On the one hand, existing studies show results which differ strongly either according to the future scenario, or from one model to another or from one model type to another, namely from global climate models to regional climate models. On the other hand, there is even a complete lack of studies focussing on Belgium regarding future snow cover and future global radiation. Given their potential impacts on the society (water management, energy supply, biodiversity, tourism), future changes in precipitation, snow cover, and global radiation require further research.

1.3 Regional versus global climate models

In absence of measurements, **reanalyses** are a feasible way to produce long-term estimates in every point of the territory. A reanalysis is an analysis of the state of the atmosphere for an extended period of time built by using a global model into which observations have been assimilated. Reanalyses are therefore the best where the density of observation is the largest i.e. mainly in developed countries such as Northern America and Europe. However, despite being constrained by the observations, reanalyses have been proven to have systematic biases as a result of deficiencies in their data assimilation system and their physics. For instance, by comparing the NCEP/NCAR reanalysis products to satellite data from Meteosat second generation Babst *et al.* (2008) found biases in global radiation ranging from $+40$ W m^{-2} to $+80$ W m^{-2} for Europe.

For the evaluation of past (before measurements) and future climate variability, **global climate models** (GCM) forced by emission scenarios provide climate scenarios covering the entire Earth. However, as most reanalyses, their spatial resolution is usually poor and turns around 40 to 200 km. In addition, GCMs are made to provide a good representation of the global mean climate so that significant regional biases can be found.

Compared to GCMs, **regional climate models** (RCM) simulate the climate over a limited area at a finer spatial resolution and are calibrated for a specific region with a more detailed physics developed for it. Coarse-resolution reanalysis or GCM fields usually prescribe the large-scale circulation at the lateral boundaries of RCM, so that RCMs provide downscaled and possibly improved reanalysis or GCM outputs over a limited area (Flato *et al.*, 2014). Further, compared to GCMs and global reanalyses, RCMs run over a limited area so that computation time is reduced. Therefore, for an identical computation time, the spatial resolution of RCMs can be increased up to 2 km. It implies that the orography and other surface characteristics are finer in RCMs than in GCMs. Finally, the GCM physics is usually less detailed than in RCMs as a result of computation time. For instance, most of the GCMs do not simulate snow processes while some RCMs do. International frameworks such as CORDEX (Coordinated Regional Climate Downscaling Experiments) evaluate RCM performances and added-values against GCMs and aim at producing regional climate projections over various regions of the world such as Europe (EURO-CORDEX) (Giorgi and Gutowski, 2015). The EURO-CORDEX effort was preceded by PRUDENCE (http://prudence.dmi.dk/) and ENSEMBLE (http://ensembles-eu.metoffice.com/), both funded by the European Union (EU) in order to perform ensemble RCM future projections over Europe. Project results are reported in the EU Climate Change Reports (EEA, 2012, 2017) and in the latest IPCC Assessment Report (AR5) (Kovats *et al.*, 2014).

In light of the above, high-resolution RCMs are particularly indicated for the simulation of the climate of Belgium. As detailed in Section 1.1, the orography, the exposition to the dominant winds, and the proximity of the North Sea determine a large spatial variability in the climate which therefore requires a fine representation of these features to be properly simulated. More specifically, the representation of orographic features is a key factor for the simulations of temperature, precipitation, and snow. Temperature is indeed influenced by elevation while snow depends on the 0 °C isotherm location and height. Moreover, the orography of Belgium is shown to have a clear effect on precipitation averages and associated extremes (Sneyers *et al.*, 1989; Journée *et al.*, 2015).

A Belgian CORDEX project (CORDEX.be) has therefore been funded between 2015 and 2017 with the aim to provide a coherent scientific basis for future climate services in Belgium by performing high-resolution historical and future simulations using RCMs (Termonia *et al.*, 2018). CORDEX.be involves three RCMs. The ALADIN and AROME combined model (ALARO-0 model)

has already been used over Belgium to model extreme events in summer such as Urban Heat Island (Hamdi *et al.*, 2014) and precipitation (De Troch *et al.*, 2013). The COSMO-CLM (COnsortium for Small-scale MOdeling) model has already been used over Belgium to model temperature, precipitations, clouds, radiation (Brisson *et al.*, 2016; Saeed *et al.*, 2017), and also urban climate (Wouters *et al.*, 2015). These RCMs have already been used for the study of future trends in the climate of Belgium as done in Brouwers *et al.* (2015). However, these RCMs both exhibit biases in temperature, precipitation, cloud cover, and radiation (De Troch *et al.*, 2013; Hamdi *et al.*, 2014; Brisson *et al.*, 2016). The third RCM involved in the CORDEX.be project is MAR ("Modèle Atmosphérique Régional" in French) which is developed in the Laboratory of Climatology and Topoclimatology of the University of Liège. MAR was never applied to Belgium before. However, compared to ALARO-0 and COSMO-CLM, MAR has the advantage to sophistically simulate snow accumulation, metamorphism, and melt (Gallée *et al.*, 2013). Nevertheless, the evaluation of the ability of MAR for the simulation of the climate of Belgium still have to be carried out.

1.4 Objectives

This PhD thesis has three objectives:

1. In the framework of the CORDEX.be project, MAR was one of the RCMs chosen to perform high-resolution simulations over Belgium (Termonia *et al.*, 2018). MAR was never applied to Belgium before and its ability for the simulation of the climate of Belgium still have to be proven. **This PhD thesis aims at evaluating the ability of MAR for the reconstruction and for future projections under RCP8.5 of the climate of Belgium. The added-value of MAR against reanalyses and GCMs is also investigated.**

2. Despite its consequences on water management, biodiversity and tourism activities, the seasonal snow cover which covers the Ardennes in winter has been poorly documented. Observations are rare and there is an absence of recent studies regarding the evolution of snow cover in Belgium. **This PhD thesis investigates the current (1959–2010) and the future (2006–2100) evolution of the Belgian winter climate, including snow cover using MAR. This thesis also deals with the potential impact of**

changes in seasonal snow cover and precipitation on hydroclimatic conditions generating floods in the south-east of Belgium. Among the several rivers which drain the Ardennes massif, we have focussed on the Ourthe River which is the largest one with a catchment area of about 3500 km^2 (Pauquet and Petit, 1993). This river is also the main tributaries of the Meuse River, which is one of the largest rivers of Western Europe, with a catchment area of about 36,000 km^2 and a length of 950 km. More specifically, we have focussed on the Ourthe River catchment upstream of Sauheid.

3. The current evolution of global radiation is well-documented and show decadal fluctuations resulting from aerosol-radiation interactions, cloud-radiation interactions and aerosol-cloud interactions. However, uncertainties remain regarding the causes of the increase in global radiation and the decrease in cloud cover observed since the 1980s. In addition, despite its potential impacts on the climate system and on the energy supply, no study has especially focused on the future evolution of global radiation in Belgium despite the growing production of solar energy expected in the country. **This PhD thesis investigates the current (1959–2010) and future evolution (2006–2100) under RCP8.5 of global radiation and cloudiness in Belgium using MAR.**

1.5 Thesis outline

This doctoral thesis consists of seven chapters which are based on the results of four papers. The structure of this doctoral thesis is summarized in Figure 1.7.

Chapter 2 provides a full description of the MAR model, its forcings data (reanalyses and GCMs), and also the observations used for its evaluation of MAR.

Chapters 3 to 6 present the results achieved during this doctoral thesis. Each of these four chapters corresponds to one paper published or to be submitted to international peer-reviewed journals:

- Chapter 3 is based on Wyard C., Scholzen C., Fettweis X., Van Campenhout J., and François L. (2017) Decrease in climatic conditions favouring

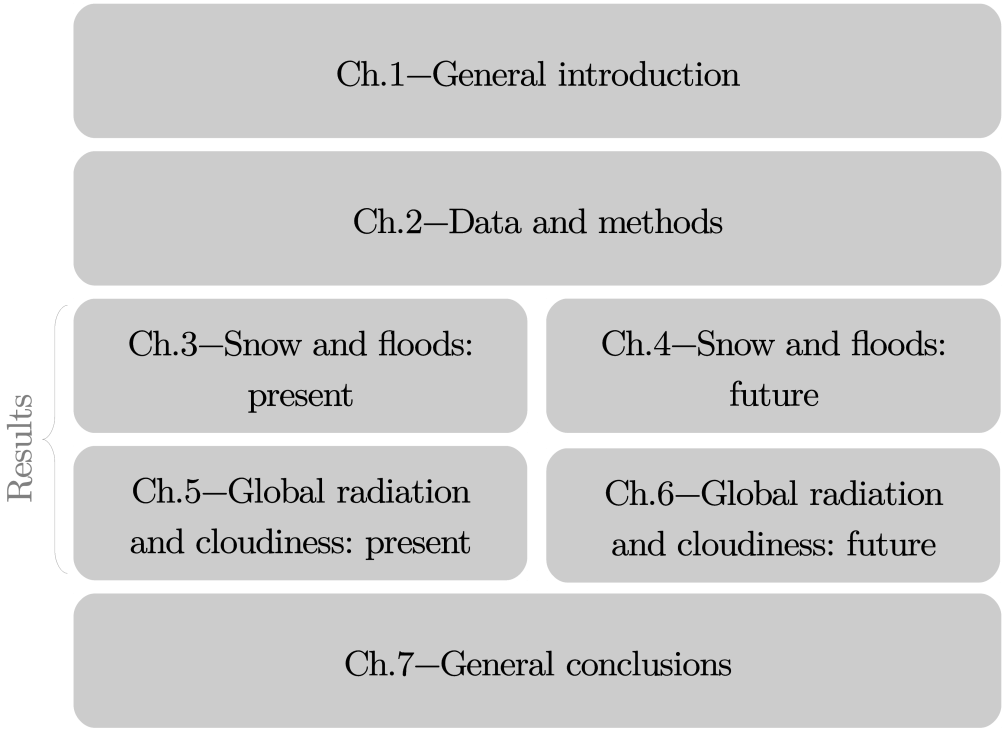

Figure 1.7: Structure of this doctoral thesis.

floods in the south-east of Belgium over 1959-2010 using the regional climate model MAR. *International Journal of Climatology*, **37 (5)**, 2782–2796, doi: 10.1002/joc.4879. This chapter deals with the current evolution of the Belgian seasonal snow cover and extreme precipitation events in winter and their impact on hydroclimatic conditions favouring floods in the Ardennes using MAR.

– Chapter 4 is based on Wyard C., Scholzen C., Doutreloup S., Fettweis X. (2018) Future projections of hydroclimatic conditions favouring floods in Belgium. In review in *International Journal of Climatology*. This chapter investigates the possible future evolution of the Belgian winter climate and its impact on hydroclimatic conditions favouring floods in the Ardennes using MAR and the RCP8.5 scenario.

– Chapter 5 is based on Wyard C., Doutreloup S., Belleflamme A., Wild M., and Fettweis X. (2018) Global Radiative Flux and Cloudiness Variability for the Period 1959–2010 in Belgium: A Comparison between Reanalyses and the Regional Climate Model MAR. *Atmosphere*, **9 (7)**, 262, doi: 10.3390/atmos9070262. This chapter deals with the ability

of MAR the simulate the historical variations in the global radiative flux in Belgium and its added-value with respect to reanalyses and GCMs. The causes of the historical variations in global radiation are also investigated in this chapter.

– Chapter 6 is based on Wyard C., Doutreloup S., Fettweis X. (2018) Future projections of global radiation and cloudiness in Belgium. To be submitted to *Bulletin de la Société Géographique de Liège*. This chapter investigates the possible future evolution of the global radiative flux in Belgium under RCP8.5 using MAR.

Finally, Chapter 7 summarizes and discusses the main results of this PhD thesis. Some perspectives for further research are also discussed.

CHAPTER 2

Data and methods

2.1 The MAR model

2.1.1 Description and experimental set-up

The regional climate model (RCM) used in this study is MAR ("Modèle Atmosphérique Régional" in French). MAR consists of a three-dimensional atmospheric module coupled to the 1-D surface vegetation atmosphere transfer scheme SISVAT (Soil Ice Snow Vegetation Atmosphere Transfer).

The atmospheric part of MAR, fully described in Gallée and Schayes (1994); Gallée (1995) and Gallée *et al.* (2013), is a hydrostatic primitive equation model. Parameterizations are performed to include physical subgrid-scale processes. Convection is parameterized according to Bechtold *et al.* (2001) while the vertical fluxes in the near-surface boundary layer are computed with the turbulence closure model of Duynkerke (1988). Cloud microphysical parameterizations are based on the studies of Kessler (1969); Lin *et al.* (1983); Meyers *et al.* (1992) and Levkov *et al.* (1992), and allow to account for cloud droplet, cloud ice crystal, raindrop and snow flake concentrations. The radiative transfer through the atmosphere uses the radiation scheme from ERA-40 based on Morcrette (2002). It uses time-varying aerosols from monthly climatology of tropospheric aerosols (black carbon, organic, sea salt, sand, and sulphate aerosols) by Tegen *et al.* (1997) and the GISS (Goddard Institute for Space Studies) volcanic aerosols while the cloud microphysics module uses fixed aerosol concentration (Meyers *et al.*, 1992). The aerosol-cloud interactions are therefore not sensitive to the historical variations of the aerosol load in the troposphere. Therefore, we can assume that only the aerosol-radiation interactions and the cloud-radiation interactions are properly taken into account in MAR.

The SISVAT surface scheme, which is detailed in De Ridder and Gallée (1998), consists of a vertical one-dimensional multi-layered model which incorporates both a soil-vegetation module, and a snow-ice module. While the former module works out the heat and moisture fluxes between the snow-uncovered land and the atmosphere, the latter module deals with the exchanges between the snow-covered land, the ice sheet surface, the sea-ice, and the atmosphere. The snow model implemented in SISVAT is CROCUS from the CEN (Centre d'Etudes de la Neige) and is described in Brun *et al.* (1992, 2012). CROCUS itself consists of a thermodynamic module, a water

balance module, a turbulence module, a snow metamorphism module, a snow/ice discretization module, and an integrated surface albedo module. The MAR-SISVAT coupling allows the consideration of three sub-pixel surface characteristics for a same MAR pixel. The coupling also allows interaction between surface and atmosphere (energy and moisture transfers), snow accumulation and snow melting on the surface, water percolation into the soil/snow, and run-off of exceeding water.

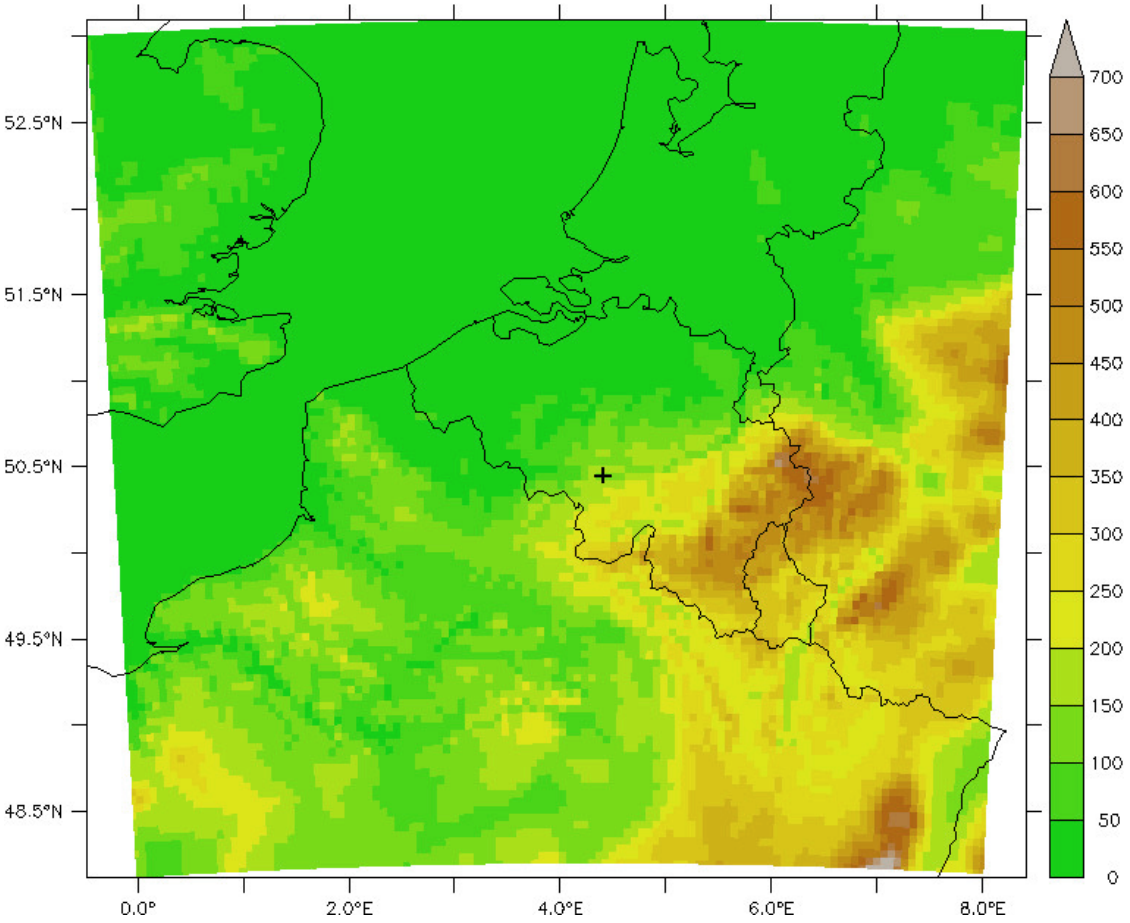

Figure 2.1: MAR "Belgian" integration domain and orography.

Lateral boundary conditions are provided by nesting the MAR RCM into reanalysis or GCM. The nesting method use by MAR is the one-way mode. The one-way nested MAR model is directly forced every 6 hours at its lateral boundaries with the following forcing fields: humidity, temperature, pressure and wind at each vertical level, and sea surface temperature (SST) above the ocean.

Although being initially designed for polar regions (Gallée and Schayes, 1994;

Fettweis *et al.*, 2013), MAR was also applied to temperate (Brasseur, 2001; Brasseur *et al.*, 2002) and tropical regions (De Ridder and Gallée, 1998; Gallée *et al.*, 2004). For the use of this research as well as the CORDEX.be project, MAR was calibrated to the climate of Belgium. Simulations were performed at a horizontal resolution of 5 km over a domain of 120x110 pixels and 24 vertical levels (between 3 m and 18 km above the surface) centred on (4.3°W ; 50.4°N) (Figure 2.1). One spin-up year was required to initialize the soil humidity. Historical runs were obtained by nesting MAR into four reanalysis products, described in Section 2.2, and two GCMs selected from the Coupled Model Intercomparison Project Phase 5 (CMIP5) archive, described in Section 2.3. Future projections were obtained by nesting MAR into both GCMs selected from the CMIP5 archive (Section 2.3) under the RCP8.5 scenario. Table 2.1 summarizes the simulations we performed with MAR over Belgium.

Table 2.1: Simulations performed with the MAR model over Belgium.

Short name	Run type	Forcing	Run period
MAR-ERA	Historical	ERA40/ERA-interim	1959-2016
MAR-NCEP1	Historical	NCEP/NCAR-v1	1949-2016
MAR-ERA-20C	Historical	ERA-20C	1900-2010
MAR-20CRV2C	Historical	20CRV2C	1900-2010
MAR-MIR-histo	Historical	MIROC5	1976-2005
MAR-NOR-histo	Historical	NorESM1-M	1976-2005
MAR-MIR-rcp85	Future projection	MIROC5	2006-2100
MAR-NOR-rcp85	Future projection	NorESM1-M	2006-2100

2.1.2 MARv3.6 versus MARv3.8

Two versions of MAR are used in this doctoral thesis, the version 3.6 and the version 3.8, both developed at the Laboratory of Climatology and Topoclimatology of the University of Liège (Liège, Belgium). Compared to MARv3.6, MARv3.8 delays the onset of precipitation and hence increases cloud cover. In addition, the convective scheme is called twice as often in MARv3.8 than in MARv3.6 so that convective clouds reside longer in the atmosphere before precipitating (Fettweis *et al.*, 2017). Finally, in MARv3.8,

the vegetation seasonality is also better taken into account by using daily Leaf Area Index (LAI) and Green Leaf Fraction (GLF) from the MERRA-2 reanalysis (Gelaro *et al.*, 2017) compared to MARv3.6 which uses monthly values.

Table 2.2: A total of 20 stations averaged statistics of the daily mean temperature observations and the outputs of **MARv3.6** forced by ERA-interim over 2008–2014: correlation coefficient (R), standard deviation (σ), root mean square error (RMSE), daily mean biases (MB) and annual daily mean temperature.

	DJF	**MAM**	**JJA**	**SON**	**Year**
R	0.97	0.98	0.95	0.98	0.97
MB [°C]	-0.34	+0.27	+1.74	+0.70	+0.59
RMSE [°C]	1.08	1.11	2.07	1.35	1.47
Mean [°C]	4.06	10.56	16.48	10.10	10.30
$\boldsymbol{\sigma}$ [°C]	5.56	4.61	3.10	4.12	4.35

Percentage of usable observations: 98.9 %

The comparison with observations from twenty weather stations spread over the Belgian territory which are described in Section 2.4.1 shows that these modifications allow to reduce temperature mean biases (MB) by 90 %, to improve the correlation coefficient (R) of daily precipitation amount by 10 % and to reduce the root mean square error (RMSE) by 5 %.

Table 2.3: A total of 20 stations averaged statistics of the daily mean temperature observations and the outputs of **MARv3.8** forced by ERA-interim over 2008–2014: correlation coefficient (R), standard deviation (σ), root mean square error (RMSE), daily mean biases (MB) and annual daily mean temperature.

	DJF	**MAM**	**JJA**	**SON**	**Year**
R	0.96	0.98	0.95	0.98	0.97
MB [°C]	-0.85	-0.19	+1.09	+0.07	+0.03
RMSE [°C]	1.51	1.25	1.52	1.11	1.39
Mean [°C]	4.06	10.56	16.48	10.10	10.30
$\boldsymbol{\sigma}$ [°C]	5.56	4.61	3.10	4.12	4.35

Percentage of usable observations: 98.9 %

Regarding daily mean temperature, MARv3.8 is colder than MARv3.6. Annual MB are valued at +0.59 °C in MARv3.6 (Table 2.2) while it only

reaches +0.03 °C in MARv3.8 (Table 2.3). Seasonal MB are also colder in MARv3.8 than in MAR3.6 whatever the season. The largest reduction in MB occurs in summer (JJA) with MB values decreasing from +1.74 °C in MARv3.6 to +1.09 °C in MARv3.8. RMSE are also on average smaller by 5 % in MARv3.8 than in MARv3.6 whatever the season.

Table 2.4: A total of 20 stations averaged statistics of the daily precipitation amount observations and the outputs of **MARv3.6** forced by ERA-interim over 2008–2014: correlation coefficient (R), standard deviation (σ), root mean square error (RMSE), daily mean biases (MB) and annual daily mean temperature.

	DJF	**MAM**	**JJA**	**SON**	**Year**
R	0.67	0.58	0.52	0.61	0.59
MB [mm day^{-1}]	+0.11	-0.08	-0.36	-0.06	-0.10
RMSE [mm day^{-1}]	3.34	3.17	5.21	3.98	4.03
Mean [mm day^{-1}]	2.48	1.69	2.68	2.36	2.30
$\boldsymbol{\sigma}$ [mm day^{-1}]	4.34	3.77	5.98	4.85	4.85

Percentage of usable observations: 95.6%

Table 2.5: A total of 20 stations averaged statistics of the daily precipitation amount observations and the outputs of **MARv3.8** forced by ERA-interim over 2008–2014: correlation coefficient (R), standard deviation (σ), root mean square error (RMSE), daily mean biases (MB) and annual daily mean temperature.

	DJF	**MAM**	**JJA**	**SON**	**Year**
R	0.75	0.60	0.56	0.67	0.64
MB [mm day^{-1}]	+0.25	-0.14	-0.43	-0.49	-0.20
RMSE [mm day^{-1}]	3.29	3.01	4.91	3.58	3.80
Mean [mm day^{-1}]	2.48	1.69	2.68	2.36	2.30
$\boldsymbol{\sigma}$ [mm day^{-1}]	4.34	3.77	5.98	4.85	4.85

Percentage of usable observations: 95.6%

Regarding daily precipitation amount, MARv3.8 in on average dryer than MARv3.6 with MB values increasing from -0.10 mm day^{-1} in MARv3.6 (Table 2.4) to -0.20 mm day^{-1} in MARv3.8 (Table 2.5). However, R increases from 0.59 in MARv3.6 to 0.64 in MARv3.8 on average which represents an improvement of about 10 %. RMSE values are also improved by about 6 % on average decreasing from 4.03 in MARv3.6 to 3.80 in

MARv3.8. This improvement is the greatest in autumn with RMSE values decreasing from 3.98 in MARv3.6 to 3.48 in MARv3.8 which represents an improvement of about 10 %.

2.2 Reanalyses

Four reanalysis products were used in this research. They were chosen because they are the most used in the literature:

- ERA-interim (horizontal resolution 0.75°; 60 vertical levels from the surface to 0.01 hPa) from ECMWF, a third generation reanalysis assimilating most available in situ and satellite data (Dee *et al.*, 2011). ERA-interim is available from 1979 but we extended this time-series by using ERA40 for the period 1958-1978 (Uppala *et al.*, 2005). ERA40 (horizontal resolution 1.125° ; 60 vertical levels) is a second generation reanalysis and was the first to assimilate satellite data.

- NCEP/NCAR-v1 (horizontal resolution 2.5°; 28 vertical levels from the surface to 0.3 hPa) from the National Centers for Environmental Prediction – National Center for Atmospheric Research (NCEP/NCAR) (Kalnay *et al.*, 1996). This first generation reanalysis assimilates aircraft, rawinsonde, ship, and station data, as well as satellite retrievals. NCEP/NCAR-v1 data are available from 1948.

- ERA-20C (horizontal resolution 1.125° ; 91 vertical levels from the surface to 0.01 hPa), the ECMWF first atmospheric reanalysis covering the entire 20^{th} century (Poli *et al.*, 2016). This third generation reanalysis only assimilates surface observations such as pressure and marine winds. ERA-20C is available for 1900-2010.

- 20CRV2C (horizontal resolution 2° ; 28 vertical levels from the surface to 0.3 hPa), NOAA's 20^{th} century reanalysis (Compo *et al.*, 2011). It is based on an ensemble mean of 56 members assimilating only surface pressure, monthly sea surface temperature and sea ice cover. 20CRV2C is available for 1900-2010.

2.3 GCM outputs

Two GCMs were used to provided the lateral conditions required by the MAR RCM to perform future projections:

- NorESM1-M: the Norwegian Climate Center's Earth System Model (Bentsen *et al.*, 2013; Iversen *et al.*, 2012);
- MIROC5: the Japanese research community's Model for Interdisciplinary Research On Climate Version Five (Watanabe *et al.*, 2010).

Both NorESM1-M and MIROC5 were selected from the CMIP5 multi-model archive (https://pcmdi.llnl.gov/), World Climate Research Program's (WCRP's) coordinated experimental framework which provided the standardized model dataset for the IPCC fifth Assessment Report (AR5). We refer to Taylor *et al.* (2012) for further information regarding the CMIP5 protocol.

NorESM1-M and MIROC5 were used in this study because we identified them as the most suited GCMs to represent the current mean (1976-2005) general atmospheric circulation and surface conditions over Europe. It is well known that the GCM ability to model the general atmospheric circulation and surface conditions must be assessed before making future projections (Brands *et al.*, 2013; Perez *et al.*, 2014; McSweeney *et al.*, 2015). On this basis, the most suitable global models for Belgium/Europe simulation are selected after carrying out a comparison with the ERA-interim reanalysis. ERA-interim is used as reference for evaluating GCM performance because it is the one used within the CORDEX initiative (http://www.cordex.org). This assessment was made by comparing all the 30 CMIP5-AR5 models through the 'skill score' methodology, a statistical classification used and discussed by Connolley and Bracegirdle (2007), and based on the probabilistic approach of Murphy *et al.* (2004). This method aims at measuring the likelihood of a model to being within the range of the observations. First, a value is calculated for the RMS deviation of the 1976–2005 averaged model field (each GCM) from the 1976–2005 averaged ERA-Interim reanalysis field. Next, the RMS value is normalized by a measure of the variability of the reference field, i.e. by the standard deviation (σ) of the 1976–2005 averaged ERA-Interim reanalysis field. Finally, this normalized value (RMS_n) is rescaled via the

Table 2.6: Skill scores calculated using the Connolley and Bracegirdle (2007) methodology for each member of the CMIP5 archive. For each investigated variables, the three GCMs exhibiting the highest skill scores are pointed out in green while the three GCMs exhibiting the lowest skill scores are pointed out in red.

GCM name	UV500	UV700	Z500	Z700	$T_{JF}850$	$T_{JJA}850$
ACCESS1-0	0.524	0.449	0.819	0.727	0.309	0.107
ACCESS1-3	0.501	0.439	0.818	0.700	0.242	0.105
BCC-CSM1-1	0.437	0.323	0.756	0.605	0.041	0.058
BNU-ESM	0.485	0.351	0.812	0.658	0.152	0.059
CanESM2	0.606	0.507	0.869	0.795	0.211	0.103
CCSM4	0.469	0.373	0.766	0.591	0.239	0.123
CESM1-BGC	0.523	0.393	0.760	0.582	0.250	0.111
CMCC-CM	0.540	0.475	0.843	0.744	0.089	0.116
CNRM-CM5	0.560	0.495	0.819	0.778	0.221	0.123
CSIRO-Mk3-6-0	0.524	0.431	0.842	0.740	0.098	0.050
FGOALS-s2	0.480	0.371	0.779	0.609	0.145	0.001
FIO-ESM	0.574	0.463	0.840	0.691	0.177	0.066
GFDL-CM3	0.635	0.570	0.829	0.791	0.000	0.000
GFDL-ESM2G	0.533	0.415	0.725	0.714	0.018	0.008
GFDL-ESM2M	0.583	0.524	0.798	0.797	0.068	0.025
GISS-E2-H	0.518	0.424	0.787	0.725	0.086	0.061
GISS-E2-R	0.554	0.000	0.791	0.000	0.000	0.000
HadGEM2-AO	0.519	0.436	0.813	0.700	0.259	0.163
HadGEM2-CC	0.561	0.489	0.834	0.788	0.213	0.089
HadGEM2-ES	0.548	0.478	0.812	0.746	0.209	0.111
INMCM4	0.502	0.406	0.822	0.731	0.277	0.033
IPSL-CM5A-LR	0.535	0.417	0.675	0.659	0.019	0.016
IPSL-CM5A-MR	0.614	0.518	0.815	0.747	0.166	0.214
IPSL-CM5B-LR	0.487	0.457	0.597	0.617	0.001	0.001
MIROC5	0.634	0.548	0.875	0.800	0.182	0.038
MIROC-ESM-CHEM	0.446	0.304	0.824	0.641	0.227	0.068
MIROC-ESM	0.536	0.399	0.838	0.688	0.199	0.082
MPI-ESM-LR	0.591	0.504	0.848	0.754	0.259	0.157
MPI-ESM-MR	0.621	0.520	0.848	0.778	0.244	0.121
MRI-CGCM3	0.401	0.317	0.673	0.554	0.013	0.005
NorESM1-M	0.655	0.542	0.892	0.821	0.135	0.075

equation

$$W = \exp\left(-0.5 \times (RMS_n)^2\right)$$

W represents a 'score' between 0 and 1, which can be regarded as an estimate of the GCM 'skill' to adequately simulate the climatological mean state over the considered period. Following the methodology of Murphy *et al.* (2004), we normalized RMS globally rather than point-wise, i.e. we scaled the spatial average of the RMS by the spatial average of the observations temporal variability. As pointed out by Connolley and Bracegirdle (2007), all the aforementioned choices imply that the method cannot be fully objective. We refer to Connolley and Bracegirdle (2007) for more details and discussions concerning this methodology. Nonetheless, this approach provides the advantage of rating the models in terms of individual variables, which facilitates the choice of selecting one model over another, depending on the use one aims to make of that model and what aspect of the climate one wants to focus on.

Skill scores were calculated over the EURO-CORDEX domain for six climate variables that we selected so as to represent the large scale atmospheric circulation as well as near-surface conditions:

- 500 hPa wind speed (UV500)
- 700 hPa wind speed (UV700)
- 500 hPa geopotential height (Z500)
- 700 hPa geopotential height (Z700)
- 850 hPa air temperature in winter (January and February (JF) ($T_{JF}850$)
- 850 hPa air temperature in summer (June, July, August (JJA) ($T_{JJA}850$)

These skill scores are listed in Table 2.6 and show that despite a strong variability among the skill scores, both NorESM1-M and MIROC5 perform significantly better than the other models as both MIROC5 and NorESM1-M are among the three best GCMs for four variables out of six. MIROC5 and NorESM1-M perform also the best over Greenland (Fettweis *et al.*, 2013) and have the advantage that the MAR preprocessing tool was already adapted to their outputs (Lang *et al.*, 2015).

2.4 Evaluation datasets

Ground-based observations from weather stations were used for the calibration and the evaluation of the MAR performances. The weather stations, their WMO code, their true coordinates and the coordinates of the centre of the nearest MAR pixel are listed in Table 2.7 while their location is shown in Figure 2.2.

Gaps in the observations were not filled except for yearly mean global radiation flux ($E_{g\downarrow}$) computed from monthly mean data (Section 2.4.3). Missing data were omitted in our statistics computations.

Table 2.7: SYNOP Weather stations used in the evaluation process of MAR, with their WMO code, their true location (Lat. 1, Lon. 1 and Alt. 1) and the location of the centre of the nearest MAR pixel (Lat. 2, Lon. 2, Alt. 2).

WMO code	**Name**	**Lat. 1 (°)**	**Lon. 1 (°)**	**Alt. 1 (m)**	**Lat. 2 (°)**	**Lon. 2 (°)**	**Alt. 2 (m)**
06400	Koksijde	51.08	2.65	4	51.11	2.65	1
06407	Oostende Airport	51.20	2.87	4	51.20	2.86	0
06414	Beitem	50.91	3.12	25	50.89	3.09	24
06428	Munte	50.93	3.73	55	50.94	3.73	37
06431	Gent/Industrie-Zone	51.18	3.82	10	51.21	3.80	5
06432	Chievres	50.57	3.83	60	50.58	3.80	63
06434	Melle	50.98	3.83	13	50.98	3.87	21
06447	Uccle	50.80	4.36	101	50.80	4.37	101
06449	Charleroi/Gosselies	50.46	4.45	187	50.49	4.44	159
06450	Antwerpen/Deurne	51.20	4.47	12	51.21	4.44	12
06451	Bruxelles National	50.88	4.52	55	50.89	4.51	61
06456	Florennes	50.24	4.65	279	50.26	4.65	286
06458	Beauvechain	50.75	4.77	105	50.76	4.80	120
06459	Ernage	50.75	4.68	155	50.58	4.65	158
06465	Schaffen	51.00	5.07	30	50.98	5.09	33
06476	Saint-Hubert	50.04	5.41	563	50.03	5.42	563
06478	Bierset	50.63	5.45	186	50.62	5.43	141
06479	Kleine-Brogel	51.17	5.47	55	51.16	5.45	61
06490	Spa/La Sauveniere	50.48	5.92	470	50.48	5.93	484
06494	Mont-Rigi	50.51	6.08	671	50.52	6.07	671
06496	Elsenborne	50.47	6.18	564	50.47	6.21	576

2.4.1 Temperature, precipitation and surface pressure

Near-surface temperature, precipitation amount and surface pressure were extracted from SYNOP data downloaded from the Ogimet website (http://www.ogimet.com) emitted every hour by 20 weather stations spread over the Belgian territory. These weather stations are listed in Table 2.7 and mapped in Figure 2.2. There data were available from the end of 2007 onwards. Daily mean temperature and surface pressure, as well as daily precipitation amount were computed from these hourly data. Gaps in the observations were not filled, and missing data were omitted in our statistics computations.

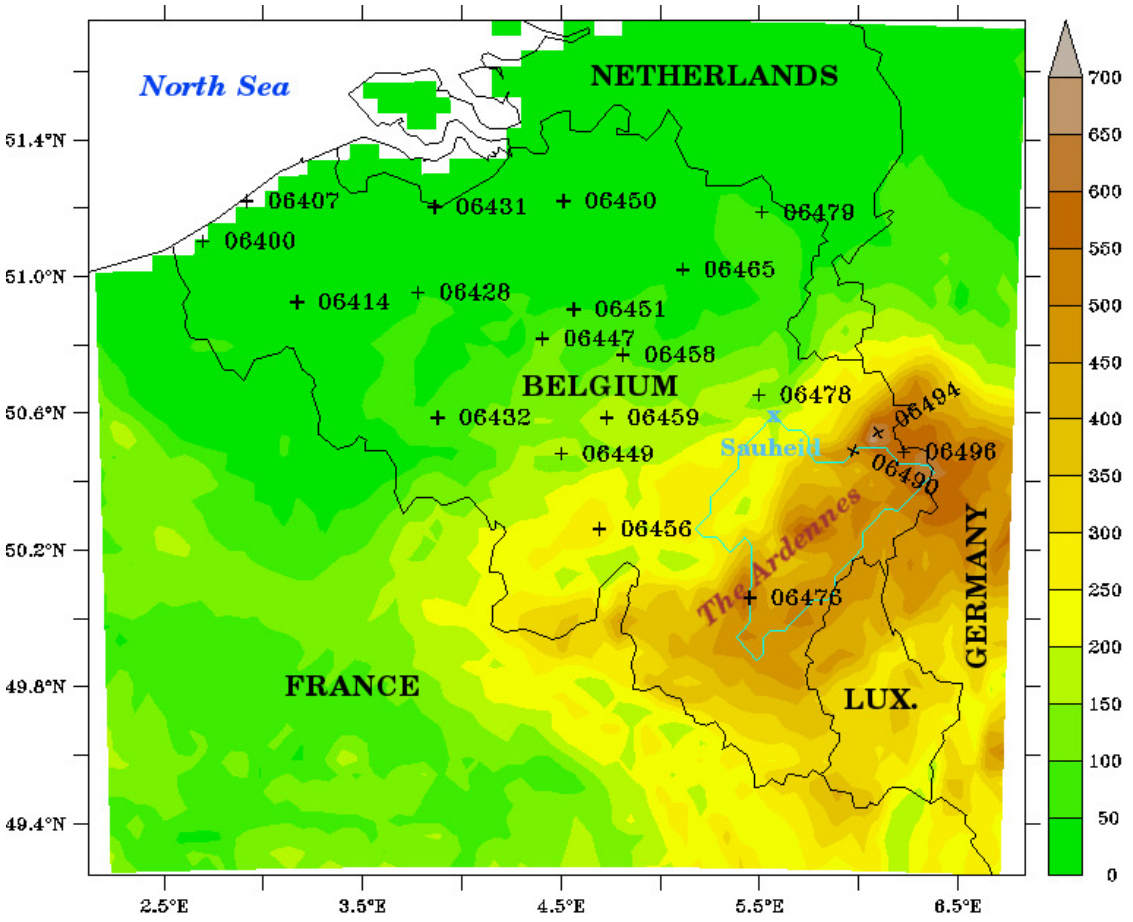

Figure 2.2: Orography of the study area, location of the weather stations used in this study with their WMO identifier, limits of the Ourthe River catchment area upstream of the gauging station of Sauheid.

2.4.2 Snow height

Snow depth measurements performed at Mont Rigi (identified by its World Meteorological Organization (WMO) code 06494 in Table 2.7 and Figure 2.2) were extracted from SYNOP data emitted at 00UTC. The Mont Rigi station is the reference station for the High Fens plateau. Snow depth measurements are performed by a snow depth laser sensor at this weather station. Contrary to manual snow depth measurements, laser sensor-driven snow depth measurements are continuously performed with the same instruments, at the same exact place and, in the case of the Mont Rigi station, within a flat, treeless open plateau, thereby limiting potential site effects which could affect those measurements. However, SYNOP data from the Mont Rigi station were only available from the end of 2007 onwards. Gaps in the observations were not filled, and missing data were omitted in our statistics computations.

2.4.3 Global radiation

Measurements of $E_{g\downarrow}$ for four ground stations over Belgium were supplied by the Royal Meteorological Institute of Belgium (RMIB): Melle (WMO code = 06434), Oostende (WMO code = 06407), Saint-Hubert (WMO code = 06476) and Uccle (WMO code = 06447) (Table 2.7, Figure 2.2).

Table 2.8: Available $E_{g\downarrow}$ time-series of more than 30 years for Belgium. The percentage of gaps in the monthly data is also indicated.

WMO code	Name	Length	Percentage of gaps	Source
06407	Oostende	1975-2014	3.7%	RMIB
06434	Melle	1967-2014	5.9%	RMIB
06447	Uccle	1951-2014	0%	RMIB
06476	Saint-Hubert	1962-2014	4.7%	RMIB

The RMIB has a long-term experience with ground-based measurements of $E_{g\downarrow}$ in Belgium with uninterrupted measurements at Uccle since 1951 (Journée and Bertrand, 2010). Uccle is one of the 22 Regional Radiation

Centres established within the World Meteorological Organisation (WMO) Regions. These data consist of monthly mean $E_{g\downarrow}$ calculated from 30 minute-average measurements. The length of all four time-series exceeds 30 years (2.8 while the percentage of gaps in the monthly data ranges from 0% to 5.9%. Seasonal and annual mean $E_{g\downarrow}$ were then computed using the monthly data. However, if more than one month was missing within a year, the annual mean was not computed, otherwise the mean $E_{g\downarrow}$ for the year was computed by filling the missing month by the climatic average of this month for the period covered by the time-series. The seasonal mean $E_{g\downarrow}$ values are not computed if there are gaps in the monthly data.

2.4.4 Total cloud cover

Total cloud cover (TCC) data for four stations were supplied by the RMIB and the Belgian agency managing the national civil airspace (Belgocontrol): Bierset (WMO code = 06478), Oostende (WMO code = 06407), Saint-Hubert (WMO code = 06476) and Uccle (WMO code = 06447) (Table 2.7, Figure 2.2). TCC data consists of hourly or 3-hourly observations carried out by human eye inspection of the sky during the day and at night. The length of all four time-series exceeds 30 years (2.9). Monthly, seasonal and annual mean TCC were calculated from the hourly or 3-hourly data. Missing values were not taken into account and a maximum of 5% of missing data is tolerated in our computations. In the end, the percentage of gaps in the monthly mean TCC ranges from 0.5% to 25.8% (Table 2.9).

Table 2.9: Available TCC time-series of more than 30 years for Belgium. The percentage of gaps in the monthly data is also indicated.

WMO code	Name	Length	Percentage of gaps	Source
06407	Oostende	1966-2014	25.8%	RMIB
06447	Uccle	1966-2010	16%	RMIB
06476	Saint-Hubert	1966-2014	0.8%	RMIB
06478	Bierset	1966-2014	0.5%	Belgocontrol

2.4.5 Flow rate

In order to identify flood events in the lower part of the Ourthe River, daily flow rates measured in the river flow gauging station of Sauheid (50.6°N ; 5.6°W) (see Figure 2.1) were extracted for the period 1974-2010 from the database of the "Direction Générale Opérationnelle de la Mobilité et des Voies Hydrauliques de la Région Wallonne". The Sauheid station was chosen because of its most downstream location in the Ourthe River before the confluence with the Vesdre and the Meuse. According to Pauquet and Petit (1993), a flow rate of 300 m^3/s is considered as the flow rate above which the Ourthe River can overflow.

2.5 Evaluation of linear trends significance using the uncertainty range for the 95% confidence interval of Snedecor

In order to compute linear trends and to assess their significance, equations of the type

$$y_j = a \times t_j + b$$

were fitted to several time-series (y_j, t_j) where y_j represents the value of the variable for the year t_j.

The significance of those trends ($a \times t_j$) was evaluated by computing their uncertainty range for the 95% confidence interval of Snedecor (Snedecor and Cochran, 1967) as done by Fettweis (2007) according to these formulas :

$$e_1 = \sum (trend(y_j) - y_j)^2$$

$$e_2 = \sum (t_j - mean(t))^2$$

$$range = \sqrt{\frac{e_1}{(t_f - t_i - 1) \times e_2}} \times k$$

where

t_j is the j^{th} year of the time-series ;

t_i is the first year of the time-series ;

t_f is the last year of the time-series ;

y_j is the value of the variable for the year t_j ;

trend(y_j) is the value of the trend of year t_j ;

mean(t) is the average year of the time-series ;

k = 1.96 for the 95% confidence interval.

The trend of a time-series is significant if its value is higher than its uncertainty range, which mainly corresponds to the interannual variability of the considered time-series.

CHAPTER 3

Current evolution of hydroclimatic conditions favouring floods in the south-east of Belgium over 1959–2010

This chapter is based on Wyard C., Scholzen C., Fettweis X., Van Campenhout J., and François L. (2017) Decrease in climatic conditions favouring floods in the south-east of Belgium over 1959-2010 using the regional climate model MAR. *International Journal of Climatology*, **37 (5)**, 2782–2796, doi: 10.1002/joc.4879

3.1 Context

Changes in seasonal snow cover cause concern in many mid- to high-latitudes countries because of its implications in water supply and flood risks (e.g. Barnett et al., 2005 ; Beniston, 2012a). Over the last decades, a significant general trend toward decreasing snow depth, snow duration and snowfall amount with interdecadal variability has been identified in various European regions such as the Alps (Durand *et al.*, 2009; Valt and Cianfarra, 2010; Beniston, 2012a), Britain (Kay, 2016), Norway (Skaugen *et al.*, 2012; Dyrrdal *et al.*, 2013), or Eastern Europe (Falarz, 2004; Brown and Petkova, 2007; Birsan and Dumitrescu, 2014). This declining snow cover is responsible for a decrease in the intensity and in the frequency of the floods dominated by snowmelt which is predicted to accelerate in the future (Bell *et al.*, 2016; Vormoor *et al.*, 2016).

In Belgium, a low-lying country of western Europe (maximum elevation = 694 m above sea level), snow can cover the summits of the Ardennes massif from one to two months per year on average, and can reach 80 cm with consequences on water management, biodiversity and tourism activities (Section 1.1). When combined with heavy rainfall events, the rapid melting of this snow cover is responsible for major floods in the Meuse River catchment, located in the south-east of Belgium. However, despite the aforementioned implications, very few studies about the recent evolution of seasonal snow cover have been carried out in Belgium. Moreover, these studies, which do not cover the last two decades (1990–2015), have been conducted either over much shorter periods (Sneyers, 1967a,b; Erpicum *et al.*, 1991), or on a more limited number of weather stations (Sneyers, 1965) to build robust statistics (Section 1.2.1).

Therefore, this research aims to assess whether seasonal snow cover and climatic conditions favouring floods have changed over the last fifty years in Belgium. For this purpose, the Regional Climate Model (RCM) MAR (for "Modèle Atmosphérique Régional" in French) was used over the period 1959–2010, forced by three reanalyses. As snow cover records over the Belgian territory are patchy, discontinuous, or made with techniques that change over time, a RCM like MAR, which was specially designed to model snow (Gallee H *et al.*, 2001; Fettweis *et al.*, 2013), is a highly valuable tool for studying the recent changes in snow cover at a high spatial resolution.

The other RCM running over Belgium, like the ALARO model, are used to model extreme events in summer such as Urban Heat Island (Hamdi *et al.*, 2014) and precipitation (De Troch *et al.*, 2013) while we are focussing here on the winter season and snow.

The RCM used and the validation data are described in Section 3.2. Section 3.3 presents and discusses the results of the evaluation of the MAR model over the Belgian territory by comparing the model outputs with daily observations from 20 weather stations of the SYNOP network over the period 2008–2014. The statistical analysis performed to study the evolution of the winter climate simulated by MAR over the period 1959–2010 is detailed in Section 3.4 while Section 3.5 details the evolution of the conditions favourable to floods in the catchment area (3,500 km^2) of the Ourthe River in the Ardennes region/massif over studied period. Conclusions and prospects are finally reported in Section 3.6.

3.2 Additional methodological aspects

The version 3.6 of MAR, described in Section 2.1 was used to reconstruct the climate of Belgium. Boundary conditions were provided by three reanalysis products: ERA40/ERA-interim, NCEP/NCAR-v1 and ERA-20C. A description of these reanalyses can be found in Section 2.2.

Data required for the evaluation of MAR consist of daily mean temperature, precipitation and snow height measurements performed over 2008-2014 for 20 weather stations spread over the Belgian territory listed in Table 2.7 and showed in Figure 2.2. A description of these datasets can be found in Section 2.4.1 and Section 2.4.2. Flow rate measurements performed in Saudheid (Figure 2.2) since 1974 are also used for the evaluation of MAR. Section 2.4.5 provides more details about these datasets.

3.3 Evaluation of MAR

Values computed by MAR forced by ERA-Interim (called MAR-ERA hereafter), by MAR forced by ERA-20C (called MAR-ERA-20C hereafter) and by MAR forced by NCEP/NCAR-v1 (called MAR-NCEP1 hereafter) are compared over 2008–2014 to daily observations from the 20 weather stations.

It should be noted that the MAR-ERA-20C evaluation period only extends from 2008 to 2010 because ERA-20C is not available after 2010. For each weather station, the closest pixel to the location of the station is chosen to represent the MAR outputs. This comparison shows the ability of MAR to simulate the daily variability of the Belgian climate, especially in winter and in the highest parts of the country.

3.3.1 Daily mean temperature

Regarding the daily mean temperature (Tave), MAR accurately simulates the Tave variability in winter (DJF) at Mont Rigi (the highest Belgian weather station), with correlation coefficients (R) above 0.95 and root mean square error (RMSE) values lower than 40% of the observed Tave standard deviation (σ) (Figure 3.1(a)). MAR-ERA provides slightly better results than MAR-NCEP1 and MAR-ERA-20C with better R and RMSE values. MAR tends to underestimate Tave in winter with daily biases ranging from -0.61°C and +0.01°C at Mont Rigi following the forcing used.

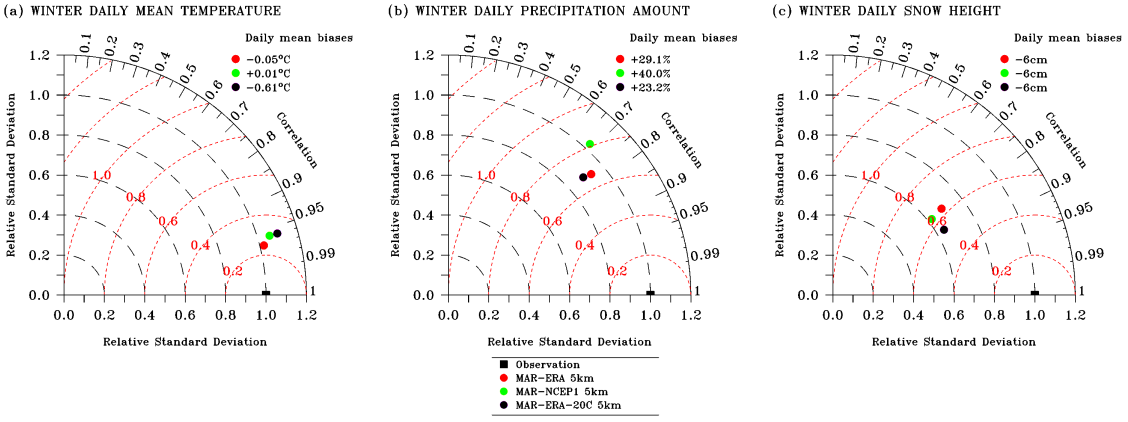

Figure 3.1: Taylor diagrams showing relative differences between MAR-ERA, MAR-NCEP1 and MAR-ERA-20C in comparison with wintertime observations of **(a)** daily mean temperature, **(b)** daily precipitation amount and **(c)** daily snow height, carried out over 2008–2014 (2008–2010 for MAR-ERA-20C) at the Mont Rigi weather station.

The statistics computed for the 20 weather stations confirm these results and show the ability of MAR to accurately simulate the Tave variability whatever the season (Figure 3.2(a)-(b)-(c)-(d)). They also show that MAR tends to overestimate Tave in spring (MAM), autumn (SON), and particularly in summer (JJA) with biases ranging from +0.95 °C and +1.84 °C (Figure 3.2(c)). Consequently, MAR overestimates Tave with annual daily

mean biases of +0.11 °C (MAR-ERA-20C), +0.59 °C (MAR-ERA) and +0.70 °C (MAR-NCEP1) (Table 3.1).

Table 3.1: A total of 20 stations averaged statistics of the daily mean temperature observations and model results over 2008–2014: correlation coefficient (R), standard deviation (σ), root mean square error (RMSE), daily mean biases (MB) and annual daily mean temperature.

	R	**σ [°C]**	**RMSE [°C]**	**MB [°C]**	**Mean [°C]**
OBS	-	6.40 (6.73)[1]	-	-	10.30 (9.69)
MAR-ERA	0.97	7.22	1.47	+0.59	10.89
MAR-NCEP1	0.96	7.23	1.65	+0.70	11.00
MAR-ERA-20C	(0.96)	(7.51)	(1.42)	(+0.11)	(9.80)
ERA-interim	0.99	6.42	0.93	+0.32	10.62
NCEP/NCAR-v1	0.95	6.65	1.71	+0.70	11.00
ERA-20C	(0.95)	(6.50)	(1.55)	(-0.24)	(9.45)

Percentage of usable observations: 98.9%

[1] The values under brackets indicate that the evaluation period only extends from 2008 to 2010.

3.3.2 Daily precipitation amount

Regarding the daily precipitation amount (PPN) at Mont Rigi, MAR accurately simulates the PPN variability in winter (dominated by stratiform precipitation) with R values above 0.70 and RMSE values lower than 100 % of the observed PPN standard deviation (Figure 3.1(b)). MAR-ERA provides again the best results. However, the model overestimates PPN in winter with daily mean biases ranging from +23.2 % and +40.0 % at Mont Rigi. Nevertheless, the statistics computed for the 20 weather stations show that MAR fails to adequately simulate the PPN variability during the other seasons (Figure 3.2(f)-(g)-(h)). Moreover, MAR tends to underestimate (convective) PPN in summer with biases ranging from -0.1 % to -12.9 % (Figure 3.2(g)). Consequently, MAR slightly underestimates PPN with annual daily mean biases valued at -0.8 % (MAR-ERA-20C), -4.3 % (MAR-ERA) and -6.4 % (MAR-NCEP1) (Table 3.2).

3.3.3 Snow height

Comparison with snow height (SH) measured at the Mont Rigi station in winter (Figure 3.1(c)) indicates that MAR simulates very well the daily SH

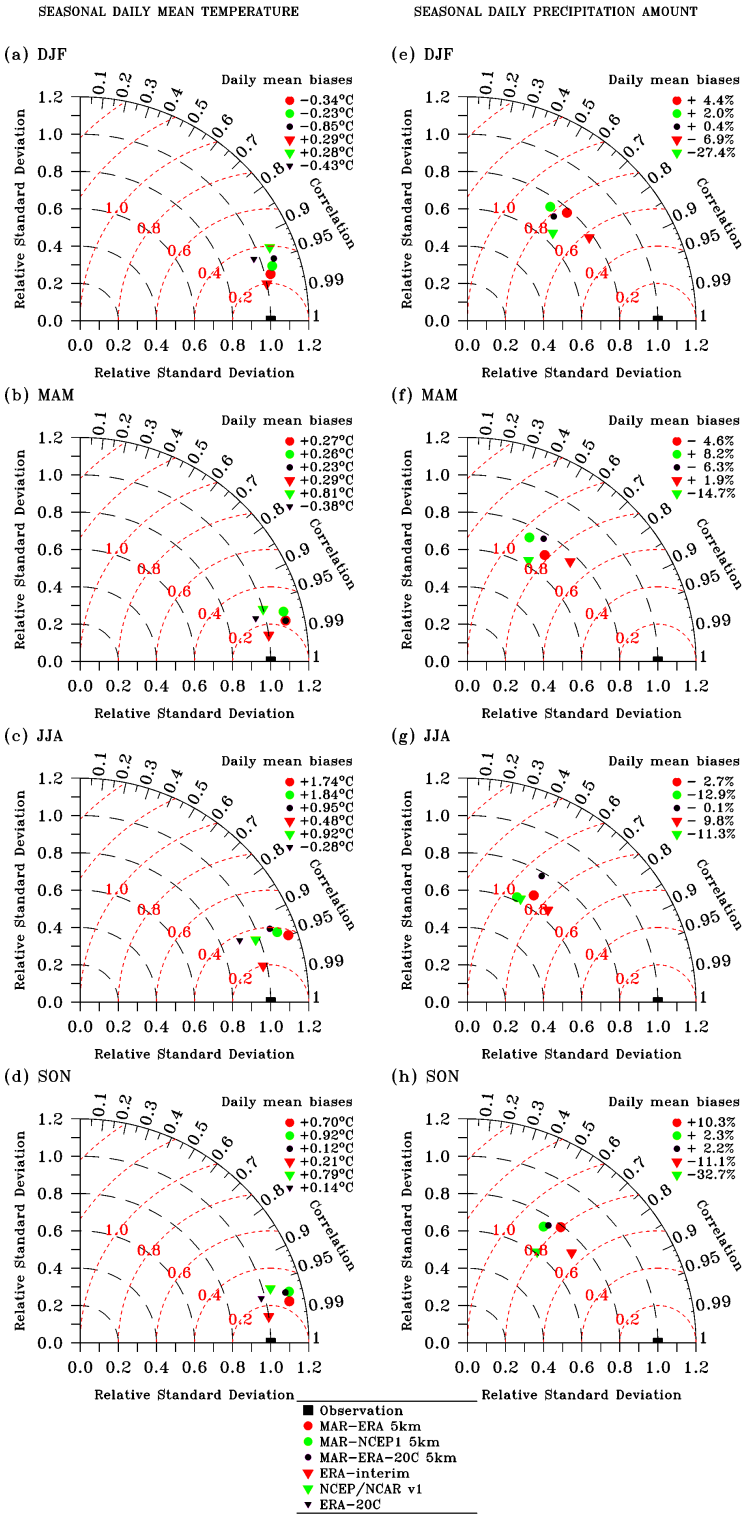

Figure 3.2: Taylor diagrams showing relative differences between MAR-ERA, MAR-NCEP1, MAR-ERA-20C, ERA-interim, NCEP/NCAR-v1 and ERA-20C in comparison with seasonal observations of **(a)-(d)** daily mean temperature, and **(e)-(h)** daily precipitation amount, carried out over 2008–2014 (except for MAR-ERA-20C and ERA-20C whose the validation period is 2008–2010). It should be noticed that there is no statistics for ERA-20C in (e)-(f)-(g)-(h) due to the data unavailability.

Table 3.2: A total of 21 stations averaged statistics of the daily precipitation amount observations and model results over 2008–2014: correlation coefficient (R), standard deviation (σ), root mean square error (RMSE), daily mean biases (MB) and annual daily mean precipitation amount.

	R	**σ (mm day^{-1})**	**RMSE (mm day^{-1})**	**MB (mm day^{-1})**	**Mean (mm day^{-1})**
OBS	-	4.85 (5.02)[1]	-	-	2.30 (2.26)
MAR-ERA	0.59	3.47	4.03	–0.10 [–4.3%]	2.20
MAR-NCEP1	0.49	3.28	4.39	–0.15 [–6.4%]	2.15
MAR-ERA-20C	(0.55)	(3.82)	(4.35)	(–0.02 [–0.8%])	(2.24)
ERA-interim	0.73	3.44	3.46	–0.17 [–7.2%]	2.13
NCEP/NCAR-v1	0.56	2.96	4.17	–0.50 [–21.7%]	1.80
ERA-20C	n.a.[2]	n.a.	n.a.	n.a.	n.a.

Percentage of usable observations: 95.6%
[1] The values under brackets indicate that the evaluation period only extends from 2008 to 2010.
[2] n.a., the data were not available to compute the statistic analysis.

variability, with R values larger than 0.80 and RMSE values below 65 % of the observed SH standard deviation. However, MAR underestimate SH with biases of around -6 cm day^{-1} which is large compared to the daily mean snow depth observed at 15 cm. Since there is no temperature biases in winter at Mont Rigi (Figure 3.1(a)), and since MAR overestimates wintertime daily precipitation amounts at Mont Rigi (Figure 3.1(b)), these negative daily mean biases in SH could be due to the too large fresh snowfall density (300 kg m^{-3}) used in MAR. A fresh snowfall density of 300 kg m^{-3} is typical in polar regions, but in temperate climates, lower values (100 kg m^{-3}) are more relevant (Judson and Doesken, 2000).

3.3.4 Climatic conditions favouring floods

Finally, the ability of the MAR model to simulate climatic conditions favourable to floods in the Ourthe catchment is assessed by comparing observed flood days with potential flood days and periods computed from the MAR results.

On the one hand, 28 flood events were identified between January 1974 and December 2010 on the basis of flow rates measured in Sauheid (flooding flow rate $>$ 300 m^3 s^{-1}), which represents a total of 67 flood days. On the other hand, in order to identify potential flood periods, run-off (RU) computed by MAR is integrated over the Ourthe catchment upstream of Sauheid, which represents an area of 2,900 km^2 (Figure 2.2). RU is then averaged over the

two days preceding the flood event (RU2), because the typical response time of the Ourthe River to precipitation ranges from 1 to 2 days (Hazenberg *et al.*, 2008). The MAR-driven run-off partly consists of precipitation water and of water from melting snow that flow on the ground because of the saturation of the soil in the MAR model. In order to only consider the part of RU2 which really contributes to the river discharge, evaporation computed by MAR is removed from RU2 ($RU2_e$). At last, since there are two types of floods in the Ourthe River, we also distinguish two types of $RU2_e$: $RU2_e$ produced by precipitation alone (see the red dots in Figure 3.3) and $RU2_e$ produced by precipitation combined with snowpack melting (see the green dots in Figure 3.3). We consider one day as favourable to floods if $RU2_e$ is statistically extreme, i.e. if $RU2_e$ is larger than its 95^{th} percentile (P95) computed over 1961-1990. P95 is used because it is commonly used in the literature to define extreme event. Moreover, the trends computed in Section 3.3.4 do not change following the considered percentile (P90, P95, P99 or P99.5).

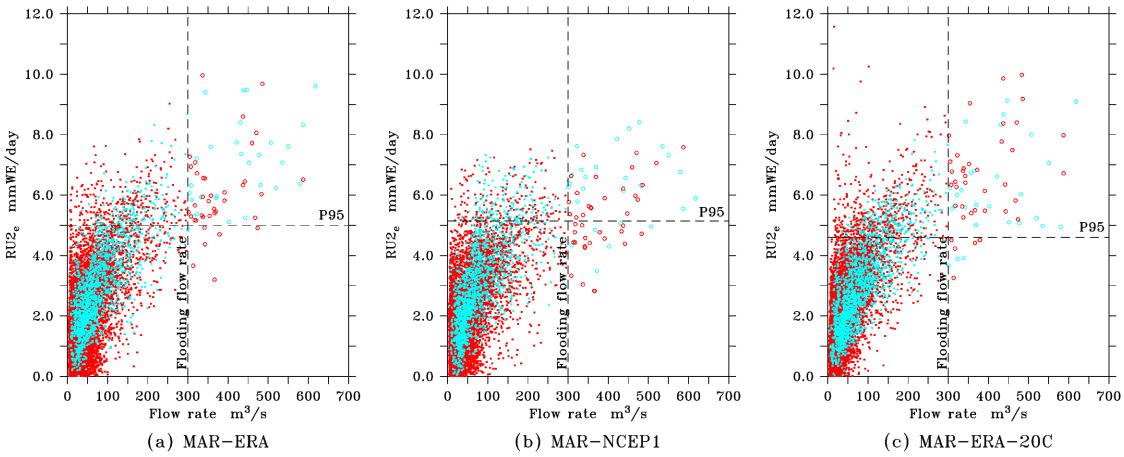

Figure 3.3: Two-day averaged run-off integrated over the Ourthe catchment area upstream of Sauheid ($RU2_e$) computed from **(a)** MAR-ERA, **(b)** MAR-NCEP1, and **(c)** MAR-ERA-20C, in relation to the flow rate measured in Sauheid. Each point represents 1 day between 1 January 1974 and 31 December 2010. The blue dots indicate that run-off is generated by snowpack melting combined with rainfall events. The red dots indicate that run-off is generated by rainfall events alone. The 95^{th} percentile of $RU2_e$ represented in the graphs is the limit above which the days are considered as favourable to floods. A flooding flow rate of 300 m^3 s^{-1} is considered.

Thereby, about 90 % (60/67) of the observed flood days correspond to potential flood days computed by MAR-ERA and MAR-ERA-20C (Figure 3.3(a) and (c)), while this proportion only reaches 60 % (41/67) with MAR-NCEP1 (Figure Figure 3.3(b)). Similarly, results in terms of flood events indicate

that about 90 % (25/28) of the observed floods correspond to periods identified as favourable to floods according to MAR-ERA-20C and MAR-ERA. By contrast, this proportion only reaches 64 % (18/28) with MAR-NCEP1. However, MAR largely overestimates the number of days which could have generated floods over 1974-2010 with excess of 327, 434, and 702 days for MAR-NCEP1, MAR-ERA and MAR-ERA-20C respectively (Figure 3.3). Indeed, floods also depend on non-climatic factors which are not represented in our estimation, such as the initial state of the soil prior to an intense run-off event, the infiltration of water into the water tables, the evolution of the surface permeability over time (as a consequence of the conversion of natural land surfaces into impervious surfaces, due to urbanization), the surface, subsurface and underground flow. The coupling between the climate model MAR and a hydrological model would allow a better representation of these mechanisms and thus a better comparison with observations. However, the aim of this work in not to study the floods evolution but only the climatic conditions favouring floods.

3.3.5 Origin of biases in MAR

In view of these results, we can conclude that whatever the reanalysis forcing the MAR model, the climate variability is well represented by the model over the Belgian territory, although MAR-ERA seems more fitting than MAR-ERA-20C and particularly MAR-NCEP1. MAR-ERA-20C and MAR-NCEP1 overall exhibit lower R and higher RMSE values than MAR-ERA in comparison with observed daily temperature and precipitation. In addition, MAR-ERA allows to find more observed floods than MAR-ERA-20C and MAR-NCEP1. We explain the better results of MAR-ERA by the difference between the assimilation system of all three reanalyses (Kalnay *et al.*, 1996; Dee *et al.*, 2011; Poli *et al.*, 2016). Indeed, all the available data are assimilated in ERA-Interim while only surface pressure and surface marine winds are assimilated in ERA-20C. Moreover, NCEP/NCAR-v1 horizontal and vertical resolution is coarser than the resolution of ERA-20C and particularly ERA-Interim. Furthermore, when directly comparing all three reanalyses with daily mean temperature and daily precipitation amount from weather stations (Figure 3.2), the correlations and the RMSE values are better than those obtained with our MAR model forced by the same reanalyses. Actually, the weather station-based data used in this

study is the same data that had been assimilated into the reanalyses (except ERA-20C), which explains the dependence between the reanalyses and the data. Nevertheless, because of the low spatial resolution of the reanalyses, MAR forced by the reanalyses exhibits lower biases especially in winter (Figures 3.2(a) and (e)). It is therefore better to use the MAR model instead of the raw reanalyses, which in addition do not adequately simulate the snow pack.

Besides the biases due to the forcing conditions, some discrepancies can also be related to the MAR model itself. For instance, as a result of the underestimation of the cloud cover in MAR, MAR underestimates temperature in winter and overestimate it in summer. Moreover, daily PPN variability is better reproduced in winter (when stratiform precipitation dominates) than in summer (when convective precipitation dominates). Surface and soil properties could also contribute to the MAR model biases through their reflectivity or their water exchanges with the atmosphere.

3.4 Changes in the winter climate over 1959-2010

A linear trend analysis is performed for the period 1959–2010 over the entire Belgian territory. This period is the longest common period between all three reanalyses forcing the MAR model. Trend significance is assessed by using the uncertainty range of Snedecor for the 95^{th} confidence interval (Snedecor and Cochran, 1967) (see Section 2.5) as used by Fettweis (2007). The trend of a time series is significant if its value is higher than its uncertainty range, which mainly corresponds to the interannual variability of the considered time series. The trend analysis particularly focuses on the winter period (December-January-February (DJF)), as more than 70 % of the floods in the Ourthe River occur during this season. Only the trends computed using the MAR-ERA results are displayed because the evaluation of the MAR model showed that the MAR-ERA results are the closest to observations (Section3.3). The trends computed using the MAR-ERA-20C results and the MAR-NCEP1 results are however available in Appendix A from Figure A.1 to Figure A.10. In Figures 3.4 to 3.8 and Figures A.1 to A.8, the limits of the Ourthe catchment area are drawn in light blue or in red. The filled

pixels indicate the places where the trends are significant.

3.4.1 Temperature

Mean winter temperature exhibits an increasing trend ranging from +0.6 °C 52yrs^{-1} to +1.0 °C 52yrs^{-1} in the Ourthe catchment (Figure 3.4(a)).

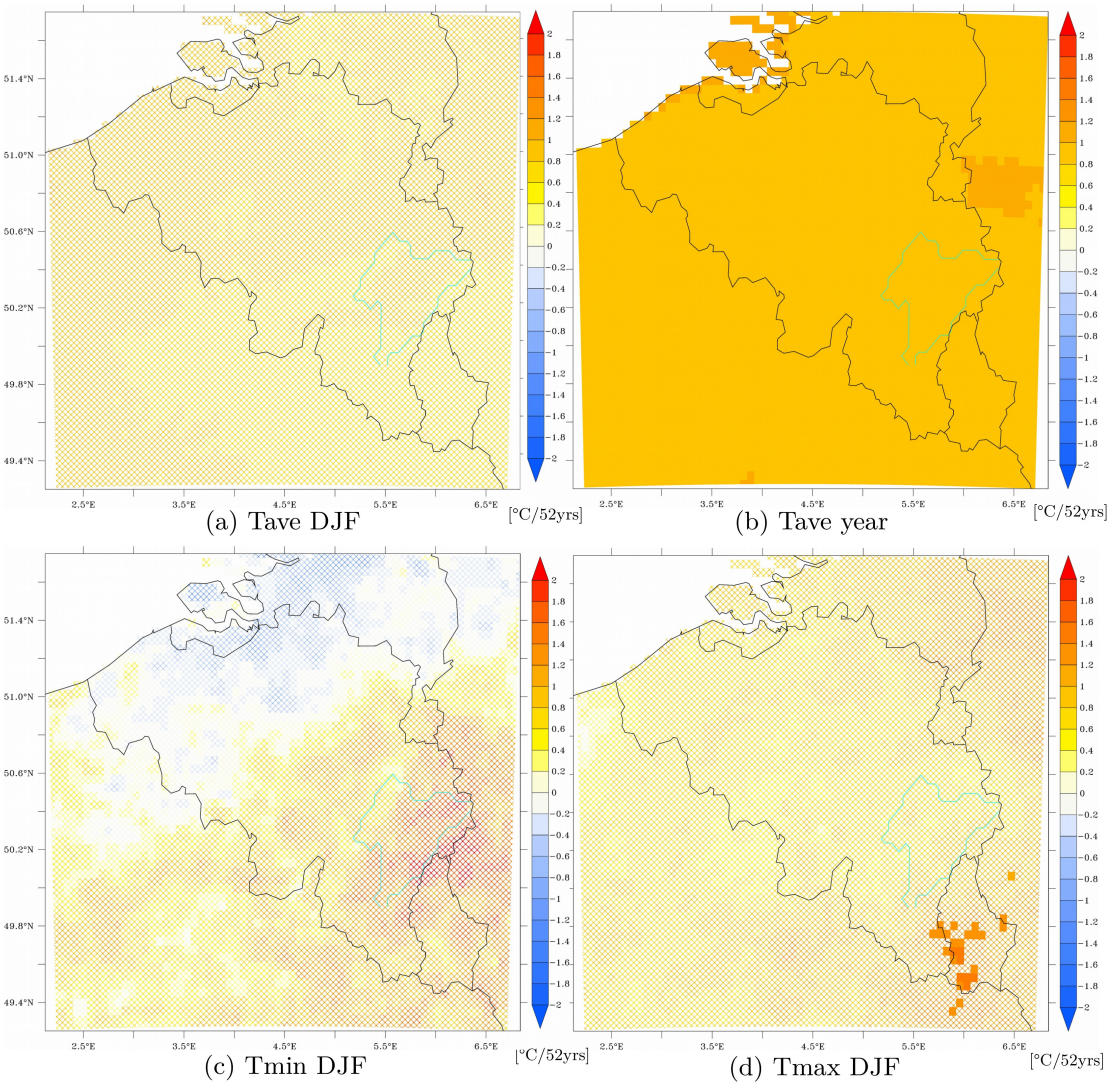

Figure 3.4: Trends computed from MAR-ERA over 1959–2010 in **(a)** the mean temperature in winter (DJF), **(b)** the yearly mean temperature, **(c)** the extreme (P5) minimum temperature in winter, and **(d)** the extreme (P95) maximum temperature in winter. Filled pixels indicate the places where trends are statistically significant.

However, the mean winter temperature trend is non-significant while mean annual temperature exhibits a significant increasing trend between +0.8 °C 52yrs^{-1}

and +1.0 °C 52yrs^{-1} in the Ourthe catchment (Figure 3.4(b)). Trends in the winter extreme minimum temperature (the 5^{th} percentile of the daily minimum temperature, in agreement with Van de Vyver (2012)) are non-significant everywhere but show a positive signal in the Ardennes (Figure 3.4(c)). Extreme maximum temperature in winter (the 95^{th} percentile of the daily maximum temperature, in agreement with Van de Vyver (2012)) also exhibits non-significant trends but show a homogeneous positive signal between +0.6 °C 52yrs^{-1} and +1.4 °C 52yrs^{-1} in the Ardennes (Figure 3.4(d)). The absence of a clear trend in winter temperature is also highlighted by Van de Vyver (2012), who found a non-statistically significant linear growth in winter extremes for the period 1952/1953–2009 over Belgium. In addition, similar results are found using the MAR-NCEP1 outputs (Appendix A, Figure A.1). However, the trends computed from MAR-ERA-20C are positive, larger and significant in any part of Belgium (Appendix A, Figure A.2). It is easily explained by the fact that air temperature is not assimilated in ERA-20C (Poli *et al.*, 2016), which overestimates the global warming in Europe.

3.4.2 Precipitation

Regarding precipitation changes in winter, no significant trend is found in the Ourthe catchment.

However, Figures 3.5(a) and (b) show a negative signal in both total rainfall and particularly snowfall valued at -10 mm 52yrs^{-2} at least. Figures 3.5(c) and (d) display a positive signal in both extreme precipitation events intensity (trend in the 95^{th} percentile of the daily precipitation amount in winter) and frequency (trend in the number of days with daily precipitation amount larger than its 95^{th} percentile computed over 1960–1991) up to +2 mm 52yrs^{-2} and up to +2 events 52yrs^{-2} respectively according to MAR-ERA. The trends computed using the MAR-ERA-20C outputs are similar but larger and thus statistically significant in some parts of the Ourthe catchment (Appendix A, Figure A.4). MAR-NCEP1 simulates opposite trends in comparison with MAR-ERA and MAR-ERA-20C (Appendix A, Figure A.3). Therefore comparison with previous studies covering Belgium is needed to check the relevance of our results. Most of these studies identify an increase in the winter precipitation amount, along with an increase in both intensity

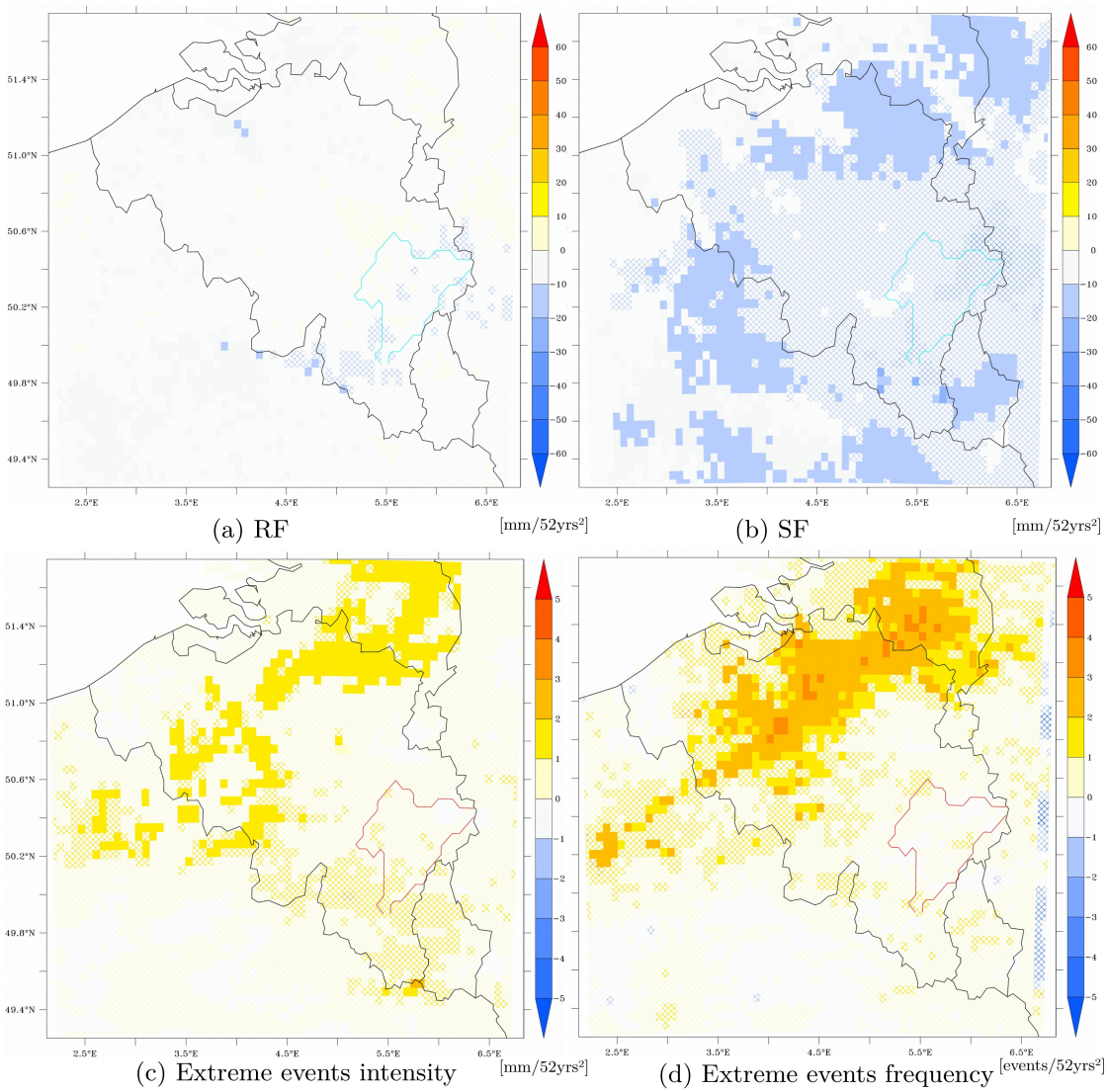

Figure 3.5: Trends computed from MAR-ERA over 1959–2010 in **(a)** the rainfall amount (RF) in winter (DJF), **(b)** the snowfall amount (SF) in winter, **(c)** the intensity of extreme precipitation events in winter (trend in the 95^{th} percentile of daily precipitation amount in winter), and **(d)** the frequency of extreme precipitation events in winter (trend in the number of days in winter with daily precipitation amount larger than its 95^{th} percentile computed over 1961–1990). Filled pixels indicate the places where the trends are statistically significant.

and frequency of extreme precipitation events during winter (Gellens, 2000; Vaes G, Willems P, 2002; De Jongh *et al.*, 2006; Ntegeka and Willems, 2008; Willems, 2013b,a; RMIB, 2015). However, since the significance of these trends depends both on the length of the time series and on the duration of the precipitation events, the aforementioned studies conclude that no statistically robust trend can be acknowledged regarding precipitation in Belgium. Despite the absence of significant long-term trends, these studies

identify multidecadal oscillations characterized by drier periods in the 1900s, around 1920 and in the mid-1970s (De Jongh *et al.*, 2006; Willems, 2013b,a) alternating with wetter periods in the 1910-1920s, the 1950-1960s and in the 1990-2000s (Ntegeka and Willems, 2008; Willems, 2013b,a).

3.4.3 Snow cover

By analysing the evolution of the seasonal snow cover in winter, a significant decreasing trend is identified in all three MAR simulations.

According to MAR-ERA, the maximum of daily snow height significantly decreases by 5 to 10 cm 52yrs^{-1} in the Ardennes, and by more than 15 cm 52yrs^{-1} in the High Fens Plateau (Figure 3.6(a)). Considering snow days as days with a snow cover of at least 5 cm of thickness, in agreement with Erpicum *et al.* (1991)), the number of snow days significantly decreases up to -15 days 52yrs^{-1} (Figure 3.6(b)). The onset of the snow cover season (the first day of the year with a snow cover height of at least 1 cm) is delayed up to +60 days 52yrs^{-1} in some parts of the Ourthe catchment (Figure 3.6(c)). By contrast, the end of the snow cover season (the last day of the year with a snow cover height of at least 1 cm) is shortened up to -60 days 52yrs^{-1} only in a small part of the Ourthe catchment area (Figure 3.6(d)). Therefore, the duration of the snow cover season seems to shorten throughout the last 52 years. Similar results are found using the outputs of MAR-NCEP1 (Appendix A, Figure A.5) and MAR-ERA-20C (Appendix A, Figure A.6). These results are in agreement with studies carried out in other regions in Europe, such as the low- and medium-elevated parts of the Alps (Durand *et al.*, 2009; Valt and Cianfarra, 2010; Beniston, 2012b), or the lowland and coastal regions of Norway (Skaugen *et al.*, 2012; Dyrrdal *et al.*, 2013).

3.4.4 Origin of trends in the winter climate of Belgium

Changes in the winter atmospheric regional circulation partly explains the trends found in our results. As detailed in Section 1.1, these circulation changes are often assessed by analysing changes in the North Atlantic Oscillation (NAO) index (Hurrell, 1995; Slonosky and Yiou, 2001; Philipp *et al.*, 2007). The NAO index is defined as the difference of the atmospheric surface

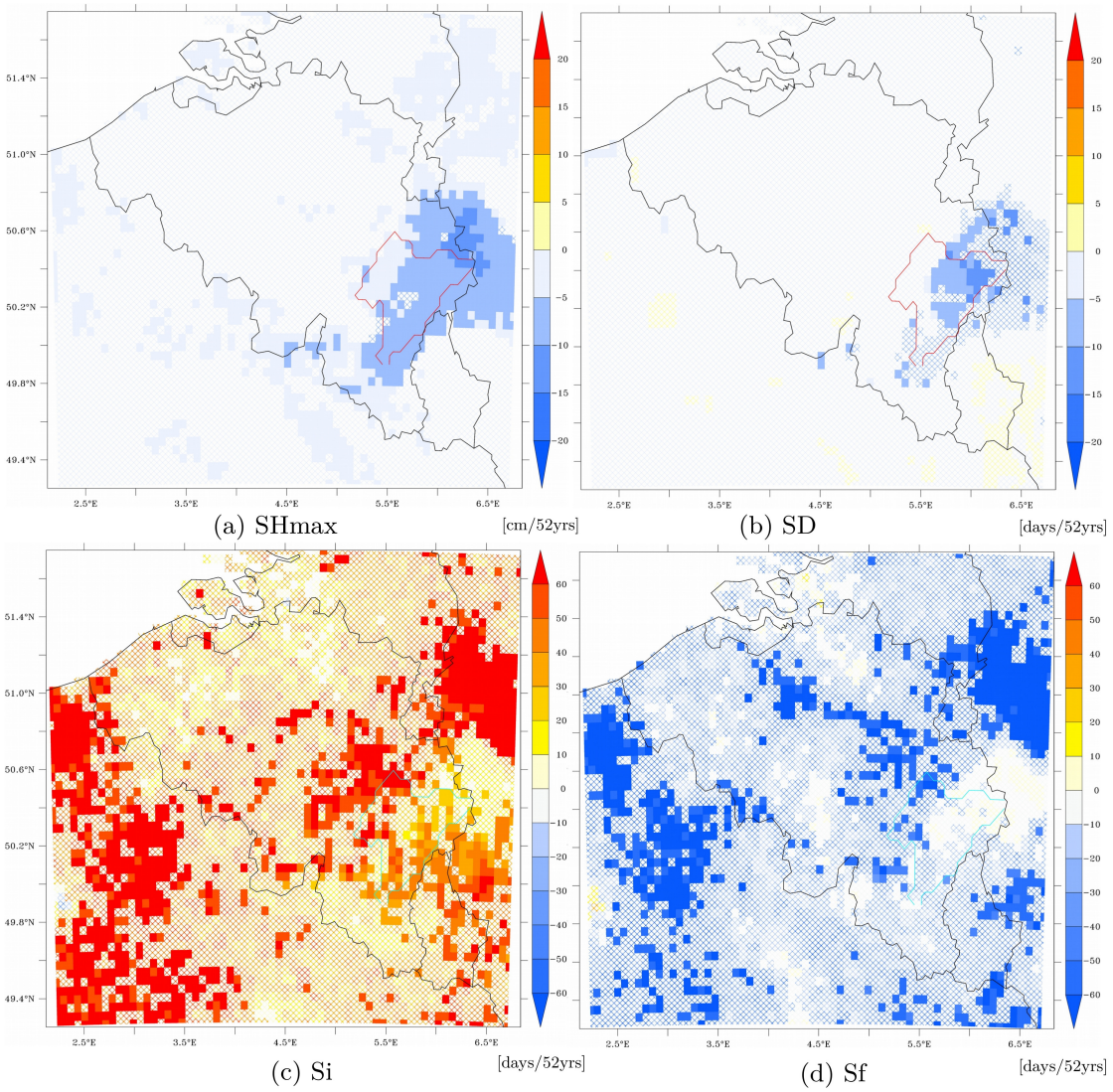

Figure 3.6: Trends computed from MAR-ERA over 1959–2010 in **(a)** the maximum daily snow depth (SHMAX) in winter (DJF), **(b)** the number of days per winter with a snow cover of at least 5 cm of thickness (SD), **(c)** the first day of the year with a snow depth of at least 1 cm (Si), and **(d)** the last day of the year with snow depth of at least 1 cm (Sf).

pressure between the Azores High and the Icelandic Low, which corresponds to the normalized difference of sea level surface pressure measured in Lisbon (Portugal) and in Stykkisholmur/Reykjavik (Iceland). In the wintertime, the NAO index is known for its high influence on the weather of Western Europe and for its high day-to-day and year-to-year variability. For instance, negative NAO index values usually correspond to cold and snowy winters in Belgium such as the winter 2009–2010 (Cattiaux *et al.*, 2010), while positive NAO index values are associated with mild and rainy winters.

As outlined by Van de Vyver (2012), the absence of clear trends in the winter temperatures of Belgium could be due to the perturbation of the warming signal by the high variability of the regional atmospheric circulation in winter, assessed from the variation of the NAO index in winter (Figure 3.7(b)).

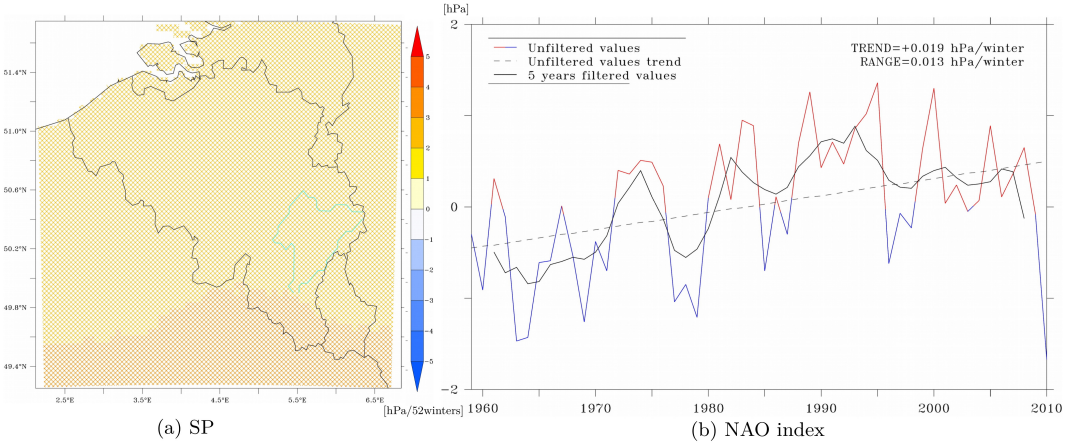

(a) SP (b) NAO index

Figure 3.7: Trends over 1959–2010 of **(a)** the mean surface pressure (SP) in winter (DJF) computed from MAR-ERA, and **(b)** the mean NAO index recorded in winter. Filled pixels indicate the places where the trends are statistically significant

Furthermore, as the decrease in snowfall does not bring more rainfall, it suggests that the (non-significant) increasing mean winter temperature would not be responsible for this declining snowfall trend and the resulting decrease in snow accumulation. Thus, changes in the winter atmospheric regional circulation explain in part this decline of both precipitation amount and snow accumulation. Figure 3.7(a), Figure A.7(a) and Figure A.8(a) show that whatever the reanalysis forcing the MAR model, an increasing trend in the daily mean surface pressure in winter of about 1 to 3 hPa 52yrs^{-1} is found, suggesting an increase in the occurrence of anticyclonic conditions in winter over the Belgian territory. In addition, Figure 3.7(b) shows a significant long-term increasing trend in the NAO index during winter over the studied period, suggesting a strengthening in the Azores High. These more anticyclonic-like conditions in winter are likely to cause the decrease in total precipitation amount including snowfall, leading thus to reduced snow accumulation. However, the MAR integration domain used in this study is not large enough to further investigate hypothetical circulation changes over Western Europe. However, this decrease in the precipitation amount over the studied period may also depend on the period selected for conducting the trend analysis as the climate of Belgium is affected by multidecadal

oscillations (Ntegeka and Willems, 2008; Willems, 2013b,a).

Nonetheless, it should be noted that the decreasing trends in both precipitation amount and snow accumulation simulated by MAR in winter are in part biased by the inability of MAR to properly simulate convective precipitation (Section 3.3.2). Indeed, MAR simulates an increase in convective precipitation during winter especially if MAR is forced by NCEP/NCAR-v1 (Figure 3.8(b)). Therefore, the decrease in precipitation in winter simulated by MAR could be resulting from an inadequate convective scheme in the model, given that MAR is a hydrostatic model running at a resolution of 5 km. In addition, the raw reanalyses and previous studies using weather station observations have opposite conclusions.

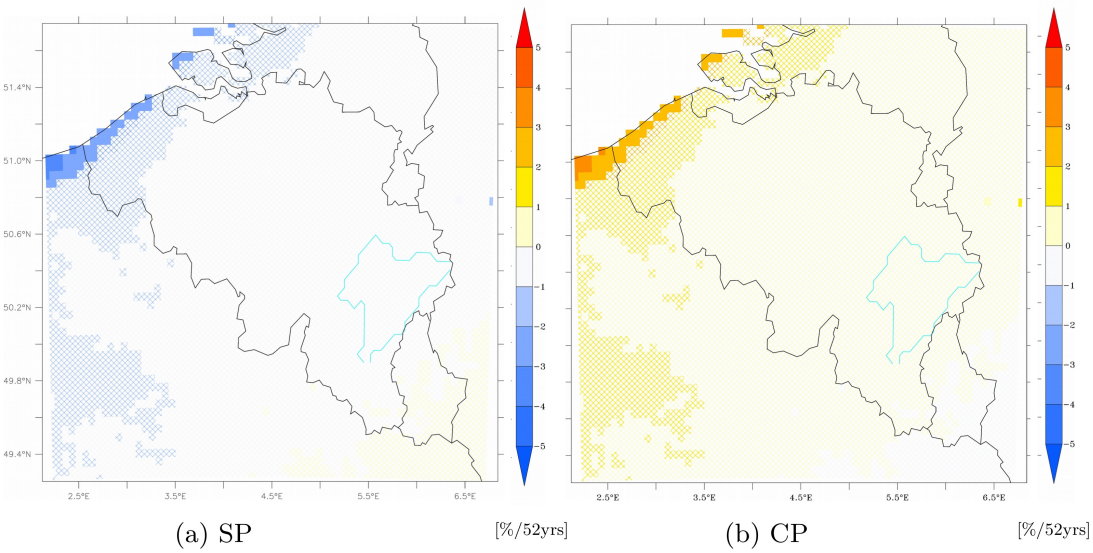

Figure 3.8: Trends computed from MAR-NCEP1 over 1959-2010 in the percentage of **(a)** the stratiform precipitation amount in winter (DJF) and **(b)** the convective precipitation amount in winter. Filled pixels indicate the places where trends are statistically significant.

In any case, the increase in convective precipitation in winter remains to be explained. As this increase is the greatest in coastal regions (Figure 3.8(b)), warmer sea surface temperatures could have enhanced instability of the perturbations which usually cross the country from north-west to south-east and thereby bring convective precipitation. The North Sea is indeed acknowledged to be one of the seas belonging to the North-East Atlantic region which have recorded the fastest warming over the last 25 years (Joyce, 2006; Sherman *et al.*, 2007).

Last of all, it should also be noted that the signal of the trends in both

the intensity and the frequency of extreme precipitation events is not clear. The trends obtained from the MAR-NCEP1 outputs (negative signal) more particularly contrast with the signal obtained from the MAR-ERA and the MAR-ERA-20C outputs, as well as with conclusions of previous studies. It brings to light that the reanalysis data (in particular NCEP/NCAR-v1) may be too coarse to allow to MAR to capture extreme precipitation events in an accurate way since we directly force the MAR model with the reanalysis.

3.5 Changes in conditions favouring winter floods over the period 1959-2010

Since more than 70 % of the floods in the Ourthe River occurred in winter, changes in conditions favourable to floods are investigated by focusing on this season. Days favourable to floods (as defined in Section 3.3.4) computed from the MAR-ERA results are summed for each winter of 1959-2010 (see TFD in Figure 3.9(c)). A distinction is also made between days favourable to floods resulting from snowpack melting combined with precipitation (see SFD in Figure 3.9(a)), and days favourable to floods from precipitation only (see PFD in Figure 3.9(b)). Then, for each of these time series, trends and their significance are computed following the method described in Appendix (see Supporting Information). Finally, a 5-year running mean is applied to the time series. The same work is also repeated for the MAR-NCEP1 and MAR-ERA-20C outputs and is available in Supporting Information, Figures A.9 and A.10.

First of all, long-term linear trends show that MAR-ERA exhibits a significant decreasing trend in SFD of -0.100 days winter^{-1} (Figure 3.9(a)). Results obtained using MAR-NCEP1 and MAR-ERA-20C confirm the decreasing trend in SFD (Figures A.9(a) and Figures A.10(a)). However, regarding PFD, the results contrast following the reanalysis forcing the MAR model since MAR-ERA shows no trend (Figure 3.9(b)), MAR-NCEP1 shows a significant decreasing trend (Figure A.9(b)) and MAR-ERA-20C computes a non-significant increasing trend (Figure A.10(b)). As a result, regarding TFD, MAR-ERA shows a non-significant decreasing trend valued at -0.084 days winter^{-1} (Figure 3.9(c)), MAR-NCEP1 exhibits a significant decrease in TFD over the studied period (Figure A.9(c)) while MAR-ERA-20C exhibits

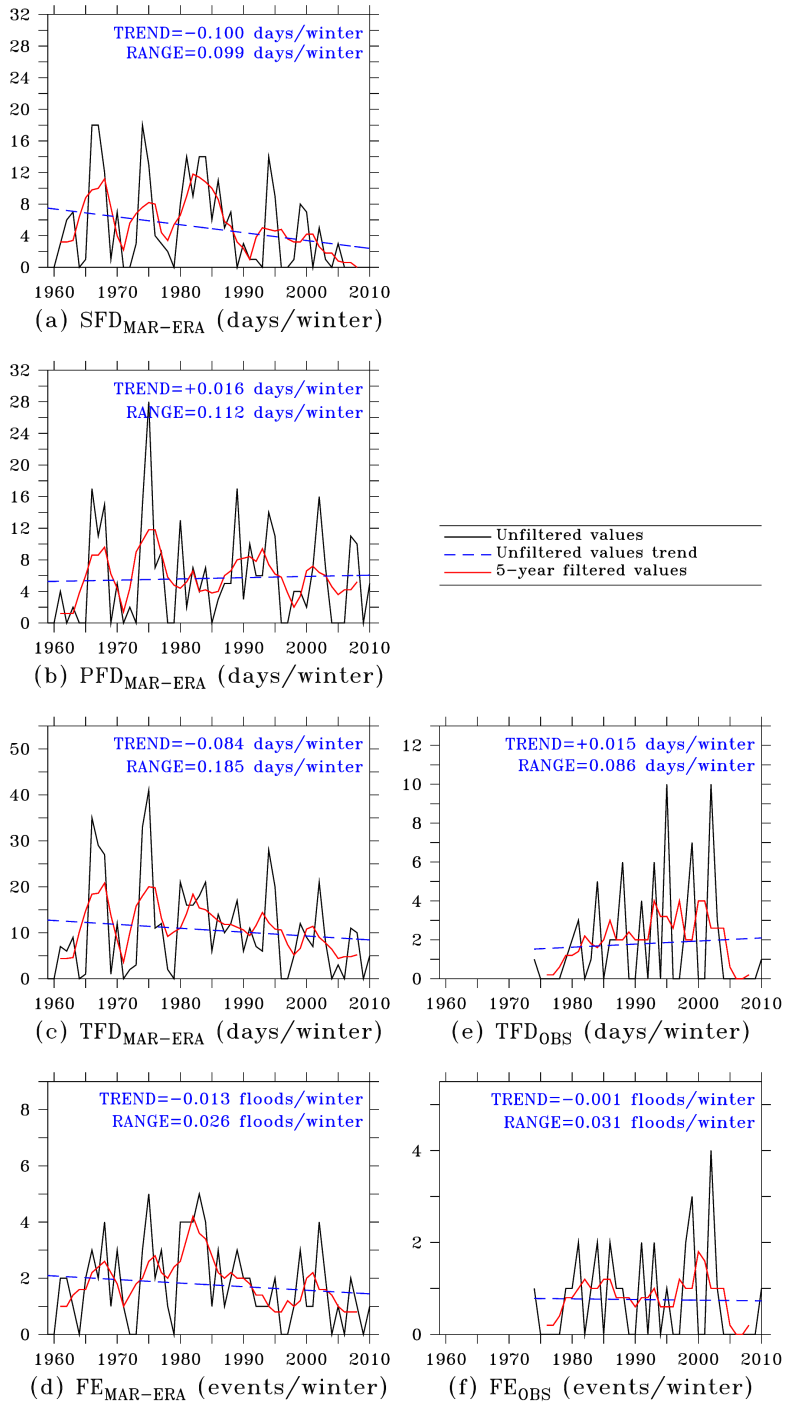

Figure 3.9: Unfiltered values, 5-year filtered values and trends computed from MAR-ERA over 1959–2010 of **(a)** the number of days per winter (DJF) favourable to floods due to snowpack melting combined with rainfall events (SFD$_{MAR-ERA}$), **(b)** the number of days per winter favourable to floods due to rainfall events alone (PFD$_{MAR-ERA}$), **(c)** the total number of days per winter favourable to floods (TFD$_{MAR-ERA}$), **(d)** the number of flood events favourable to floods per winter (FE$_{MAR-ERA}$). Unfiltered values, 5-year filtered values and trends computed from observations in Sauheid are also displayed with **(e)** the number of observed flood days per winter (TFD$_{OBS}$), and **(f)** the number of observed flood events per winter (FE$_{OBS}$).

no trend (Figure A.10(b)). Observations of effective flood days (TFDOBS) in Sauheid, based on flow rate measurements between 1974 and 2010, show no trend (Figure 3.9(e)). In terms of flood events (FE), only MAR-NCEP1 exhibits a significant trend valued at -0.042 floods winter^{-1} (Figure A.9(d)) while no significant trend can be found in the observations (Figure 3.9(f)). However, as MAR underestimates convective precipitation, especially if the model is forced by NCEP/NCAR-v1, extreme run-off events generated by this kind of precipitation are probably underestimated. Therefore, the trends in conditions favourable to floods computed from the MAR results are likely to be slightly overestimated, given that the ratio of convective precipitation events versus stratiform precipitation has been increasing since 1959 (Figure 3.8(b)).

On the basis of flood events observed over 1974–2010 in Sauheid, two periods of higher flood occurrence are identified in the 1980s, in agreement with Pauquet and Petit (1993), and also in the 2000s (see the red line in Figure 3.9(f)). The period of higher flood occurrence in the 1980s seems to be partly induced by an increase in hydroclimatic conditions favourable to floods, as a peak is also simulated by all three MAR configurations during this period in SFD (see the red line in Figures 3.9(a)). The higher observed flood occurrence in the 2000s could also be partly related to an increase in favourable hydroclimatic conditions, as all three MAR simulations, and more particularly MAR-ERA and MAR-ERA-20C, show a new peak in simulated SFD (see the red line in Figures 3.9(a)) and especially in simulated PFD (see the red line in Figures 3.9(b)). Although observations about flood events frequency are available only after 1974, we identify another peak in the 1960s in SFD (see the red line in Figures 3.9(a)), PFD (see the red line in Figures 3.9(b)). Since this peak coincides with the higher flood frequency period of the 1960s observed by Pauquet and Petit (1993), we assume that this period of higher floods frequency was also induced by favourable hydroclimatic conditions. In addition, previous studies identified the 1960s as a wetter period (Ntegeka and Willems, 2008; Willems, 2013b,a).

3.6 Chapter conclusion

The main objectives of this chapter were first to determine whether significant trends in snow cover evolution exist over the period 1959–2010 in the

Belgian Ardennes. Secondly, since most of the floods that take place in the Ardennes rivers occur in winter as a result of rapid snowpack melting and/or heavy rainfall events, this chapter also aimed to assess the changes in hydroclimatic conditions that could generate floods in the Ourthe, a river of the Ardennes. The recent changes in climate were reconstructed using the RCM MAR forced by several reanalysis datasets: ERA-Interim (1979–2014) completed by ERA40 (1958–1978), NCEP/NCAR-v1 (1958–2014), and ERA-20C (1958–2010).

Trends over the period 1959–2010 were computed from the MAR outputs by focusing on the winter months. In the Ourthe catchment area, neither MAR-ERA nor MAR-NCEP1 show any significant trends whether in winter mean temperature or in extreme (P5 and P95) temperature. Regarding precipitation in winter, MAR-NCEP1 and MAR-ERA-20C show a significant decrease in large part of the Ourthe catchment ranging from -10 mm and -40 mm 52yrs^{-2}. Trends in both intensity and frequency of extreme precipitation events show a positive signal with MAR-ERA and with MAR-ERA-20C reaching +4 mm 52yrs^{-2} and +4 extreme events 52yrs^{-2} in some parts of the Ourthe catchment. All MAR configurations exhibit a significant decrease in the maximum snow height reached during winter in the Ardennes over 1959–2010, with trends valued between -5 and -15 cm 52yrs^{-1} in the Ourthe catchment. The number of days with at least 5 cm of snow accumulation is reduced up to -15 days 52yrs^{-1}, and the beginning of the snow season is delayed up to -60 days 52yrs^{-1} in the highest parts of the Ourthe catchment. Since the NAO is known to highly impact the weather of European winters, the large interannual variability of the NAO index explains the absence of significant trends in winter temperature in Belgium in comparison with the observed global warming. The general increase of the NAO index observed since 1959 suggests a higher occurrence of anticyclonic conditions, which could be responsible for the decrease in winter precipitation and consequently for the decrease in snow accumulation. However, the multidecadal oscillations in Belgian precipitation could also explain the absence of clear trend in precipitation amount and extremes.

Regarding hydroclimatic conditions favouring floods in winter in the Ourthe catchment, the number of days favourable to floods due to snow melting combined with rainfall events is decreasing over 1959–2010 whatever the MAR simulations. This results from a decrease in snow accumulation in

winter and from a shortening of the snow season over the studied period. Regarding the number of days favourable to floods due to intense rainfall alone, the signal depends on the reanalysis used as forcing. It is due to the fact that the signal and the pattern of the trends in both the intensity and the frequency of extreme precipitation events differ depending on the MAR forcing. In a warmer climate, we could assume that the current trend of decreasing floods due to abrupt melting of the snowpack should accelerate. Yet, this decreasing trend favouring less floods in Belgium could be compensated by an increase in the occurrence of extreme rainfall events and by an increase in precipitation amount in autumn and winter as highlighted by Baguis *et al.* (2010); Willems (2013c) or Tabari *et al.* (2015). Similar simulations using global models from the CMIP5 (Coupled Model Intercomparison Project Phase 5) database as forcing should help to better predict potential changes at the end of this century. It would allow to provide dynamic downscaling results to enhance the statistical downscaling findings Tabari *et al.* (2015).

This study brings to light the differences and the limits of the reanalyses used to force the MAR model. Indeed, the comparison of the model results with observations over 2008-2014 showed that MAR-ERA produces slightly better results than MAR-ERA-20C and particularly MAR-NCEP1. In addition, the trend study shows that the results differ according the reanalysis forcing MAR. It also shows that given the unclear signal for the impact of extreme precipitation evolution on conditions favouring floods, the reanalysis data is maybe too coarse to allow to MAR to capture those events in an accurate way. A quick comparison with the literature allows to determine which reanalysis forcing the MAR model is the best to study each variables:

- When used as MAR forcing, NCEP/NCAR-v1 produces the worst results when compared with observations, especially in terms of precipitation amount measurements and consequently floods dates. The trend study shows that MAR forced by this reanalysis produces trends in opposition with previous studies and the two other MAR simulations regarding the wintertime extreme events intensity and frequency, as well as conditions favourable to floods generating by intense rainfall events. However, MAR-NCEP1 produces consistent results regarding trends in temperature, snow accumulation and snow season. The weaknesses of MAR-NCEP1 could be explained by the low spatial resolution of the

NCEP/NCAR-v1 reanalysis as the MAR model is directly forced by this reanalysis. Therefore, using MAR-NCEP1 simulations performed at an intermediate resolution as forcing of the 5 km MAR would possibly improve the results. However, it should be noted that Kay (2016) found that the direct use of data from the intermediate resolution is generally better for hydrological modelling.

- ERA-20C produces good results when compared with observations. However, the trends in winter temperature computed from MAR-ERA-20C are overestimated as well as the trends in snow season. Despite better spatial resolution than NCEP/NCAR-v1, air temperature data are not assimilated in ERA-20C which potentially explains this bias in temperature. However, MAR-ERA-20C produces consistent results regarding trends in extreme precipitations events, trends in snow accumulation and consequently trends in hydroclimatic conditions favourable to floods.
- ERA-Interim produces the best results when compared with observations and conclusions of previous studies. It is due to a better data assimilation system and a better spatial resolution in comparison with NCEP/NCAR-v1 or ERA-20C.

Finally, this study highlights the strengths and the weaknesses of the MAR model running over a temperate region. Regardless of the reanalysis used as forcing, MAR showed its ability to reconstruct the variability of the Belgian climate, especially the daily variability of temperature and snow depth. However, MAR underestimates temperature in winter and conversely, it overestimates temperature in summer. MAR also underestimates snow depth. Moreover, MAR shows difficulties to simulate precipitation in terms of daily variability and amount. Last of all, although the model allows to reconstruct hydroclimatic conditions favouring floods in the Ourthe catchment, it largely overestimates the number of days which could have generated floods over 1974–2010. Therefore, in the view of these discrepancies, improvements in the model are required such as:

- The re-parameterization of the fresh snowfall density would correct the negative bias in snow accumulation. Indeed, we used a fresh snowfall density of 300 kg m^{-3} which is typical in polar regions while lower values are more relevant in temperate climates (100 kg m^{-3}).

- The improvement of the convective scheme parameterized in MAR would partly correct precipitation biases as well as temperature biases in summer. However, it should be noted that studies using convection-permitting RCM have shown that, while some aspects of precipitation are improved, some are not improved or can even be worse (Kendon *et al.*, 2017; Chan *et al.*, 2013; Saeed *et al.*, 2017; Vanden Broucke *et al.*, 2018).
- The improvement of the surface and soil properties of MAR would also partly correct precipitation and temperature biases since test simulations demonstrate that wetter soils allow to correct the temperature biases in summer. The coupling between MAR and a complex hydrological model would possibly reduce the temperature and precipitation biases by enhancing energy and water fluxes between the surface/soil and the atmosphere (Larsen *et al.*, 2016; Wagner *et al.*, 2016). Coupling MAR with a dynamic vegetation model would improve the vegetation-climate interactions and feedbacks (Strengers *et al.*, 2010). Finally, coupling MAR to an advanced land-surface model to improve both the soil moisture-atmosphere and vegetation-atmosphere interactions would lead to improvements of several aspects of the simulated climate such as cloud cover, surface temperature and precipitation (Davin *et al.*, 2011).
- The coupling between MAR and a hydrological model would also allow to improve floods detection and simulation by taking into account mechanisms which are too simplified or not represented in the regional climate models. In this way, the hydrology of the catchment and the river flow rate would be explicitly simulated.

CHAPTER 4

Future evolution of hydroclimatic conditions favouring floods in the south-east of Belgium by 2100

This chapter is based on Wyard C., Scholzen C., Doutreloup S., Fettweis X. (2018) Future projections of hydroclimatic conditions favouring floods in Belgium. In review in *International Journal of Climatology*.

4.1 Context

Flow regimes in Belgian catchments are generally dominated by rainfall (pluvial) rather than snow, although snowmelt can be a major component of the regime for catchments that drain the Ardennes massif such as the Ourthe catchment. The Ourthe River is one of the main tributaries of the Meuse River, with a catchment area of about 3500 km^2 (Pauquet and Petit, 1993). While the Ourthe River is mainly rain-fed, the snowpack that covers the Ardennes summits during winter also influences its discharge because of its buffering effect (Driessen *et al.*, 2010). The Ourthe reaches its highest level either in winter or in spring when the snowpack is melting. In the Ourthe catchment, 70 % of flood events occur during winter. About half of the observed floods are due to abundant rainfall alone. However, the rapid melting of the snowpack that covers the Ardennes summits, combined with heavy rainfall events, are responsible for major floods in the lower part of the Ourthe River, as it was the case in February 1984, March 1988, December 1991 and, more recently, in January 2002 and January 2011 (Pauquet and Petit, 1993; de Wit *et al.*, 2007). In a changing climate, hydroclimatic conditions favouring floods in the Ourthe catchment are therefore likely to be affected by changes in both snow cover and precipitation.

Global warming is already affecting snow and ice processes by reducing the amount of snowfall, the extent of the annual average snow cover and the snow depth, and by inducing earlier snowmelt in various European regions such as the Alps (Durand *et al.*, 2009; Valt and Cianfarra, 2010; Beniston, 2012a), Britain (Kay, 2016), Norway (Skaugen *et al.*, 2012; Dyrrdal *et al.*, 2013), or Eastern Europe (Falarz, 2004; Brown and Petkova, 2007; Birsan and Dumitrescu, 2014). This declining snow cover is responsible for a decrease in the intensity and in the frequency of the floods dominated by snowmelt, which is predicted to accelerate in the future (Madsen *et al.*, 2014; Bell *et al.*, 2016; Vormoor *et al.*, 2016). Belgian high-lands are no exception to the trend, since their close to 0 °C current mean winter temperature implies that they are more affected by rising temperatures than colder or warmer regions (Hamlet and Lettenmaier, 2007; Stewart, 2009). By the use of modelisation, Wyard *et al.* (2017) found that the maximum snow height lowered by 5 to 15 cm in the Ardennes over 1959–2010, the number of days with at least 5 cm of snow accumulation are dropped by up to -15 days, and

the beginning of the snow season was delayed by up to -60 days in the highest parts of the Ourthe catchment (Section 3.4.3). Such a decline in the Belgian seasonal snow cover resulted in a significant decrease (-0.1 days winter^{-1} over 1959–2010) in conditions favourable to floods induced by rapid snow melting (Wyard *et al.*, 2017) (Section 3.5).

Regarding precipitation amount and extreme precipitation event frequency and intensity in winter, studies based either on observations (Gellens, 2000; Vaes G, Willems P, 2002; De Jongh *et al.*, 2006; Ntegeka and Willems, 2008; Willems, 2013a,b; RMIB, 2015) or modeling (Wyard *et al.*, 2017) found no significant long-term trend over the last century in any part of the Belgian territory (Section 3.4.2). Nevertheless, these studies identify multidecadal oscillations characterized by drier periods in the 1900s, around 1920 and in the mid-1970s (De Jongh *et al.*, 2006; Willems, 2013a,b) alternating with wetter periods in the 1910–1920s, the 1950–1960s and in the 1990–2000s (Ntegeka and Willems, 2008; Willems, 2013a,b), that coincide with the decadal variations of the North Atlantic Oscillation (NAO). Accordingly, hydroclimatic conditions favourable to floods induced by heavy rainfall alone show no significant long-term trend in the Ourthe catchment over 1959–2010 (Wyard *et al.*, 2017), yet follow the same decadal oscillations as the NAO (Section 3.5).

In the future, the decline in seasonal snow cover is predicted to continue while the global hydrological cycle is expected to intensify (Vaughan *et al.*, 2013). For Belgium, studies using regional climate models (RCM) forced by ensemble simulations from the Coupled Models Intercomparison Project phase 5 (CMIP5) archive (Tabari *et al.*, 2015) and by downscaled global climate model (GCM) (Brouwers *et al.*, 2015; Saeed *et al.*, 2017; Vanden Broucke *et al.*, 2018) concluded that under the RCP8.5 scenario, the intensification of the hydrological cycle will lead to increasing precipitation amount, as well as more frequent and more intense extreme precipitation events in winter by the end of the 21st century. For the Ourthe River, Driessen *et al.* (2010) concluded that "*towards the end of the century, all scenarios show a decrease in summer discharge, partially because of the diminished buffering effect by the snow pack, and an increased discharge in winter*". Regarding hydroclimatic conditions favouring floods in the Ourthe catchment, we would expect (despite the absence of high resolution projections for snow cover in Belgium) the decline due to snow melting to continue in the future, while

conditions favourable to floods due to abundant rainfall alone would increase significantly. The question is whether or not this increase in conditions favourable to floods due to abundant rainfall would counterbalance the decrease in conditions favourable to floods due to snow pack melting by the end of the 21^{st} century.

This study aims to assess the impact of climate change on the winter climate of Belgium and its consequences on hydroclimatic conditions favourable to floods in the Ourthe catchment. This investigation is achieved by using high-resolution projections of snow cover and precipitation. Such projections were obtained by downscaling two GCMs, NorESM1-M and MIROC5, from the CMIP5 archive using the MAR ("Modèle Atmosphérique Régional") RCM. By contrast to GCMs, RCMs run over a limited area and at finer spatial resolution (down to 5 km for MAR). This implies that the orography and other surface characteristics are finer in RCMs than in GCMs whose typical resolutions turn around 40-200 km. The representation of orographic features is a key factor for the simulation of temperature, precipitation and snow. Temperature generally decreases with altitude while snow depends on the 0 °C isotherm location and elevation. The orography of Belgium which ranges from sea level to about 700 m a.s.l. is known to have a clear effect on precipitation averages (Journée *et al.*, 2015) and associated extremes (Brisson *et al.*, 2011; Sneyers *et al.*, 1989; Van Meijgaard, 1995; Van de Vyver, 2012; Wyard *et al.*, 2017; Zamani *et al.*, 2016). In addition, snow processes are usually not accounted for in GCMs, while they are in some RCMs. MAR is one of these RCMs as its snow module, CROCUS, allows the representation of snow accumulation and metamorphism, snow melting on the surface, water percolation into the soil/snow, and run-off of exceeding water (Brun *et al.*, 1992). The ability of MAR to simulate the current winter climate of Belgium in terms of its seasonal snow cover, precipitation extremes and hydroclimatic conditions favouring floods has been evaluated in Wyard *et al.* (2017).

This chapter is organised as follows: Section 4.2 provides additional methodological aspects. Section 4.3 details the evaluation of MAR forced by two GCMs over 1976–2005 using Historical runs. The evolution of the Belgian winter climate under the RCP8.5 scenario throughout the 21^{st} century is then investigated in Section 4.4, while Section 4.4.4 presents the trends for the hydroclimatic conditions favouring floods in the Ourthe catchment.

Conclusions and prospects are finally reported in Section 4.5.

4.2 Additional methodological aspects

By contrast to Section 3 and Wyard *et al.* (2017) which used MAR version 3.6, this Section uses MAR version 3.8, described in Section 2.1, to reconstruct the climate of Belgium. A comparison between MARv3.6 and MARv3.8 is provided in Section 2.1.2.

Historical runs were obtained by nesting MAR into the ERA40/ERA-interim reanalysis (MAR-ERA), described in Section 2.2, and the GCMs NorESM1-M and MIROC5 (MAR-NOR-histo and MAR-MIR-histo) over 1976–2005. NorESM1-M and MIROC5 are two GCMs from the CMIP5 archive that we selected by using the skill score methodology of Connolley and Bracegirdle (2007) as described in Section 2.3. MAR-ERA was later considered as reference for the present-day climate.

Future projections were obtained by nesting MAR into NorESM1-M and MIROC5, under the RCP8.5 scenario over 2006–2100 (MAR-NOR-rcp85 and MAR-MIR-rcp85).

It should be noted that conditions favouring floods were computed for the Ourthe catchment upstream of Sauheid. This part of the Ourthe catchment has an area of 2900 km^2 and its limits are drawn in light blue in Figure 4.2 to Figure 4.6.

4.3 Evaluation over the current climate

The aim of this section is to evaluate the ability of MAR forced by two GCMs selected from the CMIP5 archive, MAR-NOR-histo and MAR-MIR-histo, to simulate the present-day winter climate over Belgium. A good representation of the current climate is indeed a necessary condition required to realistically simulate future climate changes. A model that fails to reproduce the current climate generates projections that lack reliability and validity since the response of the climate to a warming is not linear (Fettweis *et al.*, 2013). In order to evaluate the consistency of MAR forced by NorESM1-M and MIROC5, we compared the climatic mean of both MAR-NOR-histo and MAR-MIR-histo to MAR-ERA for the period 1976–2005 regarding

temperature, precipitation, snow cover and conditions favourable to floods. As previously done in Fettweis *et al.* (2013), the differences between MAR forced by both GCMs and MAR-ERA are considered statistically significant if they are larger than the interannual variability of MAR-ERA over 1976–2005.

4.3.1 Temperature

The seasonal climatology of the mean winter temperature (TAVE) and the number of frost days per winter (FD) computed over 1976–2005 from MAR-ERA is displayed in Figure 4.1). Compared to this reference climatology, MAR-NOR-histo is warmer while MAR-MIR-histo is colder over 1976–2005 (Figure 4.2).

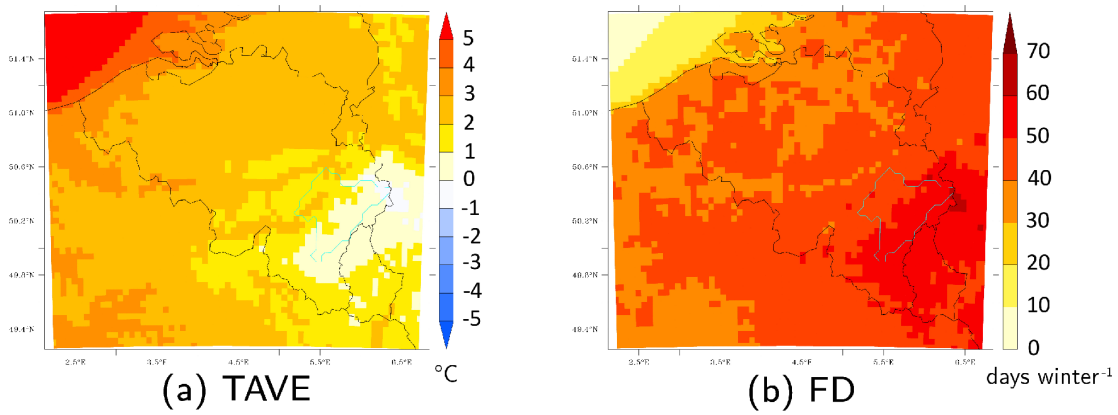

Figure 4.1: The 1976-2005 average **(a)** mean temperature (TAVE), and **(b)** number of frost days (FD), simulated by MAR-ERA in winter.

MAR-NOR-histo significantly overestimates TAVE by up to +3 °C (Figure 4.2(a)). These biases are large compared to the 1976–2005 TAVE simulated by MAR-ERA in winter which ranges from -1 to 4 °C (Figure 4.1(a)). FD, which is defined as the number of days with daily minimum temperature below 0 °C, is significantly underestimated in MAR-NOR-histo, by -10 days winter^{-1} in Low Belgium and up to -25 days winter^{-1} in the highest parts of the Ardennes massif (Figure 4.2(c)). These biases are also large compared to the 1976–2005 FD simulated by MAR-ERA in winter which ranges from 30 to 70 days winter^{-1} (Figure 4.1(b)).

MAR-MIR-histo, for its part, underestimates TAVE over land area. However, these negative biases are non-significant (Figure 4.2(b)). FD is significantly

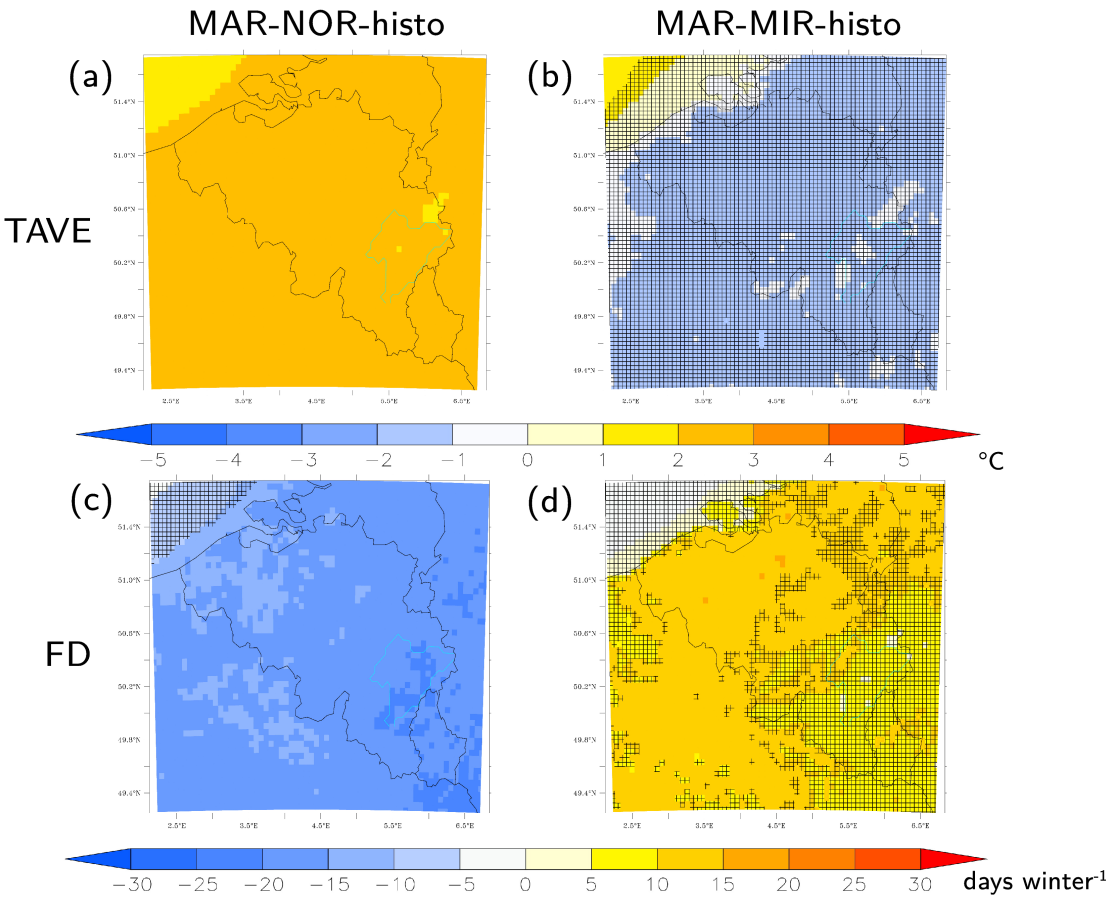

Figure 4.2: Anomalies in winter (DJF) of MAR-NOR-histo and MAR-MIR-histo with respect to MAR-ERA over 1976-2005 regarding **(a)-(b)** the mean temperature (TAVE), **(c)-(d)** the number of frost days (FD). Filled pixels indicate the places where the anomalies are statistically significant with respect to the MAR-ERA interannual variability. Hashed pixels indicate the places where the anomalies are statistically non-significant.

overestimated in MAR-MIR-histo over Low and Middle Belgium by +10 to +15 days winter^{-1} (Figure 4.2(d)).

4.3.2 Precipitation

The seasonal climatology of precipitation computed over 1976–2005 from MAR-ERA is displayed in Figure 4.3). Compared to this reference climatology, MAR-NOR-histo is wetter while MAR-MIR-histo is dryer over 1976–2005 (Figure 4.4).

MAR-NOR-histo shows significant positive biases in total precipitation in winter (PPNtot) over the Ardennes massif, ranging from +40 to +140 mm winter^{-1} (Figure 4.4(a)). Biases in PPNtot result from an overestimation of the

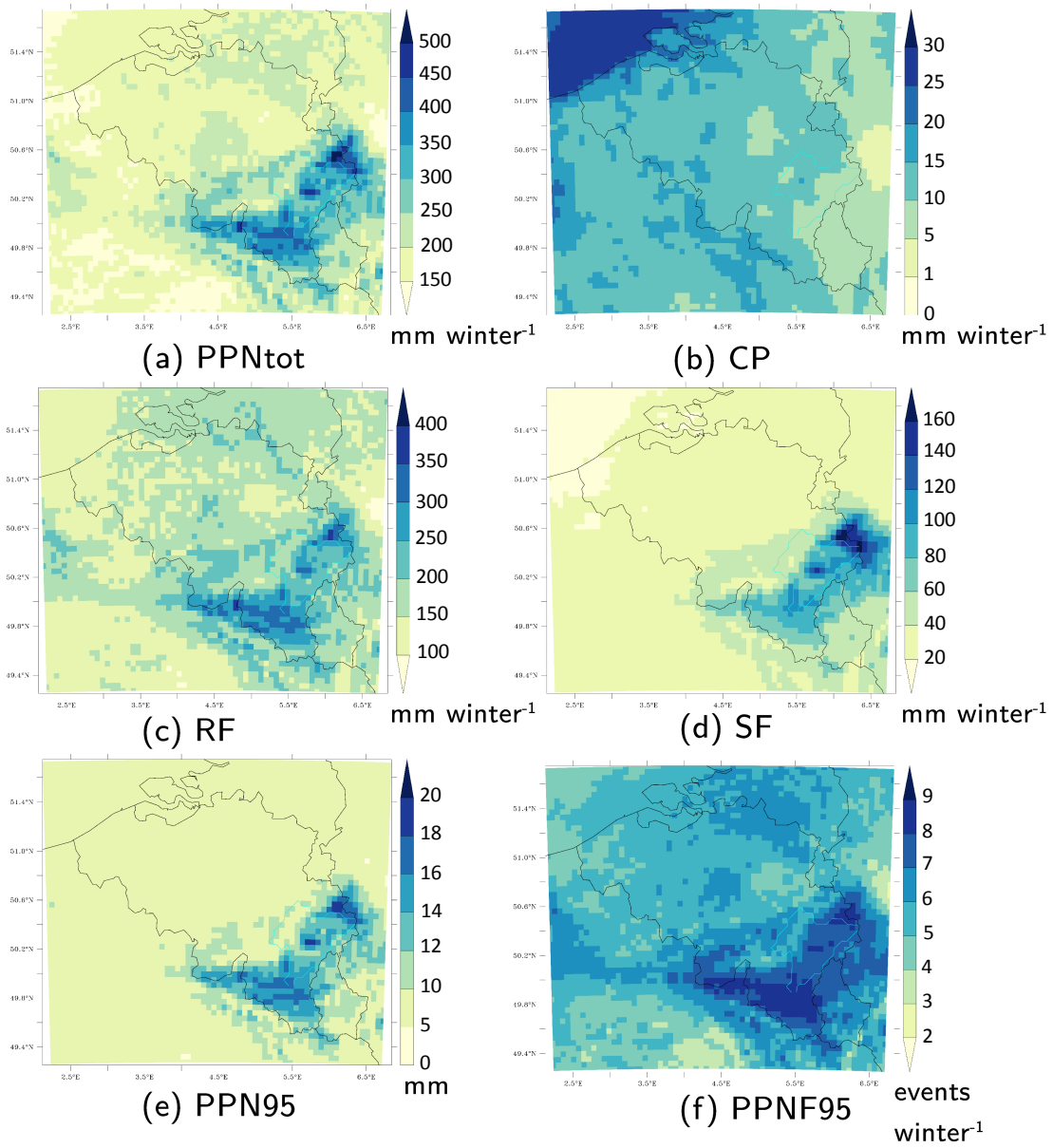

Figure 4.3: The 1976-2005 average **(a)** total precipitation amount (PPNtot), **(b)** convective precipitation amount (CP), **(c)** rainfall amount (RF), **(d)** snowfall amount (SF), **(e)** extreme precipitation intensity, and **(f)** extreme precipitation frequency, simulated by MAR-ERA in winter.

amount of rainfall (RF) as biases in RF show the same pattern as biases in PPNtot and range from +40 to +160 mm winter^{-1} (Figure 4.4(c)). Biases in PPNtot and RF are the largest where altitude is the highest. Regarding the intensity of extreme precipitation events in winter (PPN95, the 95^{th} percentile of the daily precipitation amount in winter as defined in Wyard *et al.* (2017)), MAR-NOR-histo amplifies PPN95, although the parts of the Belgian

territory where these biases are significant are very limited (Figure 4.4(e)).

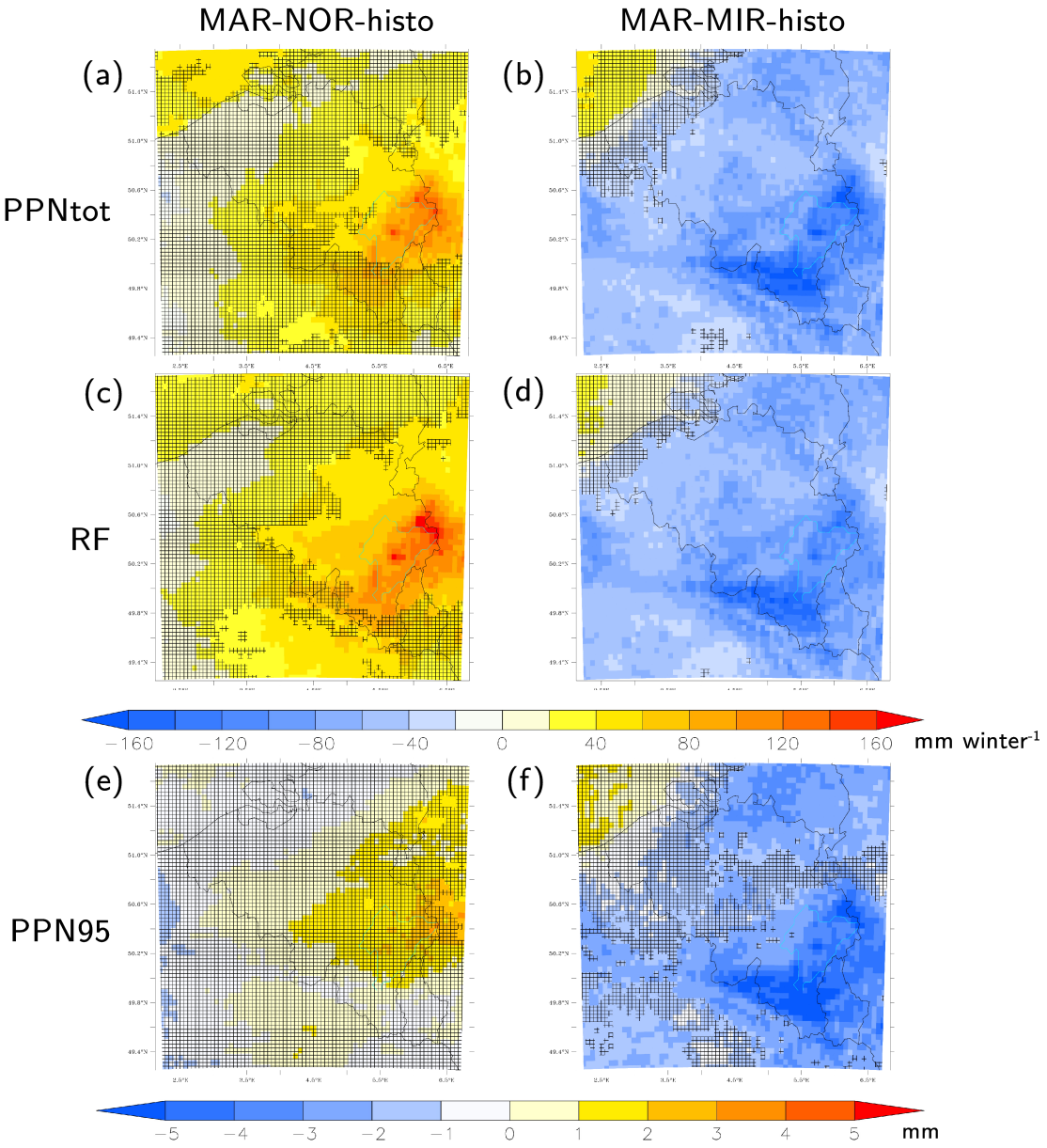

Figure 4.4: Anomalies in winter (DJF) of MAR-NOR-histo and MAR-MIR-histo with respect to MAR-ERA over the period 1976-2005 regarding **(a)-(b)** the total amount of precipitation (PPNtot), **(c)-(d)** the amount of rainfall (RF), **(e)-(f)** the intensity of extreme (P95) precipitation (PPN95). Filled pixels indicate the places where the anomalies are statistically significant with respect to the MAR-ERA interannual variability. Hashed pixels indicate the places where the anomalies are statistically non-significant.

MAR-MIR-histo shows the opposite behaviour with respect to MAR-NOR-histo. MAR-MIR-histo shows significant negative biases in PPNtot over the entire Belgian territory except coastal regions. These biases range from -20 to -160 mm winter^{-1} (Figure 4.4(b)). Biases in PPNtot result from an

underestimation of RF as biases in RF show the same pattern as biases in PPNtot and range from -20 to -160 mm winter^{-1} (Figure 4.4(d)). Regarding PPN95, MAR-MIR-histo significantly attenuates it over the southern and the north-eastern parts of Belgium, with values ranging from -1 to more than -5 mm (Figure 4.4(f)). It should be noted that the biases in PPNtot, RF and PPN95 are the largest in south-western foothills of the Ardennes massif, which is the direction from which most of the winter perturbations originates from. As temperature is underestimated in MAR-MIR-histo, this suggests that saturation is not reached in this part of the country due to a lack of humidity.

4.3.3 Snow

Compared to the 1976–2005 climatology computed from MAR-ERA (Figure 4.5), MAR-NOR-histo underestimates daily mean snow height (SHAVE) and maximum daily snow height (SHMAX), especially over the Belgian summits, but the biases are non-significant (Figure 4.6(a)-(c)).

Conversely, MAR-MIR-histo overestimates SHAVE and SHMAX, but the biases are only significant for SHMAX over the lowest part of Belgium with biases ranging from +3 to more than +5 cm ((Figure 4.6(b)-(d)) whereas MAR-ERA simulates average SHMAX values up to 5 cm (Figure 4.5(c)). Since only rainfall biases are significant (Section 4.3.2) and as the pattern of the biases in SHMAX is the same as the biases in FD (Figure 4.2(d)), we conclude that the overestimation of SHMAX over Low Belgium is due to an excess in the occurrence of minimum temperature below 0 °C in this part of the country (Section 4.3.1).

4.3.4 Conditions favouring floods

Finally, the ability of MAR forced by both GCMs to simulate hydroclimatic conditions favourable to floods has been investigated. As in Wyard *et al.* (2017), one day was defined as favourable to floods if the run-off computed by MAR, integrated and averaged over the Ourthe catchment area and finally averaged over the two days preceding a flood event, is larger than its 95^{th} percentile computed over a period of 30 years (1976-2005). Moreover, as there are two types of floods in the Ourthe catchment, we made the

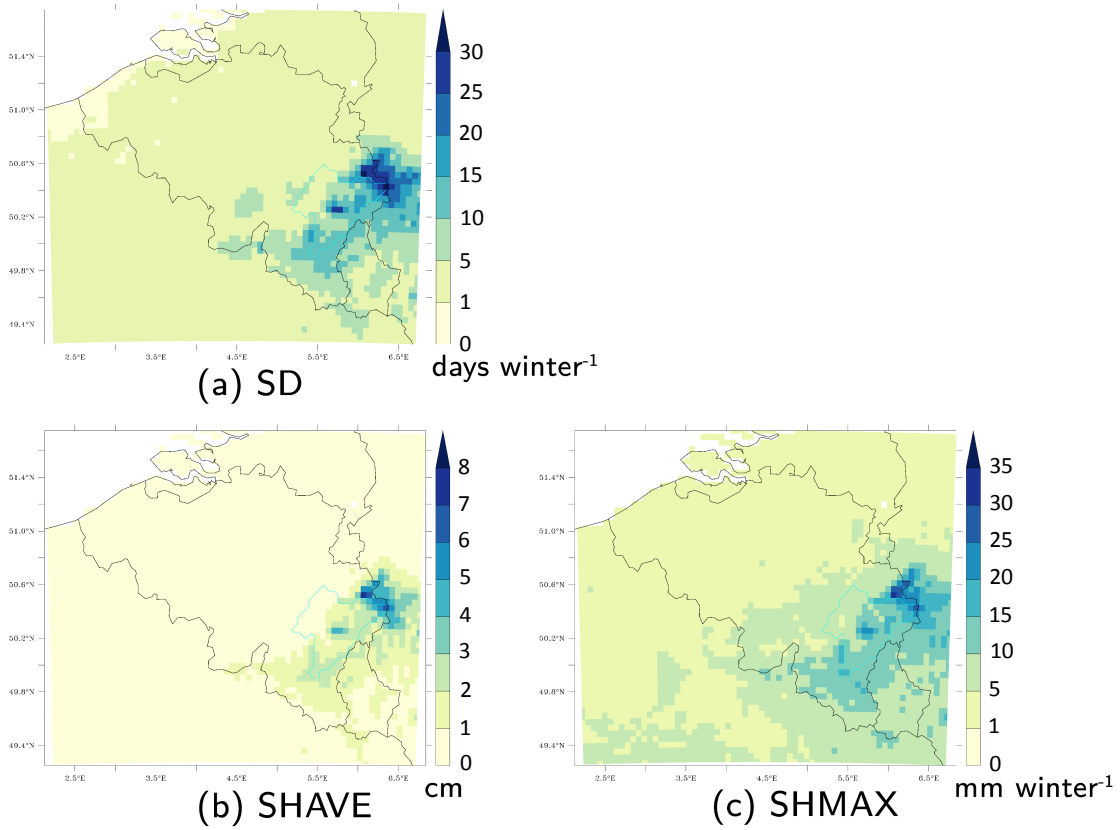

Figure 4.5: The 1976-2005 average **(a)** number of snow days (SD), **(b)** snow height (SHAVE), and **(c)** maximum snow height (SHMAX), simulated by MAR-ERA in winter.

distinction between extreme run-off events generated by snow melt combined to rainfalls (SFD for Snow melting Flood Days) and extreme run-off events generated by heavy rainfall alone (PFD for Precipitation Flood Days). The total number of days favourable to floods is the sum of SFD and PFD (TFD = SFD + PFD).

Compared to MAR-ERA, SFD and PFD are slightly overestimated in MAR-NOR-histo, although the differences valued at +0.1 days winter^{-1} for SFD and +1.1 days winter^{-1} for PFD (Table 4.1) are non-significant as they are smaller than the interannual variability of MAR-ERA over 1976-2005. As a result, the biases found in TFD in the Ourthe catchment computed from MAR-NOR-histo are also non-significant.

MAR-MIR-histo, for its part, overestimates SFD by +2.7 days winter^{-1} and conversely underestimates PFD by -2 days winter^{-1}, while TFD is slightly overestimates by +0.8 days winter^{-1} (Table 4.1). For SFD, this positive bias originates from the overestimation of snow accumulation in the Ourthe

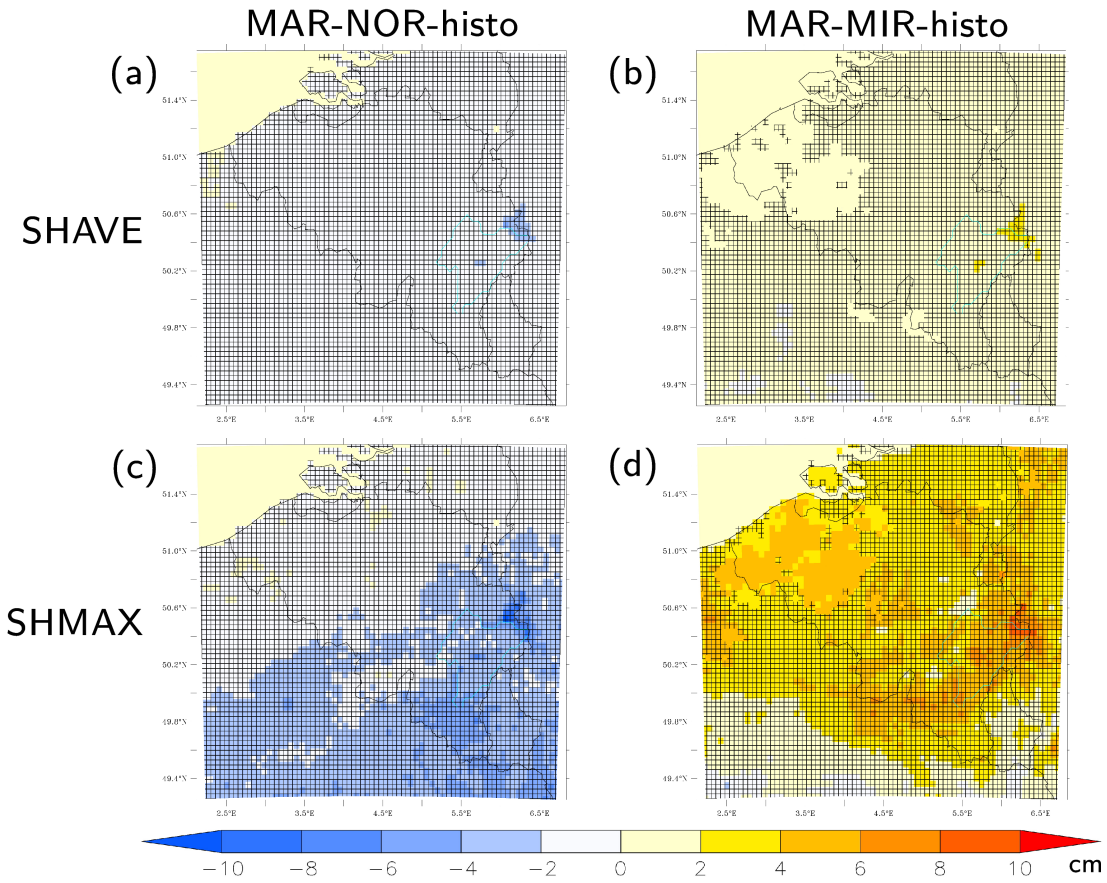

Figure 4.6: Anomalies in winter (DJF) of MAR-NOR-histo and MAR-MIRhisto with respect to MAR-ERA over the period 1976-2005 regarding **(a)-(b)** the daily mean snow height (SHAVE), **(c)-(d)** the maximum daily snow height (SHMAX). Filled pixels indicate the places where the anomalies are statistically significant with respect to the MAR-ERA inter-annual variability. Hashed pixels indicate the places where the anomalies are statistically non-significant.

Table 4.1: Average number of days favourable to floods per winter due to snowpack melting (SFD) and due to rainfalls (PFD) as well as the total average number of days favourable to floods (TFD = SFD + PFD) modelled by MAR-ERA, MAR-NOR-histo and MAR-MIR-histo over 1976–2005.

Simulation	**SFD** [days winter^{-1}]	**PFD** [days winter^{-1}]	**TFD** [days winter^{-1}]
MAR-ERA	4.2 ± 3.5	5.5 ± 3.0	9.7 ± 3.9
MAR-NOR-histo	4.3 ± 3.1	6.6 ± 3.2	10.9 ± 4.5
MAR-MIR-histo	7.0 ± 2.7	3.5 ± 2.9	10.5 ± 3.9

catchment due to too low temperatures (Sections 4.3.1 and 4.3.3). Regarding TFD, the negative bias results from the underestimation of PPN95 in the Ardennes massif (Section 4.3.2). Since these biases are also non-significant when compared to the interannual variability of MAR-ERA, we conclude that both MAR-NOR-histo and MAR-MIR-histo satisfactorily simulate extreme run-off events.

4.3.5 Origin of biases

The comparison of MAR-NOR-histo and MAR-MIR-histo with MAR-ERA has brought to light that the simulations forced by the two GCMs exhibit opposite biases. MAR-NOR-histo is too warm and too wet on average while MAR-MIR-histo is too cold, too dry and too snowy with respect to MAR-ERA. The good side of this statement is that using simulations which have opposite biases provides a good range of potential future scenarios. Nonetheless, discrepancies between all these three MAR simulations remain to be explained. Seeing that MAR-ERA, MAR-NOR-histo and MAR-MIR-histo use the exact same MAR set-up, the differences between these three simulations can only be explained by their forcing data.

Biases found in the GCMs from CMIP5 have been widely investigated in the literature. By comparing NorESM1-M with observations and reanalyses over 1976–2005, Bentsen *et al.* (2013) highlight that NorESM1-M overestimates cloud liquid water content (and thus precipitation), particularly in the extratropical storm track regions. Bentsen *et al.* (2013) also found that the model overestimates air temperature over Western Europe. These biases are in agreement with the overestimation in rainfall and the overestimated near-surface air temperature in winter over Belgium found in MAR-NOR-histo. Watanabe *et al.* (2010) compared MIROC5 to observational data, reanalyses and other global models, and thereby showed that the model slightly underestimates precipitation in general, which is in agreement with the underestimated winter precipitation found in MAR-MIR-histo.

As explained in Section 1.1, the European wintertime climate is known to be strongly constrained by the occurrence and the persistent of quasi-stationary circulation patterns of larger scale, also referred to as "weather regimes" (Reinhold and Pierrehumbert, 1982; Legras and Ghil, 1985; Vautard, 1990; Philipp *et al.*, 2007). Biases in the frequency of occurrence of each weather

regime simulated by the GCMs could therefore be responsible for the biases found in our MAR simulations. Studies usually classify these circulation patterns in four categories (Cassou, 2008; Cattiaux *et al.*, 2010, 2013). The positive phase of the NAO (NAO+) is generally associated with mild and rainy winters, while the negative phase of the NAO (NAO-) is associated with cold and snowy winters over Belgium. The persistence of a high-pressure system over Northern Europe or the British Isles, often referred to as "Scandinavian blocking" (SB) conditions, leads to cold and dry weather over Western Europe. Finally, the persistence of a high-pressure system over the Northern Atlantic, also referred to as "Atlantic ridge" (AR), allows inflow of arctic maritime air and is associated with cold and snowy winters. Cattiaux *et al.* (2013) investigated the ability of each GCM from CMIP5 to simulate the present-day mean frequencies of occurrence of all four circulation patterns in winter over Europe. For the period 1979–2008, NorESM1-M overestimates the NAO+ mean frequency by about +18%, while it underestimates the NAO- and SB mean frequencies by about -5% and -15% respectively. This explains why MAR-NOR-histo shows positive biases in temperature and (liquid) precipitation and negative biases in snow accumulation over a similar period (1976-2005). MIROC5, for its part, overestimates the NAO- and AR mean frequencies by about +20% and +10% respectively, while underestimating the NAO+ and SB mean frequencies by about -25% and -5% respectively. This explains why MAR-MIR-histo shows negative biases in temperature and (liquid) precipitation, and positive biases in snow accumulation.

4.4 Future changes in the Belgian winter climate

This section aims to assess the evolution of the Belgian climate during the winter months (DJF) by the end of the 21^{st} century under the RCP8.5 scenario. Changes in the future Belgian climate were assessed by comparing the 2071–2100 mean winter climate computed by MAR-NOR-rcp85 and MAR-MIR-rcp85 to the 1976-2005 mean winter climate computed by MAR-NOR-histo and MAR-MIR-histo. As previously done in Fettweis *et al.* (2013), for a given climate variable, its future changes were considered as significant if they were larger than its 1976–2005 interannual variability.

In addition, the evolution of the winter climate was also computed over 2006–2100 for the Ourthe catchment.

4.4.1 Temperature

For the end of the 21^{st} century, MAR-MIR-rcp85 exhibits larger changes in temperature than MAR-NOR-rcp85 with respect to the present-day climate (Figure 4.7). Changes in both MAR simulations are larger than their biases over the present-day climate.

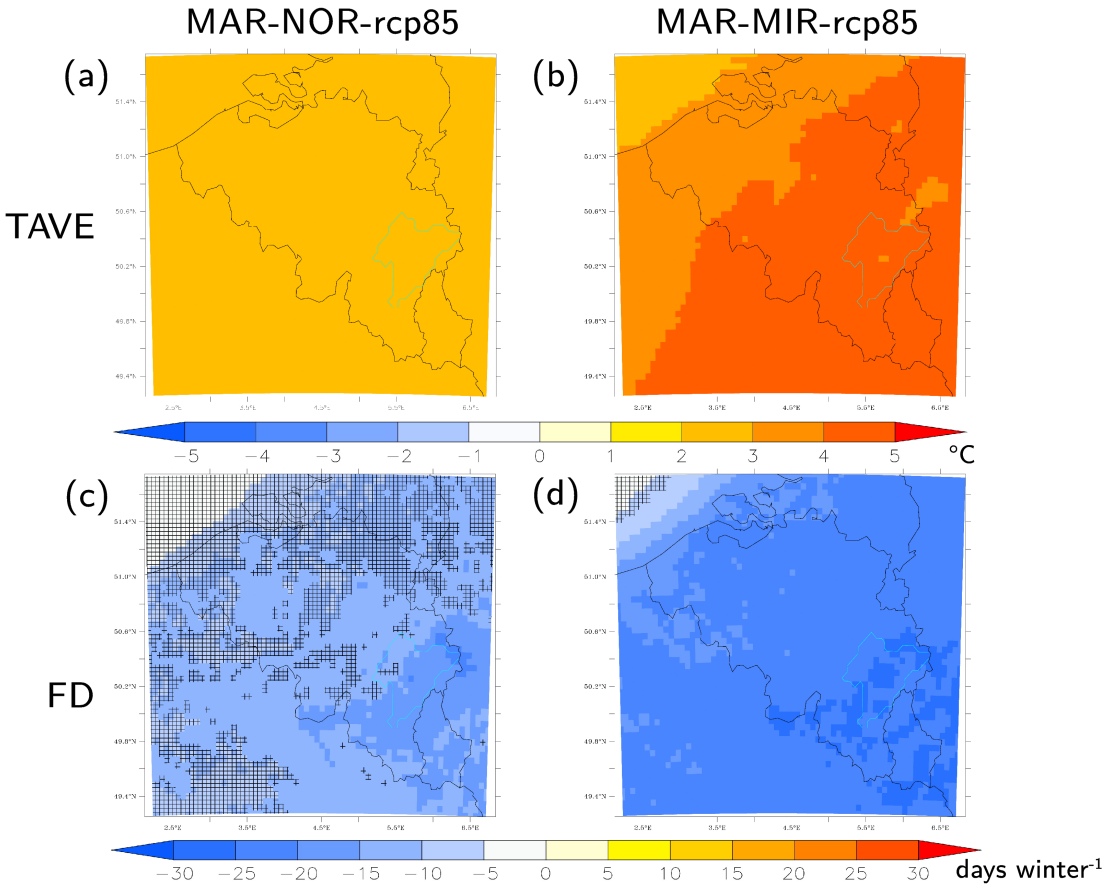

Figure 4.7: Changes in winter (DJF) of MAR-NOR-rcp85 and MAR-MIR-rcp85 with respect to MAR-NOR-histo and MAR-MIR-histo for the period 2071–2100 with respect to 1976–2005 regarding **(a)-(b)** the mean temperature (TAVE), **(c)-(d)** the number of frost days (FD). Filled pixels indicate the places where the changes are statistically significant with respect to the MAR-NOR-histo and MAR-MIR-histo interannual variability over 1976–2005. Hashed pixels indicate the places where the changes are statistically non-significant.

The 2071–2100 TAVE computed by MAR-NOR-rcp85 exhibits a significant increase by +2 to +3 °C over the entire Belgian territory with respect

to the 1976–2005 TAVE (Figure 4.7(a)). These values range from +3 to +5 °C for TAVE simulated by MAR-MIR-rcp85 (Figure 4.7(b)), depending on the altitude. The higher the altitude, the larger is the increase in TAVE. The results also show a significant decrease in future FD. MAR-NOR-rcp85 simulates a decrease in FD between -10 and -25 days winter^{-1} (Figure 4.7(c)), while MAR-MIR-rcp85 simulates a decrease in FD by -15 days winter^{-1} in coastal regions to -30 days winter^{-1} in the highest parts of Belgium (Figure 4.7(d)).

High-resolution simulations performed with COSMO-CLM (Brisson *et al.*, 2011) and ALARO (De Troch *et al.*, 2013) show similar results. Under RCP8.5, these RCMs exhibit a significant increase in TAVE valued at +6.2 °C for Uccle (Middle Belgium) by the end of the century (Brouwers *et al.*, 2015). They also found that temperature changes are larger in High Belgium than in Low and Middle Belgium.

4.4.2 Precipitation

By comparing the 2071–2100 mean climate with the 1976–2005 mean climate, MAR-NOR-rcp85 and MAR-MIR-rcp85 show no significant changes in RF over most of the Belgian territory (Figure 4.8(a)-(b)). Only MAR-NOR-rcp85 simulates a significant increase in RF over coastal regions, ranging from +40 to +70 mm winter^{-1} (from +20 to +50 % winter^{-1}) depending on the distance to the North Sea. The larger the distance is, the smaller the increase in RF is. In addition, MAR-NOR-rcp85 and MAR-MIR-rcp85 agree on a significant decrease in the amount of snowfall (SF) over the Ardennes massif, with values ranging from -20 to -80 mm winter^{-1} (from -50 to -70 % winter^{-1}) (Figure 4.8(c)-(d)). Compared to MAR-NOR-rcp85, MAR-MIR-rcp85 simulates significant changes in SF over the entire Belgian territory, which are on average +10 mm winter^{-1} (+10 % winter^{-1}) larger. It should be noted that the significant decrease in SF is not counterbalanced by a significant increase in rainfall, which suggests that solid precipitation is not converted into liquid precipitation. MAR-NOR-rcp85 and MAR-MIR-rcp85 also agree on a significant increase in the amount of convective precipitation in winter (CP) as shown in Figure 4.8(e)-(f).

Regarding extreme precipitation events in winter, the signal is not clear. MAR-NOR-rcp85 simulates an increase in their intensity (PPN95) over very

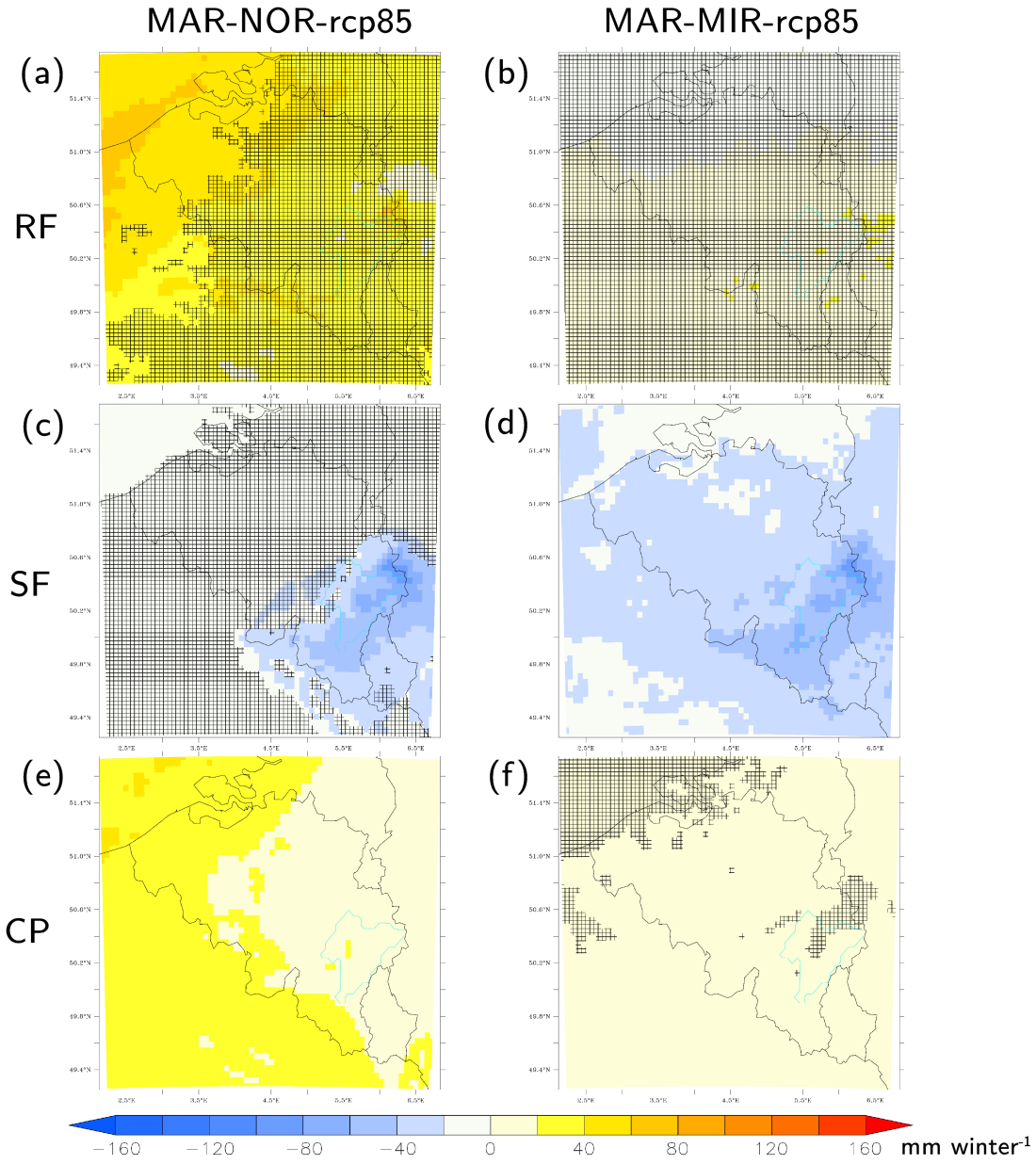

Figure 4.8: Changes in winter (DJF) of MAR-NOR-rcp85 and MAR-MIR-rcp85 with respect to MAR-NOR-histo and MAR-MIR-histo for 2071–2100 with respect to 1976–2005 regarding **(a)-(b)** the amount of rainfalls (RF), **(c)-(d)** the amount of snowfalls (SF), and **(e)-(f)** the amount of convective precipitation (CP). Filled pixels indicate the places where the changes are statistically significant with respect to the MAR-NOR-histo and MAR-MIR-histo interannual variability over 1976–2005. Hashed pixels indicate the places where the changes are statistically non-significant.

limited parts of coastal regions (Figure 4.9(a)). These changes range from +1 to +3 mm (from +10 to +40 %) by the end of the century. The pattern of these changes is the same as for CP in both MAR future projections

(Figure 4.8(e)). MAR-NOR-rcp85 also simulates a significant increase in the frequency of extreme precipitation events (PPNF95, number of days per winter with daily precipitation amount larger than its 95^{th} percentile computed over 1976–2005) between +1 and +2 days winter^{-1} (from +40 to +80 % winter^{-1}) over limited parts of northern Belgium (Figure 4.9(c)). On the contrary, MAR-MIR-rcp85 shows a non-significant negative signal in both PPN95 and PPNF95 (Figure 4.9(b)-(d)).

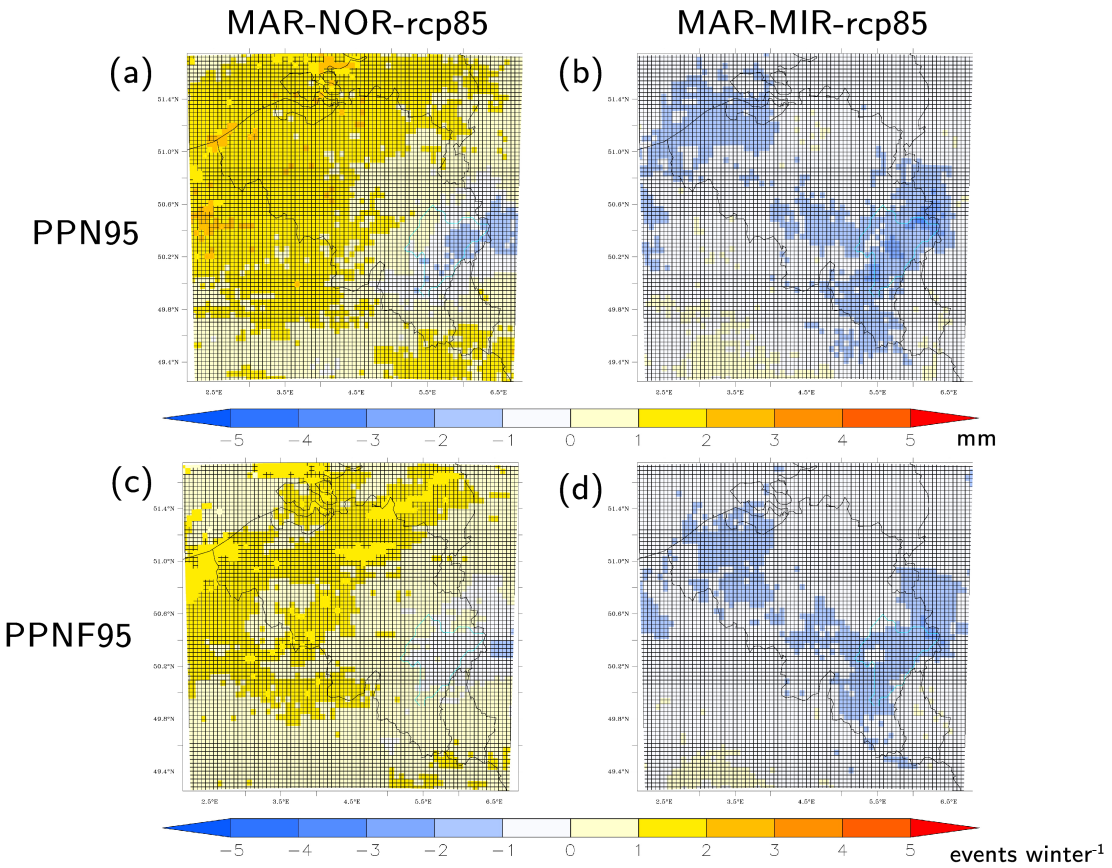

Figure 4.9: Changes in winter (DJF) of MAR-NOR-rcp85 and MAR-MIR-rcp85 with respect to MAR-NOR-histo and MAR-MIR-histo for 2071–2100 with respect to 1976–2005 regarding **(a)-(b)** the intensity of extreme (P95) precipitation events (PPN95), and **(c)-(d)** the frequency of extreme precipitation events (PPNF95). Filled pixels indicate the places where the changes are statistically significant with respect to the MAR-NOR-histo and MAR-MIR-histo interannual variability over 1976–2005. Hashed pixels indicate the places where the changes are statistically non-significant.

Ensemble simulations from CMIP5 exhibit an increase in PPNtot valued at +19.62 ±21.64 % (Tabari *et al.*, 2015), while high resolution future projections simulate an increase in PPNtot of +38 % winter^{-1} over central Belgium (Brouwers *et al.*, 2015). As in MAR-NOR-rcp85, this increase is

expected to be greater in coastal regions. Brouwers *et al.* (2015) stated that this coastal effect is greatly dependent on the interaction between changes in air currents, the temperature contrast between land and sea, and the increase in temperature. The models that predict the greatest increase in precipitation near the coast are also those with the greatest temperature gradient between the North Sea and Uccle. Regarding extreme precipitation events, Saeed *et al.* (2017), using the COSMO-CLM RCM, simulated a significant increase in their intensity by Mid-century (2060-2069), which is predicted to continue beyond this period (Brouwers *et al.*, 2015). Vanden Broucke *et al.* (2018) also found an increase in both the frequency and the intensity of extreme daily precipitation accumulation by the end of the 21^{st} century. This amplification is again expected to be the largest in coastal regions. Although MAR-NOR-rcp85 also simulates an intensification of extreme precipitation events, the changes computed from both MAR future simulations are not significant and diverge.

4.4.3 Snow cover

Both MAR-NOR-rcp85 and MAR-MIR-rcp85 simulate a decrease in snow cover by the end of the century that is larger than their biases over the present-day climate. However, as shown in Figure 4.10(a)-(c)-(e), neither SHAVE, SHMAX, nor SD (the number of days per winter with a snow cover of at least 5 cm of thickness) change significantly in the MAR-NOR-rcp85 simulations.

MAR-MIR-rcp85 however, simulates a significant, larger decrease in all these three variables over the Ardennes and hence in the Ourthe catchment (Figure 4.10(b)-(d)-(f)). As shown in Figure 4.10(b), MAR-MIR-rcp85 shows a significant decrease in SHAVE from -2 to -8 cm, which is significant in the highest parts of the Ardennes. A significant decrease in SHMAX is also simulated by MAR-MIR-rcp85, with values ranging from -2 to -6 cm over lowlands, and from -6 cm to more than -10 cm in the Ardennes (Figure 4.10(d). SD is also significantly decreasing over the highest parts of the Ardennes in MAR-MIR-rcp85, with values larger than -10 days winter^{-1} (Figure 4.10(f)).

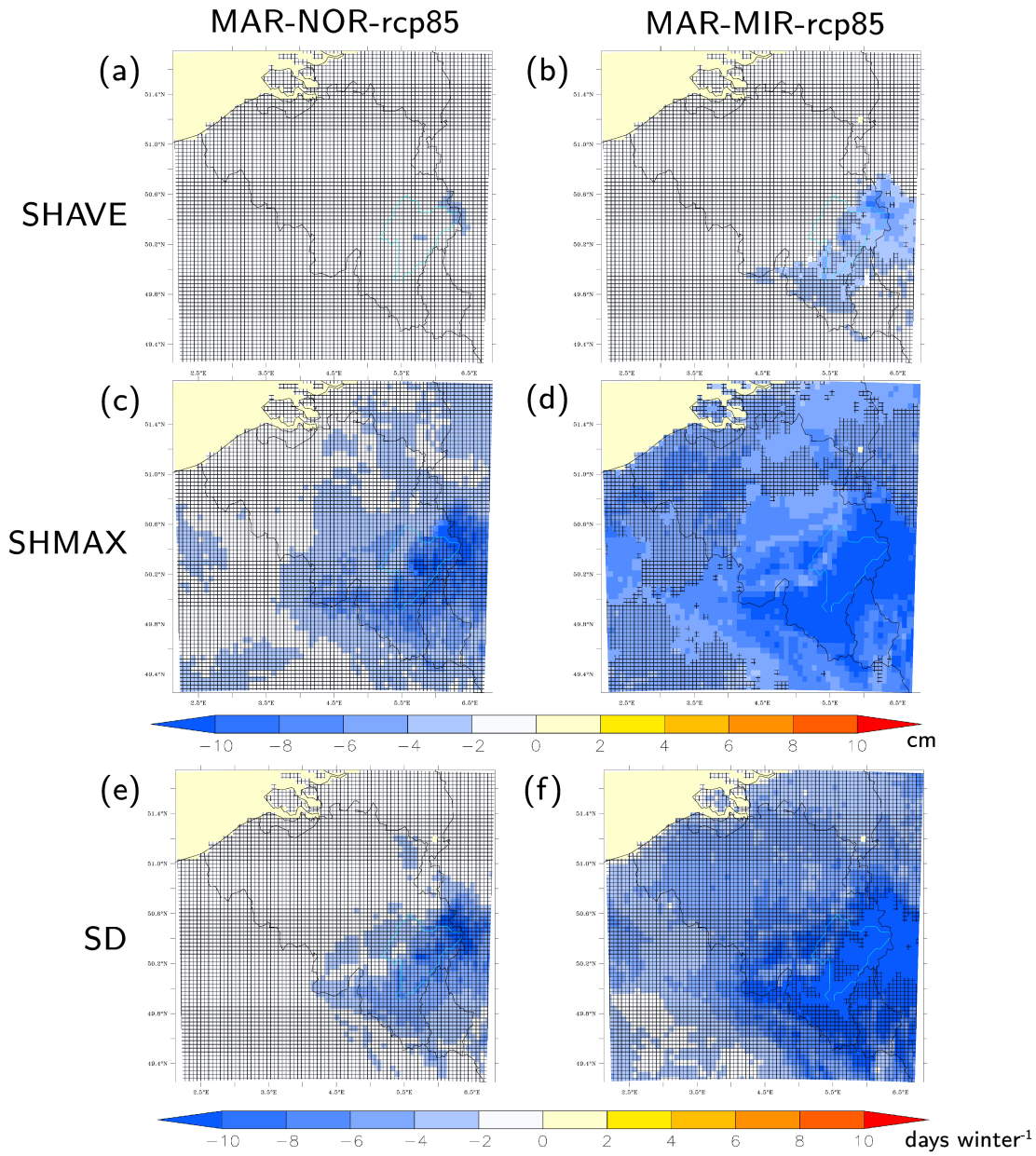

Figure 4.10: Changes in winter (DJF) of MAR-NOR-rcp85 and MAR-MIR-rcp85 with respect to MAR-NOR-histo and MAR-MIR-histo for 2071–2100 with respect to 1976–2005 regarding **(a)-(b)** the daily average snow height (SHAVE), **(c)-(d)** the maximum daily snow height (SHMAX), and **(e)-(f)** the number of snow days (SD). Filled pixels indicate the places where the changes are statistically significant with respect to the MAR-NOR-histo and MAR-MIR-histo interannual variability over 1976–2005. Hashed pixels indicate the places where the changes are statistically non-significant.

4.4.4 Conditions favouring floods

The 2071–2100 SFD is valued at 1.2 days winter^{-1} in MAR-NOR-rcp85 and 1.8 days winter^{-1} in MAR-MIR-rcp85 (Table 4.2). Compared to

1976–2005 (Table 4.1), this represents a significant decrease of -73% and -74% respectively (Table 4.2), which results from decreased SHMAX and SD simulated in the Ardennes (Section 4.4.3). The evolution of SFD between 1976 and 2100 is plotted in Figure 4.11(a)-(d). Despite a large interannual variability, a steady decline in SFD can be observed in both MAR future simulations. The linear trend in SFD computed for the period 2006–2100 is significant and valued at -0.023 days winter^{-1} in MAR-NOR-rcp85 (Figure 4.11(a)) and -0.024 days winter^{-1} in MAR-MIR-rcp85 (Figure 4.11(d)).

Table 4.2: Average number of days favourable to floods per winter due to snowpack melting (SFD) and due to rainfalls (PFD) as well as the total average number of days favourable to floods (TFD = SFD + PFD) modelled by MAR-ERA, MAR-NOR-histo and MAR-MIR-histo for the period 2071–2100.

Simulation	**SFD** [days winter^{-1}]	**PFD** [days winter^{-1}]	**TFD** [days winter^{-1}]
MAR-NOR-rcp85	**1.2**[1]**(-73%)**[2]	8.3 (+26%)	9.5 (-13%)
MAR-MIR-rcp85	**1.8 (-74%)**	4.8 (+39%)	**6.6 (-37%)**

[1] The values in bold are statistically significant.
[2] The values under brackets refer to changes with respect to 1976–2005.

The 2071–2100 PFD is valued at 8.3 days winter^{-1} in MAR-NOR-rcp85 and 4.8 days winter^{-1} in MAR-MIR-rcp85 (Table 4.2). Compared to 1976–2005 (Table 4.1), this represents a non-significant increase of +26% and +39% respectively (Table 4.2), which results from a non-significant increase in RF, PPN95 and PPNF95 simulated in the Ardennes (Section 4.4.2). The evolution of PFD between 1976 and 2100 is plotted in Figure 4.11(b)-(e). The linear trend in PFD computed for the period 2006–2100 is non-significant and valued at +0.025 days winter^{-1} in MAR-NOR-rcp85 (Figure 4.11(b)) and +0.016 days winter^{-1} in MAR-MIR-rcp85 (Figure 4.11(e)).

The resulting 2071–2100 TFD is valued at 9.5 days winter^{-1} in MAR-NOR-rcp85 and 6.6 days winter^{-1} in MAR-MIR-rcp85 (Table 4.2). Compared to 1976–2005 (Table 4.1), this represents a decrease of -13% and -37% respectively, which is significant in MAR-MIR-rcp85 (Table 4.2). This negative signal indicates that the trend in TFD is dominated by the decrease in SFD. The evolution of TFD between 1976 and 2100 is plotted in Figure 4.11(c)-(f). The linear trend in TFD computed for the period 2006–2100 is non-significant

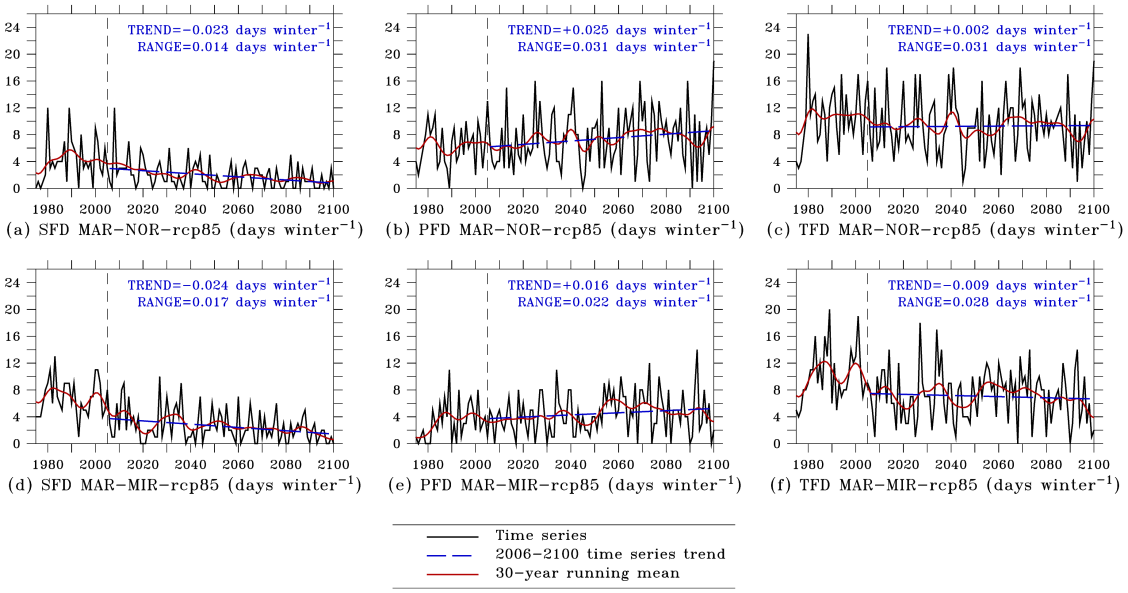

Figure 4.11: Time series, 30-year running mean, and trends computed from MAR-NOR-rcp85 and MAR-MIR-rcp85 of (a)-(d) the number of days per winter (DJF) favourable to floods due to snowpack melting combined with rainfall events (SFD), (b)-(e) the number of days per winter favourable to floods due to rainfall events alone (PFD), (c)-(f) the total number of days per winter favourable to floods (TFD)

and valued at +0.002 days winter^{-1} in MAR-NOR-rcp85 (Figure 4.11(c)) and -0.009 days winter^{-1} in MAR-MIR-rcp85 (Figure 4.11(f)).

4.4.5 Origin of discrepancies and uncertainties in future projections

Under the RCP8.5 scenario, both models generally agree on future increasing temperature, increasing RF and CP, decreasing SHMAX and SD in winter by the end of the century. Consequently, both models simulate decreasing SFD and a (non-significant) increase in PFD in the Ourthe catchment. However, MAR-MIR-rcp85 generally shows larger temperature increase, as well as larger SF and snow cover decrease than MAR-NOR-rcp85, while the latter shows larger RF, CP and PPN95 increase than MAR-MIR-rcp85. Discrepancies in our future projections remain to be explained. As already stated in Section 4.3.5, these discrepancies can only be related to the MAR boundary conditions, namely the CMIP5 GCM outputs which were downscaled using MAR. The comparison between the trends computed from the MAR future projections and those computed from NorESM1-M and MIROC5 regarding

RF and SF confirms that the trends and the discrepancies between our MAR simulations result from their forcing (Figure B.1, Appendix B).

Van Uytven and Willems (2018) analysed 160 CMIP5 climate simulations and showed that for the time horizon 2071-2100, the AOGCMs uncertainty overpasses the uncertainty linked to the greenhouse gas concentrations. This statement suggests that discrepancies between NorESM1-M and MIROC5 are mainly related to the physics of these two AOGCMs. For instance, under the same RCP scenario, both AOGCMs do not simulate the same increase in temperature or the same answer of large-scale dynamics (Cattiaux *et al.*, 2012). Cattiaux *et al.* (2013) compared the 2071-2100 mean frequencies of occurrence of the main weather regimes simulated by the CMIP5 AOGCMs with their 1981-2010 mean frequencies. They found that NorESM1-M exhibits more frequent AR regime (+5 %) and NAO- regime (+3 %), while MIROC5 exhibits more frequent NAO- regime (+8 %) and NAO+ regime (2 %) in the future. The larger increase in winter temperature simulated by MAR-MIR-rcp85 may therefore partly result from the increase in the frequency of NAO+ regime simulated by MIROC5.

Besides discrepancies and uncertainties related to the MAR forcings, issues related to the parameterizations implemented in the MAR RCM provide an additional source of uncertainty in our future projections. For instance, (Wyard *et al.*, 2017) showed that MAR underestimates CP. Therefore, the projected increase in winter CP simulated by MAR also adds uncertainty in the reliability of PPNtot, PPN95, PPNF95 and PFD simulated by MAR. The uncertainty linked to the model physics can account for the largest source of uncertainty in future projections.

4.5 Chapter conclusion

This chapter aims at evaluating the future evolution of hydroclimatic conditions favouring winter floods in the Ourthe catchment by the end of the 21st century under the RCP8.5 scenario. For this purpose, two GCMs from CMIP5, NorESM1-M and MIROC5, were selected by using the skill score methodology of Connolley and Bracegirdle (2007) and were dynamically downscaled using the MAR RCM. Historical simulations (MAR-NOR-histo and MAR-MIR-histo) and future projections (MAR-NOR-rcp85 and MAR-MIR-rcp85) were then performed using the version 3.8 of MAR forced by

these two GCMs. An evaluation of the historical simulations was first conducted by comparing MAR-NOR-histo and MAR-MIR-histo to MAR forced by the ERA-interim reanalyses (MAR-ERA) for the period 1976–2005 with focus on the winter months (DJF). An evaluation of future trends in the Belgian winter climate was then carried out by comparing the 2071–2100 future mean climate to the 1976–2005 present-day mean climate.

The evaluation of the MAR forced by GCM simulations shows that MAR-NOR-histo is on average warmer and wetter in winter than MAR-ERA, while MAR-MIR-histo is colder, drier and more snowy. For instance, MAR-NOR-histo significantly overestimates TAVE up to +3 °C, while MAR-MIR-histo exhibits cold but non-significant biases in TAVE up to -2 °C. Significant biases are also found in precipitation. MAR-NOR-histo overestimates RF up to +140 mm winter^{-1} on the Ardennes summits, while MAR-MIR-histo underestimates RF up to -140 mm winter^{-1} in the south-western foothills of the Ardennes. No significant bias is found in snow accumulation except in MAR-MIR-histo which significantly overestimates SHMAX in the coastal regions. Regarding hydroclimatic conditions favouring floods, discrepancies between MAR-ERA, MAR-NOR-histo, and MAR-MIR-histo are found to be non-significant. Biases in the MAR simulations are explained by biases in the frequency of occurrence of weather regimes simulated by the forcing GCMs. NorESM1-M favours NAO+ regime and therefore mild winters whereas MIROC5 favours NAO- regime and therefore cold and dry winters in Belgium.

Future trends show that both MAR-NOR-rcp85 and MAR-MIR-rcp85 agree on future increasing temperature (up to +5 °C in MAR-MIR-rcp85), increasing CP (up to +40 mm winter^{-1} in MAR-NOR-rcp85) and decreasing SF (up to -80 mm winter^{-1}), SHMAX (more than -10 cm winter^{-1} in MAR-MIR-rcp85), SD (more than -10 days winter^{-1} in MAR-MIR-rcp85) by comparing the 2071–2100 mean climate to 1976–2005. Only MAR-NOR-rcp85 shows a significant increase in RF, although only in coastal regions. We emphasize that our results are in agreement with previous findings (Brouwers *et al.*, 2015; Tabari *et al.*, 2015; Saeed *et al.*, 2017). It should also be noted that MAR-MIR-rcp85 shows a larger increase in temperature and a larger decrease in the snow cover than MAR-NOR-rcp85, while the latter exhibits larger increasing CP and RF, which is the largest close to the North Sea. These discrepancies between MAR-NOR-rcp85 and MAR-MIR-rcp85

are hardly explained by their present-day biases and appear to be linked to discrepancies in future changes in large-scale dynamics, as well as to non-dynamical processes. MIROC5 favours NAO+ regime, which may explain why MAR-MIR-rcp85 simulates a larger increase in temperature. Moreover, a more intense snow-albedo feedback may explain why this simulation shows the largest increase in temperature and the largest snow cover depletion. For its part, NorESM1-M favours AR regime. AR regime is known to bring unstable arctic maritime air from the north of Belgium, which may therefore explain why MAR-NOR-rcp85 simulates a larger increase in CP and RF in the coastal regions.

Regarding, the future evolution of hydroclimatic conditions favouring floods in the Ourthe catchment, both MAR future projections simulate a significant decrease in SFD and a (non-significant) increase in PFD. Compared to 1976–2005, the 2071–2100 mean SFD decreases by about -70%, while PFD is increasing by +26% in MAR-NOR-histo and by +39% in MAR-MIR-rcp85. As a result, TFD shows no significant trend. However, given that CP is predicted to increase in the future (the part of CP was very small in the present-day climate) and given that MAR is known to underestimate CP, uncertainties are large regarding the evolution of precipitation, their extremes and therefore also TFD. Despite the significant improvements implemented in the convective scheme of MARv3.8 (Section 2.1.2), substantial biases in the computation of CP remain. We therefore stress that the parameterization of convection in MAR requires further improvement.

As further perspectives, given that part of the biases found in our simulations were inherited from the forcing GCMs, it may be relevant to reiterate this study with the updated forcing data, so as to assess the sensitivity of our RCM MAR to the GCM uncertainty.

CHAPTER 5

Current evolution of global radiation and cloudiness over 1959-2010

This chapter is based on Wyard C., Doutreloup S., Belleflamme A., Wild M., and Fettweis X. (2018) Global Radiative Flux and Cloudiness Variability for the Period 1959–2010 in Belgium: A Comparison between Reanalyses and the Regional Climate Model MAR. *Atmosphere*, **9 (7)**, 262, doi: 10.3390/atmos9070262.

5.1 Context

The amount of solar radiation reaching the Earth's surface or global radiative flux (hereafter referred to as $E_{g\downarrow}$) governs a wide range of processes that support life on Earth. It generates changes in the water cycle and carbon cycle and cause droughts or heat waves (Wild, 2012). Furthermore, renewable energies, such as solar power, are a growing part of the energy sector. Thus the supply system could be more vulnerable to $E_{g\downarrow}$ changes (Jerez *et al.*, 2015). Given the impacts on our environment and our electricity production, an accurate insight into changes in the $E_{g\downarrow}$ and the causes of such changes is crucial.

Measurements provide the best estimate of $E_{g\downarrow}$ variability where they are taken. Worldwide monitoring of $E_{g\downarrow}$ from ground-based stations began in the late 1950s. These ground-based measurements suggest that the period 1950-1980 was marked by a decrease in $E_{g\downarrow}$ better known as "global dimming" (Gilgen *et al.*, 1998; Liepert, 2002; Sanchez-Lorenzo *et al.*, 2015; Stanhill and Cohen, 2008). This dimming was followed by a partial recovery ("brightening") in some regions of the world, including Europe and North America (Sanchez-Lorenzo *et al.*, 2015; Pinker *et al.*, 2005; Wild *et al.*, 2005). Variations in total cloud cover (hereafter referred to as TCC) and in the aerosol atmospheric load were identified as the most likely causes of these decadal variations. On the one hand, low to medium clouds reflect solar radiation towards space, which affects variations on monthly to decadal time scales (cloud-radiation interactions) (Chiacchio and Wild, 2010; Norris and Wild, 2007). On the other hand, aerosols such as sulphate particles can directly modify $E_{g\downarrow}$ by scattering and/or absorbing solar radiation (aerosol-radiation interactions) (Marmer *et al.*, 2007; Schulz *et al.*, 2006; Cherian *et al.*, 2014; Yang *et al.*, 2016a,b). In addition, these two factors are not completely independent since aerosols can modify cloud properties (aerosol-cloud interactions) by changing the amount of cloud condensation nuclei which also changes the albedo (Twomey, 1977) and the lifetime of clouds (Lohmann and Feichter, 2005). In addition, an early brightening over 1930-1950 is suggested by existing data (Sanchez-Lorenzo *et al.*, 2015; Wild *et al.*, 2009). However, the early brightening is not a robust signal because of data scarcity. Finally, it should be noted that ground stations have the disadvantage to be too sparse and heterogeneous to extrapolate changes over

the entire Earth (Roesch *et al.*, 2011; Bengulescu *et al.*, 2017).

Currently, a number of gridded global $E_{g\downarrow}$ products exist from remote sensing (Zhang *et al.*, 2015) and reanalyses (Compo *et al.*, 2011; Dee *et al.*, 2011; Kalnay *et al.*, 1996; Poli *et al.*, 2016; Uppala *et al.*, 2005). Satellite remote sensing is one of the most practical ways to derive $E_{g\downarrow}$ with relatively high spatial resolution and accuracy, but with limited temporal coverage because satellite measurements began in the early 1980s. Moreover, observation of polar-orbiting satellite could have considerable errors due to limited measurement frequency (two times a day) (Wang and Zhao, 2017). For the period before the satellite remote sensing era, estimates from reanalyses are a feasible way to produce long-term global $E_{g\downarrow}$ estimates. A reanalysis is a global analysis of the state of the atmosphere for an extended period of time built using a global climate model (GCM) in which observations have been assimilated into. Although the $E_{g\downarrow}$ products from these reanalyses are the best model-based approximations of $E_{g\downarrow}$, the various reanalysis $E_{g\downarrow}$ products, despite being constrained by the same sets of observations, have been proven to have systematic biases (Babst *et al.*, 2008; Allan *et al.*, 2004; Träger-Chatterjee *et al.*, 2010; Zhang *et al.*, 2016). For instance, Babst *et al.* (2008) compared the NCEP/NCAR $E_{g\downarrow}$ products to satellite data from Meteosat second generation and found biases ranging from $+40$ W m^{-2} to $+80$ W m^{-2} for Europe. Zhang *et al.* (2016) compared six global reanalyses (NCEP/NCAR-v1, NCEP-DOE, CFSR, ERA-Interim, MERRA, and JRA-55) to surface measurements from different observation networks [GEBA; BSRN; GC-NET; Buoy; and CMA] (674 sites in total) for the period 2001–2009 and found global positive mean biases ranging from $+11.25$ W m^{-2} to $+49.80$ W m^{-2}. Zhang *et al.* (2016) also found that ERA-interim show the best agreement with observations whatever the observation network. The large discrepancies found in the reanalyses $E_{g\downarrow}$ products mainly result from inaccuracies in the cloud parameterization (Babst *et al.*, 2008; Allan *et al.*, 2004; Träger-Chatterjee *et al.*, 2010; Zhang *et al.*, 2016).

Regional climate models (RCM) can partly reduce the biases found in the reanalysis-based products. Compared to GCMs and global reanalyses, RCMs run over a limited area so that computation time is reduced. Therefore, for an identical computation time, the spatial resolution of RCMs can be increased up to 2 km. For instance, it implies that the orography and other surface characteristics are finer in RCMs than in GCMs and reanalyses whose

typical resolutions turn around 40-200 km. In addition, GCMs are made to provide a good representation of the global mean climate while RCMs can be calibrated for a specific region with a more detailed physics developed for it. As coarse-resolution GCM or reanalysis fields are usually used as boundary conditions for high-resolution RCM, RCMs provide downscaled and possibly improved GCM outputs over a limited area (Flato *et al.*, 2014). International frameworks such as CORDEX (Coordinated Regional Climate Downscaling Experiments) evaluate RCM performances and aim at producing regional climate projections over various regions of the world such as Europe (EURO-CORDEX) (Giorgi and Gutowski, 2015). The MAR ("Modèle Atmosphérique Régional" in French) RCM has recently been chosen to be part of the EURO-CORDEX project, thanks to the Belgian CORDEX.be project in which the model is involved (Termonia *et al.*, 2018). CORDEX.be aims to provide a coherent scientific basis for future climate services in Belgium.

Given the importance of MAR in providing future climate projections over Belgium and potential impacts of long-term $E_{g\downarrow}$ variability on our environment and our electricity production, it is pertinent to assess the ability of MAR to simulate historical changes in $E_{g\downarrow}$. It is also pertinent to investigate the added value of MAR with respect to reanalyses.

After a brief description of MAR, the reanalysis products used to drive MAR and the observed data set are described in Section 2. Section 5.3 presents and discusses the evaluation of MAR and reanalyses by comparing their outputs to ground-based observations of $E_{g\downarrow}$ and TCC. Section 5.4 details the trend analysis performed for the dimming and brightening periods over Belgium to study the evolution of (i) annual $E_{g\downarrow}$ (Section 5.4.1) and TCC, and (ii) seasonal $E_{g\downarrow}$, TCC, low, medium and high cloud cover computed using the MAR data (Section 5.4.2). The origin of changes in cloudiness are investigated in Section 5.4.3. Conclusions and prospects are reported in Section 5.5.

5.2 Additional methodological aspects

The version 3.8 of MAR, described in Section 2.1 was used to reconstruct the evolution of $E_{g\downarrow}$ and TCC over the last fifty years in Belgium. Boundary conditions were provided by four reanalysis products: ERA40/ERA-interim, NCEP/NCAR-v1, ERA-20C and 20CRV2C. A description of these reanalyses

can be found in Section 2.2. Compared to Chapter 3, we used one additional reanalysis product, 20CRV2C, in order to compare it to ERA20C. Both 20CRV2C and ERA20C are reanalysis covering the entire 20^{th} century.

Data required for the evaluation of MAR consist of seasonal and annual mean $E_{g\downarrow}$ and TCC performed for four ground-based stations spread over the Belgian territory listed in Tables 2.8 and 2.9 and showed in Figure 2.2. A complete description of these datasets can be found in Sections 2.4.3 and 2.4.4.

5.3 Evaluation of MAR

In this section, $E_{g\downarrow}$ and TCC values computed by the different MAR simulations (MAR-ERA, MAR-NCEP1, MAR-ERA20C and MAR-20CRV2C) and the corresponding reanalyses forcing MAR (ERA40/ERA-interim, NCEP/NCAR-v1, ERA-20C and 20CRV2C) are compared to $E_{g\downarrow}$ and TCC measurements obtained from various ground stations (Tables 2.8 and 2.9). As all stations show similar results, we only display here the statistics computed from $E_{g\downarrow}$ and TCC measured at Saint-Hubert because it has the most complete time-series for both investigated parameters. The time-series for Saint-Hubert of both annual mean $E_{g\downarrow}$ and TCC are displayed in Figures 5.1 and 5.2 respectively. The statistics computed for the other stations are available in Figures C.1 to C.6 in Appendix C.

5.3.1 Global radiation

Over 1962–2010, regarding annual mean $E_{g\downarrow}$ modelled by MAR, MAR-ERA shows the best agreement with observed $E_{g\downarrow}$ at Saint-Hubert with a correlation coefficient (R) of 0.77. MAR-NCEP1 performs worst with R=0.66 (Figures 5.1(a) and 5.3(a)). The centred root mean square error (CRMSE) is smallest for MAR-ERA-20C (CRMSE = 6.2 W m^{-2}), largest for MAR-NCEP1 (CRMSE = 8.0 W m^{-2}) (Figure 5.3(c)) and smaller than the interannual variability (the standard deviation (STD) of the observations) (Figure 5.3(d)). Furthermore, the comparison suggests that MAR slightly overestimates $E_{g\downarrow}$ with mean annual biases (MB) ranging from +7.7 W m^{-2} (MAR-NCEP1) to +9.9 W m^{-2} (MAR-ERA) (Figure 5.3(b)). On a seasonal time-scale, we find the lowest values of R in summer (June-July-August, JJA)

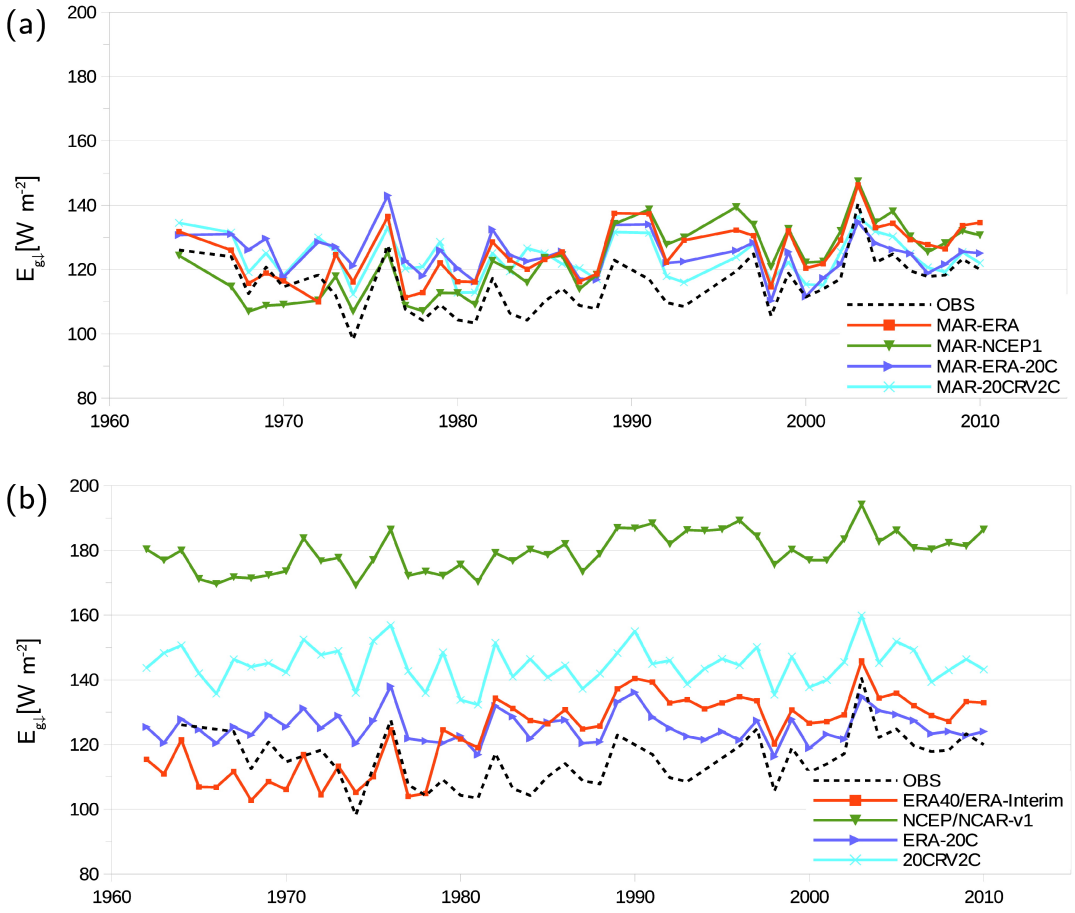

Figure 5.1: Time series of $E_{g\downarrow}$ observed at Saint-Hubert) and $E_{g\downarrow}$ modelled by **(a)** MAR and **(b)** reanalyses at the nearest grid point to Saint-Hubert.

ranging from 0.62 (MAR-20CRV2C) to 0.70 (MAR-ERA) while CRMSE was among the largest with values above 13.8 W m^{-2}. The other seasons exhibit values of R of at least 0.72 (MAR-NCEP1 in autumn (September-October-November, SON)). The lowest CRMSE was found in winter (December-January-February, DJF) with values below 3.9 W m^{-2} (MAR-NCEP1). MAR tends to overestimate $E_{g\downarrow}$ for all seasons except winter. We find the largest MB in summer with values ranging from +22.3 W m^{-2} (MAR-ERA-20C) to +29.2 W m^{-2} (MAR-20CRV2C). In winter, MB is negative and ranges from -3.9 W m^{-2} (MAR-NCEP1) to -0.1 W m^{-2} (MAR-ERA-20C).

Finally, we observe the same general behaviour for $E_{g\downarrow}$ modelled by MAR compared to $E_{g\downarrow}$ directly from the driving reanalyses. The values of R between reanalyses and measurements are as high as between MAR and the measurements. MB, for its part, is largely reduced in MAR compared

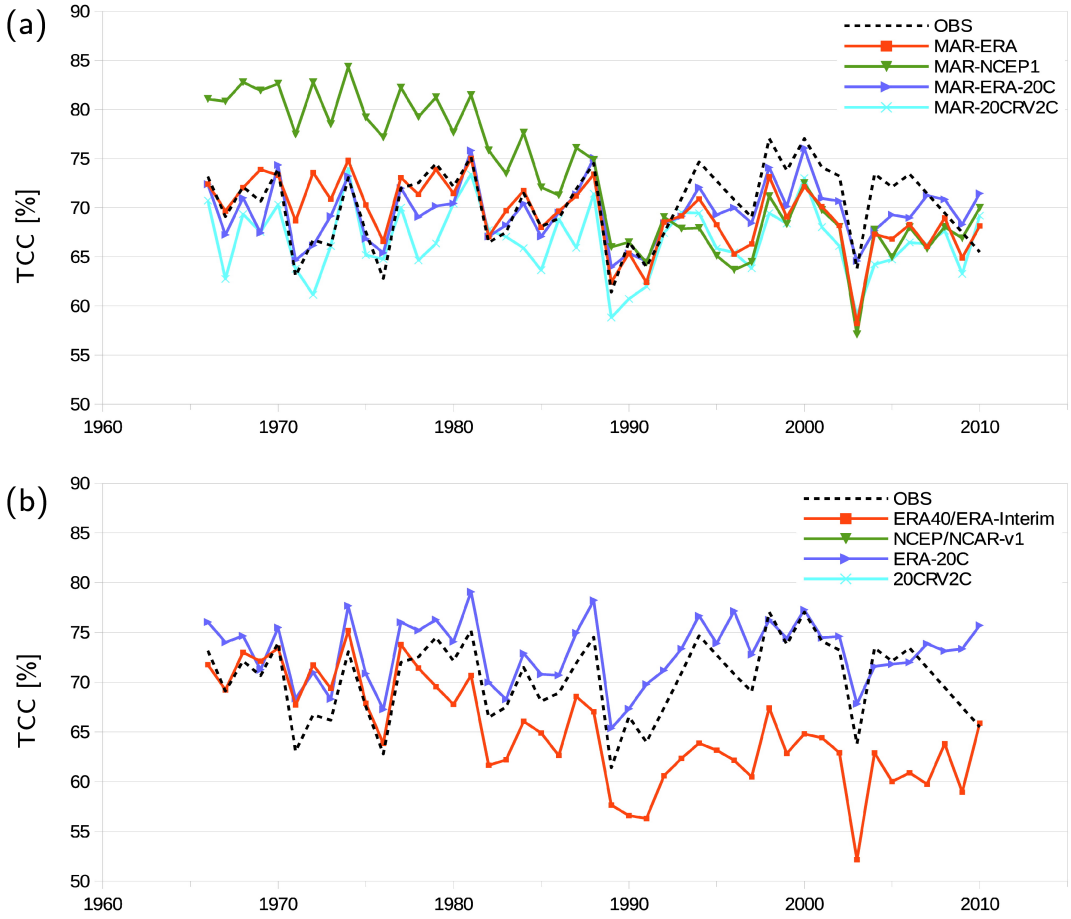

Figure 5.2: Time-series of the TCC observed at Saint-Hubert and TCC modelled by **(a)** MAR and **(b)** reanalyses at the nearest grid point to Saint-Hubert. TCC data from NCEP/NCAR-v1 and 20CRV2C were not available.

to the reanalyses (Figures 5.1(b) and 5.3(b)). For instance, MAR-NCEP1 shows an annual MB of +7.7 W m^{-2} while this value reaches +64.3 W m^{-2} in NCEP/NCAR-v1 in agreement with Zhang *et al.* (2016). We also find differences between ERA40 (1962–1978) and ERA-interim (1979–2010) which are fortunately not observed in the associated MAR simulation (MAR-ERA) (Figure 5.1). Indeed, ERA40 systematically underestimates $E_{g\downarrow}$ (annual MB = -4.96 W m^{-2}) while ERA-interim overestimates $E_{g\downarrow}$ (annual MB = +15.6 W m^{-2}) in agreement with Zhang *et al.* (2016). In addition, the forcing reanalyses and MAR have generally comparable CRMSE values. This is because the interannual variability of MAR is fully driven by the forcings. However, the forcing reanalyses exhibit much larger RMSE than MAR because of their larger biases.

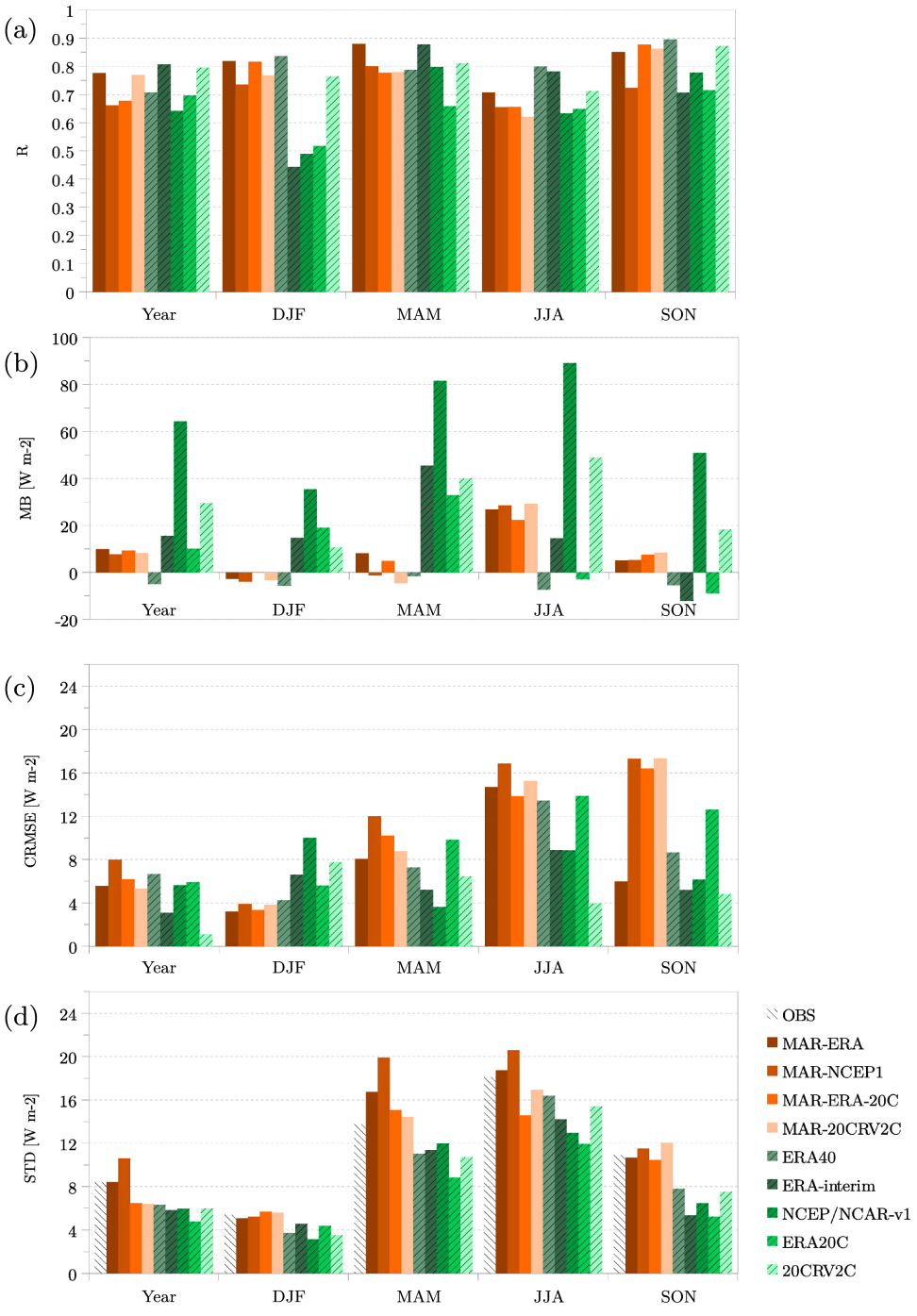

Figure 5.3: Modelled $E_{g\downarrow}$ vs observed $E_{g\downarrow}$ at Saint-Hubert for 1962-2010: **(a)** annual and seasonal correlation coefficient (R), **(b)** mean bias (MB), **(c)** centred root mean square error (CMRSE) and **(d)** standard deviation (STD). It should be noted that ERA40 covers 1962-1978 while ERA-interim covers 1979–2010.

5.3.2 Total cloud cover

Regarding annual mean TCC, models do not compare as well to observations (Figures 5.2 and 5.4). For the period 1966–2010, TCC modelled by MAR at Saint-Hubert shows R values ranging from 0.18 (MAR-NCEP1) to 0.82 (MAR-ERA-20C) (Figure 5.4(a)). We find MB values for MAR ranging from -3.6% (MAR-20CRV2C) to +3.0% (MAR-NCEP1) (Figure 5.4(b)). Values of CRMSE range from 2.2% (MAR-ERA-20C) to 7.1% (MAR-NCEP1) (Figure 5.4(c)) and are smaller than the interannual variability (Figure 5.4(d)). As for $E_{g\downarrow}$, the MAR performances also depend on the season. In summer, R is the lowest and does not exceed 0.57 in MAR-ERA. Values of MB are negative and range from -5.2% (MAR-ERA-20C) to -13.9% (MAR-20CRV2C) while the CRMSE of MAR-20CRV2C reaches 9.8% in summer. In winter, R values are among the largest reaching 0.72 in MAR-ERA. Values of MB are positive and range from +3.0% (MAR-ERA-20C) to +8.4% (MAR-NCEP1) with the largest CRMSE in winter reaching 4.8% in MAR-NCEP1. As for $E_{g\downarrow}$, this comparison highlights that MAR-NCEP1 shows the worst results. In order to explain this apparent artefact in TCC modelled by MAR-NCEP1, we have compared all three cloud types computed by MAR: low cloud cover (LCC) defined as the cloud fraction below 680 hPa), medium cloud cover (MCC) defined as the cloud fraction between 680 and 440 hPa, and high cloud cover (HCC) defined as the cloud fraction above 440 hPa (Figure 5.5, Appendix C). The results suggest that this artefact likely results from an inaccurate simulation of HCC and therefore from biases in the forcing fields of MAR in the high troposphere (Figure 5.5(c)).

The comparison with the statistics computed from TCC modelled by the reanalyses was uneasy as TCC data from NCEP/NCAR-v1 and 20CRV2C were not available. However, TCC modelled by MAR shows comparable R and MB and CRMSE but MAR shows larger CRMSE and than the corresponding reanalyses. The inhomogeneity between ERA40 and ERA-interim between 1978 and 1979 is also present in TCC. Regardless of the season (except in summer), MB is systematically positive in ERA40 while it is negative in ERA-interim at Saint-Hubert (Figures 5.2(b) and 5.4(a)).

Figure 5.4: Modelled TCC vs observed TCC at Saint-Hubert for 1966-2010: **(a)** annual and seasonal correlation coefficient (R), **(b)** mean bias (MB), **(c)** centred root mean square error (CMRSE) and **(d)** standard deviation (STD). It should be noted that ERA40 covers 1966-1978 while ERA-interim covers 1979-2010. (TCC data from NCEP/NCAR-v1 and 20CRV2C were not available).

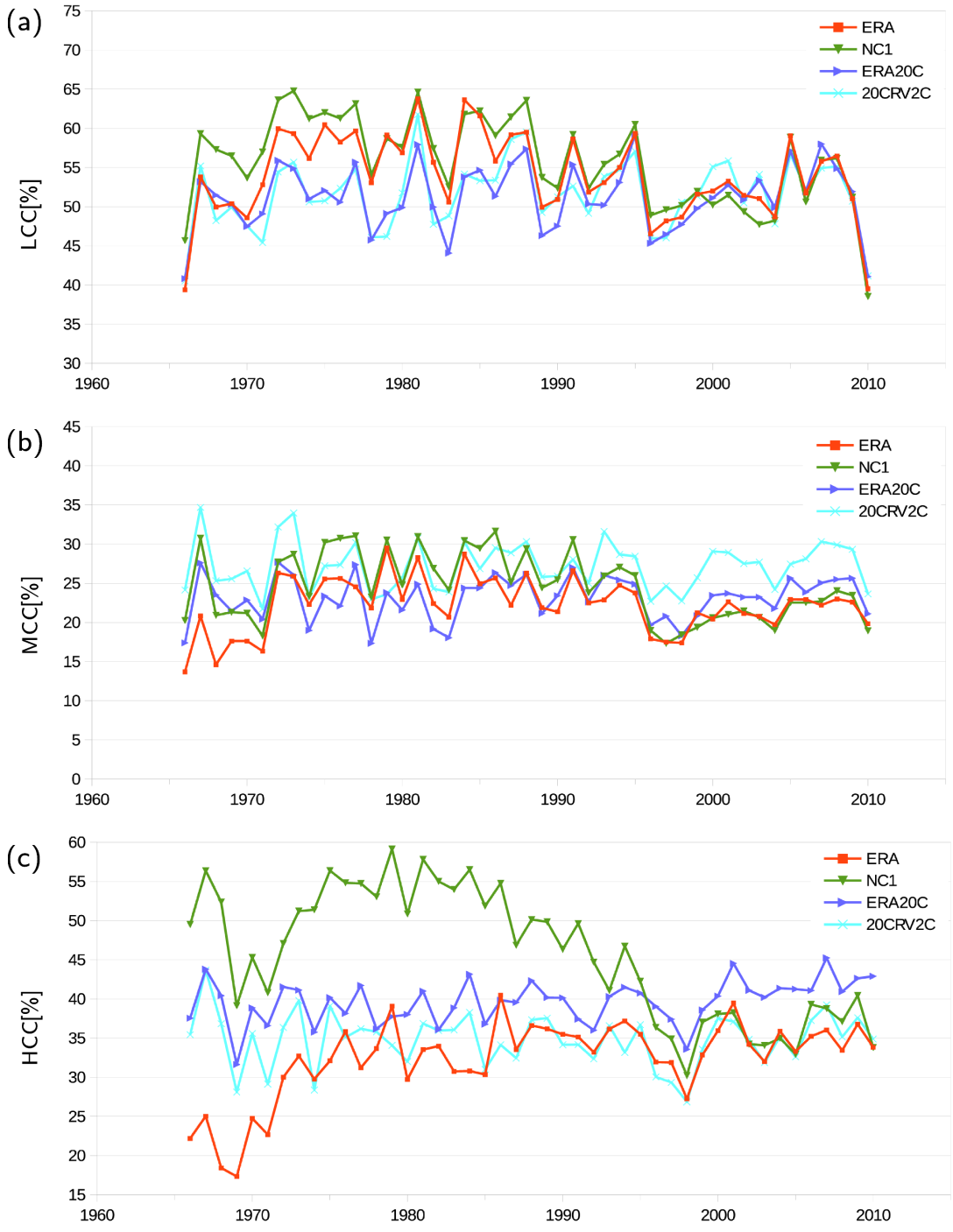

Figure 5.5: Time-series of **(a)** LCC, **(b)** MCC, and **(c)** HCC modelled by MAR at Saint-Hubert.

5.3.3 Origin of biases in MAR

Biases in $E_{g\downarrow}$ are in agreement with biases found in TCC. For instance, the underestimation of $E_{g\downarrow}$ in winter is in agreement with the overestimation of

TCC found in the models. It is the opposite in summer. Winter exhibits the smallest CRMSE and the highest R for both variables while summer exhibits the largest CRMSE and the lowest R. More generally, several studies highlight the difficulties encountered by all climate models to represent cloud physics. Markovic *et al.* (2009) show that ERA40 has a tendency to underestimate very low values of $E_{g\downarrow}$ during winter and suggest that this might be due to an underestimation of the reflectivity of optically thick clouds during winter in ERA40. Träger-Chatterjee *et al.* (2010) show that cloud physics and $E_{g\downarrow}$ have not been improved in ERA-interim compared to ERA40, despite improvements in the water cycle representation, model resolution, and in the data assimilation system. Zhang *et al.* (2016) show that reanalyses tend to overestimate $E_{g\downarrow}$ as a result of underestimation in cloud fraction. Alexandri *et al.* (2015)show that cloud fractional cover, cloud optical thickness and aerosol optical depth are the most important factors that explain the biases in $E_{g\downarrow}$ found in the RegCM4 RCM over the European domain. Finally, Wyard *et al.* (2017) show that MAR underestimates convective clouds with consequences on summer temperature (overestimation) and precipitation (underestimation). Given that MAR simulates smaller $E_{g\downarrow}$ and TCC than the reanalyses, which overestimates both $E_{g\downarrow}$, and TCC, we assume that the cloud optical depth (COD) is larger in MAR than in the reanalyses. Furthermore, part of the biases $E_{g\downarrow}$ can result from the fixed aerosol concentration used in cloud microphysics module of MAR so that the aerosol-cloud interactions are not sensitive to the historical variations of the aerosol load in the troposphere. Fan *et al.* (2018) show that inaccuracies in the aerosol-cloud interactions contribute to biases found in the GCMs of CMIP5 (Coupled Model Intercomparison Project Phase 5). Finally, the reliability of cloudiness observations is also questionable given that synoptic observations are performed by human inspection of the sky (Wild, 2009).

5.4 Changes over the dimming (1959–1979) and the brightening (1980–2010) periods

5.4.1 Trends in annual global radiation and total cloud cover

A linear trend analysis is performed for 1959–1979 and 1980–2010, corresponding to the dimming and the brightening periods reported in the literature (Wild, 2012). As in Section 5.3, we use observations and simulations for Saint-Hubert shown in Figures 5.1 and 5.2. It should be noted that TCC observations are only available from 1966 for Saint-Hubert. Therefore, trends in TCC and $E_{g\downarrow}$ measured in Saint-Hubert are computed over 1966–1979 for the dimming period. As done by Wyard *et al.* (2017), trend significance is assessed by using the Snedecor uncertainty range for the 95 % confidence interval (Snedecor and Cochran, 1967) described in Chapter 2.5.

Table 5.1: Trends and their Snedecor uncertainty range for the 95 % confidence interval computed for 1959–1979 (dimming period) and 1980–2010 (brightening period) for Saint-Hubert.

	$E_{g\downarrow}$ [W m^{-2}]				TCC [%]			
	1959–1979		**1980–2010**		**1959–1979**		**1980–2010**	
	Trend [decade^{-1}]	**Range** [decade^{-1}]	**Trend** [decade^{-1}]	**Range** [decade^{-1}]	**Trend** [decade^{-1}]	**Range** [decade^{-1}]	**Trend** [decade^{-1}]	**Range** [decade^{-1}]
OBS	(-12.9)[1]	(15.0)	**+6.2**[2]	3.0	(-0.1)	(5.3)	+2.0	2.2
MAR-ERA	**-10.4**	6.3	**+3.8**	2.7	**+7.1**	3.0	**-1.3**	1.2
	(+0.2)	(9.5)			(-0.1)	(3.1)		
MAR-NCEP1	-1.6	5.5	**+7.9**	2.8	-0.5	2.3	**-5.9**	1.4
	(-9.6)	(10.1)			(+1.9)	(4.8)		
MAR-ERA-20C	-0.2	5.0	-1.6	2.9	-0.3	2.5	+0.2	1.3
	(-1.6)	(9.5)			(+1.6)	(4.9)		
MAR-20CRV2C	-1.2	5.3	+0.2	2.7	+0.3	3.1	-0.7	1.5
	(-2.5)	(9.9)			(+2.0)	(6.1)		
ERA40/ERA-int.[3]	**-5.8**	5.3	+1.7	2.2	**+5.8**	3.2	-1.3	1.5
	(+0.1)	(8.3)			(+0.9)	(4.7)		
NCEP/NCAR-v1	-2.4	4.2	**+2.1**	1.9	n.a.	n.a.	n.a.	n.a.
	(+2.9)	(6.7)						
ERA-20C	-0.5	3.9	+0.001	2.0	+1.1	2.7	+0.5	1.3
	(-0.3)	(6.9)			(+0.1)	(4.7)		
20CRV2C	-0.8	4.5	+1.7	2.3	n.a.	n.a.	n.a.	n.a.
	(+2.7)	(8.6)						

[1] The values between brackets indicate that they are computed for 1966–1979.
[2] The values in bold indicate that the trends are statistically significant at the 95 % confidence level, namely that they are larger than the associated uncertainty range.
[3] As ERA40/ERA-Interim is biased by the transition from ERA40 to ERA-Interim between 1978 and 1979, we removed the MB of each part of the time-series (1959–1978 and 1979–2010) to homogenise the time-series before computing the trend.

During the dimming period, we find a non-significant negative trend in $E_{g\downarrow}$ measurements for Saint-Hubert for the period 1966–1979 valued at -12.9 W m^{-2} $decade^{-1}$ (Table 5.1). During the brightening period, we find a significant positive trend at Saint-Hubert for the period 1980–2010 valued at +6.2 W m^{-2} $decade^{-1}$. TCC observed in Saint-Hubert shows no significant trend although synoptic cloud observations are subject to large uncertainties (Wild, 2009). This nonetheless suggests that cloudiness changes are not the only factor affecting solar radiation variability. Indeed, RMIB (2015) highlighted a significant decrease in $E_{g\downarrow}$ at Uccle for the period 1951–1984 valued at -6.3 %. They attribute this trend to a sustained increase in anthropogenic aerosols. De Bock *et al.* (2014) and RMIB (2015) report a significant increase in $E_{g\downarrow}$ at Uccle valued at +5 ± 2 W m^{-2} $decade^{-1}$ for 1985–2014. They also associate to a non-significant decrease in aerosol optical depth at Uccle for 1985-2014 that is valued at -8 ± 5 % $decade^{-1}$ which presents a stabilization after 2002. This decline in aerosol optical depth results from the enormous efforts to curb emissions and air pollution since the 1980s (Sliggers and Kakebeeke, 2004). The most important effort is probably the 1979 Convention on Long-range Transboundary Air Pollution which has later been extended by eight protocols that identify specific measures to be taken by Parties to cut their emissions of air pollutants (Sliggers and Kakebeeke, 2004).

Regarding $E_{g\downarrow}$ modelled by MAR, there are no significant trends for 1966–1979. However, trends are negative during 1959–1979 but only MAR-ERA shows a significant trend valued at -10.4 W m^{-2} $decade^{-1}$ for this period (Table 5.1). This decreasing $E_{g\downarrow}$ coincides with an increasing trend in the simulated TCC which is significant in MAR-ERA and valued at +7.1 % $decade^{-1}$. On the contrary, for 1980–2010, the trends in $E_{g\downarrow}$ are positive, except in MAR-ERA-20C, and significant in MAR-ERA (+3.8 W m^{-2} $decade^{-1}$) and MAR-NCEP1 (+7.9 W m^{-2} $decade^{-1}$) as in observations. This increasing $E_{g\downarrow}$ coincides with a decreasing trend in simulated TCC except in MAR-ERA-20C. These trends are significant in MAR-ERA and MAR-NCEP1 and valued at -1.3 % $decade^{-1}$ and -5.9 % $decade^{-1}$ respectively. The strong negative trend in MAR-NCEP1 seems to partly result from biases in the forcing fields of MAR in the high troposphere before the 1990s as highlighted in Section 5.3.2. It should be noted that MAR-ERA-20C and MAR-20CRV2C systematically show non-significant and weaker

trends than MAR-ERA, MAR-NCEP1, and observations. This suggests that these reanalysis products covering the whole 20th century (ERA-20C and 20CRV2C) are less reliable, possibly because they assimilate surface observations only.

We also computed the trends from $E_{g\downarrow}$ and TCC modelled by the reanalyses. As ERA40/ERA-Interim is biased by the transition from ERA40 to ERA-Interim between 1978 and 1979, we removed the MB of each part of the time-series (1959–1978 and 1979–2010) to homogenise the time-series before computing the trend. The signal of the trends in $E_{g\downarrow}$ modelled by the reanalyses is of the same order as the one modelled by MAR forced by the corresponding reanalyses (Table 5.1). This suggests that the trends found in the MAR outputs are partially driven by the forcing reanalyses. However, MAR amplifies the trends in $E_{g\downarrow}$ compared to the observations and the forcing reanalyses. As highlighted in Section 5.3.3, the cloud optical depth is likely larger in MAR than in the reanalyses. Therefore, changes in TCC impact $E_{g\downarrow}$ in MAR more than in the reanalyses.

5.4.2 Trends in seasonal global radiation and total cloud cover

A linear trend analysis is performed for 1959–1979 and 1980–2010 for each pixel of the MAR domain in order to highlight spatial and seasonal variabilities. Trend significance is again assessed by using the Snedecor uncertainty range for the 95 % confidence interval. Only the trends from the MAR-ERA outputs are computed as they fit the best to observations in agreement with Zhang *et al.* (2016) (Sections 5.3 and 5.4.1).

Over 1959–1979 (dimming period), MAR-ERA outputs show an overall significant decrease in $E_{g\downarrow}$ for all seasons (Figure 5.6(a)-(d)). The decrease in $E_{g\downarrow}$ is especially marked in spring (March-April-May, MAM) and summer and reaches values between -16 and -18 W m^{-2} decade^{-1} in some regions of the country (Figure 5.6(b)-(c)). Chiacchio and Wild (2010) and Sanchez-Lorenzo *et al.* (2015) found similar results over a larger European domain. MAR-ERA show a significant increase in TCC in all seasons Figure 5.6(e)-(h)). This increase in TCC is the most marked in spring, summer, and autumn and can reach values between +8 and +10 % decade^{-1} in some parts of the country (Figure 5.6(f)-(h)).

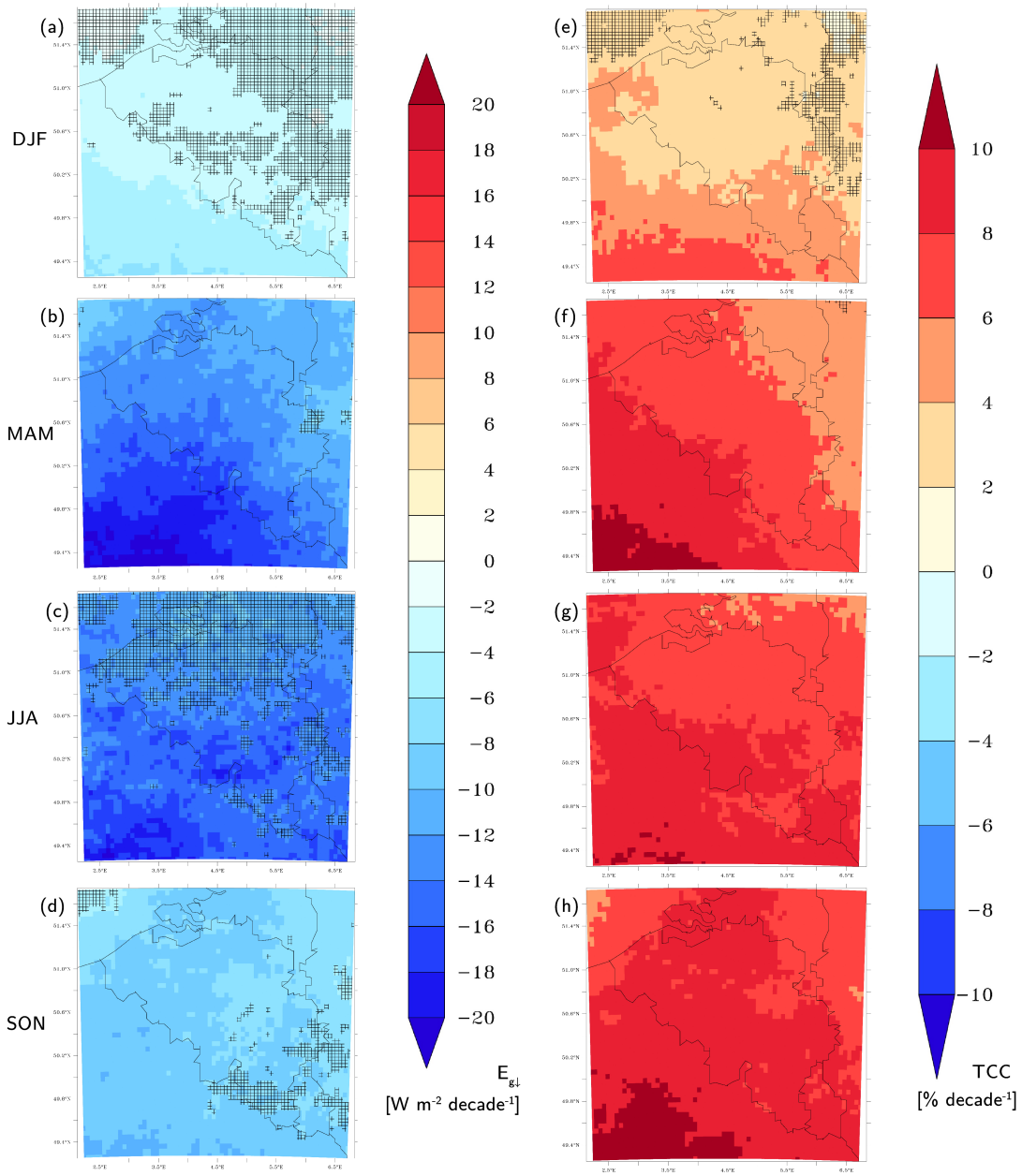

Figure 5.6: Seasonal trends in **(a)-(d)** $E_{g\downarrow}$ and **(e)-(h)** TCC computed from the MAR-ERA outputs for 1959–1979 (dimming period). Filled pixels indicate the places where the trends are statistically significant at the 95% confidence level. Hashed pixels indicate the places where the trends are statistically non-significant.

The patterns of the trends in TCC and in $E_{g\downarrow}$ are broadly similar which confirms that changes in cloud cover drive trends in surface solar radiation. To refine our analysis, we also compute trends for all three MAR cloud types (LCC, MCC and TCC) defined in Section 5.3.2. These trends show that the increase in TCC for 1959–1979 is mainly caused by a significant

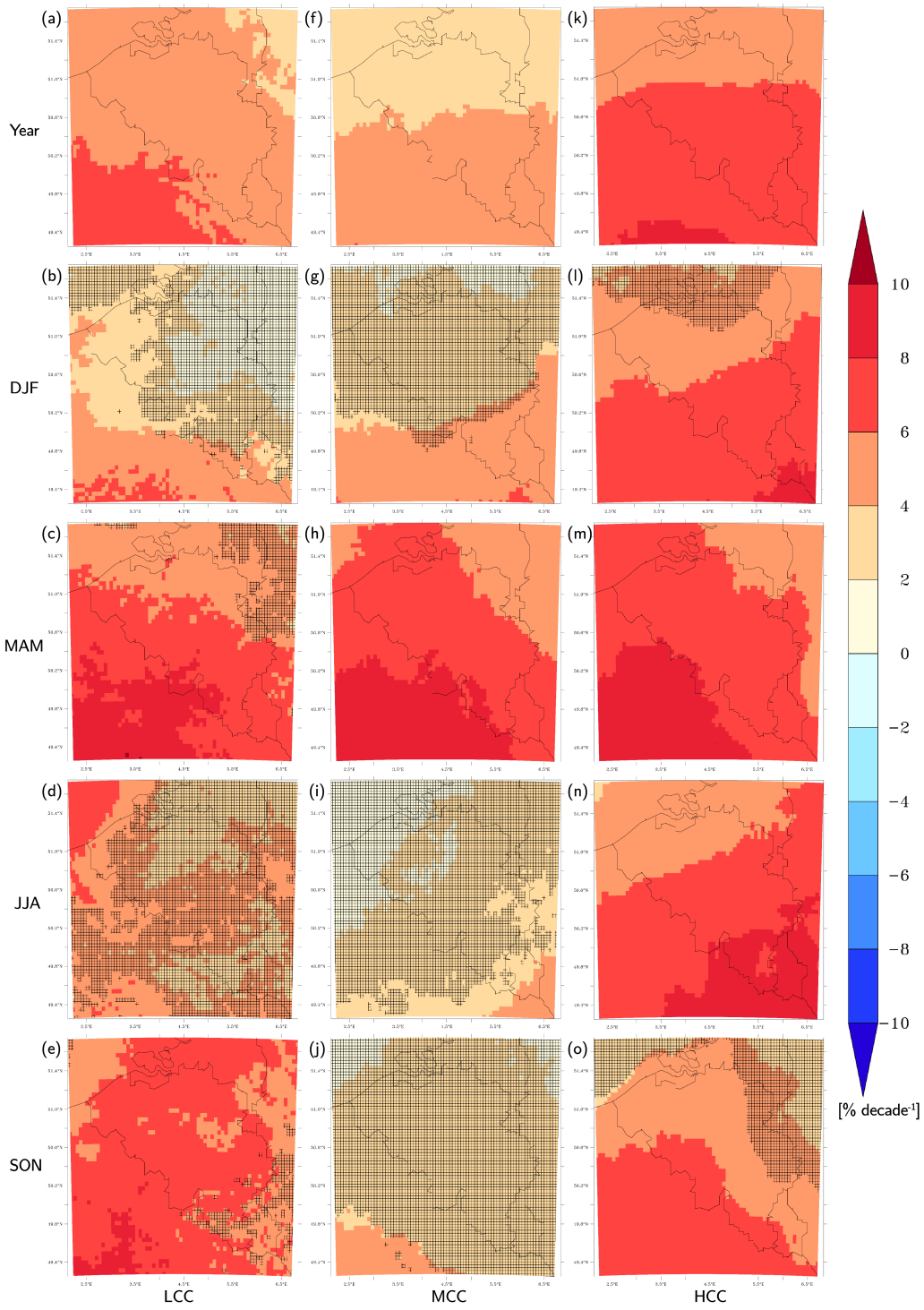

Figure 5.7: Annual and seasonal trends in **(a)-(e)** LCC, **(f)-(j)** MCC, and **(k)-(o)** HCC computed from the MAR-ERA outputs for 1959–1979 (dimming period). Filled pixels indicate the places where the trends are statistically significant at the 95% confidence level. Hashed pixels indicate the places where the trends are statistically non-significant.

increase in LCC (Figure 5.7(a)-(e)) and HCC (Figure 5.7(k)-(o)). It should be noted that HCC is known to affect longwave radiation mainly while we are studying shortwave radiation changes (Forster *et al.*, 2013). MCC shows a significant increase in spring over 1959–1979 with values ranging from +2 and +10 % decade^{-1} (Figure 5.7(h)).

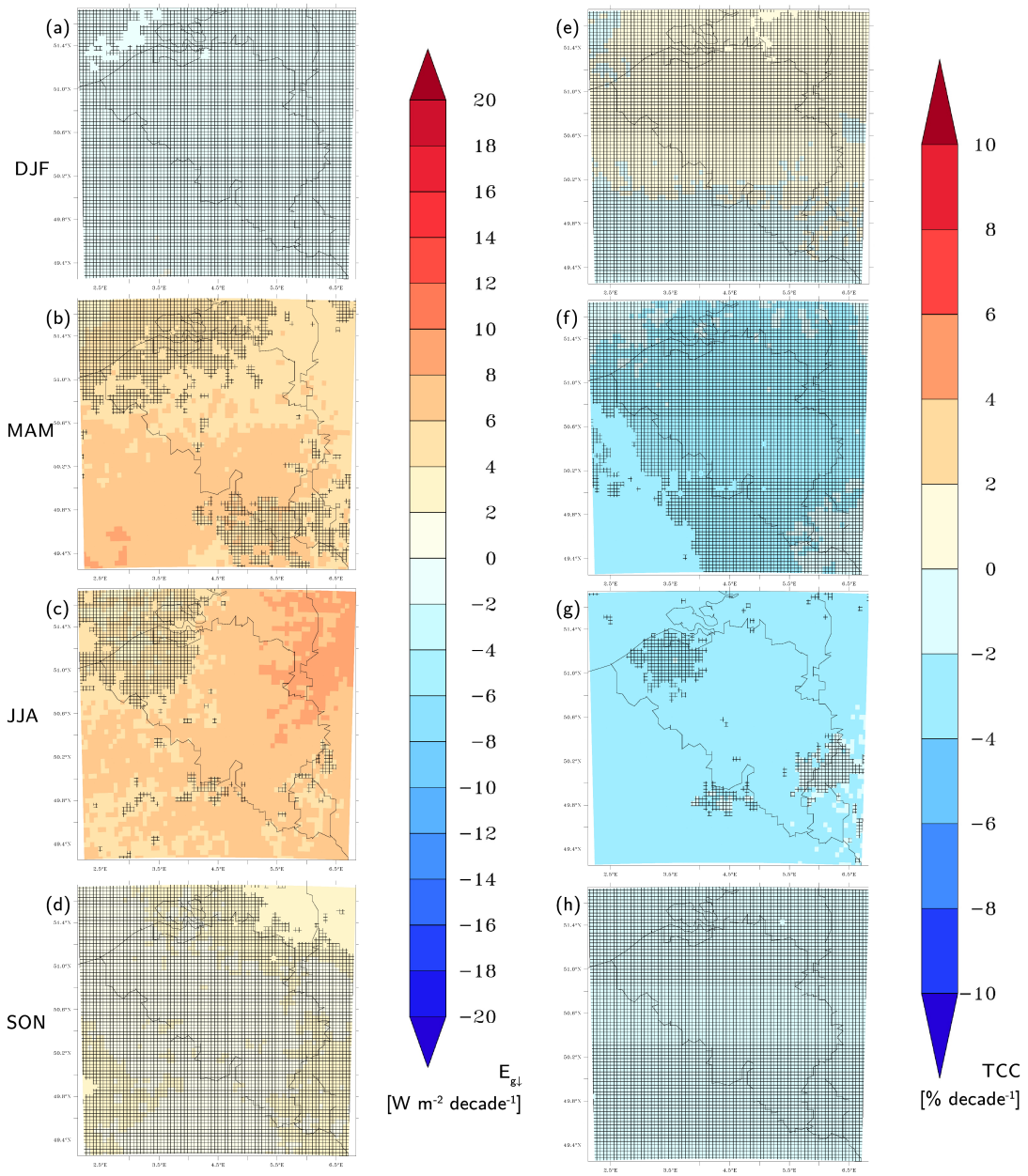

Figure 5.8: Seasonal trends in **(a)-(d)** $E_{g\downarrow}$ and **(e)-(h)** TCC computed from the MAR-ERA outputs for 1980–2010 (brightening period). Filled pixels indicate the places where the trends are statistically significant at the 95% confidence level. Hashed pixels indicate the places where the trends are statistically non-significant.

Over 1980–2010 (brightening period), measurements at Saint-Hubert show positive significant trends in spring and summer valued at +10.7 W m^{-2} $decade^{-1}$ and +12.0 m^{-2} $decade^{-1}$ respectively (Table C.2, Appendix C). Seasonal trends computed from MAR-ERA outputs also show a significant increase in $E_{g\downarrow}$ in spring and summer with values between +4 and +10 W m^{-2} $decade^{-1}$ (Figure 5.8(b)-(c)). Regarding TCC, observations show non-significant trends for all seasons (Table C.2) while values modelled by MAR-ERA show a significant decrease in TCC, especially in summer (Figure 5.8(g)) reaching -2 to -4 % $decade^{-1}$ over the entire country.

Seasonal trends in cloud types computed in MAR-ERA show a significant decrease in LCC for 1980–2010, especially in spring with values ranging between -2 and -6 % $decade^{-1}$ depending on the location (Figure 5.9(c)). Our results are in agreement with Eastman and Warren (2013), who also find a decrease in observed cloudiness in Western Europe for 1971–2009. Previous studies also stated that the brightening results from the combination of both decreasing aerosol emissions and decreasing LCC and MCC (De Bock *et al.*, 2014). However, after the 1990s, the decrease in cloudiness might have become the dominant factor according to the results of Mateos *et al.* (2014), drawing similar conclusions over Spain, and to the results of Sanchez-Lorenzo *et al.* (2017) and Pfeifroth *et al.* (2018) over Europe.

5.4.3 Origin of changes in cloudiness

The analysis of the linear trends (Sections 5.4.1 and 5.4.2) has highlighted that $E_{g\downarrow}$ changes are driven by changes in low and medium cloud cover. In this section, we investigated the origin of such changes. As output from MAR is dependent on the reanalysis product used to force the model (Section5.4.1), we analysed the forcing variables from all four reanalyses at two pressure levels (700 and 500 hPa) which are the characteristic levels of low and medium cloud cover. We especially paid attention to the air temperature (TA), specific (HUS) and relative (HUR) humidity. We used the data from the pixel containing Saint-Hubert shown in Figure 5.10, and computed the linear trends and their significance for the periods 1959–1979 and 1980–2010 (Table 5.2).

For the period 1959–1979 (dimming period), both ERA40/ERA-Interim and NCEP/NCAR-v1 show a significant increase in HUR at 500 hPa valued at +

Table 5.2: Annual trends and their Snedecor uncertainty range for the 95 % confidence interval computed for 1959–1979 and 1980–2010.

	1959–1979		**1980–2010**	
ERA40/ERA-interim	**Trend** [decade^{-1}]	**Range** [decade^{-1}]	**Trend** [decade^{-1}]	**Range** [decade^{-1}]
TA700 [°C]	-0.2	0.4	+0.1	0.2
TA500 [°C]	-0.3	0.3	+0.2	0.2
HUS700 [g kg^{-1}]	+0.1	0.1	-0.02	0.03
HUS500 [g kg^{-1}]	**+0.05**[1]	0.04	-0.005	0.001
HUR700 [%]	**+4.1**	2.7	**-1.3**	1.1
HUR500 [%]	**+5.4**	2.9	**-1.1**	0.9
NCEP/NCAR-v1	**Trend** [decade^{-1}]	**Range** [decade^{-1}]	**Trend** [decade^{-1}]	**Range** [decade^{-1}]
TA700 [°C]	-0.1	0.4	+0.2	0.2
TA500 [°C]	-0.2	0.3	+0.2	0.2
HUS700 [g kg^{-1}]	+0.05	0.1	-0.03	0.04
HUS500 [g kg^{-1}]	+0.01	0.02	-0.004	0.01
HUR700 [%]	+1.6	2.1	**-1.5**	1.0
HUR500 [%]	**+2.8**	2.1	**-1.5**	0.9
ERA-20C	**Trend** [decade^{-1}]	**Range** [decade^{-1}]	**Trend** [decade^{-1}]	**Range** [decade^{-1}]
TA700 [°C]	-0.2	0.4	**+0.3**	0.2
TA500 [°C]	-0.1	0.3	**+0.3**	0.2
HUS700 [g kg^{-1}]	-0.02	0.1	+0.05	0.03
HUS500 [g kg^{-1}]	-0.02	0.1	+0.02	0.01
HUR700 [%]	+0.8	1.8	-0.1	0.9
HUR500 [%]	+0.1	1.8	-0.1	0.8
20CRV2C	**Trend** [decade^{-1}]	**Range** [decade^{-1}]	**Trend** [decade^{-1}]	**Range** [decade^{-1}]
TA700 [°C]	-0.2	0.4	**+0.2**	0.2
TA500 [°C]	-0.2	0.3	**+0.3**	0.2
HUS700 [g kg^{-1}]	-0.01	0.1	+0.03	0.04
HUS500 [g kg^{-1}]	-0.02	0.03	+0.015	0.02
HUR700 [%]	+1.2	2.0	-0.4	0.9
HUR500 [%]	+0.04	1.7	-0.3	0.9

[1] The values in bold indicate that the trends are statistically significant at the 95 % confidence level, namely that they are larger than the associated uncertainty range.

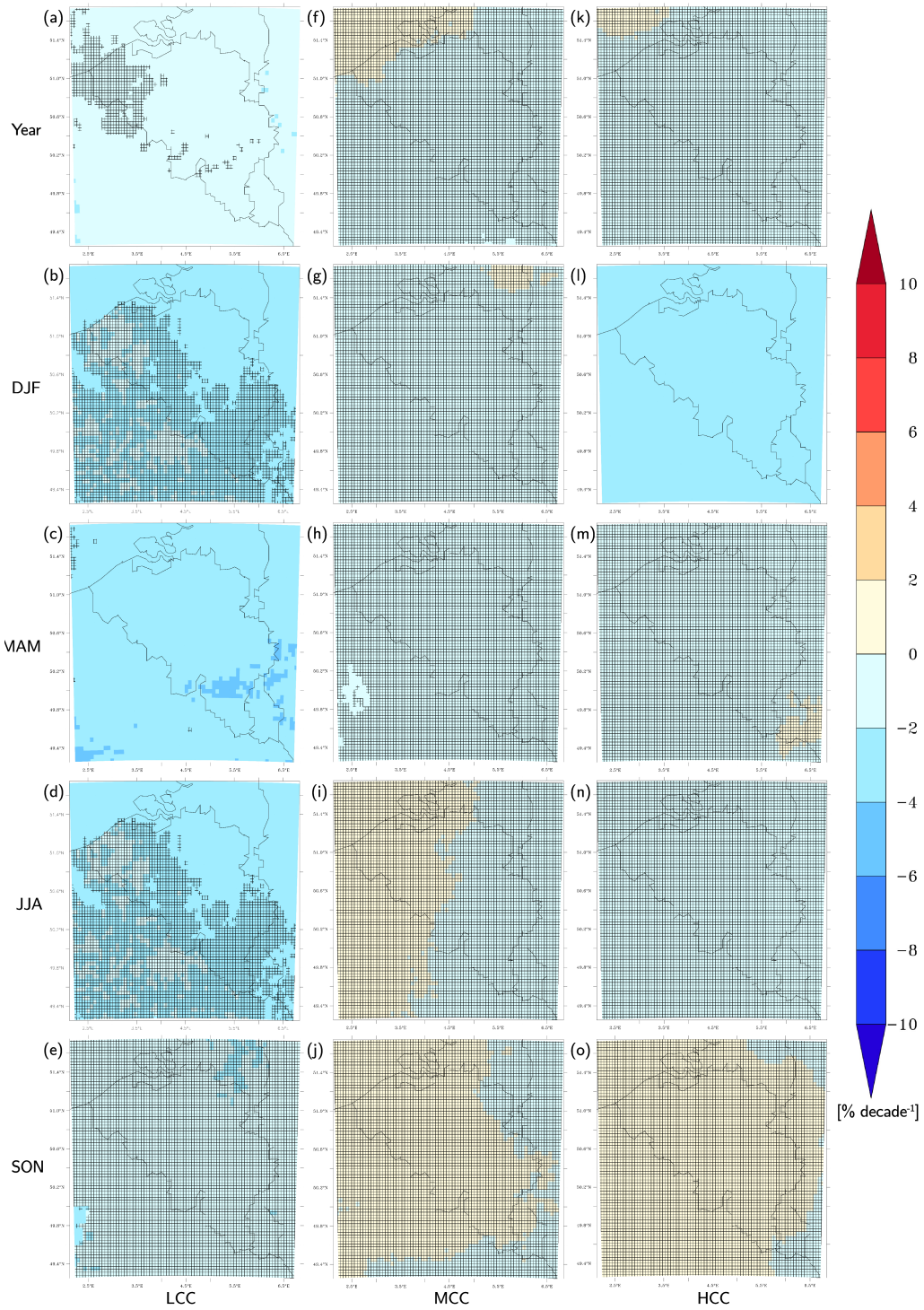

Figure 5.9: Annual and seasonal trends in **(a)-(e)** LCC, **(f)-(j)** MCC, and **(k)-(o)** HCC computed from the MAR-ERA outputs for 1980–2010 (brightening period). Filled pixels indicate the places where the trends are statistically significant at the 95% confidence level. Hashed pixels indicate the places where the trends are statistically non-significant.

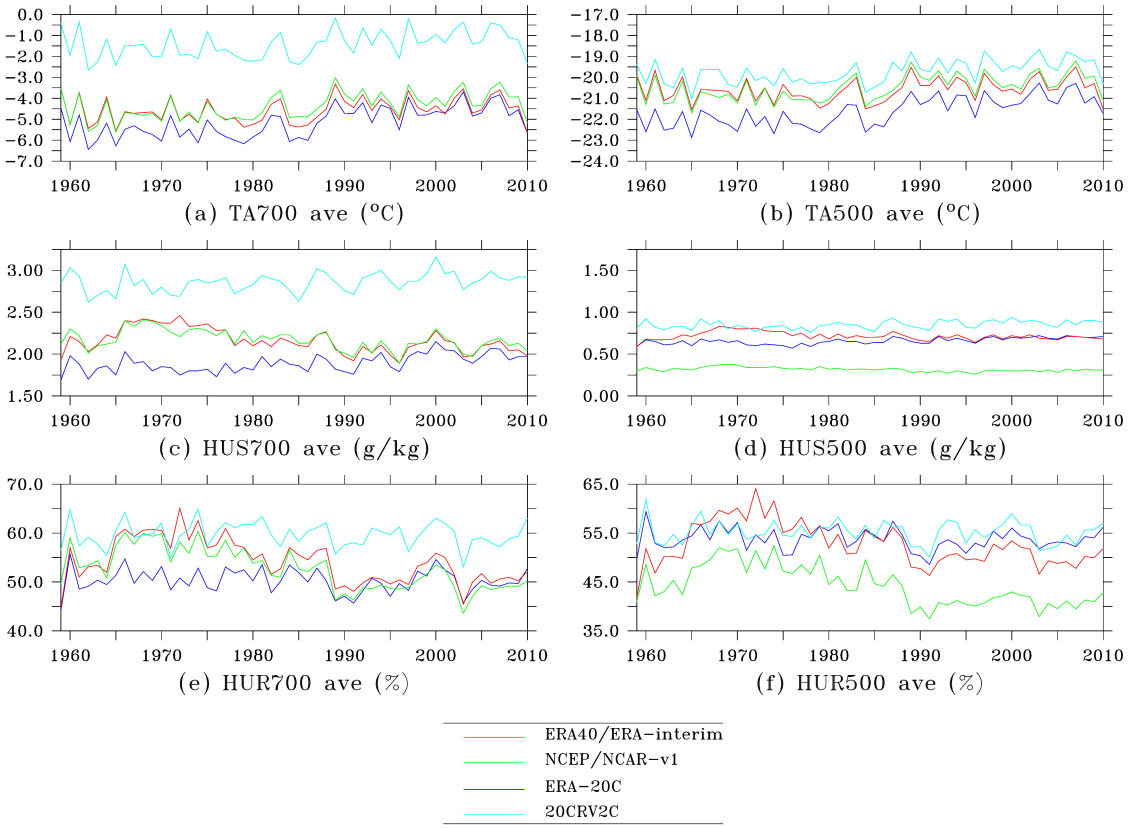

Figure 5.10: Reanalysis data used as MAR forcings at Saint-Hubert at two different pressure levels (700hPa and 500 hPa): **(a)-(b)** temperature (TA), **(c)-(d)** specific humidity (HUS), **(e)-(f)** relative humidity (HUR).

5.4 % decade^{-1} and +2.8 % decade^{-1} respectively (Table 5.2). ERA40/ERA-Interim also shows a significant increase in HUR at 700 hPa valued at +4.1 % decade^{-1}. This coincides with a positive but non-significant trend in TA at both pressure levels but also with a negative but non-significant increase in HUS. Only ERA40/ERA-interim show a significant trend in HUS at 500 hPa valued at + 0.05 g kg^{-1} decade^{-1}. Both ERA20C and 20CRV2C simulate changes in HUR and TA similar to ERA40/ERA-interim and NCEP/NCAR-v1 but these changes are weaker. In addition, ERA20C and 20CRV2C exhibit positive (but non-significant) trends in HUS at 700 and 500 hPa while these trends are negative in ERA40/ERA-interim and NCEP/NCAR-v1 for 1959–1979. Given these trends, increasing LCC and MCC during the dimming period could result from decreasing TA and increasing HUS generating an increase in HUR which could have therefore enhanced cloud development. The initial changes in TA and HUS could be explained by changes in the atmospheric circulation. In addition, we know

that the dimming period was characterized by a high polluted atmosphere (Sliggers and Kakebeeke, 2004). As aerosols suspended in the troposphere could served as condensation nuclei (aerosol-cloud interactions), they could be responsible for the increase in LCC and MCC during the dimming period by enhancing cloud development. Then, the increase in cloud cover could generate less $E_{g\downarrow}$ and therefore decreasing TA, which could generate an increase/decrease in HUR.

For the period 1980–2010 (brightening period), both ERA40/ERA-Interim and NCEP/NCAR-v1 show a significant decrease in HUR at both pressure levels ranging from -1.3 % decade^{-1} (ERA40/ERA-interim) to -1.5 % decade^{-1} (NCEP/NCAR-v1) at 700 hPa, and from -1.1 % decade^{-1} (ERA40/ERA-interim) to -1.5 % decade^{-1} (NCEP/NCAR-v1) at 500hPa. This coincides with a positive but non-significant trend in TA at both pressure levels but also with a negative but non-significant trend in HUS. ERA20C and 20CRV2C both exhibit weak non-significant decreasing trends in HUR. These trends coincide with a significant increase in TA at both pressure levels ranging from +0.2 (20CRV2C) to +0.3 °C decade^{-1} (ERA20C) at 700 hPa, and reaching +0.3 °C decade^{-1} (ERA20C and (20CRV2C) at 500 hPa. However, ERA20C and 20CRV2C also show an increase in HUS while ERA40/ERA-Interim and NCEP/NCAR-v1 show a decrease. This increase in HUS is significant in ERA20C at both pressure levels and is valued at +0.054 g kg^{-1} decade^{-1} at 700hPa and +0.022 g kg^{-1} decade^{-1} at 500hPa. In addition, compared to ERA40/ERA-Interim and NCEP/NCAR-v1, ERA20C is dryer and colder at both investigated pressure levels whereas 20CRV2C is warmer and wetter (Figure 5.10). These trends suggest that, decreasing LCC and MCC during the brightening period could result from increasing TA and decreasing HUS generating a decrease in HUR which could have therefore inhibited cloud development. The initial changes in TA and HUS could be explained by changes in the atmospheric circulation. Eastman and Warren (2013) attribute the declining cloud cover observed over Western Europe to a poleward shift of the polar jet stream since the 1970s. Bender *et al.* (2012) highlight a poleward shift of extratropical storm tracks (which induces a poleward shift of the polar jet stream) for 1983–2008 as a consequence of global warming. This poleward shift of extratropical storm tracks is accompanied by a reduction in total cloud cover leading to a positive cloud feedback (Bender *et al.*, 2012). The conclusions of these

studies are not in opposition with our hypothesis since increasing TA during the brightening period (1980–2010) could result from more frequent tropical air advections over Western Europe. In addition, we know that the brightening period was characterized by a strong decrease in the aerosol loading in the troposphere (De Bock *et al.*, 2014; Sliggers and Kakebeeke, 2004). This decline in aerosol loading could be responsible for the decrease in LCC and MCC during the brightening period by inhibiting cloud development. Then, the decrease in cloud cover could have generated more $E_{g\downarrow}$ and therefore increasing TA, which could generate an decrease in HUR.

In summary, there are two hypothesis to explain the changes in cloud cover during the dimming and the brightening periods: the "atmospheric circulation hypothesis" and the "aerosol cloud interactions hypothesis". On the one hand, atmospheric circulations changes could have modified TA and HUS and therefore HUR with consequences on cloud development and later $E_{g\downarrow}$ (atmospheric circulation hypothesis). On the other hand, aerosol-cloud interactions could have modified cloud development and therefore $E_{g\downarrow}$ with consequences on TA, and HUR. We cannot settle on a single hypothesis to explain LCC and MCC changes (especially since statistics are rarely significant) but they are most probably due to the combination of several factors. There are indeed proofs for both hypothesis, especially during the brightening period (De Bock *et al.*, 2014; Eastman and Warren, 2013; Bender *et al.*, 2012).

It should be noted that the similar trend values found in ERA40/ERA-interim and NCEP/NCAR-v1 at 700 and 500 hPa confirm that the apparent artefact found in TCC computed by MAR-NCEP1 results (Section 5.3.2) from biases in the forcing fields of MAR in the high troposphere (above 440 hPa).

5.5 Chapter conclusion

The main objective of this chapter was to assess the ability of the MAR RCM to reproduce observed changes in $E_{g\downarrow}$ in Belgium with respect to reanalyses and observations. To this end, MAR was forced by different reanalyses: ERA-Interim (1979-2010) completed by ERA40 (1958–1978), NCEP/NCAR-v1 (1958–2010), ERA20C (1958-2010) and 20CRV2C (1958–2010). This study focusses on the 1959–2010 period, which is the longest

common period covered by all reanalyses used as MAR forcing. In addition, we consider two distinct periods in our analysis: 1959–1979 (dimming) and 1980–2010 (brightening). Measurements of $E_{g\downarrow}$ from RMIB as well as cloud cover observations from Belgocontrol and RMIB were used for the evaluation of MAR and the forcing reanalyses.

The comparison of $E_{g\downarrow}$ and TCC modelled by MAR and reanalyses with measurements performed at several ground stations shows that MAR allows us to largely reduce the mean biases present in the reanalyses. However, MAR does not significantly improve R and CRMSE as the interrannual variability of RCMs is prescribed by their forcings. The comparison also shows that the biases are the largest in summer for both $E_{g\downarrow}$ and TCC and that MAR generally overestimates $E_{g\downarrow}$ while it underestimates TCC. This suggests that biases in $E_{g\downarrow}$ results in large part from inaccuracies in TCC. Improvements in cloud physics are still required despite the modification performed in the new version of MAR (MARv3.8). The comparison with forcing reanalyses finally suggests that the cloud optical depth is larger in MAR than in the reanalyses as the reanalyses show larger biases in $E_{g\downarrow}$ while MAR and reanalyses exhibit similar biases in TCC .

The analysis of the linear trends in annual and seasonal $E_{g\downarrow}$ and low, medium, and high clouds brings to light that only MAR-ERA successfully simulates consistent trends in $E_{g\downarrow}$ probably because ERA40/ERA-interim has a better spatial resolution and assimilates more observations than the other reanalyses used in this study. Neither MAR-ERA-20C nor MAR-20CRV2C show any of these trends, probably because both ERA-20C and 20CRV2C reanalyses assimilate surface observations only. MAR-NCEP1, for its part, overestimates the trend computed for the brightening period because of biases in the forcing fields in the high troposphere especially before the 1990s. Our results show that annual $E_{g\downarrow}$ trends are mainly driven by $E_{g\downarrow}$ changes in spring and summer. They also suggest that, in Belgium, the aerosol-radiation interactions cannot be neglected, especially for the dimming period because trends in observed TCC are non-significant while trends in observed $E_{g\downarrow}$ are significant. The increase in $E_{g\downarrow}$ observed in Belgium since the 1980s and especially since the 2000s could mainly be explained by a decrease in low and medium cloud cover strengthening the effect of the decrease in aerosol loading on $E_{g\downarrow}$ that has been observed in Europe since the 1980s. The origin of these changes in cloudiness is not

clear and could results from changes in both atmospheric-circulation and aerosol-cloud interactions. Further analyses are therefore required. First of all, as this trend is not simulated when MAR is forced by 20CRV2C and ERA-20C, comparing the MAR forcing fields (temperature, humidity, and wind) from these 20th century reanalyses with ERA-interim will help to detect the meteorological variables which are responsible for this decrease in cloudiness. Sensitivity experiments with MAR could be performed using variables from two different reanalyses, e.g. wind from ERA-interim and other fields from ERA-20C. Afterwards, a circulation type classification (as the one developed by Belleflamme *et al.* (2014)) could be used to associate the daily cloudiness to some types of general circulation. The temporal evolution of these circulation types could then be studied as it was done in Bednorz *et al.* (2016) and Łupikasza and Lipiński (2017). Finally, it might also be interesting to verify if such a decrease in cloudiness would be projected if MAR was forced by GCM-based future projections. This would suggest that such a change could be a consequence of global warming.

CHAPTER 6

Future evolution of global radiation and cloudiness by 2100

This chapter is based on Wyard C., Doutreloup S., Fettweis X. (2018) Future projections of global radiation and cloudiness in Belgium. To be submitted to *Bulletin de la Société Géographique de Liège*.

6.1 Context

Over the last century, the amount of solar radiation reaching the Earth's surface ($E_{g\downarrow}$), also referred to as solar surface radiation or global radiation, has undergone substantial variations such as a worldwide dimming between the 1950s and the 1980s followed by a partial brightening since the 1980s in Europe and Northern America. There is increasing evidence that these fluctuations in $E_{g\downarrow}$ have impacted various aspects of the climate system such as temperature, hydrological cycle, the cryosphere or the carbon cycle. For instance, these fluctuations have been responsible for the absence of a significant temperature rise between the 1950s and the 1980s, masking the greenhouse gas effect on temperature rise (Wild *et al.*, 2007). There is also evidence of a deceleration of the hydrological cycle during the dimming and a more recent recovery over land surfaces impacting the rate of terrestrial evaporation and precipitation (Wild and Liepert, 2010). The variations in $E_{g\downarrow}$ were mainly attributed to changes in the aerosol atmospheric load and also to variations in the cloud cover caused by these aerosols. However, it should be noted that the recent decrease in cloud cover has been attributed to circulation changes such as the polar shift of extratropical storm tracks bringing more frequent anticyclonic conditions (Section 5.4.3). Such circulations changes were suspected to be due to global warming (Bender *et al.*, 2012; Eastman and Warren, 2013).

In a warming climate, changes in the amount of $E_{g\downarrow}$ will therefore depend not only on our aerosol emissions but also on the response of cloud properties and large scale circulation to global warming. In addition, these changes have the potential to affect the climate system and also our energy supply. Despite these implications and the large climate modelling community, very few studies have investigated the future long-term trends in $E_{g\downarrow}$. Only a limited number of papers describe the scenarios of $E_{g\downarrow}$ changes based on GCM simulations from CMIP5 (Crook *et al.*, 2011; Gaetani *et al.*, 2014; Wild *et al.*, 2015), RCM simulations of EURO-CORDEX (Pašičko *et al.*, 2012; Panagea *et al.*, 2014; Jerez *et al.*, 2015) or both (Bartók *et al.*, 2017) mainly in terms of future solar energy production. Belgium is no exception since no study has especially focused on the future evolution of $E_{g\downarrow}$ despite the growing production of solar energy expected in the country (Section 1.2.2). Therefore, this study aims at evaluating the future evolution

of $E_{g\downarrow}$ using high-resolution climate projections performed over Belgium. Such projections were obtained by downscaling two GCMs, NorESM1-M and MIROC5, from the CMIP5 archive using the MAR ("Modèle Atmosphérique Régional") RCM at a spatial resolution of 5 km. Wyard *et al.* (2018) have proven the ability of MAR to simulate $E_{g\downarrow}$ and cloud fraction as well as its added-value with respect to GCMs (Section 5.3).

This chapter is organised as follows: Section 6.2 provides additional methodological aspects. Section 6.3 details the evaluation of the MAR forced by two GCMs runs over 1976–2005. The evolution of $E_{g\downarrow}$ and its causes are then investigated and discussed in Section 6.4. Conclusion and prospects are finally reported in Section 6.5.

6.2 Additional methodological aspects

The version 3.8 of MAR, described in Section 2.1 was used to perform climate simulations over Belgium.

Historical runs were obtained by nesting MAR into the ERA40/ERA-interim reanalysis (MAR-ERA), described in Section 2.2, and the GCMs NorESM1-M and MIROC5 (MAR-NOR-histo and MAR-MIR-histo) over 1976–2005. NorESM1-M and MIROC5 are two GCMs from the CMIP5 archive we selected by using the skill score methodology of Connolley and Bracegirdle (2007) as described in Section 2.3. It should be noted that MAR-ERA was later considered as reference for the present-day climate.

Future projections were obtained by nesting MAR into NorESM1-M and MIROC5, under the RCP8.5 scenario over 2006–2100 (MAR-NOR-rcp85 and MAR-MIR-rcp85).

6.3 Evaluation over the current climate

The aim of this section is to evaluate the ability of MAR forced by two GCMs selected from the CMIP5 archive, MAR-NOR-histo and MAR-MIR-histo, to simulate the present-day winter climate over Belgium. A good representation of the current climate is indeed a necessary condition required to realistically simulate future climate changes. A model that fails to reproduce the current climate generates projections that lack reliability and validity since the

response of the climate to a warming is not linear (Fettweis *et al.*, 2013). In order to evaluate the consistency of MAR forced by NorESM1-M and MIROC5, we compared the climatic mean of both MAR-NOR-histo and MAR-MIR-histo to MAR-ERA for the period 1976–2005 regarding $E_{g\downarrow}$, and cloud fraction. As previously done in Fettweis *et al.* (2013), the differences between MAR forced by both GCMs and MAR-ERA are considered as statistically significant if they are larger than the interannual variability of MAR-ERA over 1976–2005.

6.3.1 Global radiation

The seasonal climatology of $E_{g\downarrow}$ computed over 1976–2005 from MAR-ERA is displayed in Figure 6.1. Compared to this reference climatology, MAR-NOR-histo shows positive and significant mean annual biases $E_{g\downarrow}$ over the North Sea and the surrounding coastal area ranging from +5 to +15 W m^{-2} (Figure 6.2(a)). The seasonal mean biases show overall the same pattern whatever the season. The biases are larger during the summer months (JJA) and range from +20 to +30 W m^{-2} but their significance is limited to the sea (Figure 6.2(c)) because their values are small compared to the 1976-2005 mean $E_{g\downarrow}$ simulated by MAR-ERA in summer, which ranges from 220 to 240 W m^{-2}(Figure 6.1(d)). In contrast, the significant mean seasonal biases are the smallest during the winter months (DJF) and do not exceed +10 W m^{-2} (Figure 6.2(b)). They however cover a larger land surface that is mainly located near the coast(Figure 6.2(b)) because they are very large compared to the 1976-2005 mean $E_{g\downarrow}$ simulated by MAR-ERA in winter, which ranges from 14 to 26 W m^{-2} (Figure 6.1(b)). It should be noted that MAR-NOR-histo shows significant negative biases in the highest part of the Ardennes massif up to -10 W m^{-2} in winter.

The biases exhibited by MAR-MIR-histo are also positive but on average larger and therefore significant over a larger part of Belgium (Figure 6.2(f) to (j)). The yearly mean biases are significant over the entire domain and range from +10 W m^{-2} in the south-eastern part of Belgium to +20 W m^{-2} in the north-western part of the country and the North Sea (Figure 6.2(f)). The largest biases are found in spring (MAM) with values ranging from +15 to +30 W m^{-2} that are significant almost everywhere (Figure 6.2(h)). As MAR-NOR-histo, MAR-MIR-histo exhibits the smallest biases in winter,

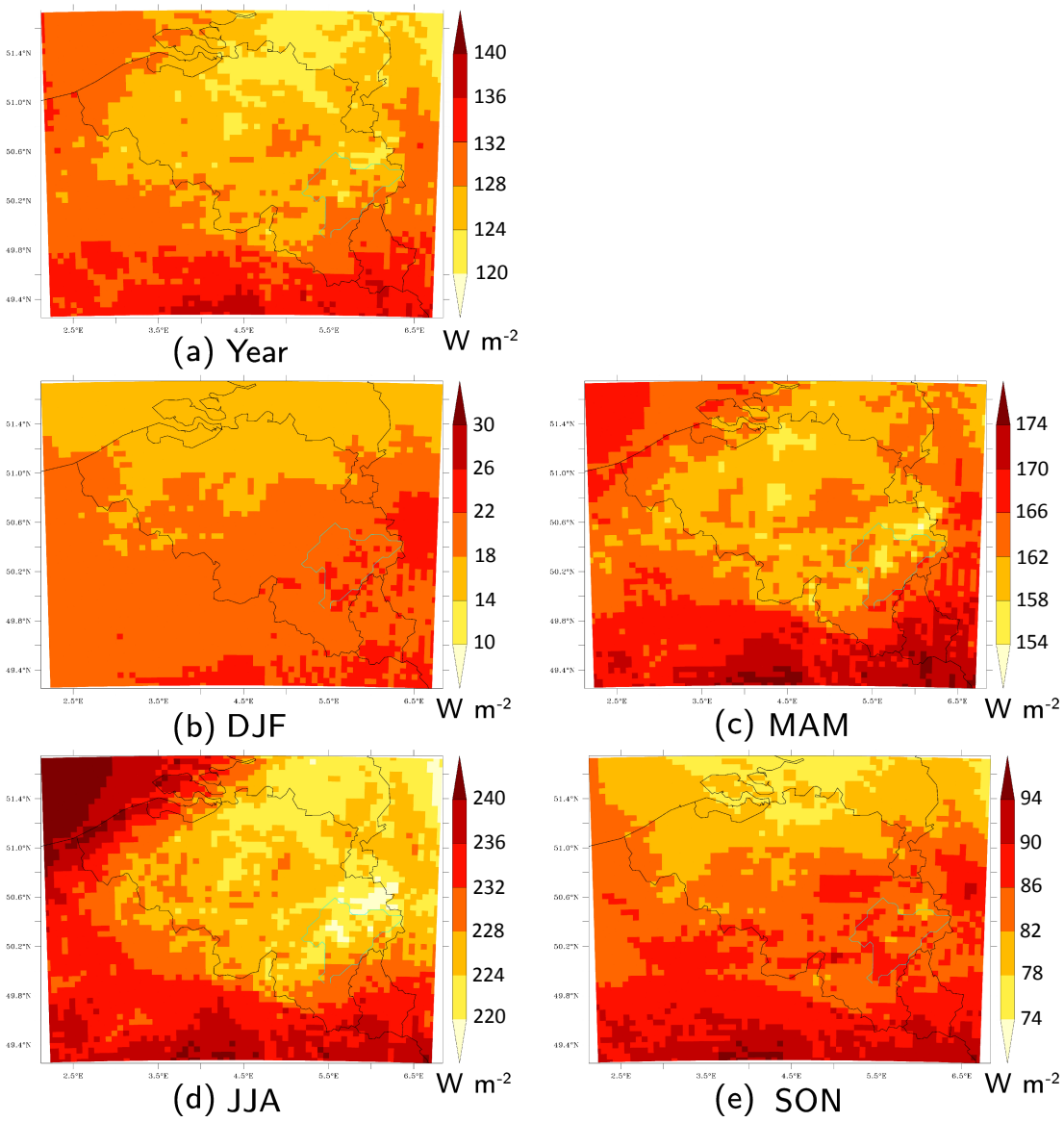

Figure 6.1: The 1976-2005 **(a)** annual, **(b)** winter (DJF), **(c)** spring (MAM), **(d)** summer (JJA), **(e)** autumn (SON), mean $E_{g\downarrow}$ simulated by MAR-ERA.

up to +10 W m^{-2}, which are significant over the entire domain except the Ardennes massif (Figure 6.2(g)).

The magnitude of the biases seems to be dependent on the distance to the North Sea: the shorter the distance, the larger the biases. In addition, the presence of the Ardennes massif appears to impact $E_{g\downarrow}$ especially in winter.

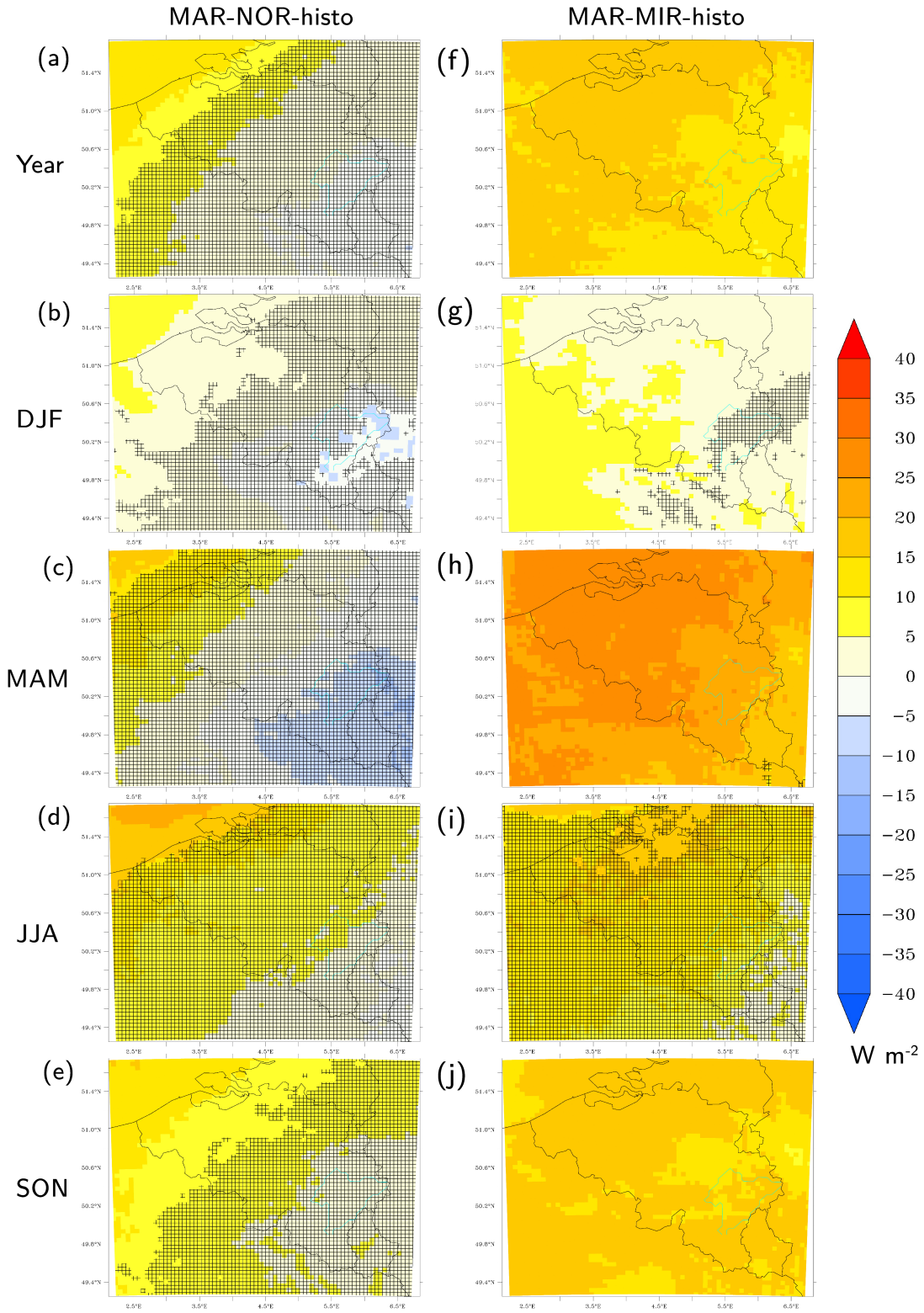

Figure 6.2: Seasonal anomaly in $E_{g\downarrow}$ simulated by **(a)-(b)-(c)-(d)-(e)** MAR-NOR-histo and **(f)-(g)-(h)-(i)-(j)** MAR-MIR-histo with respect to MAR-ERA over the period 1976-2005. Filled pixels indicate the places where the anomaly are statistically significant with respect to the MAR-ERA interannual variability. Hashed pixels indicate the places where the anomalies are statistically non-significant.

6.3.2 Cloud cover

The seasonal climatology of TCC computed over 1976–2005 from MAR-ERA is displayed in Figure 6.3.

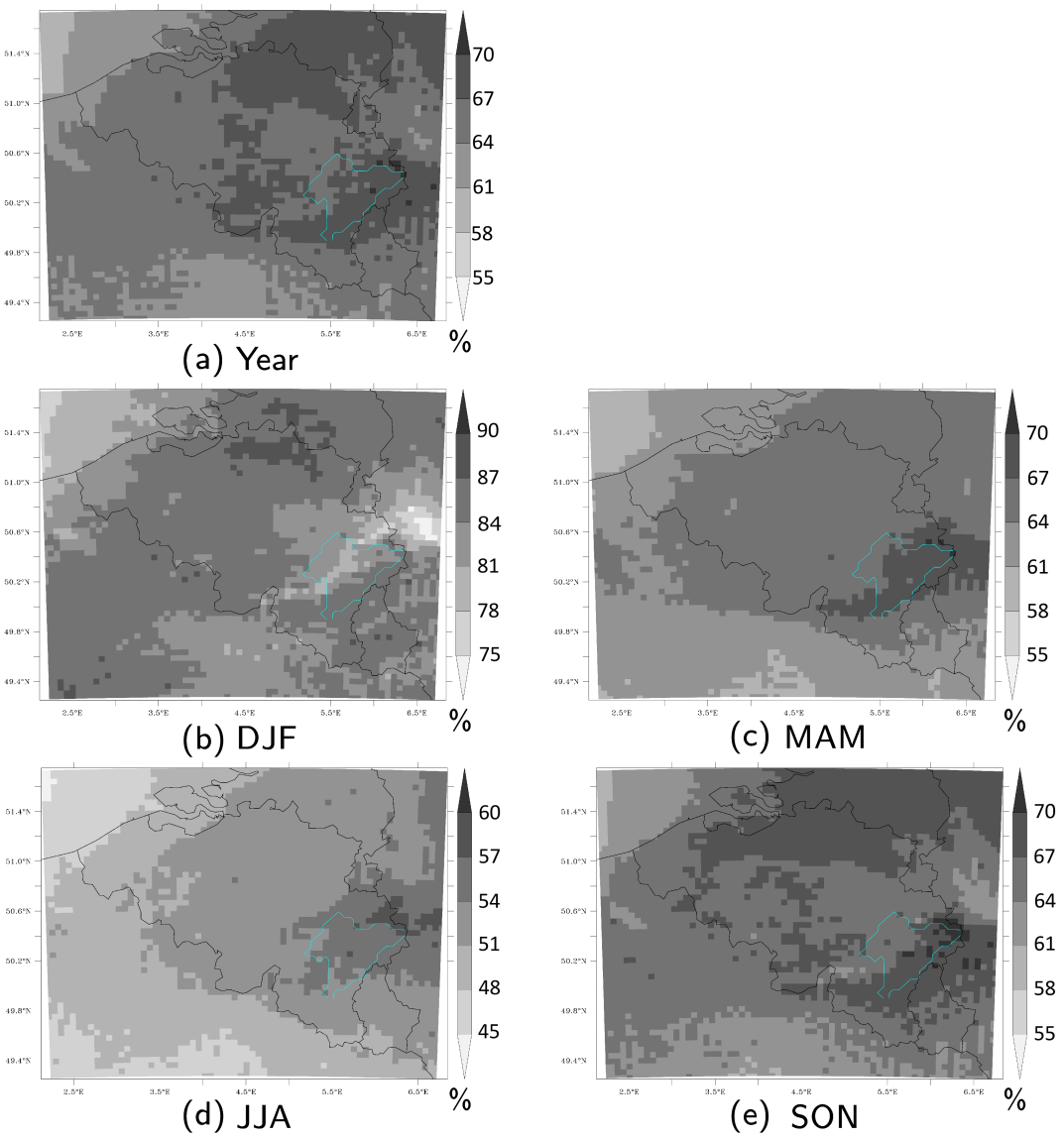

Figure 6.3: The 1976-2005 **(a)** annual, **(b)** winter (DJF), **(c)** spring (MAM), **(d)** summer (JJA), **(e)** autumn (SON), mean TCC simulated by MAR-ERA.

Compared to this reference climatology, both MAR-NOR-histo and MAR-MIR-histo exhibit negative biases in total cloud cover which are on average significant over the north-western part of the country whatever the season (Figure 6.4). As for $E_{g\downarrow}$, the magnitude of the biases depends on the distance to the North Sea: the shorter the distance to the sea, the larger the biases.

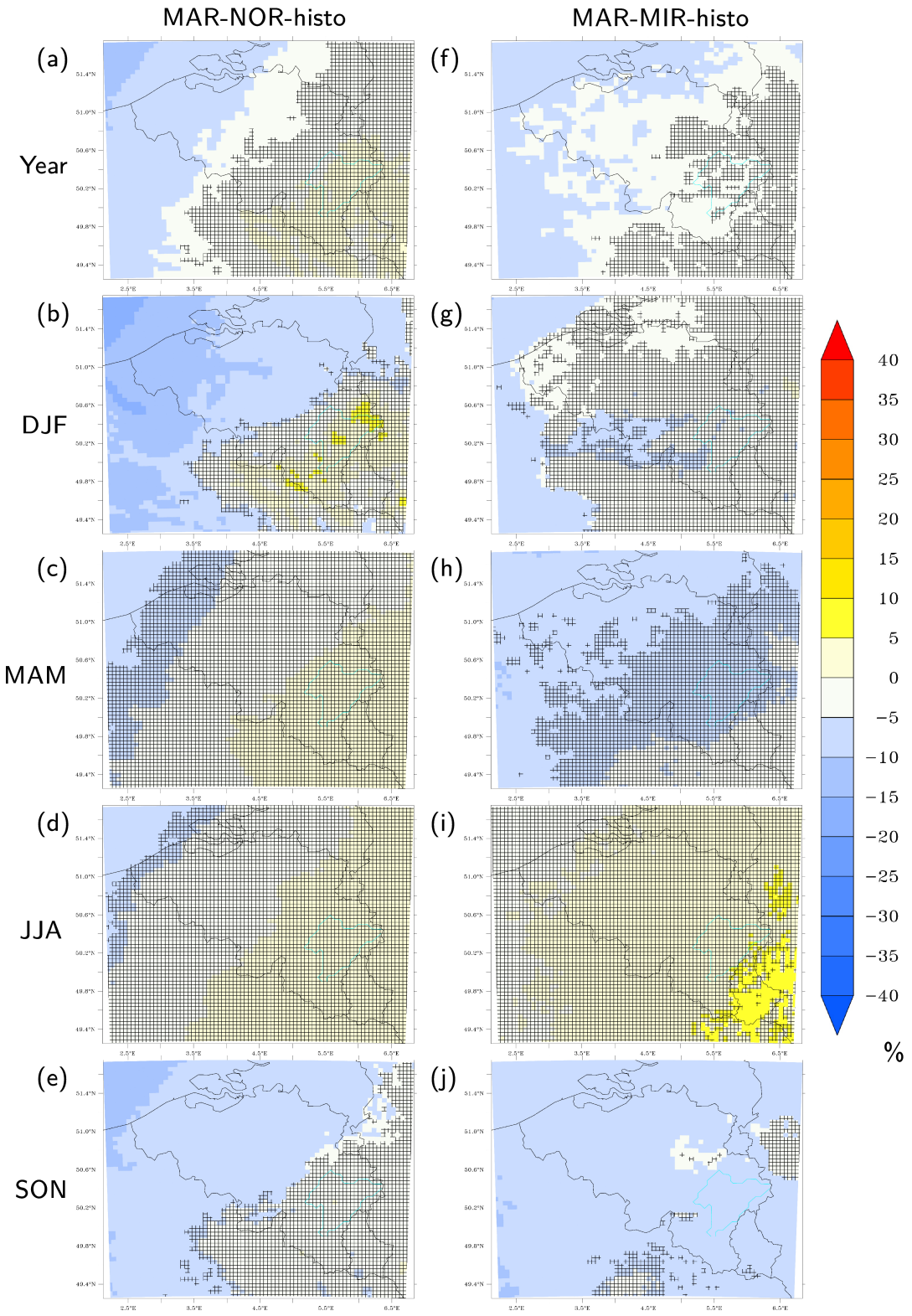

Figure 6.4: Seasonal anomaly in TCC simulated by **(a)-(b)-(c)-(d)-(e)** MAR-NOR-histo and **(f)-(g)-(h)-(i)-(j)** MAR-MIR-histo with respect to MAR-ERA over the period 1976-2005. Filled pixels indicate the places where the anomaly are statistically significant with respect to the MAR-ERA interannual variability. Hashed pixels indicate the places where the anomalies are statistically non-significant.

MAR-NOR-histo shows yearly mean biases up to -15 % (Figure 6.4(a)). Winter shows the largest seasonal biases in TCC with values ranging from -5 % to -20 % which are significant to the north of the Sambre-Meuse line (Figure 6.4(b)). Spring and summer exhibit biases that are significant mainly over the North Sea (Figure 6.4(c)-(d)). Autumn, for its part, shows significant biases over the same area as winter but not exceeding +15 % (Figure 6.4(e)).

Compared to MAR-NOR-histo, MAR-MIR-histo exhibits biases that are smaller but significant over a larger area except in winter and in summer (Figure 6.4(f) to (j)). Whatever the season, biases do not exceed +10 % over the North sea and the Belgian territory.

We have then performed the comparison for all three cloud types computed by MAR: low cloud cover (LCC) defined as the cloud fraction below 680 hPa, medium cloud cover (MCC) defined as the cloud fraction between 680 and 440 hPa, and high cloud cover (HCC) defined as the cloud fraction above 440 hPa. The climatology of annual mean LCC, MCC and HCC computed over 1976–2005 from MAR-ERA is displayed in Figure 6.5.

The comparison between annual mean LCC, MCC and HCC modelled by MAR-NOR-histo and MAR-MIR-histo with MAR-ERA shows that both simulations significantly underestimates LCC (Figure 6.6(a)-(d)) but overestimates MCC (Figure 6.6(b)-(e)) and HCC (Figure 6.6(c)-(f)). This suggests that the biases in TCC are driven by the underestimation in LCC which ranges from -5 % to -15 % in MAR-NOR-histo and from -15 to -20 % in MAR-MIR-histo. Such biases are very large compared to the 1976-2005 mean LCC simulated by MAR-ERA which ranges from 40 to 55 % (Figure 6.5(c)). Regarding the overestimation of MCC and HCC, values and patterns are almost the same in MAR-NOR-histo with values between +5 and +10 % while MAR-MIR-histo shows smaller biases in MCC (up to +5 %) than in HCC (up to +15 %). Still these MCC biases in MAR-MIR-histo remain significant as they are very large compared to the 1976-2005 mean MCC simulated by MAR-ERA which ranges from 15 to 24 % (Figure 6.5(b)).

6.3.3 Discussion

The evaluation of the MAR simulations forced by GCMs has brought to light significant biases in both $E_{g\downarrow}$ and cloud fraction. Compared to MAR-

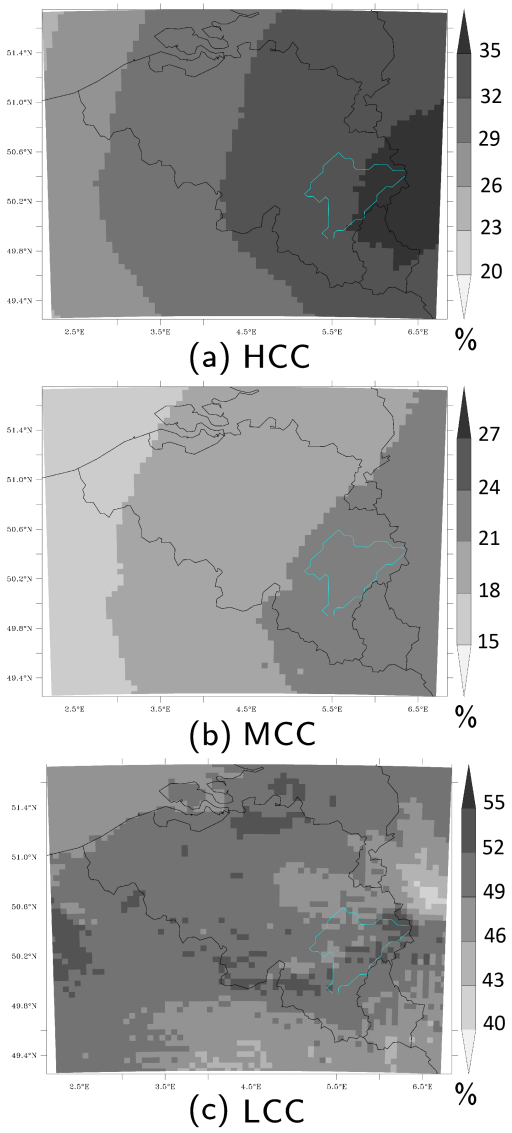

Figure 6.5: The 1976-2005 annual mean **(a)** LCC, **(b)** MCC, **(c)** HCC, simulated by MAR-ERA.

ERA, both MAR-NOR-histo and MAR-MIR histo overestimate $E_{g\downarrow}$ and underestimate TCC. The magnitude and the pattern of the biases depend on the season. For instance, they are quite limited in summer in both MAR-NOR-histo and MAR-MIR-histo. On the contrary, biases in winter and autumn are significant over larger parts of Belgium. Regarding TCC, its underestimation is due to the underestimation of LCC as MCC and HCC are overestimated in both simulations. Given the pattern and the sign of the biases in LCC, we conclude that the overestimation of $E_{g\downarrow}$ results from an underestimation of LCC. It should be noted that the aforementioned biases

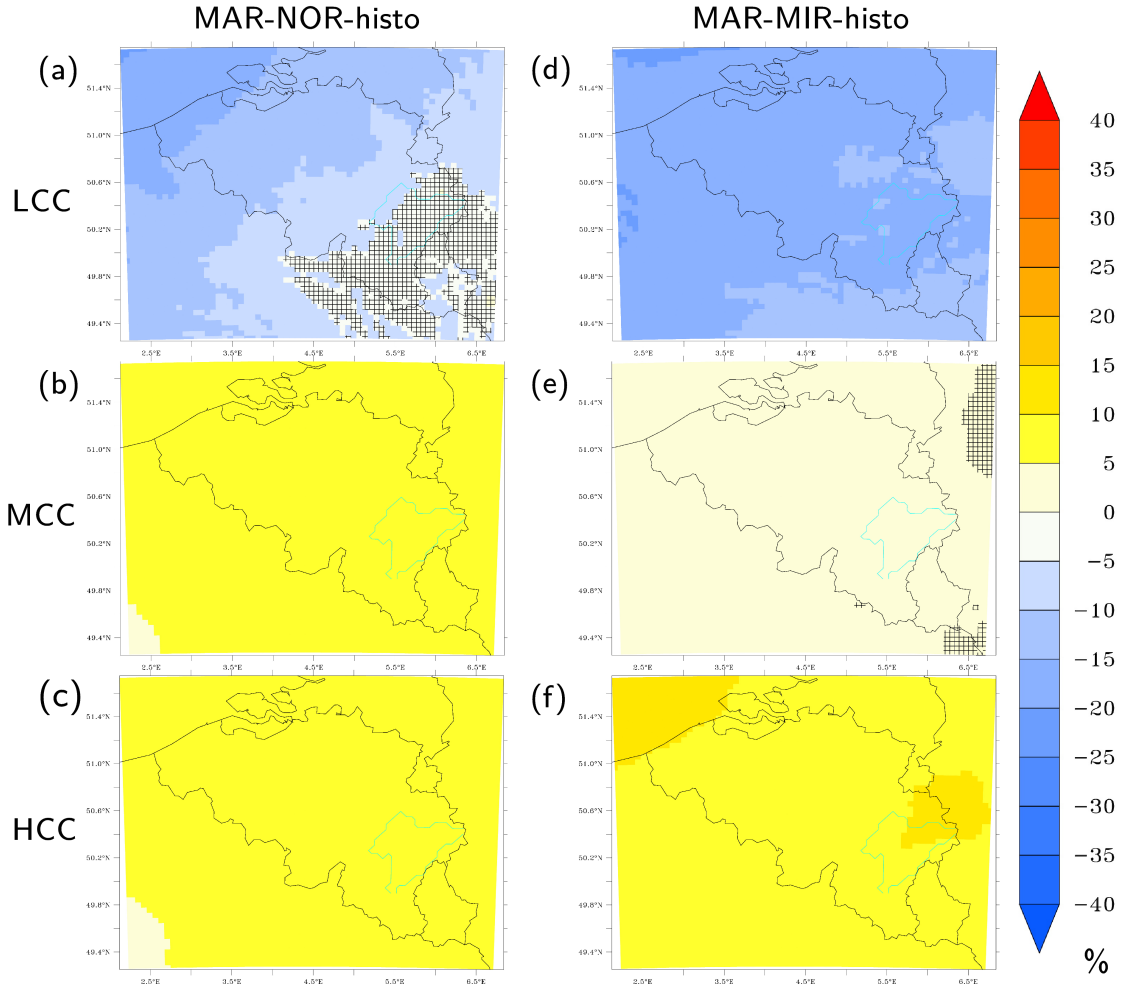

Figure 6.6: Mean annual anomaly in LCC, MCC and HCC simulated by **(a)-(b)-(c)** MAR-NOR-histo and **(d)-(e)-(f)** MAR-MIR-histo with respect to MAR-ERA over the period 1976-2005. Filled pixels indicate the places where the anomaly are statistically significant with respect to the MAR-ERA interannual variability. Hashed pixels indicate the places where the anomalies are statistically non-significant.

are the largest in MAR-MIR-histo.

The underestimation of LCC is a well-known problem in climate modelling (Zhang *et al.*, 2005). In the case of RCMs, this underestimation can result from the prevailing large-scale conditions on the one hand and from the parameterization of cloud properties on the other hand.

Biases found in the GCMs from CMIP5 have been widely investigated in the literature. Compared to observations and reanalyses, both NorESM1-M and MIROC5 exhibits negative biases in TCC (and positive biases in $E_{g\downarrow}$) over Europe (Watanabe *et al.*, 2010; Bentsen *et al.*, 2013; Bartók *et al.*, 2017) which have been attributed to their parameterization of cloud

properties. However, cloud fraction computed by GCMs is not a field used as RCM boundary conditions. RCMs, including MAR, are rather forced by temperature, humidity, pressure and wind so that only biases in these variables can generate biases in the cloud fraction computed by RCMs. Bentsen *et al.* (2013) found that NorESM1-M overestimates air temperature over Western Europe which would explain why LCC is underestimated in MAR. As the climate of Europe is highly constrained by the dominant weather regimes (Section 1.1), biases in their frequency of occurrence can also generate biases in cloud cover and therefore in $E_{g\downarrow}$. For instance, Chiacchio and Wild (2010) found negative correlations between NAO index values and LCC and MCC trends over Northern Europe in spring and summer for the period 1985–2000. Cattiaux *et al.* (2013) showed that NorESM1-M tends to slightly underestimate the NAO+ regime frequency by about -5% which should imply an overestimation of TCC in MAR-NOR-histo which is not the case. On the contrary, MIROC5 overestimates the summer NAO+ regime frequency by about +20% but MAR-MIR-histo shows no significant bias in TCC in summer except over the North Sea. This suggests that the biases in TCC found in our MAR simulations are more related to the parameterization of cloud properties implemented in MAR. In fact, Wyard *et al.* (2018) compared reanalyses and MAR forced by these reanalyses simulations to ground-based measurements of TCC and $E_{g\downarrow}$ (Section 5.3). They found similar TCC biases in reanalyses and in MAR while biases in $E_{g\downarrow}$ were reduced by up to 90% in MAR with respect to reanalyses. They concluded that the cloud optical depth is larger in MAR than in reanalyses. Bartók *et al.* (2017) came to the same conclusion. By comparing GCMs and RCMs outputs with observations of TCC and $E_{g\downarrow}$, they concluded that "*inconsistencies between the $E_{g\downarrow}$ simulations of GCMs and RCMs are mainly dominated by the parameterization of local processes and by the compensating errors resulting from this parameterization*".

6.4 Future changes in Belgium

This section aims to assess the evolution of global radiation and cloud cover by the end of the 21^{st} century under the RCP8.5 scenario. Changes in the future Belgian climate were assessed by comparing the 2071–2100 mean climate computed by MAR-NOR-rcp85 and MAR-MIR-rcp85 to the 1976–

2005 mean climate computed by MAR-NOR-histo and MAR-MIR-histo. As done in Fettweis *et al.* (2013), for a given climate variable, its future changes were considered as significant if they were larger than its 1976–2005 interannual variability.

6.4.1 Global radiation

Compared to 1976–2005, only MAR-NOR-rcp85 shows significant changes, namely an increase in the mean annual $E_{g\downarrow}$ with values between +5 and +10 W m^{-2} over the entire Belgium (Figure 6.7(a)). This increase is dominated by changes in spring and particularly in summer which exhibits significantly increasing $E_{g\downarrow}$ over most part of Belgium with values ranging from +10 to +20 W m^{-2} (Figure 6.7(d)). On the contrary, MAR-MIR-rcp85 shows no significant change whatever the season (Figure 6.7(f) to (j)).

It should be noted that the amplitude of these future changes is smaller than their biases over the present-day climate. Therefore, these future changes are likely not robust.

6.4.2 Cloud cover

Regarding TCC, both MAR-NOR-rcp85 and MAR-MIR-rcp85 simulate a significant decrease in yearly mean TCC which does not exceed -10 % (Figure 6.8(a)-(f)). In addition, the signal is negative whatever the season.

MAR-NOR-rcp85 shows a decrease in yearly mean TCC which is homogeneous over the entire domain with values between -5 and -10 % (Figure 6.8(a)). As winter shows no significant trend, this decrease in the yearly mean TCC values are dominated by significant changes in spring, summer and autumn which all broadly exhibit the same pattern and values between -5 and -10 % (Figure 6.8(b)-(c)-(d)-(e)). It should be noted that in autumn, the only places where the trends are not significant are the highest part of the Ardennes massif.

MAR-MIR-rcp85, for its part, shows larger changes to the western part of the domain than to the eastern part with values between -5 and -10 % to the west and under -5 % to the east (Figure 6.8(f)). Winter and summer show no significant change while spring and autumn show decreasing trends which do not exceed -10 % (Figure 6.8(g)-(h)-(i)-(j)). As MAR-NOR-rcp85,

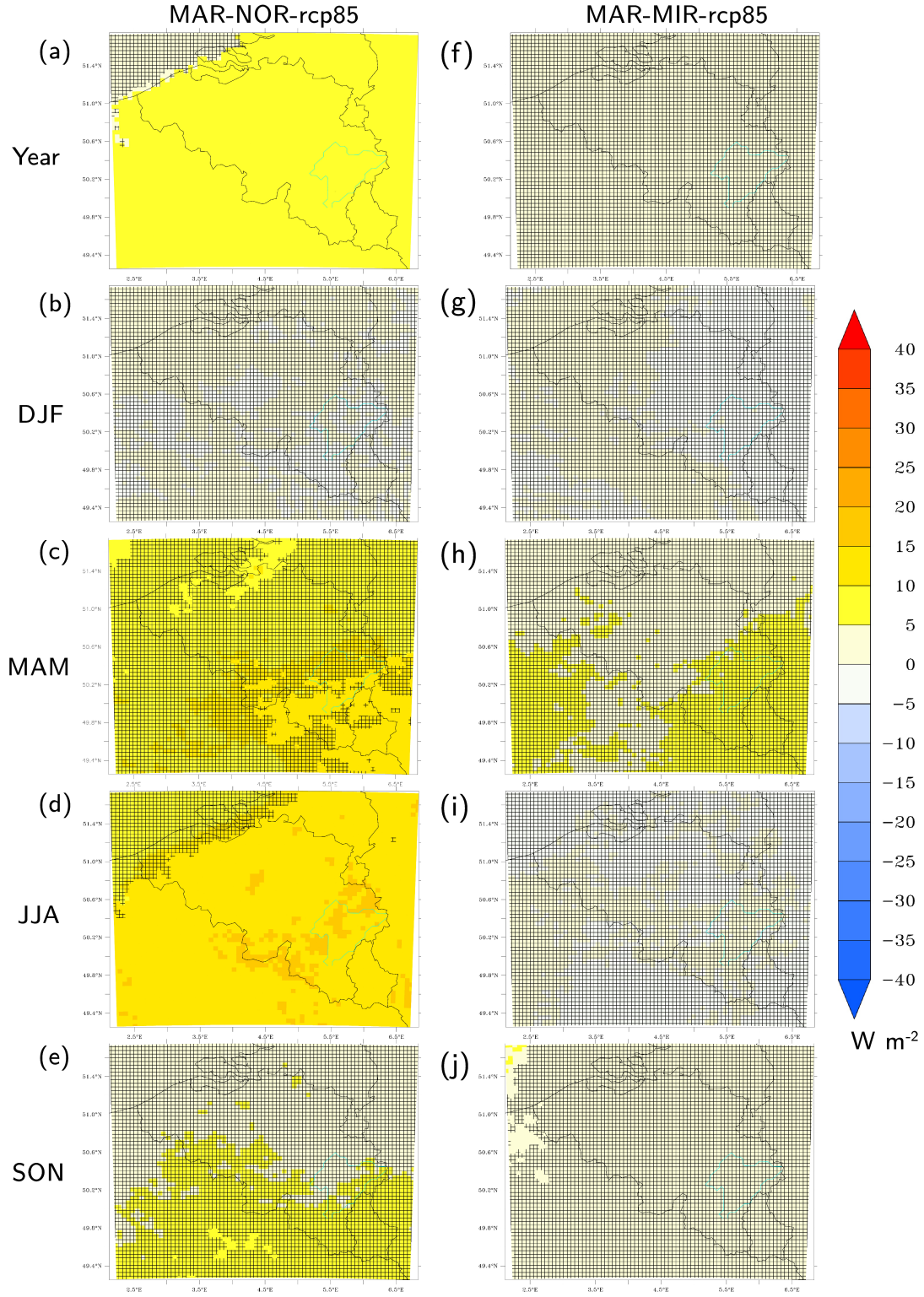

Figure 6.7: Seasonal changes in $E_{g\downarrow}$ simulated by **(a)-(b)-(c)-(d)-(e)** MAR-NOR-rcp85 and **(f)-(g)-(h)-(i)-(j)** MAR-MIR-rcp85 over 2071–2100 with respect to 1976–2005. Filled pixels indicate the places where the changes are statistically significant with respect to the MAR-NOR-histo and MAR-MIR-histo interannual variability over 1976–2005. Hashed pixels indicate the places where the changes are statistically non-significant.

MAR-MIR-rcp85 shows no significant trend over the Ardennes massif but over a larger extent.

Both MAR-NOR-rcp85 and MAR-MIR-rcp85 exhibit a significant decrease in the annual LCC and MCC over the entire MAR domain whereas HCC changes are non-significant (MAR-NOR-rcp85) or limited to the coastal area (MAR-MIR-rcp85) (Figure 6.9). Both MAR future projections agree on an LCC decrease of -5 to -10 % (Figure 6.9(a)-(d)) while MCC is affected by a smaller decrease with values lower than -5 %, except in MAR-NOR-rcp85, which sees an MCC decrease over the Ardennes close in value to the LCC decrease (Figure 6.9(b)-(e)). HCC also sees a smaller decrease (lower than -5 %) than LCC (Figure 6.9(c)-(f)). The value and significance of the TCC changes being similar to those of LCC, we can conclude that the decrease in TCC is dominated by the decrease in LCC.

It should be noted that the amplitude of these future changes is again smaller than their biases over the present-day climate. Therefore, these future changes are likely not robust.

6.4.3 Discussion

The comparison between the 2071–2100 mean climate to 1976–2005 shows that only MAR-NOR-rcp85 simulates significant changes in $E_{g\downarrow}$ and more precisely an increase in the yearly mean $E_{g\downarrow}$ dominated by changes in spring and particularly summer. This increase in $E_{g\downarrow}$ coincides with decreasing TCC and particularly decreasing LCC and MCC simulated by MAR-NOR-rcp85 and to a lesser extent by MAR-MIR-rcp85. However, the significant decrease in LCC and MCC simulated by MAR-MIR-rcp85 does not lead to a significant increase in $E_{g\downarrow}$. It should nevertheless be noted that the amplitude of these future changes is smaller than their biases over the present-day climate. Therefore, these future changes are likely not robust.

Still, the behaviour of MAR-MIR-rc85 remains to be explained. Regarding the yearly mean cloud optical depth (COD), MAR-MIR-rcp85 shows positive but non-significant changes over the entire Belgium contrary to MAR-NOR-rcp85 which shows positive changes but non-significant over the Ardennes only (Figure 6.10(a)-(b)). This positive signal in COD simulated by MAR-MIR-rcp85 over the entire Belgium may explain why the latter shows no change in $E_{g\downarrow}$ despite significant decreasing LCC and MCC: the decrease in

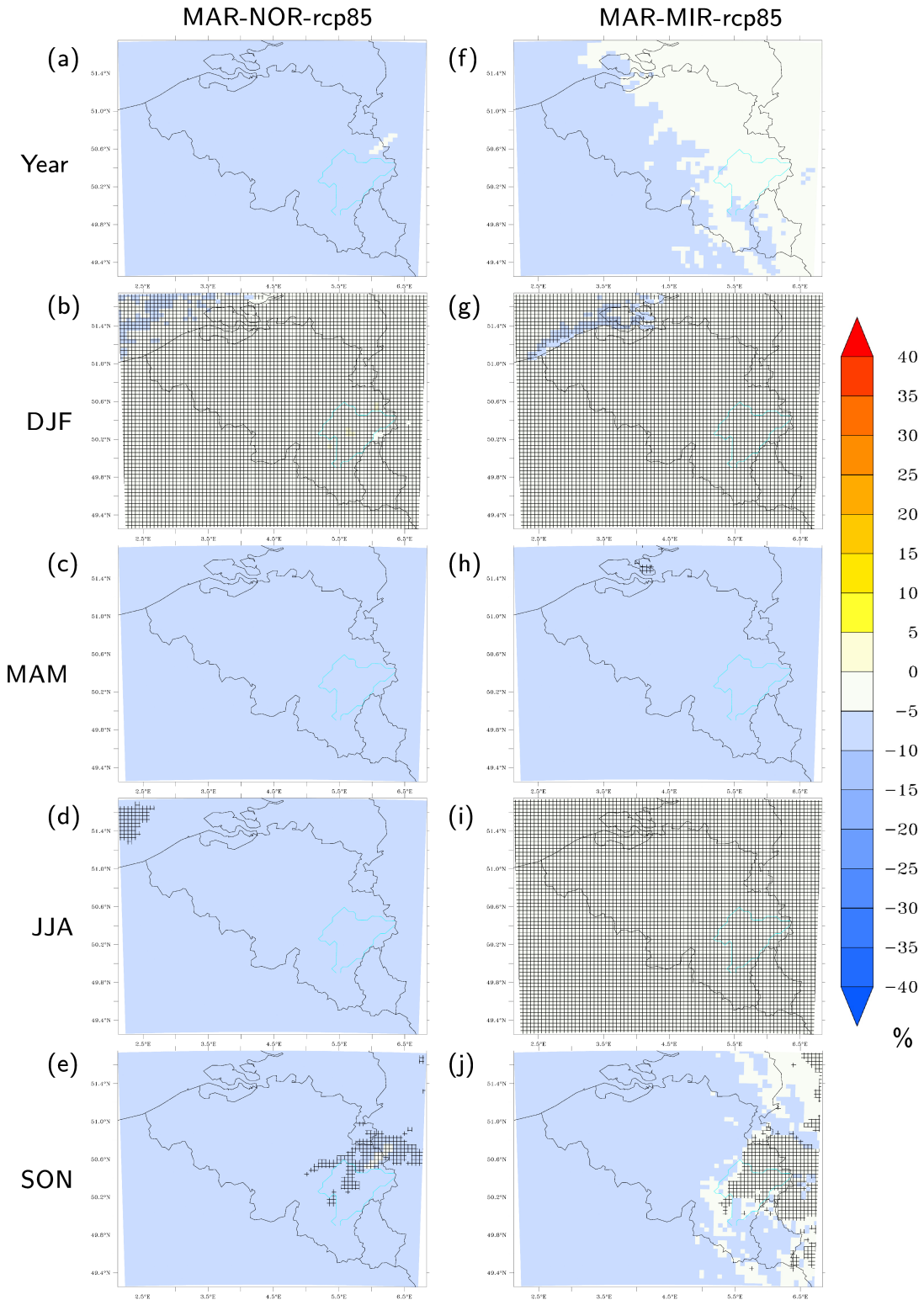

Figure 6.8: Seasonal changes in TCC simulated by **(a)-(b)-(c)-(d)-(e)** MAR-NOR-rcp85 and **(f)-(g)-(h)-(i)-(j)** MAR-MIR-rcp85 over 2071–2100 with respect to 1976–2005. Filled pixels indicate the places where the changes are statistically significant with respect to the MAR-NOR-histo and MAR-MIR-histo interannual variability over 1976–2005. Hashed pixels indicate the places where the changes are statistically non-significant.

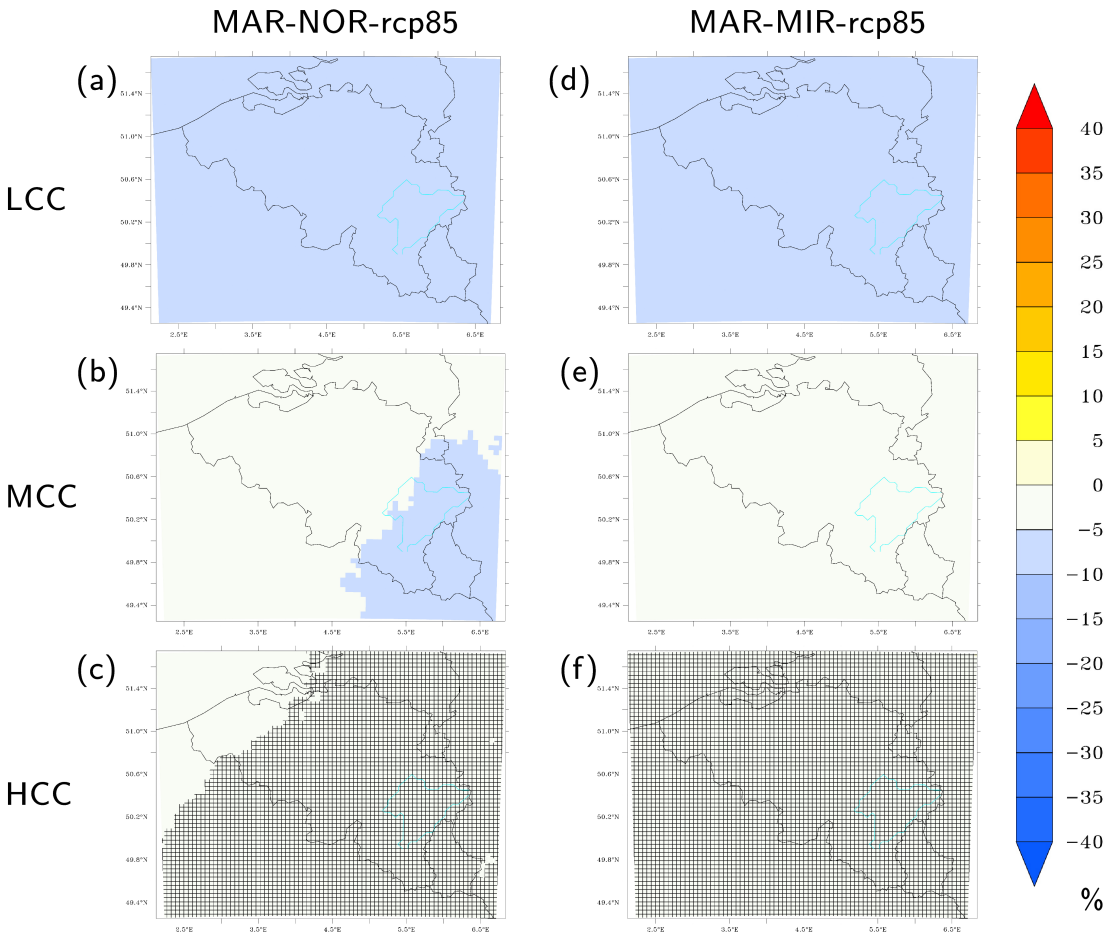

Figure 6.9: Mean annual changes in LCC, MCC and HCC simulated by **(a)-(b)-(c)** MAR-NOR-rcp85 and **(d)-(e)-(f)** MAR-MIR-rcp85 over 2071–2100 with respect to 1976–2005. Filled pixels indicate the places where the changes are statistically significant with respect to the MAR-NOR-histo and MAR-MIR-histo interannual variability over 1976–2005. Hashed pixels indicate the places where the changes are statistically non-significant.

TCC is counterbalanced by an increase in its COD. We have also looked at the changes in the yearly mean ice water content (IWC) and liquid water content of clouds (LWC). Both simulations exhibit decreasing IWC which are even significant over the southern part of Belgium in MAR-NOR-rcp85 with relative changes ranging from -2 to -10 % (Figure 6.10(c)-(d)). On the contrary, MAR-NOR-rcp85 exhibits a non-significant decrease in LWC while MAR-MIR-rcp85 exhibits a non-significant increase (Figure 6.10(e)-(f)). This would also explain why MAR-MIR-rcp85 simulates no change in $E_{g\downarrow}$ as the decrease in IWC is counterbalanced by an increase in LWC.

Focusing on Europe, studies show that the sign of $E_{g\downarrow}$ changes depends on

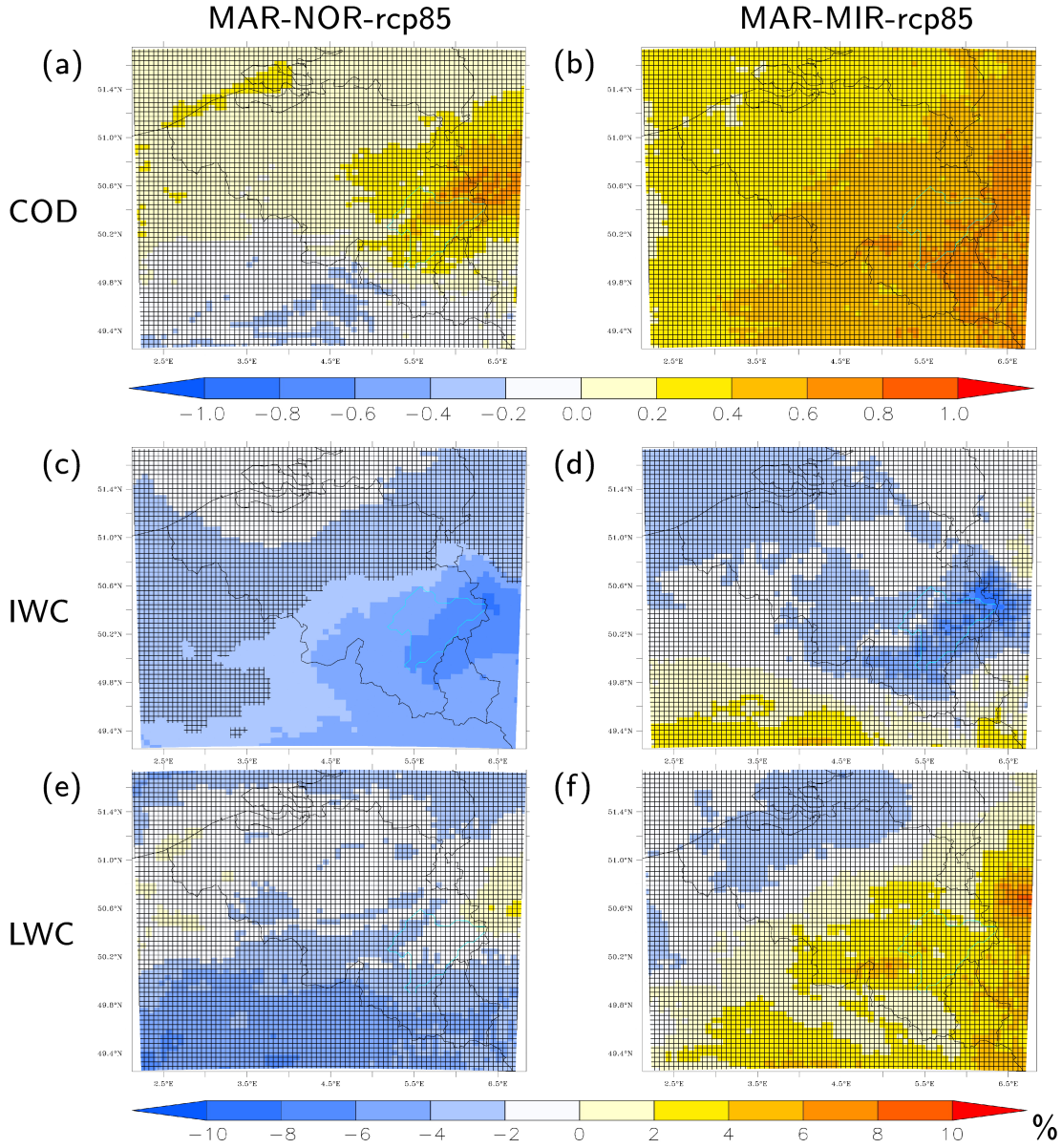

Figure 6.10: Mean annual changes in **(a)-(b)** COD and relative mean annual changes in **(c)-(d)** IWC and **(e)-(f)** LWC simulated by MAR-NOR-rcp85 and MAR-MIR-rcp85 over 2071–2100 with respect to 1976–2005. Filled pixels indicate the places where the changes are statistically significant with respect to the MAR-NOR-histo and MAR-MIR-histo inter-annual variability over 1976–2005. Hashed pixels indicate the places where the changes are statistically non-significant.

the use of global or regional climate model simulations (Jerez *et al.*, 2015; Wild *et al.*, 2015; Bartók *et al.*, 2017). Studies using GCM simulations from CMIP5 concluded on an increase in $E_{g\downarrow}$ (Wild *et al.*, 2015; Bartók *et al.*, 2017) while a decrease is found all over Europe except in Mediterranean regions when RCM simulations from EURO-CORDEX are used (Jerez *et al.*,

2015; Bartók *et al.*, 2017). Bartók *et al.* (2017) state that this difference results from the different behaviour of cloud cover in global and regional climate models. In our case, contrary to Jerez *et al.* (2015) and Bartók *et al.* (2017), our RCM simulations (MAR-NOR-rcp85) are in agreement with their forcing GCM (Bartók *et al.*, 2017) regarding their trends in $E_{g\downarrow}$ and TCC. This implies that the trends simulated by the MAR RCM over Belgium are fully driven by the lateral boundary conditions. Wyard *et al.* (2018) also came to this conclusion by comparing the MAR outputs to reanalyses and observations (Section 5.4). The reason why our RCM simulations are so dependent on their lateral boundary conditions is the small size of the MAR integration domain over Belgium while Jerez *et al.* (2015) and Bartók *et al.* (2017) used continentale-scale RCM simulations. Indeed, Leduc and Laprise (2009) and Flato *et al.* (2014) stated that small domains allow less freedom for RCMs to generate small-scale features.

Regarding the discrepancies between MAR-NOR-rcp85 and MAR-MIR-rcp85, they result from their forcing GCM since the same MAR configuration (domain size, calibration) is used for both these simulations. As a reminder, control simulations show similar behaviour and biases, both significantly underestimating TCC and LCC, and significantly overestimating MCC, HCC and $E_{g\downarrow}$. The future climate sensitivities can therefore hardly be linked to the present-day biases found in the historical simulations, as already highlighted by Cattiaux *et al.* (2013). Another possible reason to the discrepancies between MAR-NOR-rcp85 and MAR-MIR-rcp85 is large-scale dynamics. Cattiaux *et al.* (2013) compared the 2071–2100 mean frequencies of occurrence of the main weather regimes simulated by the CMIP5 GCMs to their 1981-2010 mean frequencies. As the signal of the yearly mean trends in $E_{g\downarrow}$ is driven by the summer trends, we look at the circulation changes for this season. Both NorESM1-M and MIROC5 exhibits more frequent blocking (BL) regime of about +10% and +5 % respectively (Cattiaux *et al.*, 2013). BL regime corresponds to the persistance of anticyclonic conditions over Northern Europe which favour clear-sky conditions in our regions. These more frequent BL conditions are therefore consistent with the significant decline of TCC, LCC and MCC found in our future projections. This also explains why the decrease in TCC and the resulting increase in $E_{g\downarrow}$ are stronger in summer for the MAR-NOR-rcp85 simulation than in MAR-MIR-rcp85 as the former simulates a larger increase in the BL regime

than the later. It should be noted that circulation changes such as more frequent anticyclonic conditions have been suspected to be responsible for the increase in $E_{g\downarrow}$ observed since the 2000s (Bender *et al.*, 2012; Eastman and Warren, 2013; Wyard *et al.*, 2018) (Section 5.4.3). As the more frequent BL regime in summer is simulated by all CMIP5 GCMs (Cattiaux *et al.*, 2013), our results suggest that such circulation changes are a consequence of global warming.

Besides discrepancies and uncertainties related to the MAR forcings, issues related to the parameterizations implemented in the MAR RCM are also an additional source of uncertainties in our future projections. For instance, by comparing MAR with observations, Wyard *et al.* (2017, 2018) have brought to light that MAR underestimates cloud fraction and more particularly convective clouds, as a results of issues in the parameterization of convection as well as cloud microphysics (Section 3.3 and Section 5.3). Hence, as convection is expected to increase in a warmer climate, the decrease in cloud fraction projected by MAR and consequently the increase in $E_{g\downarrow}$ are certainly overestimated as MAR fails to properly simulate this kind of clouds.

Finally, it should be noted that our future projections were performed under constant aerosol emissions whereas their future concentrations in the atmosphere is one of the key factors for the future evolution of cloud properties and $E_{g\downarrow}$.

6.5 Chapter conclusion

This chapter aims at evaluating the future evolution of $E_{g\downarrow}$ by the end of the 21st century under the RCP8.5 scenario. For this purpose, two GCMs from CMIP5, NorESM1-M and MIROC5, were selected by using the skill score methodology of Connolley and Bracegirdle (2007) and were dynamically downscalled using the MAR RCM. Historical simulations (MAR-NOR-histo and MAR-MIR-histo) and future projections (MAR-NOR-rcp85 and MAR-MIR-rcp85) were then performed using version 3.8 of MAR forced by these two GCMs. An evaluation of the historical simulations was first conduted by comparing MAR-NOR-histo and MAR-MIR-histo to MAR forced by the ERA-interim reanalyses (MAR-ERA) for the period 1976–2005. An evaluation of future trends in the $E_{g\downarrow}$ and cloud cover was then carried

out by comparing the 2071–2100 future mean climate to the 1976–2005 present-day mean climate.

The evaluation of the MAR forced by GCMs simulations has brought to light significant biases in both MAR-NOR-histo and MAR-MIR histo. They both overestimate the mean annual $E_{g\downarrow}$ especially in coastal regions where the biases can reach +15 W m^2 in MAR-NOR-histo and +30 W m^2 in MAR-MIR-histo. This overestimation results from the underestimation of the mean annual TCC, which reaches -15 % in MAR-NOR-histo while it is smaller in MAR-MIR-histo (lower than -10 %) but covers as larger area. The magnitude and the pattern of the biases depend on the season and are quite limited in summer. Regarding TCC, its underestimation is due to the underestimation of LCC as MCC and HCC are overestimated in both control simulations. Biases in the MAR simulations are mainly related to the parameterization of clouds properties implemented in MAR and also to biases in the GCM forcing fields.

The amplitude of the future trends is smaller than the biases over the present-day climate. Therefore, these future changes are likely not robust. Still, our results show decreasing TCC, between -5 and -10 %, and particularly decreasing LCC and MCC simulated by MAR-NOR-rcp85 and to a lesser extent by MAR-MIR-rcp85. However, the significant decrease in LCC and MCC simulated by MAR-MIR-rcp85 does not lead to a significant increase in $E_{g\downarrow}$ as it is the case for MAR-NOR-rcp85. The latter exhibits a significant increase in the yearly mean $E_{g\downarrow}$ over the entire Belgium valued between +10 and +20 W m^2. Existing studies show that contrary to Jerez *et al.* (2015) and Bartók *et al.* (2017), our RCM simulations (MAR-NOR-rcp85) are in agreement with their forcing GCM (Bartók *et al.*, 2017) regarding their trends in $E_{g\downarrow}$ and TCC. This implies that the trends simulated by the MAR RCM over Belgium are fully driven by the lateral boundary conditions as a consequence of the size of the domain (120x110 grid points). Regarding the discrepancies between MAR-NOR-rcp85 and MAR-MIR-rcp85, they are hardly explained by their present-day biases and appear to be linked to discrepancies in future changes in large-scale dynamics. Both NorESM1-M and MIROC5 simulates an increase in the blocking (BL) regime frequency in summer with an increase of +10 and 5 % respectively (Cattiaux *et al.*, 2013). This implies more frequent anticyclonic conditions over Belgium favouring cloudless sky. These more frequent BL conditions are therefore consistent

with the significant decline of TCC, LCC and MCC found in our future projections. This also explain why the decrease in TCC and the resulting increase in $E_{g\downarrow}$ are stronger in summer for MAR-NOR-rcp85 than for MAR-MIR-rcp85 as the former simulates a larger increase in the BL regime than the latter. It should be noted that circulation changes such as more frequent anticyclonic conditions have been suspected to be responsible for the increase in $E_{g\downarrow}$ observed since the 2000s (Bender *et al.*, 2012; Eastman and Warren, 2013; Wyard *et al.*, 2018). As the more frequent BL regime in summer is simulated by all CMIP5 GCMs (Cattiaux *et al.*, 2013), our results suggest that such circulation changes are a consequence of global warming.

In addition, as in Wyard *et al.* (2017) and Wyard *et al.* (2018), our results show again that the parameterization of convection as well as cloud microphysics implemented in MAR requires improvements in order to reduce uncertainties related to the MAR physics (Section 3.3 and Section 5.3). These issues in the MAR physics likely cause an amplification of the aforementioned trends simulated by MAR.

Finally, as further perspectives, given that part of the biases found in our simulations were inherited from the forcing GCMs, it may be relevant to reiterate this study with the updated forcing data (from CMIP6), so as to assess the sensitivity of our RCM MAR to the GCM uncertainty. Then, the influence of future changes of temperature and $E_{g\downarrow}$ on energy yields of photovoltaic systems could be assessed as done in Wild *et al.* (2015).

CHAPTER 7

General conclusions and perspectives

7.1 Conclusions

Although initially designed for the polar regions, the regional climate model MAR was applied for the first time to Belgium which has a temperate climate. The aim was first to assess the performances of MAR over Belgium and then to study the current and future evolution of hydroclimatic conditions favouring floods and also the current and future evolution of global radiation. For this purpose, historical simulations were performed by downscaling four reanalyses using MAR: ERA40/ERA-interim (1959–2016), NCEP/NCAR-v1 (1949–2016), ERA-20C (1900–2010) and 20CRV2C (1900–2010). Future projections (2006–2100) and their control simulations (1976–2005) were then performed by downscaling two global climate models (GCM) under the RCP8.5 scenario: NorESM1-M and MIROC5. These two GCMs were selected among the 30 GCMs of the CMIP5 database using the skills scores methodology of Connolley and Bracegirdle (2007). The horizontal resolution used for both historical and future simulations is 5 km. It is the best resolution which can be used given the physics of the MAR model.

On the one hand, the evaluation of the MAR performances was made by comparing MAR forced by reanalyses to the raw reanalyses and ground-based observations over 1959–2010. This period is the longest common period to all four reanalyses used as MAR lateral boundary conditions. On the other hand, the evaluation of MAR forced by GCMs was made by comparing the 1976–2005 mean climate computed by these simulations to the MAR forced by ERA-interim.

The current evolution of the Belgian climate was assessed by performing a linear trend analysis using MAR forced by reanalysis simulations for the period 1959–2010. The future evolution of the Belgian climate was determined by comparing the 2071–2100 mean climate simulated by MAR forced by GCM future simulations under RCP8.5 to the 1976–2005 mean climate simulated by MAR forced by GCM historical simulations.

The main conclusions regarding the objectives of this PhD thesis are discussed hereafter.

7.1.1 On the added value of MAR and the sources of uncertainty in the simulations

The evaluation of the MAR performances shows that MAR successfully simulates the spatial variability of the Belgian climate and also its daily, seasonal yearly, and decadal variations. Compared to ground-based measurements from 20 weather stations over 2008–2014, **MAR exhibits non-significant biases** regarding temperature, precipitation, and snow height. Regarding global radiation and cloud cover, the comparison to 4 ground-based stations which has measured global radiation and cloud cover over at least 1975–2014 shows that MAR exhibits non-significant biases. The MAR results are particularly satisfying during the winter months and over the higher Belgian altitudes where the climate is the coldest. This is likely related to the fact that MAR was initially designed for the simulation of polar climates. For instance, correlation coefficient (R) values for daily snow height are above 0.90 while R values for daily precipitation amount are above 0.70.

The **added-value of an RCM like MAR with respect to global models** was also proven. Using MAR largely reduces the biases found in the global climate simulations including reanalyses. This is particularly remarkable regarding global radiation with biases reduced from 25 % to 92 % depending on the reanalysis used. MAR also allows a more detailed spatial variability for global radiation and cloud cover (5 km). However, it should be noted that compared to reanalyses, R and root mean square error (RMSE) are not improved by MAR suggesting that interannual variability of MAR is fully driven by the prevailing large-scale conditions prescribed by the lateral boundary conditions. This is due to the small size of the integration domain used in this research (600 km x 550 km). In fact, it has been proven that small domains allow less freedom for RCMs to generate small-scale features.

In addition, this **dependency of the MAR results to its forcing** data was also highlighted by the trend analysis. The results show that the sign of the trends found in MAR is fully driven by the forcing models and their ability to simulate large-scale circulation:

- Regarding reanalysis, MAR produces the best results when it is forced by the ERA-interim reanalysis probably because this reanalysis assimilates much more data and has a much better horizontal and vertical resolution than all three other reanalyses (NCEP/NCAR-v1, ERA-20C,

20CRV2C) used in this research. On the contrary, NCEP/NCAR-v1 amplifies the trends in global radiation and cloud cover or generates opposite trends than observed in the extreme precipitation events. The low spatial resolution of NCEP/NCAR-v1 (2.5°x2.5°) is likely responsible for these poor results. Despite having a better spatial resolution than NCEP/NCAR-v1, ERA-20C and 20CRV2C do not produce consistent trends. This is probably because they only assimilate surface observations such as pressure, marine winds, sea surface temperature, and sea ice cover, and also show biases in the free atmosphere.

— Regarding GCMs, the future changes found in our MAR results are fully driven by the lateral boundary conditions. We show that discrepancies in the sign and the magnitude of future changes found between our future simulations are linked to the large-scale dynamics modelled by the forcing GCMs. However, these changes in large-scale dynamics vary from one GCM to another especially for the winter season so that the response of the large-scale dynamics to warmer temperature is highly uncertain and therefore brings high uncertainties in the future trends of cloud cover and global radiation particularly.

The seasonal biases found in the MAR results has brought to light **weaknesses in the MAR physics** causing **uncertainties in the trends** simulated by MAR. The main weaknesses of MAR are related to the parameterization of convection, cloud properties, vegetation seasonality, soil humidity and to aerosol-cloud interactions which are not taken into account in MAR:

— Regarding daily precipitation amount, R and RMSE values are the best in winter when stratiform precipitation dominates. On the contrary, R and RMSE values and even biases (underestimation) are the largest in summer when convective precipitation dominates. This is explained by **limitations of the convective scheme implemented in MAR**, which is the parameterization of Bechtold *et al.* (2001)). Such a parameterization was required because MAR does not explicitly simulate convection. However this kind of parameterization was made for a minimum space grid of 10 km while MAR is used at 5 km. This likely explains why the convective scheme of MAR does not properly simulate convective precipitation events, their amount and their location.

— Although the temporal and spatial variations of temperature are very

well represented by MAR (R values above 0.95), seasonal biases in daily mean temperature were also brought to light. MAR overestimates temperature except in winter. The overestimation of temperature is the largest in summer. These biases are correlated with those found in cloud cover and in global radiation. We found an overestimation of cloud cover in winter which goes along with an underestimation of global radiation. The opposite behaviour is found in summer. We therefore conclude that the biases in temperature and in global radiation are related to an **improper representation of cloud properties and especially of convective clouds** since biases and R values are the worst in summer when convective clouds dominate over stratiform clouds. Furthermore, parts of the biases can result from the fixed aerosol concentration used in the cloud microphysics module of MAR so that the aerosol-cloud interactions are not sensitive to the historical variations of the aerosol load in the troposphere. The modifications implemented in MARv3.8 strengthen this hypothesis. In fact, by calling the convective schemes of MAR twice as often as in MARv3.6, biases in temperature are reduced by 90 %. Moreover, **MAR appears to be sensitive to its surface properties as well.** Vegetation seasonality was also improved in MARv3.8 and contributed to the reduction of temperature and precipitation biases with respect to MARv3.6. Test simulations have also shown that MAR is sensitive to soil humidity variations especially in summer.

These weaknesses in the MAR physics bring uncertainties in the trends computed from the MAR results which are summarized hereafter (Section 7.1.2 and Section 7.1.3). This is especially the case for trends in precipitation amount and extremes as convective precipitation is predicted to increase in a warming climate while MAR does not simulate it properly (Section 4). Potential improvements are further discussed in Section 7.2).

7.1.2 On the current and future evolution of hydroclimatic conditions favouring floods

Regarding hydroclimatic conditions favouring floods, we focused on the Ourthe catchment. In this river, about 70 % of floods occur during the winter months. A distinction is made between winter floods generated by a

rapid melting of the snow pack covering the Ardennes eventually combined with rainfall, and the winter floods generated by abundant rainfall alone.

The current evolution of hydroclimatic conditions favouring floods was first assessed for the 1959–2010 period (**Chapter 3**). Whatever the reanalysis forcing MAR, the results show a significant decrease in the hydroclimatic conditions favouring floods due to snow melting over current climate. The causes of a such a decrease are the significant depletion of the snow accumulation in the Ardennes over this period, the decrease in the number of days with a snow accumulation of at least 5 cm but also a significant shortening of the snow season. The onset of the snow season is delayed over the years while the end of the snow season is shortened. Regarding the hydroclimatic conditions favouring floods due to rainfall alone, the results show no significant long-term trend. In fact, no significant trend was found in the amount of precipitation as well as in the frequency and the intensity of extreme precipitation events in winter, except in coastal regions. However, we found decadal oscillations characterized by drier periods in the 1900s, around 1920, and in the mid 1970s alternating with wetter periods in the 1910–1920s, the 1950–1960s, and in the 1990–2000s along with the decadal variations of the North Atlantic Oscillation (NAO). Therefore, trend and their significance depend on the considered period. Finally, the trend in the total number of days favourable to floods in winter is negative and significant over the studied period as a result of the decrease in hydroclimatic conditions favourable to floods due to snow melting.

By the end of the 21^{st} century, under the RCP8.5 scenario, we expect that the decline of the seasonal snow cover might be counterbalanced and later overpassed by an increase in the amount of precipitation over the Ardennes (Wyard *et al.*, 2017). However, our results do not confirm these hypotheses (**Chapter 4**). Compared to the 1976–2005 mean climate, the 2071–2100 mean climate shows a significant decrease in the snow accumulation, which results in a significant decrease in the hydroclimatic conditions favouring floods due to snow melting. Further, our results show no significant changes in the extreme precipitations events in winter although these trends are subject to uncertainties due to the limitations of the convective scheme of MAR (Section 7.1.1). Therefore, the trends in hydroclimatic conditions favouring floods due to heavy rainfall are not significant. The resulting future changes in the total number of days favourable to floods in winter

remain negative and significant when MAR is forced by MIROC5. Indeed, compared to NorESM1-M, MIROC5 simulates a larger increase in winter temperature because it simulates a stronger snow-albedo feedback and a larger increase in the circulation types which favour mild winters in Belgium (positive NAO index).

7.1.3 On the current and future evolution of global radiation and cloudiness

The current evolution of global radiation ($E_{g\downarrow}$) is well documented. A worldwide dimming was measured between the 1950s and the 1980s. This dimming period was then followed by a partial brightening since the 1980s in Europe and Northern America. These historical variations were caused by complex interactions between aerosols, clouds and radiation. In this context, MAR was useful to confirm the causes of these variations.

The current evolution of $E_{g\downarrow}$ was first assessed for the period 1959–2010 (**Chapter 5**). In addition, we consider two distinct periods in our analysis: 1959–1979 (dimming) and 1980–2010 (brightening). For both the dimming and the brightening periods, our results show that the annual $E_{g\downarrow}$ trends are mainly driven by $E_{g\downarrow}$ changes in spring and summer. They also suggest that, in Belgium, the aerosol-radiation interactions cannot be neglected, especially for the dimming period, because trends in observed total cloud cover are non-significant while trends in observed $E_{g\downarrow}$ are significant. The increase in $E_{g\downarrow}$ observed in Belgium since the 1980s and especially since the 2000s could mainly be explained by a decrease in low and medium cloud cover. This would strengthen the effect of the decrease in aerosol load on $E_{g\downarrow}$ that has been observed in Europe since the 1980s. The origin of these changes in cloudiness is not clear and could result from changes in both aerosol-cloud interactions and atmospheric-circulation. In fact, our results show increasing air temperature, decreasing specific relative humidity at 500 and 700 hPa. On the one hand, the decreasing aerosol load in the atmosphere observed in Belgium from the 1980s to the very beginning of the 2000s could be responsible for the decrease in low and medium cloud cover (during the brightening period) by inhibiting cloud development. Then, the decrease in cloud cover could have generated more $E_{g\downarrow}$ and therefore increased air temperature, which could generate a decrease in relative humidity. On the

other hand, a poleward shift of extratropical storm tracks was also observed during the brightening period and would imply more frequent tropical air advections and more frequent anticyclonic conditions over Western Europe. Such changes would explain the increasing temperature and decreasing specific humidity which then would have generated a decrease in relative humidity and thus inhibited cloud development. However, the origin of these changes in the large-scale circulation could result from the natural oscillations of the climate or from the global warming.

The analysis of the impact of future warmer temperature on the large-scale circulation and on global radiation answers this question (**Chapter 6**). By the end of the the 21^{st} century, under the RCP8.5 scenario, Cattiaux *et al.* (2013) showed that the GCMs of CMIP5, including NorESM1-M and MIROC5, simulate an increase in the blocking regime frequency in summer over Europe. For Belgium, this implies more frequent anticyclonic conditions favouring cloudless conditions. Compared to the 1976–2005 mean climate, the 2071–2100 mean simulated with MAR forced by GCMs future projections exhibits significant decreasing total cloud cover, and particularly decreasing low and medium cloud cover. However, this declining cloud cover leads to contrasting changes in $E_{g\downarrow}$ depending on the GCM used to force MAR. When MAR is forced by MIROC5 (MAR-MIR-rcp85), no significant trend is found in $E_{g\downarrow}$ whatever the season. On the contrary, we find a significant increase in $E_{g\downarrow}$ when MAR is forced by NorESM1-M (MAR-NOR-rcp85) especially in summer. However, these future changes are likely not robust since their magnitude is smaller than their biases over present-day climate with regard to global radiation and total cloud cover. Still, the more frequent blocking conditions are therefore consistent with the significant decline of total, low and medium cloud cover found in our future projections. This also explains why the decrease in total cloud cover and the resulting increase in $E_{g\downarrow}$ are stronger in summer for MAR-NOR-rcp85 than for MAR-MIR-rcp85 as the former simulates a larger increase in the blocking regime than the latter. In addition, as the more frequent blocking regime in summer is simulated by all CMIP5 GCMs, our results suggest that such circulation changes are a consequence of global warming.

7.2 Potential improvements in the MAR physics

The evaluation of the MAR performances over Belgium has brought to light several deficiences in the physics of the model which cause biases and produce uncertainty in the trends computed from the model results. Suggested improvements in the MAR physics are discussed hereafter.

7.2.1 Improvement of convection parameterization in MAR

As summurized in Section 7.1.1, deficiencies in the convective scheme implemented in MAR are responsible for biases in precipitations, temperature, cloud cover, and global radiation. These biases would be partly corrected by improvement of parameterization of convection in MAR.

As a reminder, the parameterization of convection is required in MAR because MAR is a hydrostatic model and convection is a subgrid process (see Section 2.1.1). The convective scheme which is currently implemented in MAR is the Bechtold *et al.* (2001) scheme which is also used in the ERA40 reanalyses. One solution would be to find a more effecient parameterization of convection. Doutreloup *et al.* (2018) implemented five convective schemes in MAR and assessed the sensitivity of MAR, running at 10 km, to these "new" convective schemes. The convective schemes which were implemented in MAR by Doutreloup *et al.* (2018) are: Bechtold coming from the MESO-NH regional model, Betts-Miller-Janjić, Kain-Fritsch, and modified Tiedtke coming from the WRF RCM. The results show that MAR still has significant biases in precipitation whatever the convective scheme used in the simulations and that each convective scheme has its advantages and disadvantages. Given these results, it appears that the deficiencies in the representation of convection in MAR cannot be solved by using other parameterizations of convection either because it remains a parameterization or because the source of the problem is elsewhere such as soil humidity and evapotranspiration which fuel convection. The latter is further discussed in Section 7.2.3.

In order to avoid a parametrizetaion of convection, a solution would be to turn MAR into a non-hydrostatic RCM in order to use finer spatial resolution and therefore explicitly resolve convection. In the literature, the

maximum space-grid for which the hydrostatic equilibrium holds is 10 km while we performed our MAR simulations at a space grid of 5 km. At such a fine resolution, vertical acceleration cannot be neglected so that vertical motion should be explicitly resolved. Ideally, convective cells and orographic precipitations (over the Ardennes for instance) require horizontal spatial resolution finer than 1 km to be properly resolved. In fact, several studies have assessed the added value of non-hydrostatic RCMs using a space grid between 1.5 and 2.8 km. Chan *et al.* (2013) and Kendon *et al.* (2017) have shown that, while some aspects of precipitation are improved (daily precipitation extreme intensity in summer), some are not improved or can even be worse (larger seasonal biases, overestimation of extreme frequency). Over Belgium, Saeed *et al.* (2017) and Vanden Broucke *et al.* (2018) have shown that 2.8 km convection-permitting simulations improve the modelling of the most extreme precipitation events on an hourly time scale, and that they modify the future signals of daily precipitation extremes compared to non-convection-permitting simulations during summer. However employing a finer space grid is computationally expensive and therefore requires either a smaller integration domain and/or a greater computational power.

7.2.2 Improvement of cloud microphysics in MAR

Biases in cloud cover has been highlighted throughout the manuscript as a consequence of deficiencies in the cloud microphysics module of MAR. Part of the biases can result from the fixed aerosol concentration used in the cloud microphysics module of MAR so that the aerosol-cloud interactions are not sensitive to the historical variations of the aerosol load in the troposphere.

Cloud microphysics parameterization is an issue encountered by all climate models as explained in Section 5.3.3. It is indeed quite challenging to represent subgrid processes such as droplet nucleation, droplet growth, collisions between droplets and different hydrometeors, freezing/melting, sedimentation, effect of aerosols, interactions with radiation, etc. Today, the modelisation of aerosol-cloud interactions still remains a challenge (Lebo *et al.*, 2017). Studies have shown that a modelisation of aerosol-cloud interactions using time-varying aerosols allows to reduce biases in RCMs (Zubler *et al.*, 2011a,b). It would therefore be interesting to use time-varying aerosols in the cloud microphysics module of MAR.

7.2.3 Improvement of the surface and soil properties in MAR

The improvement of the surface and soil properties of MAR would partly correct precipitation and temperature biases. Test simulations demonstrate that wetter soils allow to correct the temperature biases and to reduce precipitation biases in summer. Changing the leaf area index (LAI) and green leaf fraction (GLF) data in version 3.8 of MAR has demonstrated the sensitivity of the model to its surface properties.

Currently, MAR is fully coupled to the SISVAT surface scheme (see Section 2.1.1). Although SISVAT is already a complex surface model, several aspects of the model are quite simple such as the hydrology of the soil layers and the vegetation dynamics. For instance, only the first meter of soil is resolved in MAR and there is no horizontal exchange from one grid cell to another. Moreover, soil moisture remains constant over time so that the lowest precipitations are overestimated while the heaviest precipitations are underestimated. Surface properties such as land use, roughness length, LAI, and vegetation seasonality are prescribed from external data and remain constant throughout the years and whatever the atmospheric forcing. Soil moisture-atmosphere (Seneviratne *et al.*, 2010) and vegetation-atmosphere (McPherson, 2007) interactions and feedback are therefore impacted by such a poor representation with consequences on temperature, precipitation and the intensity of droughts and heat waves for instance. In fact, land-atmosphere interactions are known for their positive feedback on droughts and heat waves (Miralles *et al.*, 2018). Therefore, improving the hydrological part and the surface properties dynamics of SISVAT would partly correct biases and strengthen the trends found in MAR. It should be noted that, in a warming climate, it has been demonstrated that these land-atmosphere and vegetation atmosphere feedbacks would affect the climate response to higher greenhouse gas concentration in the atmosphere by modifying the moisture, energy and carbon fluxes between the atmosphere and the surface. (Seneviratne *et al.*, 2006, 2010; Strengers *et al.*, 2010; Ukkola *et al.*, 2018). A good representation of land-atmosphere and vegetation atmosphere feedbacks is therefore required for more robust future projections.

The coupling between MAR and a complex hydrological model might possibly reduce the temperature and precipitation biases by enhancing energy and

water fluxes between the surface/soil and the atmosphere (Larsen *et al.*, 2016; Wagner *et al.*, 2016). Coupling MAR with a dynamic vegetation model might improve the vegetation-climate interactions and feedbacks (Strengers *et al.*, 2010). Finally, coupling MAR to an advanced land-surface model to improve both the soil moisture-atmosphere and vegetation-atmosphere interactions might lead to improvements of several aspects of the simulated climate such as cloud cover, surface temperature, and precipitation (Davin *et al.*, 2011).

7.3 Perpectives

The good results of MAR for the simulation of snow, hydroclimatic conditions and global radiation offer possibilities of further applications. Four of these applications are discussed hereafter.

7.3.1 Using the same methodology for other catchments

Given the satisfying results of MAR for the simulation of seasonal snow cover, winter precipitations, and hydroclimatic conditions favouring floods in the Ourthe catchment, the MAR model can be used to study the long-term evolution of hydroclimatic conditions for other Belgian and European catchments. We would favour rivers with pluvial, nival, nivo-pluvial or pluvio-nival regimes.

7.3.2 Using a hydrological model to simulate river discharge

Besides the reduction of temperature and precipitation biases as explained in Section 7.2.3, the coupling between MAR and a hydrological model would allow to improve flood simulation by taking into account mechanisms which are too simplified or not represented in the regional climate models. In this way, the hydrology of the catchment and the river discharge would be explicitly simulated. This kind of coupling could therefore be used for the study of specific flood events but also for the study of historical and future trends in the river discharge. In addition, this kind of coupling could also be used for discharge and flood forecasts. In fact, the set-up of MAR

developed for this PhD thesis has recently been used to perform 10-day weather forecasts for Belgium (http://climato.be/cms/index.php?climato=fr_previsions-meteo).

A project aiming at coupling MAR to the WOLF 2D hydraulic model to simulate and forecast the discharge of the Ourthe river is currently in progress.

7.3.3 Studying the impact of snow cover changes on the ecosystem of the High Fens

As a reminder, the peculiar climate which characterizes the summits of Belgium, especially in the High Fens plateau, allows the existence of a remarkable ecosystem at this range of altitude (between 500 and 700 m a.s.l.) and latitude (between 49° and 51°N). This ecosystem is characterized by active bogs, wet heathland, alpine and even subarctic animal and plant species such as *Tetrao tetrix*, *Boloria aquilonaris*, *Eriophorum vaginatum*, *Vaccinium oxycoccos* or *Drosera rotundifolia*. Most of these plant species survive to extreme cold temperature in winter thanks to the protective snow cover that acts as a thermal insulator. The high plateaus are therefore subject to nature protection and restoration projects such as LIFE projects mainly funded by the European Union (Plunus *et al.*, 2012). However, as a result of global warming, plant and animal species are predicted to move northward and to higher altitudes which won't be possible for the species which already survive on the summits.

As the evaluation of MAR has shown the ability of the model to simulate the climate of the Ardennes, our MAR future projections could be used to study the impacts of climate changes on the living conditions of the plant and animal species which currently survive on the Ardennes high plateaus. One key variable is the seasonal snow cover because of its protective effect.

7.3.4 Using MAR for the evaluation of photovoltaic system yield

The yield of photovoltaic systems depends on both the air temperature and global radiation. As renewable energies, such as solar power, are a growing part of the energy sector, the supply system could be more vulnerable to $E_{g\downarrow}$

cimate changes. Given the good performances of MAR for the simulation of global radiation and temperature on various timescales, the MAR outputs could be used to study the impact of climate changes on the yield of photovoltaic systems in Belgium as done by Jerez *et al.* (2015) or Wild *et al.* (2015) for other countries.

As MAR can also be used for weather forecasts, yield forecast can also be computed using the MAR outputs.

References

Alexandre J., Erpicum M., and Vernemmen C. (1992) Le Climat. *Géographie de la Belgique*, Denis, J. E., Ed., Crédit Communal, Bruxelles, chap. Le Climat, 88–128.

Alexandri G., Georgoulias A. K., Zanis P., Katragkou E., Tsikerdekis A., Kourtidis K., and Meleti C. (2015) On the ability of RegCM4 regional climate model to simulate surface solar radiation patterns over Europe: an assessment using satellite-based observations. *Atmospheric Chemistry and Physics*, **15 (22)**, 13 195–13 216, doi: 10.5194/acp-15-13195-2015.

Allan R. P., Ringer M. A., Pamment J. A., and Slingo A. (2004) Simulation of the Earth's radiation budget by the European centre for medium-range weather forecasts 40-year reanalysis (ERA40). *Journal of Geophysical Research Atmospheres*, **109 (18)**, 1–13, doi: 10.1029/2004JD004816.

Babst F., Mueller R. W., and Hollmann R. (2008) Verification of NCEP reanalysis shortwave radiation with mesoscale remote sensing data. *IEEE Geosci. Remote Sens. Lett.*, **5**, 34–37, doi: 10.1109/LGRS.2007.907537.

Baguis P., Roulin E., Willems P., and Ntegeka V. (2010) Climate change scenarios for precipitation and potential evapotranspiration over central Belgium. *Theoretical and Applied Climatology*, **99 (3-4)**, 273–286, doi: 10.1007/s00704-009-0146-5.

Bartók B., Wild M., Folini D., Lüthi D., Kotlarski S., Schär C., Vautard R., Jerez S., and Imecs Z. (2017) Projected changes in surface solar radiation in CMIP5 global climate models and in EURO-CORDEX regional climate models for Europe. *Climate Dynamics*, **49 (7-8)**, 2665–2683, doi: 10.1007/s00382-016-3471-2.

Bechtold P., Bazile E., Guichard F., Mascart P., and Richard E. (2001) A mass-flux convection scheme for regional and global models. *Quarterly Journal of the Royal Meteorological Society*, **127 (573)**, 869–886, doi: 10.1002/qj.49712757309.

Bednorz E., Kaczmarek D., and Dudlik P. (2016) Atmospheric conditions governing anomalies of the summer and winter cloudiness in Spitsbergen. *Theoretical and Applied Climatology*, **123 (1-2)**, 1–10, doi: 10.1007/s00704-014-1326-5.

Bell V. A., Kay A. L., Davies H. N., and Jones R. G. (2016) An assessment of the possible impacts of climate change on snow and peak river flows across Britain. *Climatic Change*, **136 (3-4)**, 539–553, doi: 10.1007/s10584-016-1637-x.

Belleflamme A., Fettweis X., and Erpicum M. (2014) Do global warming-induced circulation pattern changes affect temperature and precipitation over Europe during summer? *International Journal of Climatology*, **1499 (June 2014)**, 1484–1499, doi: 10.1002/joc.4070.

Bender F., Ramanathan V., and Tselioudis G. (2012) Changes in extratropical storm track cloudiness 1983–2008: observational support for a˜poleward shift. *International Journal of Climatology*, **38**, 2037–2053, doi: 10.1007/s00382-011-1065-6.

Bengulescu M., Blanc P., Boilley A., and Wald L. (2017) Do modelled or satellite-based estimates of surface solar irradiance accurately describe its temporal variability? *Advances in Science and Research*, **14**, 35–48, doi: 10.5194/asr-14-35-2017.

Beniston M. (2012a) Impacts of climatic change on water and associated economic activities in the Swiss Alps. *Journal of Hydrology*, **412-413**, 291–296, doi: 10.1016/j.jhydrol.2010.06.046.

Beniston M. (2012b) Is snow in the Alps receding or disappearing? *Wiley Interdisciplinary Reviews: Climate Change*, **3 (4)**, 349–358, doi: 10.1002/wcc.179.

Bentsen M., Bethke I., Debernard J. B., Iversen T., Kirkevåg A., Seland Ø., Drange H., Roelandt C., Seierstad I. A., Hoose C., and Kristjánsson J. E. (2013) The Norwegian Earth System Model, NorESM1-M – Part

1: Description and basic evaluation of the physical climate. *Geoscientific Model Development*, **6 (3)**, 687–720, doi: 10.5194/gmd-6-687-2013.

Birsan M.-v. and Dumitrescu A. (2014) Snow variability in Romania in connection to large-scale. *International Journal of Climatology*, **144 (February 2013)**, 134–144, doi: 10.1002/joc.3671.

Brands S., Herrera S., Fernández J., and Gutiérrez J. M. (2013) How well do CMIP5 Earth System Models simulate present climate conditions in Europe and Africa?: A performance comparison for the downscaling community. *Climate Dynamics*, **41 (3-4)**, 803–817, doi: 10.1007/s00382-013-1742-8.

Brasseur O. (2001) Development and Application of a Physical Approach to Estimating Wind Gusts. *Monthly Weather Review*, **129**, 5–25.

Brasseur O., Gallée H., Creutin J.-D., Lebel T., and Marbaix P. (2002) High resolution simulations of precipitation over the Alps with the perspective of coupling to hydrological models 0. *Advance in Global Change Research*, **10**, 75–99.

Brisson E., Demuzere M., Kwakernaak B., and Van Lipzig N. P. M. (2011) Relations between atmospheric circulation and precipitation in Belgium. *Meteorology and Atmospheric Physics*, **111 (1)**, 27–39, doi: 10.1007/s00703-010-0103-y.

Brisson E., Van Weverberg K., Demuzere M., Devis A., Saeed S., Stengel M., and van Lipzig N. P. M. (2016) How well can a convection-permitting climate model reproduce decadal statistics of precipitation, temperature and cloud characteristics? *Climate Dynamics*, **47 (9-10)**, 3043–3061, doi: 10.1007/s00382-016-3012-z.

Brouwers J., Peeters B., Van Steertegem M., van Lipzig N., Wouters H., Beullens J., Demuzere M., Willems P., Ridder K. D., Maiheu B., Troch R. D., Termonia P., Vansteenkiste T., Craninx M., Maetens W., Defloor W., and Cauwenberghs K. (2015) MIRA Climate Report 2015, about observed and future climate changes in Flanders and Belgium. Tech. rep., 147 pages pp. doi: 10.13140/RG.2.1.2055.8809.

Brown R. D. and Petkova N. (2007) Snow cover variability in Bulgarian mountainous regions, 1931–2000. *International Journal of Climatology*, **27 (9)**, 1215–1229, doi: 10.1002/joc.1468.

Brun É., David P., Sudul M., and Brunot G. (1992) A numerical model to simulate snow-cover stratigraphy for operational avalanche forecasting. *Journal of Glaciology*, **38 (128)**, 13–22.

Brun É., Vionnet V., Morin S., Boone A., Martin É., Faroux S., Le Moigne P., and Willemet J.-M. (2012) Le modèle de manteau neigeux Crocus et ses applications. *La Météorologie*, **8 (76)**, 44, doi: 10.4267/2042/47245.

Cassou C. (2008) Intraseasonal interaction between the Madden–Julian Oscillation and the North Atlantic Oscillation. *Nature*, **455 (7212)**, 523–527, doi: 10.1038/nature07286.

Cattiaux J., Douville H., and Peings Y. (2013) European temperatures in CMIP5: origins of present-day biases and future uncertainties. *Climate Dynamics*, **41 (11-12)**, 2889–2907, doi: 10.1007/s00382-013-1731-y.

Cattiaux J., Vautard R., Cassou C., Yiou P., Masson-Delmotte V., and Codron F. (2010) Winter 2010 in Europe: A cold extreme in a warming climate. *Geophysical Research Letters*, **37 (20)**, n/a–n/a, doi: 10.1029/2010GL044613.

Cattiaux J., Yiou P., and Vautard R. (2012) Dynamics of future seasonal temperature trends and extremes in Europe: A multi-model analysis from CMIP3. *Climate Dynamics*, **38 (9-10)**, 1949–1964, doi: 10.1007/s00382-011-1211-1.

Chan S. C., Kendon E. J., Fowler H. J., Blenkinsop S., Ferro C. A. T., and Stephenson D. B. (2013) Does increasing the spatial resolution of a regional climate model improve the simulated daily precipitation? *Climate Dynamics*, 1475–1495, doi: 10.1007/s00382-012-1568-9.

Cherian R., Quaas J., Salzmann M., and Wild M. (2014) Pollution trends over Europe constrain global aerosol forcing as simulated by climate models. *Geophysical Research Letters*, **41 (6)**, 2176–2181, doi: 10.1002/2013GL058715.

Chiacchio M. and Wild M. (2010) Influence of NAO and clouds on long-term seasonal variations of surface solar radiation in Europe. *Journal of Geophysical Research*, **115**, D00D22, doi: 10.1029/2009JD012182.

Compo G. P., Whitaker J. S., Sardeshmukh P. D., Matsui N., Allan R. J., Yin X., Gleason B. E., Vose R. S., Rutledge G., Bessemoulin P., BroNnimann S., Brunet M., Crouthamel R. I., Grant A. N., Groisman P. Y., Jones P. D., Kruk M. C., Kruger A. C., Marshall G. J., Maugeri M., Mok H. Y., Nordli O., Ross T. F., Trigo R. M., Wang X. L., Woodruff S. D., and Worley S. J. (2011) The Twentieth Century Reanalysis Project. *Quarterly Journal of the Royal Meteorological Society*, **137 (654)**, 1–28, doi: 10.1002/qj.776.

Connolley W. M. and Bracegirdle T. J. (2007) An Antarctic assessment of IPCC AR4 coupled models. *Geophysical Research Letters*, **34 (22)**, L22 505, doi: 10.1029/2007GL031648.

Crook J. A., Jones L. A., Forster P. M., and Crook R. (2011) Climate change impacts on future photovoltaic and concentrated solar power energy output. *Energy & Environmental Science*, **4 (9)**, 3101, doi: 10.1039/c1ee01495a.

Davin E. L., Stöckli R., Jaeger E. B., Levis S., and Seneviratne S. I. (2011) COSMO-CLM2: a new version of the COSMO-CLM model coupled to the Community Land Model. *Climate Dynamics*, **37 (9-10)**, 1889–1907, doi: 10.1007/s00382-011-1019-z.

De Bock V., De Backer H., Van Malderen R., Mangold A., and Delcloo A. (2014) Relations between erythemal UV dose, global solar radiation, total ozone column and aerosol optical depth at Uccle, Belgium. *Atmospheric Chemistry and Physics*, **14 (22)**, 12 251–12 270, doi: 10.5194/acp-14-12251-2014.

De Jongh I. L. M., Verhoest N. E. C., and De Troch F. P. (2006) Analysis Of A 105-year time series of precipitation observed at Uccle, Belgium. *International Journal of Climatology*, **26 (14)**, 2023–2039, doi: 10.1002/joc.1352.

De Ridder K. and Gallée H. (1998) Land Surface–Induced Regional Climate Change in Southern Israel. *Journal of applied Meteorology*, **37**, 1470–1485.

De Troch R., Hamdi R., Van de Vyver H., Geleyn J.-F., and Termonia P. (2013) Multiscale Performance of the ALARO-0 Model for Simulating Extreme Summer Precipitation Climatology in Belgium. *Journal of Climate*, **26 (22)**, 8895–8915, doi: 10.1175/JCLI-D-12-00844.1.

de Wit M., Peeters H., Gastaud P., Dewil P., Maeghe K., and Baumgart J. (2007) Floods in the Meuse basin: Event descriptions and an international view on ongoing measures. *International Journal of River Basin Management*, **5 (4)**, 279–292, doi: 10.1080/15715124.2007.9635327.

Dee D. P., Uppala S. M., Simmons a. J., Berrisford P., Poli P., Kobayashi S., Andrae U., Balmaseda M. a., Balsamo G., Bauer P., Bechtold P., Beljaars a. C. M., van de Berg L., Bidlot J., Bormann N., Delsol C., Dragani R., Fuentes M., Geer a. J., Haimberger L., Healy S. B., Hersbach H., Hólm E. V., Isaksen L., Kållberg P., Köhler M., Matricardi M., Mcnally a. P., Monge-Sanz B. M., Morcrette J. J., Park B. K., Peubey C., de Rosnay P., Tavolato C., Thépaut J. N., and Vitart F. (2011) The ERA-Interim reanalysis: Configuration and performance of the data assimilation system. *Quarterly Journal of the Royal Meteorological Society*, **137 (656)**, 553–597, doi: 10.1002/qj.828.

Doutreloup S., Wyard C., Amory C., Kittel C., Erpicum M., and Fettweis X. (2018) Sensitivity to convective schemes on precipitation simulated by the regional climate model MAR over Belgium (1987-2017). *In review in Atmosphere*.

Driessen T. L. a., Hurkmans R. T. W. L., Terink W., Hazenberg P., Torfs P. J. J. F., and Uijlenhoet R. (2010) The hydrological response of the Ourthe catchment to climate change as modelled by the HBV model. *Hydrology and Earth System Sciences Discussions*, **14**, 651–665, doi: 10.5194/hessd-6-7143-2009.

Durand Y., Giraud G., Laternser M., Etchevers P., Mérindol L., and Lesaffre B. (2009) Reanalysis of 47 Years of Climate in the French Alps (1958–2005): Climatology and Trends for Snow Cover. *Journal of Applied Meteorology and Climatology*, **48 (12)**, 2487–2512, doi: 10.1175/2009JAMC1810.1.

Duynkerke P. G. (1988) Application of the E-ϵ turbulence closure model to the neutral and stable atmospheric boundary layer. *Journal of the Atmospheric Sciences*, **45 (5)**, 865–880.

Dyrrdal A. V., Saloranta T., Skaugen T., and Stranden H. B. (2013) Changes in snow depth in Norway during the period 1961–2010. *Hydrology Research*, **44 (1)**, 169, doi: 10.2166/nh.2012.064.

Eastman R. and Warren S. G. (2013) A 39-yr survey of cloud changes from land stations worldwide 1971-2009: Long-term trends, relation to aerosols, and expansion of the tropical belt. *Journal of Climate*, **26 (4)**, 1286–1303, doi: 10.1175/JCLI-D-12-00280.1.

EEA (2012) *Climate change, impacts and vulnerability in Europe 2012*. doi: 10.2800/66071.

EEA (2017) *Climate change, impacts and vulnerability in Europe 2016 - An indicator-based report*, Vol. 46. 419 pp., doi: 10.2800/534806.

Erpicum M., Mabille G., and Vlassis P. (1991) Erpicum_1991(variabilité enneigement belgique).pdf. *Publications de l'Association Internationale de Climatologie*, **4 (Actes du Colloque de Fribourg (CH), du 11 au 13 septembre 1991)**, 267–273.

Erpicum M., Nouri M., and Demoulin A. (2018) The Climate of Belgium and Luxembourg. *Landscapes and landforms of Belgium and Luxembourg*, Demoulin A., Ed., Springer Berlin Heidelberg, Cham, chap. The climat, 35–41, doi: 10.1007/978-3-319-58239-9_3.

Falarz M. G. (2004) Variability and trends in the duration and depth of snow cover in Poland in the 20th century. *International Journal of Climatology*, **24 (13)**, 1713–1727, doi: 10.1002/joc.1093.

Fan T., Zhao C., Dong X., Liu X., Yang X., Zhang F., Shi C., Wang Y., and Wu F. (2018) Quantify contribution of aerosol errors to cloud fraction biases in CMIP5 Atmospheric Model Intercomparison Project simulations. *International Journal of Climatology*, **(February)**, 1–17, doi: 10.1002/joc.5490.

Fettweis X. (2007) Reconstruction of the 1979–2006 Greenland ice sheet surface mass balance using the regional climate model MAR. *The Cryosphere*, **1 (1)**, 21–40, doi: 10.5194/tc-1-21-2007.

Fettweis X., Franco B., Tedesco M., van Angelen J. H., Lenaerts J. T. M., van den Broeke M. R., and Gallée H. (2013) Estimating Greenland ice

sheet surface mass balance contribution to future sea level rise using the regional atmospheric climate model MAR. *The Cryosphere*, **7**, 469–489, doi: doi:10.5194/tc-7-469-2013.

Fettweis X., Wyard C., Doutreloup S., and Belleflamme A. (2017) Noël 2010 En Belgique : Neige En Flandre Et Pluie En Haute-Ardenne. *BSGLg*, **68 (1)**, 97–107.

Flato G., Marotzke J., Abiodun B., Braconnot P., Chou S., Collins W., Cox P., Driouech F., Emori S., Eyring V., Forest C., Gleckler P., Guilyardi E., Jakob C., Kattsov V., Reason C., and Rummukainen M. (2014) *Climate Change 2013 - The Physical Science Basis*. Cambridge University Press, Cambridge, 741–866 pp., doi: 10.1017/CBO9781107415324.

Forster P., Lohmann U., Flanner M., Robock A., and Wyant M. (2013) Clouds and aerosols. *Climate Change 2013 the Physical Science Basis: Working Group I Contribution to the Fifth Assessment Report of the Intergovernmental Panel on Climate Change*, **9781107057**, 571–658, doi: 10.1017/CBO9781107415324.016.

Gaetani M., Huld T., Vignati E., Monforti-Ferrario F., Dosio A., and Raes F. (2014) The near future availability of photovoltaic energy in Europe and Africa in climate-aerosol modeling experiments. *Renewable and Sustainable Energy Reviews*, **38**, 706–716, doi: 10.1016/j.rser.2014.07.041.

Gallée H. (1995) Simulation of the Mesocyclonic Activity in the Ross Sea, Antarctica. *Monthly Weather Review*, **123**, 2051–2069, doi: https://doi.org/10.1175/1520-0493(1995)123<2051:SOTMAI>2.0.CO;2.

Gallée H. and Schayes G. (1994) Development of a Three-Dimensional Meso-Primitive Equation Model: Katabatic Winds Simulation in the Area of Terra Nova Bay, Antarctica. *Monthly Weather Review*, **122 (4)**, 671–685, doi: 10.1175/1520-0493(1994)122<0671:DOATDM>2.0.CO;2.

Gallée H., Trouvilliez A., Agosta C., Genthon C., Favier V., and Naaim-bouvet F. (2013) Transport of Snow by the Wind: A Comparison Between Observations in Adélie Land, Antarctica, and Simulations Made with the Regional Climate Model MAR. *Boundary-Layer Meteorology*, **146 (1)**, 133–147, doi: 10.1007/s10546-012-9764-z.

Gallée H., Moufouma-Okia W., Bechtold P., Brasseur O., Dupays I., Marbaix P., Messager C., Ramel R., and Lebel T. (2004) A high-resolution simulation of a West African rainy season using a regional climate model. *Journal of Geophysical Research*, **109 (D5)**, D05108, doi: 10.1029/2003JD004020.

Gallee H, Guyomarc'h G, and Brun E (2001) Impact Of Snow Drift On The Antarctic Ice Sheet Surface Mass Balance: Possible Sensitivity To Snow-Surface Properties. *Boundary-Layer Meteorology*, **99 (1)**, 1–19(19), doi: 10.1023/A:1018776422809.

Gelaro R., McCarty W., Suárez M. J., Todling R., Molod A., Takacs L., Randles C. A., Darmenov A., Bosilovich M. G., Reichle R., Wargan K., Coy L., Cullather R., Draper C., Akella S., Buchard V., Conaty A., da Silva A. M., Gu W., Kim G. K., Koster R., Lucchesi R., Merkova D., Nielsen J. E., Partyka G., Pawson S., Putman W., Rienecker M., Schubert S. D., Sienkiewicz M., and Zhao B. (2017) The modern-era retrospective analysis for research and applications, version 2 (MERRA-2). *Journal of Climate*, **30 (14)**, 5419–5454, doi: 10.1175/JCLI-D-16-0758.1.

Gellens D. (2000) Trend and Correlation Analysis of k-Day Extreme Precipitationover Belgium. *Theoretical and Applied Climatology*, **66 (1-2)**, 117–129, doi: 10.1007/s007040070037.

Gilgen H., Wild M., and Ohmura A. (1998) Means and trends of shortwave irradiance at the surface estimated from global energy balance archive data. *Journal of Climate*, **11 (8)**, 2042–2061, doi: 10.1175/1520-0442-11.8.2042.

Giorgi F. and Gutowski W. J. (2015) Regional Dynamical Downscaling and the CORDEX Initiative. *Annual Review of Environment and Resources*, **40 (1)**, 467–490, doi: 10.1146/annurev-environ-102014-021217.

Hamdi R. and Van de Vyver H. (2011) Estimating urban heat island effects on near-surface air temperature records of Uccle (Brussels, Belgium): an observational and modeling study. *Advances in Science and Research*, **6 (2007)**, 27–34, doi: 10.5194/asr-6-27-2011.

Hamdi R., Van de Vyver H., De Troch R., and Termonia P. (2014) Assessment of three dynamical urban climate downscaling methods: Brussels's future urban heat island under an A1B emission scenario. *International Journal of Climatology*, **34**, 978–999, doi: 10.1002/joc.3734.

Hamlet A. F. and Lettenmaier D. P. (2007) Effects of 20th century warming and climate variability on flood risk in the western U.S. *Water Resources Research*, **43 (6)**, 1–17, doi: 10.1029/2006WR005099.

Hazenberg P., Leijnse H., Uijlenhoet R., and Delobbe L. (2008) Hydrological modeling of the Ourthe catchment using both radar and raingauge data. *Proceedings of the International Symposium onWeather Radar and Hydrology, Grenoble, France, 10–15 March 2008.*

Hurrell J. W. (1995) Decadal Trends in the North Atlantic Oscillation: Regional Temperatures and Precipitation. *Science*, **269 (5224)**, 676–679, doi: 10.1126/science.269.5224.676.

Iversen T., Bentsen M., Bethke I., Debernard J. B., Kirkevåg A., Seland Ø., Drange H., Kristjánsson J. E., Medhaug I., Sand M., and Seierstad I. A. (2012) The Norwegian Earth System Model, NorESM1-M – Part 2: Climate response and scenario projections. *Geoscientific Model Development Discussions*, **5 (3)**, 2933–2998, doi: 10.5194/gmdd-5-2933-2012.

Jerez S., Tobin I., Vautard R., Montávez J. P., López-Romero J. M., Thais F., Bartok B., Christensen O. B., Colette A., Déqué M., Nikulin G., Kotlarski S., van Meijgaard E., Teichmann C., and Wild M. (2015) The impact of climate change on photovoltaic power generation in Europe. *Nature Communications*, **6 (November 2016)**, 10 014, doi: 10.1038/ncomms10014.

Journée M. and Bertrand C. (2010) Improving the spatio-temporal distribution of surface solar radiation data by merging ground and satellite measurements. *Remote Sensing of Environment*, **114 (11)**, 2692–2704, doi: 10.1016/j.rse.2010.06.010.

Journée M., Delvaux C., and Bertrand C. (2015) Precipitation climate maps of Belgium. *Advances in Science and Research*, **12**, 73–78, doi: 10.5194/asr-12-73-2015.

Joyce A. (2006) The coastal temperature network and ferry route programme: long-term temperature and salinity observations. Tech. Rep. Science Series Data report no. 43, Cefas, 129 pp., Lowestoft.

Judson A. and Doesken N. (2000) Density of Freshly Fallen Snow in the Central Rocky Mountains. *Bulletin of the American Meteorological Society*, **81 (7)**, 1577–1587.

Kalnay E., Kanamitsu M., Kistler R., Collins W., Deaven D., Gandin L., Iredell M., Saha S., White G., Woollen J., Zhu Y., Leetmaa A., Reynolds R., Chelliah M., Ebisuzaki W., Higgins W., Janowiak J., Mo K. C., Ropelewski C., Wang J., Jenne R., and Joseph D. (1996) The NCEP/NCAR 40-Year Reanalysis Project. *Bulletin of the American Meteorological Society*, **77 (3)**, 437–471, doi: 10.1175/1520-0477(1996)077<0437:TNYRP>2.0.CO;2.

Kay A. L. (2016) A review of snow in Britain: The historical picture and future projections. *Progress in Physical Geography*, doi: 10.1177/0309133316650617.

Kendon E. J., Ban N., Roberts N. M., Fowler H. J., Roberts M. J., Chan S. C., Evans J. P., Fosser G., and Wilkinson J. M. (2017) Do convection-permitting regional climate models improve projections of future precipitation change? *Bulletin of the American Meteorological Society*, **98 (1)**, 79–93, doi: 10.1175/BAMS-D-15-0004.1.

Kessler E. (1969) *On the distribution and continuity of water substance in atmospheric circulations*. Met. monog ed., American Meteorological Society, Boston, 84 pp.

Kovats S., Valentini R., Bouwer L. M., Georgopoulou E., Jacob D., Martin E., Rounsevell M., and Soussanna J. F. (2014) Chapter 23: Europe. *Climate Change 2014: Impacts, Adaptation and Vulnerability. IPCC WGII AR5*, **(October 2013)**, 1–93.

Lang C., Fettweis X., and Erpicum M. (2015) Future climate and surface mass balance of Svalbard glaciers in an RCP8.5 climate scenario: a study with the regional climate model MAR forced by MIROC5. *The Cryosphere*, **9 (3)**, 945–956, doi: 10.5194/tc-9-945-2015, URL https://www.the-cryosphere.net/9/945/2015/.

Larsen M. A. D., Christensen J. H., Drews M., Butts M. B., and Refsgaard J. C. (2016) Local control on precipitation in a fully coupled climate-hydrology model. *Scientific Reports*, **6 (1)**, 22 927, doi: 10.1038/srep22927.

Lebo Z. J., Shipway B. J., Fan J., Geresdi I., Hill A., Miltenberger A., Morrison H., Rosenberg P., Varble A., and Xue L. (2017) Challenges for cloud modeling in the context of aerosol - Cloud - Precipitation interactions. *Bulletin of the American Meteorological Society*, **98 (8)**, 1749–1752, doi: 10.1175/BAMS-D-16-0291.1.

Leduc M. and Laprise R. (2009) Regional climate model sensitivity to domain size. *Climate Dynamics*, **32 (6)**, 833–854, doi: 10.1007/s00382-008-0400-z.

Legras B. and Ghil M. (1985) Persistent Anomalies, Blocking and Variations in Atmospheric Predictability. *Journal of the Atmospheric Sciences*, **42 (5)**, 433–471, doi: 10.1175/1520-0469(1985)042<0433:PABAVI>2.0.CO;2.

Levkov L., Rockel B., Kapitza H., and Raschke E. (1992) 3D mesoscale numerical studies of cirrus and stratus clouds by their time and space evolution. *Contributions to atmospheric physics*, **65 (1)**, 35–58.

Liepert B. G. (2002) Observed reductions of surface solar radiation at sites in the United States and worldwide from 1961 to 1990. *Geophysical Research Letters*, **29 (10)**, 61–1–61–4, doi: 10.1029/2002GL014910.

Lin Y.-L., Farley R. D., and Orville H. D. (1983) Bulk Parameterization of the Snow Field in a Cloud Model. *Journal of Climate and Applied Meteorology*, **22 (6)**, 1065–1092, doi: 10.1175/1520-0450(1983)022<1065:BPOTSF>2.0.CO;2.

Lohmann U. and Feichter J. (2005) Global indirect aerosol effects: a review. *Atmospheric Chemistry and Physics*, **5 (3)**, 715–737, doi: 10.5194/acp-5-715-2005.

Łupikasza E. and Lipiński O. (2017) Cloud cover over spitsbergen and its relation to atmospheric circulation (1983-2015). *Geographia Polonica*, **90 (1)**, 21–38, doi: 10.7163/GPol.0076.

Madsen H., Lawrence D., Lang M., Martinkova M., and Kjeldsen T. (2014) Review of trend analysis and climate change projections of extreme precipitation and floods in Europe. *Journal of Hydrology*, **519 (PD)**, 3634–3650, doi: 10.1016/j.jhydrol.2014.11.003.

Markovic M., Jones C. G., Winger K., and Paquin D. (2009) The surface radiation budget over north america: Gridded data assessment and evaluation of regional climate models. *International Journal of Climatology*, **29 (15)**, 2226–2240, doi: 10.1002/joc.1860.

Marmer E., Langmann B., Fagerli H., and Vestreng V. (2007) Direct shortwave radiative forcing of sulfate aerosol over Europe from 1900 to 2000. *Journal of Geophysical Research Atmospheres*, **112 (23)**, 1–16, doi: 10.1029/2006JD008037.

Mateos D., Sanchez-Lorenzo A., Antón M., Cachorro V. E., Calbó J., Costa M. J., Torres B., and Wild M. (2014) Quantifying the respective roles of aerosols and clouds in the strong brightening since the early 2000s over the Iberian Peninsula. *Journal of Geophysical Research: Atmospheres*, **119 (17)**, 10,382–10,393, doi: 10.1002/2014JD022076.

McPherson R. A. (2007) A review of vegetation-atmosphere interactions and their influences on mesoscale phenomena. *Progress in Physical Geography*, **31 (3)**, 261–285, doi: 10.1177/0309133307079055.

McSweeney C. F., Jones R. G., Lee R. W., and Rowell D. P. (2015) Selecting CMIP5 GCMs for downscaling over multiple regions. *Climate Dynamics*, **44 (11-12)**, 3237–3260, doi: 10.1007/s00382-014-2418-8.

Meyers M. P., DeMott P. J., and Cotton W. R. (1992) New Primary Ice-Nucleation Parameterizations in an Explicit Cloud Model. *Journal of Applied Meteorology*, **31 (7)**, 708–721, doi: 10.1175/1520-0450(1992)031<0708:NPINPI>2.0.CO;2.

Miralles D. G., Gentine P., Seneviratne S. I., and Teuling A. J. (2018) Land-atmospheric feedbacks during droughts and heatwaves: state of the science and current challenges. *Annals of the New York Academy of Sciences*, **(June)**, doi: 10.1111/nyas.13912.

Morcrette J.-J. (2002) Assessment of the ECMWF Model Cloudiness and Surface Radiation Fields at the ARM SGP Site. *Monthly Weather Review*, **130 (2)**, 257–277, doi: 10.1175/1520-0493(2002)130<0257:AOTEMC>2.0.CO;2.

Moss R. H., Edmonds J. A., Hibbard K. A., Manning M. R., Rose S. K., van Vuuren D. P., Carter T. R., Emori S., Kainuma M., Kram T., Meehl

G. A., Mitchell J. F. B., Nakicenovic N., Riahi K., Smith S. J., Stouffer R. J., Thomson A. M., Weyant J. P., and Wilbanks T. J. (2010) The next generation of scenarios for climate change research and assessment. *Nature*, **463 (7282)**, 747–756, doi: 10.1038/nature08823.

Murphy J. M., Sexton D. M. H., Barnett D. N., Jones G. S., Webb M. J., Collins M., and Stainforth D. A. (2004) Quantification of modelling uncertainties in a large ensemble of climate change simulations. *Nature*, **430 (7001)**, 768–772, doi: 10.1038/nature02771.

Norris J. R. and Wild M. (2007) Trends in aerosol radiative effects over Europe inferred from observed cloud cover, solar "dimming," and solar "brightening". *Journal of Geophysical Research*, **112 (D8)**, D08 214, doi: 10.1029/2006JD007794.

Ntegeka V. and Willems P. (2008) Trends and multidecadal oscillations in rainfall extremes, based on a more than 100-year time series of 10 min rainfall intensities at Uccle, Belgium. *Water Resources Research*, **44 (7)**, 1–15, doi: 10.1029/2007WR006471.

Panagea I. S., Tsanis I. K., Koutroulis A. G., and Grillakis M. G. (2014) Climate change impact on photovoltaic energy output: The case of Greece. *Advances in Meteorology*, **2014**, doi: 10.1155/2014/264506.

Pašičko R., Branković Č., and Šimić Z. (2012) Assessment of climate change impacts on energy generation from renewable sources in Croatia. *Renewable Energy*, **46**, 224–231, doi: 10.1016/j.renene.2012.03.029.

Pauquet A. and Petit F. (1993) Pauquet_1993(Ourthe,floods frequency).pdf. *Bulletin de la Société Belge d'Etudes Géographiques= Tijdschrift van de Belgische Vereniging voor Aardrijkskundige Studies*, **2**, 361–375.

Peel M. C., Finlayson B. L., and Mcmahon T. A. (2007) Updated world map of the Köppen-Geiger climate classification. *Hydrology and Earth System Sciences Discussions*, **4 (2)**, 439–473, doi: 10.5194/hess-11-1633-2007.

Perez J., Menendez M., Mendez F. J., and Losada I. J. (2014) Evaluating the performance of CMIP3 and CMIP5 global climate models over the north-east Atlantic region. *Climate Dynamics*, **43 (9-10)**, 2663–2680, doi: 10.1007/s00382-014-2078-8.

Pfeifroth U., Bojanowski J. S., Clerbaux N., Manara V., Sanchez-lorenzo A., Walawender J. P., and Hollmann R. (2018) Satellite-based trends of solar radiation and cloud parameters in Europe. *Advances in Science and Research*, **15**, 31–37, doi: 10.5194/asr-15-31-2018.

Philipp A., Della-Marta P. M., Jacobeit J., Fereday D. R., Jones P. D., Moberg . A., and Wanner H. (2007) Long-Term Variability of Daily North Atlantic–European Pressure Patterns since 1850 Classified by Simulated Annealing Clustering. *Journal of Climate*, **20**, 4065–4095, doi: 10.1175/JCLI4175.1.

Pinker R. T., Zhang B., and Dutton E. G. (2005) Do Satellites Detect Trends in Surface Solar Radiation? *Science*, **308 (5723)**, 850–854, doi: 10.1126/science.1103159.

Plunus J., Parkinson D., Frankard P., and Marc D. (2012) Le dernier maillon de la chaîne des tourbières des hauts-plateaux Ardennais: le projet life+ "Restauration des habitats naturals de l'Ardenne Liégeoise". *Forêt Wallonne asbl*, 38–49.

Poli P., Hersbach H., Dee D. P., Berrisford P., Simmons A. J., Vitart F., Laloyaux P., Tan D. G. H., Peubey C., Thépaut J. N., Trémolet Y., Hólm E. V., Bonavita M., Isaksen L., and Fisher M. (2016) ERA-20C: An atmospheric reanalysis of the twentieth century. *Journal of Climate*, **29 (11)**, 4083–4097, doi: 10.1175/JCLI-D-15-0556.1.

Reinhold B. B. and Pierrehumbert R. T. (1982) Dynamics of Weather Regimes: Quasi-Stationary Waves and Blocking. *Monthly Weather Review*, **110 (9)**, 1105–1145, doi: 10.1175/1520-0493(1982)110<1105:DOWRQS>2.0.CO;2.

RMIB (2015) *Vigilance Climatique*. Royal Meteorological Institute of Belgium, Brussels, 86 pp.

RMIB (2018) Atlas climatique de Belgique. URL https://www.meteo.be/meteo/view/fr/16788784-Atlas+Climatique.html, URL https://www.meteo.be/meteo/view/fr/16788784-Atlas+Climatique.html.

Roesch A., Wild M., Ohmura A., Dutton E. G., Long C. N., and Zhang T. (2011) Assessment of BSRN radiation records for the computation of

monthly means. *Atmospheric Measurement Techniques*, **4 (2)**, 339–354, doi: 10.5194/amt-4-339-2011.

Saeed S., Brisson E., Demuzere M., Tabari H., Willems P., and van Lipzig N. P. (2017) Multidecadal convection permitting climate simulations over Belgium: sensitivity of future precipitation extremes. *Atmospheric Science Letters*, **18 (1)**, 29–36, doi: 10.1002/asl.720.

Sanchez-Lorenzo A., Enriquez-Alonso A., Wild M., Trentmann J., Vicente-Serrano S. M., Sanchez-Romero A., Posselt R., and Hakuba M. Z. (2017) Trends in downward surface solar radiation from satellites and ground observations over Europe during 1983–2010. *Remote Sensing of Environment*, **189 (December 2016)**, 108–117, doi: 10.1016/j.rse.2016.11.018.

Sanchez-Lorenzo A., Wild M., Brunetti M., Guijarro J. A., Hakuba M. Z., Calbõ J., Mystakidis S., and Bartok B. (2015) Reassessment and update of long-term trends in downward surface shortwave radiation over Europe (1939-2012). *Journal of Geophysical Research: Atmospheres*, **120 (18)**, 9555–9569, doi: 10.1002/2015JD023321.

Schulz M., Textor C., Kinne S., Balkanski Y., Bauer S., Berntsen T., Berglen T., Boucher O., Dentener F., Guibert S., Isaksen I. S. a., Iversen T., Koch D., Kirkevåg A., Liu X., Montanaro V., Myhre G., Penner J. E., Pitari G., Reddy S., Seland Ø., Stier P., and Takemura T. (2006) Radiative forcing by aerosols as derived from the AeroCom present-day and pre-industrial simulations. *Atmospheric Chemistry and Physics*, **6**, 5225–5246, doi: 10.5194/acpd-6-5095-2006.

Seneviratne S. I., Corti T., Davin E. L., Hirschi M., Jaeger E. B., Lehner I., Orlowsky B., and Teuling A. J. (2010) Investigating soil moisture–climate interactions in a changing climate: A review. *Earth Science Reviews*, **99 (3-4)**, 125–161, doi: 10.1016/j.earscirev.2010.02.004.

Seneviratne S. I., Lüthi D., Litschi M., and Schär C. (2006) Land-atmosphere coupling and climate change in Europe. *Nature*, **443 (7108)**, 205–209, doi: 10.1038/nature05095.

Sherman K., Belkin I., Reilly J. O., and Hyde K. (2007) Variability of Large Marine Ecosystems in response to global climate change. ICES CM 2007/D:20. *CM Documents-ICES*, **D: 20**, 46.

Skaugen T., Stranden H. B., and Saloranta T. (2012) Trends in snow water equivalent in Norway (1931–2009). *Hydrology Research*, **43 (4)**, 489, doi: 10.2166/nh.2012.109.

Sliggers J. and Kakebeeke W., (Eds.) (2004) *Clearing the Air: 25 Years of the Convention on LongRange Transboundary Air Pollution*. The United Nations, New York and Geneva.

Slonosky V. C. and Yiou P. (2001) The North Atlantic Oscillation and its relationship with near surface temperature. *Geophysical Research Letters*, **28 (5)**, 807–810, doi: 10.1029/2000GL012063.

Snedecor G. and Cochran W. (1967) *Statistical Methods, 6th edn.* Iowa state ed., Ames, Iowa, USA.

Sneyers R. (1965) La statistique de l'enneigement du sol en Belgique. *Archiv für Meteorologie, Geophysik und Bioklimatologie, Serie B*, **13 (4)**, 503–520.

Sneyers R. (1967a) L'épaisseur maximale de la couche de neige en Belgique. *Internationale Tagung für alpine Meteorologie in Brig und Zermatt, 14–17 September 1966*, Institut Suisse de Météorologie, Zürich, Switzerland, 124–131.

Sneyers R. (1967b) *Les propriétés statistiques de l'enneigement du sol en Belgique*. Royal Meteorological Institure of Belgium, Brussels.

Sneyers R., Vandiepenbeeck M., and Vanlierde R. (1989) Principal component analysis of belgian rainfall. *Theor. Appl. Climatol.*, **39 (4)**, 199–204.

Stanhill G. and Cohen S. (2008) Solar radiation changes in Japan during the 20th century: Evidence from sunshine duration measurementes. *Journal of the Meteorological Society of Japan*, **86 (1)**, 57–67, doi: 10.1175/JCLI3354.1.

Stewart I. T. (2009) Changes in snowpack and snowmelt runoff for key mountain regions. *Hydrological Processes*, **23 (1)**, 78–94, doi: 10.1002/hyp.7128.

Strengers B. J., Müller C., Schaeffer M., Haarsma R. J., Severijns C., Gerten D., Schaphoff S., Van Den Houdt R., and Oostenrijk R. (2010) Assessing 20th century climate-vegetation feedbacks of land-use change

and natural vegetation dynamics in a fully coupled vegetation-climate model. *International Journal of Climatology*, **30 (April)**, 2055–2065, doi: 10.1002/joc.2132.

Tabari H., Taye M. T., and Willems P. (2015) Water availability change in central Belgium for the late 21st century. *Global and Planetary Change*, **131**, 115–123, doi: 10.1016/j.gloplacha.2015.05.012.

Taylor K. E., Stouffer R. J., and Meehl G. A. (2012) An Overview of CMIP5 and the Experiment Design An Overview of CMIP5 and the Experiment Design. *Bulletin of the American Meteorological Society*, **93 (4)**, 485–498.

Tegen I., Hollrig P., Chin M., Fung I., Jacob D., and Penner J. (1997) Contribution of different aerosol species to the global aerosol extinction optical thickness: Estimates from model results. *Journal of Geophysical Research*, **102 (97)**, 23 895, doi: 10.1029/97JD01864.

Termonia P., Schaeybroeck B. V., Cruz L. D., Troch R. D., Caluwaerts S., Giot O., Hamdi R., Willems P., Tabari H., Uytven E. V., Hosseinzadehtalaei P., Lipzig N. V., Wouters H., Broucke S. V., Ypersele J.-p. V., Marbaix P., Villanueva-birriel C., Fettweis X., Wyard C., Ridder K. D., Gobin A., Lauwaet D., Stavrakou T., Bauwens M., Luyten P., Eynde D. V. D., and Pottiaux E. (2018) The CORDEX.be initiative as a foundation for climate services in Belgium. *Climate Services*, **7**, 49–61, doi: https://doi.org/10.1016/j.cliser.2018.05.001.

Träger-Chatterjee C., Müller R. W., Trentmann J., and Bendix J. (2010) Evaluation of ERA-40 and ERA-interim re-analysis incoming surface shortwave radiation datasets with mesoscale remote sensing data. *Meteorologische Zeitschrift*, **19 (6)**, 631–640, doi: 10.1127/0941-2948/2010/0466.

Twomey S. (1977) The Influence of Pollution on the Shortwave Albedo of Clouds. *Journal of the Atmospheric Sciences*, **34 (7)**, 1149–1152, doi: 10.1175/1520-0469(1977)034<1149:TIOPOT>2.0.CO;2.

Ukkola A. M., Pitman A. J., Donat M. G., De Kauwe M. G., and Angélil O. (2018) Evaluating the Contribution of Land-Atmosphere Coupling to Heat Extremes in CMIP5 Models. *Geophysical Research Letters*, **45 (17)**, 9003–9012, doi: 10.1029/2018GL079102.

Uppala S. M., Kllberg P. W., Simmons A. J., Andrae U., Bechtold V. D. C., Fiorino M., Gibson J. K., Haseler J., Hernandez A., Kelly G. A., Li X., Onogi K., Saarinen S., Sokka N., Allan R. P., Andersson E., Arpe K., Balmaseda M. A., Beljaars A. C. M., Berg L. V. D., Bidlot J., Bormann N., Caires S., Chevallier F., Dethof A., Dragosavac M., Fisher M., Fuentes M., Hagemann S., Hólm E., Hoskins B. J., Isaksen L., Janssen P. A. E. M., Jenne R., Mcnally A. P., Mahfouf J.-F., Morcrette J.-J., Rayner N. A., Saunders R. W., Simon P., Sterl A., Trenberth K. E., Untch A., Vasiljevic D., Viterbo P., and Woollen J. (2005) The ERA-40 re-analysis. *Quarterly Journal of the Royal Meteorological Society*, **131 (612)**, 2961–3012, doi: 10.1256/qj.04.176.

Vaes G, Willems P B. J. (2002) 100 years of Belgian rainfall: are there trends? *Water Sci. Technol.*, **45 (2)**, 55–61.

Valt M. and Cianfarra P. (2010) Recent snow cover variability in the Italian Alps. *Cold Regions Science and Technology*, **64 (2)**, 146–157, doi: 10.1016/j.coldregions.2010.08.008.

Van de Vyver H. (2012) Evolution of extreme temperatures in Belgium since the 1950s. *Theoretical and Applied Climatology*, **107 (1-2)**, 113–129, doi: 10.1007/s00704-011-0456-2.

Van Meijgaard E. (1995) Excessive rainfall over the belgian ardennes in december 1993: evaluation of model predictions. *Meteorol. App.*, **2 (1)**, 39–52.

Van Uytven E. and Willems P. (2018) Greenhouse gas scenario sensitivity and uncertainties in precipitation projections for central Belgium. *Journal of Hydrology*, **558**, 9–19, doi: 10.1016/j.jhydrol.2018.01.018.

Vanden Broucke S., Wouters H., Demuzere M., and van Lipzig N. P. M. (2018) The influence of convection-permitting regional climate modeling on future projections of extreme precipitation: dependency on topography and timescale. *Climate Dynamics*, **0 (0)**, 0, doi: 10.1007/s00382-018-4454-2.

Vaughan D., Comiso J., Allison I., Carrasco J., Kaser G., Kwok R., Mote P., Murray T., Paul F., Ren J., Rignot E., Solomina O., Steffen K., and Zhang T. (2013) Observations: Cryosphere. *Climate Change 2013: The Physical Science Basis. Contribution of Working Group I to the Fifth Assessment Report of the Intergovernmental Panel on Climate Change.*

Vautard R. (1990) Multiple Weather Regimes over the North Atlantic: Analysis of Precursors and Successors. *Monthly Weather Review*, **118 (10)**, 2056–2081, doi: 10.1175/1520-0493(1990)118<2056:MWROTN>2.0.CO;2.

Vormoor K., Lawrence D., Schlichting L., Wilson D., and Wong W. K. (2016) Evidence for changes in the magnitude and frequency of observed rainfall vs. snowmelt driven floods in Norway. *JOURNAL OF HYDROLOGY*, **538**, 33–48, doi: 10.1016/j.jhydrol.2016.03.066.

Wagner S., Fersch B., Yuan F., YU Z., and Kunstmann H. (2016) Fully coupled atmospheric-hydrologicalmodeling at regional and long-termscales: Development, application, and analysis of WRF-HMS. *Water Resources Research*, **52**, 3187–3211, doi: 10.1002/2015WR018185.Received.

Wang Y. and Zhao C. (2017) Can MODIS cloud fraction fully represent the diurnal and seasonal variations at DOE ARM SGP and Manus sites? *Journal of Geophysical Research*, **122 (1)**, 329–343, doi: 10.1002/2016JD025954.

Watanabe M., Suzuki T., O'ishi R., Komuro Y., Watanabe S., Emori S., Takemura T., Chikira M., Ogura T., Sekiguchi M., Takata K., Yamazaki D., Yokohata T., Nozawa T., Hasumi H., Tatebe H., and Kimoto M. (2010) Improved Climate Simulation by MIROC5: Mean States, Variability, and Climate Sensitivity. *Journal of Climate*, **23 (23)**, 6312–6335, doi: 10.1175/2010JCLI3679.1.

Wild M. (2009) Global dimming and brightening: A review. *Journal of Geophysical Research*, **114 (November 2008)**, D00D16, doi: 10.1029/2008JD011470.

Wild M. (2012) Enlightening global dimming and brightening. *Bulletin of the American Meteorological Society*, **93 (1)**, 27–37, doi: 10.1175/BAMS-D-11-00074.1.

Wild M., Folini D., Henschel F., Fischer N., and Müller B. (2015) Projections of long-term changes in solar radiation based on CMIP5 climate models and their influence on energy yields of photovoltaic systems. *Solar Energy*, **116**, 12–24, doi: 10.1016/j.solener.2015.03.039.

Wild M. and Liepert B. (2010) The Earth radiation balance as driver of the global hydrological cycle. *Environmental Research Letters*, **5 (2)**, 1–8, doi: 10.1088/1748-9326/5/2/025203.

Wild M., Ohmura A., and Makowski K. (2007) Impact of global dimming and brightening on global warming. *Geophysical Research Letters*, **34 (4)**, L04 702, doi: 10.1029/2006GL028031.

Wild M., Trüssel B., Ohmura A., Long C. N., König-Langlo G., Dutton E. G., and Tsvetkov A. (2009) Global dimming and brightening: An update beyond 2000. *Journal of Geophysical Research Atmospheres*, **114 (10)**, 1–14, doi: 10.1029/2008JD011382.

Wild M., Gilgen H., Roesch A., Ohmura A., Long C. N., Dutton E. G., Forgan B., Kallis A., Russak V., and Tsvetkov A. (2005) From Dimming to Brightening: Decadal Changes in Solar Radiation at Earth's Surface. *Science*, **308 (5723)**, 847–850, doi: 10.1126/science.1103215.

Willems P. (2013a) Adjustment of extreme rainfall statistics accounting for multidecadal climate oscillations. *Journal of Hydrology*, **490**, 126–133, doi: 10.1016/j.jhydrol.2013.03.034.

Willems P. (2013b) Multidecadal oscillatory behaviour of rainfall extremes in Europe. *Climate Change*, **120**, 931–944, doi: 10.1007/s10584-013-0837-x.

Willems P. (2013c) Revision of urban drainage design rules after assessment of climate change impacts on precipitation extremes at Uccle, Belgium. *Journal of Hydrology*, **496**, 166–177, doi: 10.1016/j.jhydrol.2013.05.037.

Wouters H., Demuzere M., Ridder K. D., and van Lipzig N. P. (2015) The impact of impervious water-storage parametrization on urban climate modelling. *Urban Climate*, **11**, 24–50, doi: 10.1016/j.uclim.2014.11.005.

Wyard C., Doutreloup S., Belleflamme A., Wild M., and Fettweis X. (2018) Global Radiative Flux and Cloudiness Variability for the Period 1959–2010 in Belgium: A Comparison between Reanalyses and the Regional Climate Model MAR. *Atmosphere*, **9 (7)**, 262, doi: 10.3390/atmos9070262.

Wyard C., Scholzen C., Fettweis X., Van Campenhout J., and François L. (2017) Decrease in climatic conditions favouring floods in the south-east of Belgium over 1959-2010 using the regional climate model MAR.

International Journal of Climatology, **37 (5)**, 2782–2796, doi: 10.1002/joc.4879.

Yang X., Zhao C., Guo J., and Wang Y. (2016a) Intensification of aerosol pollution associated with its feedback with surface solar radiation and winds in beijing. *Journal of Geophysical Research*, **121 (8)**, 4093–4099, doi: 10.1002/2015JD024645.

Yang X., Zhao C., Zhou L., Wang Y., and Liu X. (2016b) Distinct impact of different types of aerosols on surface solar radiation in China. *Journal of Geophysical Research*, **121 (11)**, 6459–6471, doi: 10.1002/2016JD024938.

Zamani S., Gobin A., Van de Vyver H., and Gerlo J. (2016) Atmospheric drought in Belgium - statistical analysis of precipitation deficit. *International Journal of Climatology*, **36 (8)**, 3056–3071, doi: 10.1002/joc.4536.

Zhang M. H., Lin W. Y., Klein S. A., Bacmeister J. T., Bony S., Cederwall R. T., Del Genio A. D., Hack J. J., Loeb N. G., Lohmann U., Minnis P., Musat I., Pincus R., Stier P., Suarez M. J., Webb M. J., Wu J. B., Xie S. C., Yao M. S., and Zhang J. H. (2005) Comparing clouds and their seasonal variations in 10 atmospheric general circulation models with satellite measurements. *Journal of Geophysical Research D: Atmospheres*, **110 (15)**, 1–18, doi: 10.1029/2004JD005021.

Zhang X., Liang S., Wang G., Yao Y., Jiang B., and Cheng J. (2016) Evaluation of the reanalysis surface incident shortwave radiation products from NCEP, ECMWF, GSFC, and JMA using satellite and surface observations. *Remote Sensing*, **8 (3)**, doi: 10.3390/rs8030225.

Zhang X., Liang S., Wild M., and Jiang B. (2015) Analysis of surface incident shortwave radiation from four satellite products. *Remote Sensing of Environment*, **165**, 186–202, doi: 10.1016/j.rse.2015.05.015.

Zubler E. M., Folini D., Lohmann U., Lüthi D., Muhlbauer A., Pousse-Nottelmann S., Schär C., and Wild M. (2011a) Implementation and evaluation of aerosol and cloud microphysics in a regional climate model. *Journal of Geophysical Research Atmospheres*, **116 (2)**, 1–18, doi: 10.1029/2010JD014572.

Zubler E. M., Folini D., Lohmann U., Lüthi D., Schär C., and Wild M. (2011b) Simulation of dimming and brightening in Europe from 1958

to 2001 using a regional climate model. *Journal of Geophysical Research Atmospheres*, **116 (18)**, 1–13, doi: 10.1029/2010JD015396.

Appendix

A Additional figures for Chapter 3

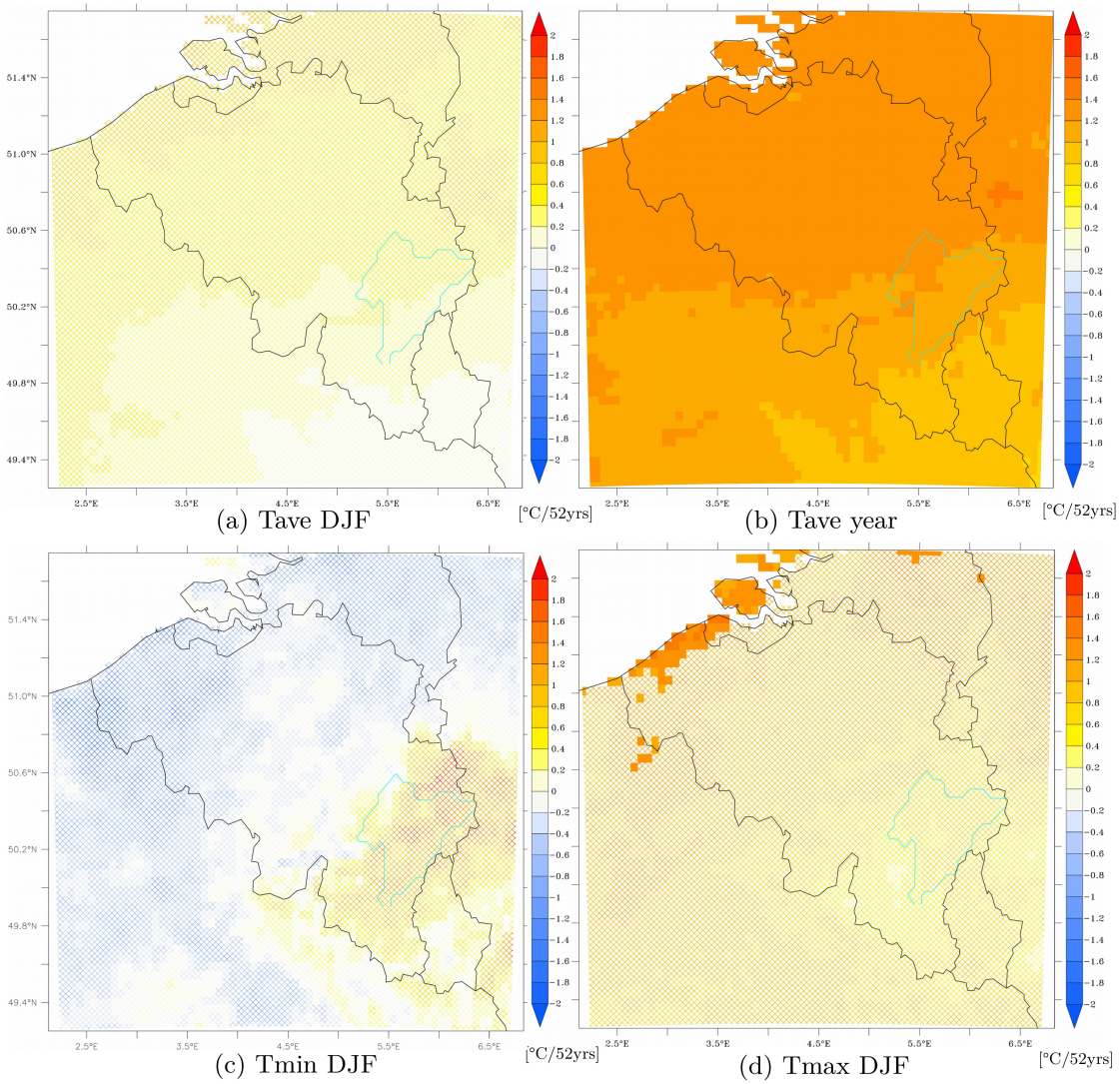

Figure A.1: Trends computed from MAR-NCEP1 over 1959–2010 in **(a)** the mean temperature in winter (DJF), **(b)** the yearly mean temperature, **(c)** the extreme (P5) minimum temperature in winter, and **(d)** the extreme (P95) maximum temperature in winter. Filled pixels indicate the places where trends are statistically significant.

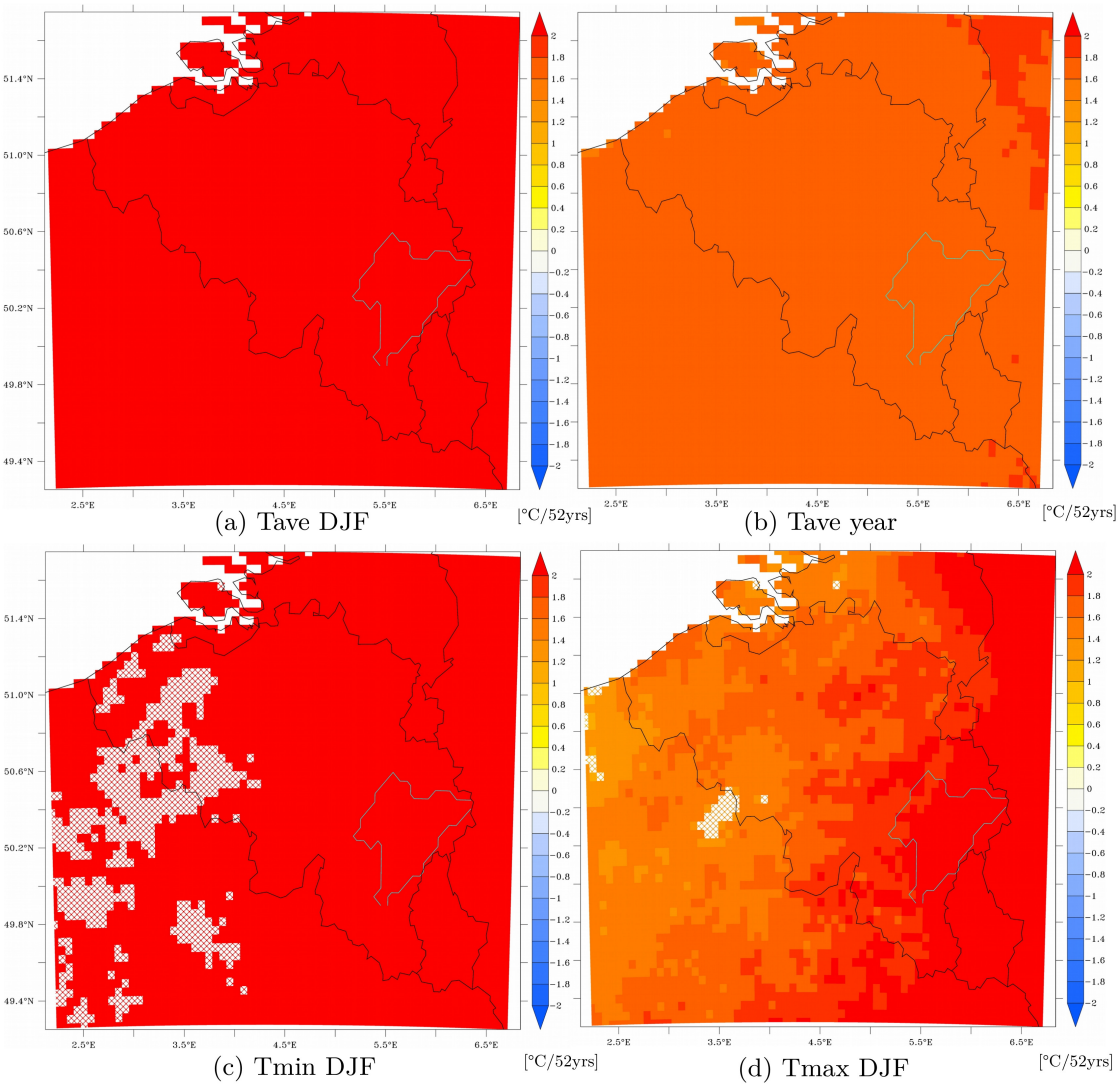

Figure A.2: Trends computed from MAR-ERA-20C over 1959–2010 in **(a)** the mean temperature in winter (DJF), **(b)** the yearly mean temperature, **(c)** the extreme (P5) minimum temperature in winter, and **(d)** the extreme (P95) maximum temperature in winter. Filled pixels indicate the places where trends are statistically significant.

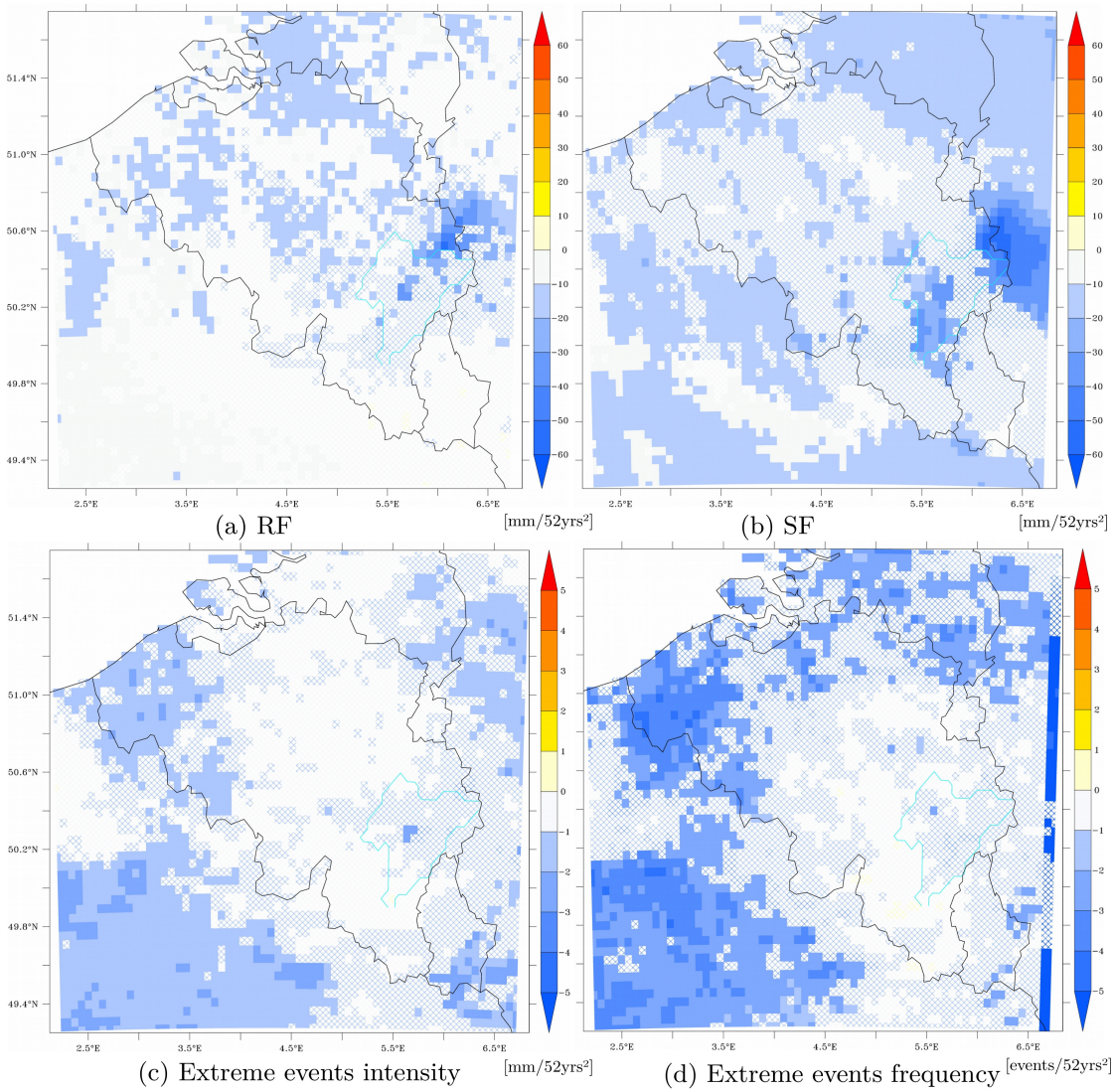

Figure A.3: Trends computed from MAR-NCEP1 over 1959–2010 in **(a)** the rainfall amount (RF) in winter (DJF), **(b)** the snowfall amount (SF) in winter, **(c)** the intensity of extreme precipitation events in winter (trend in the 95^{th} percentile of daily precipitation amount in winter), and **(d)** the frequency of extreme precipitation events in winter (trend in the number of days in winter with daily precipitation amount larger than its 95^{th} percentile computed over 1961–1990). Filled pixels indicate the places where the trends are statistically significant

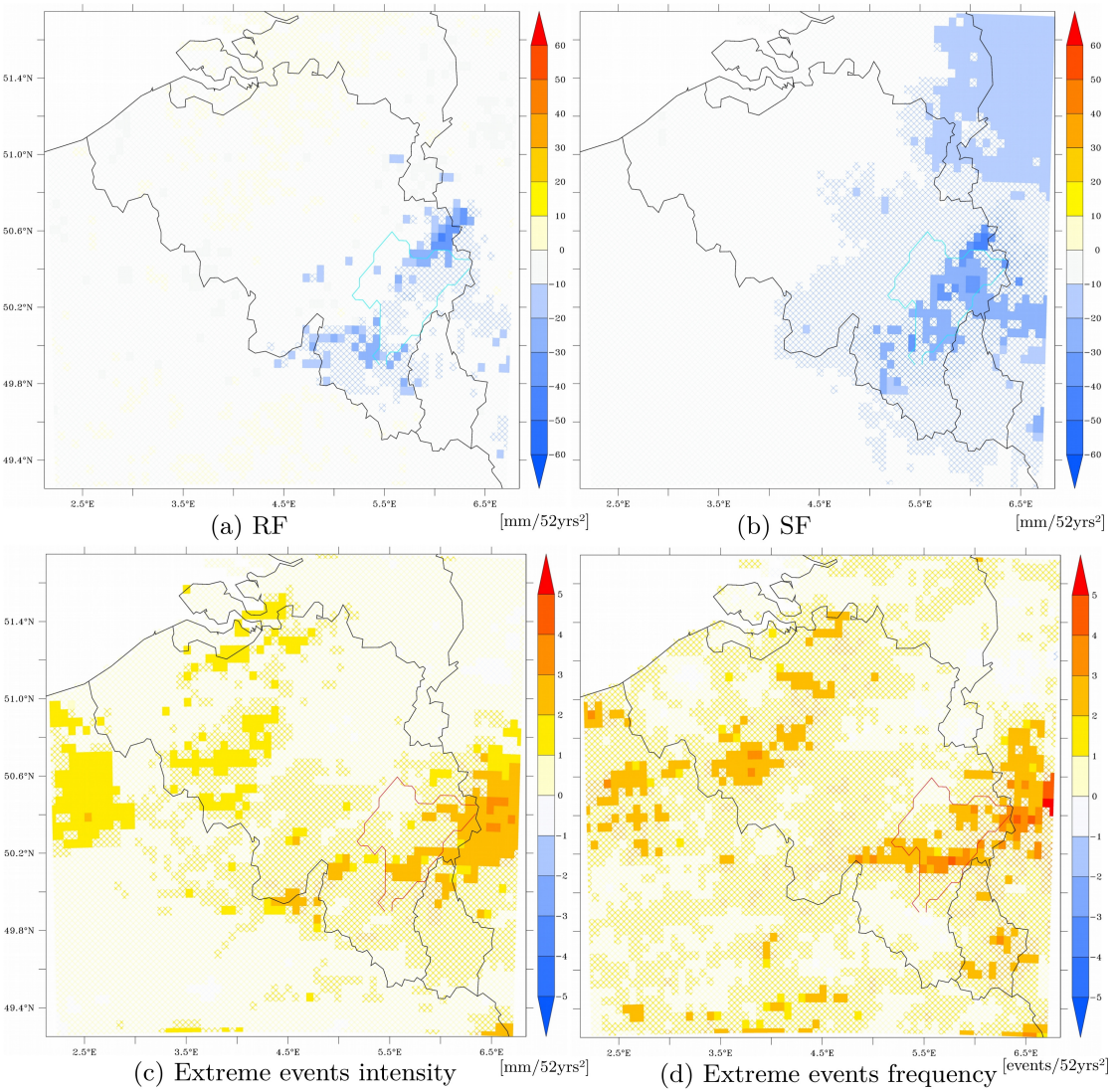

Figure A.4: Trends computed from MAR-ERA-20C over 1959–2010 in **(a)** the rainfall amount (RF) in winter (DJF), **(b)** the snowfall amount (SF) in winter, **(c)** the intensity of extreme precipitation events in winter (trend in the 95^{th} percentile of daily precipitation amount in winter), and **(d)** the frequency of extreme precipitation events in winter (trend in the number of days in winter with daily precipitation amount larger than its 95^{th} percentile computed over 1961–1990). Filled pixels indicate the places where the trends are statistically significant

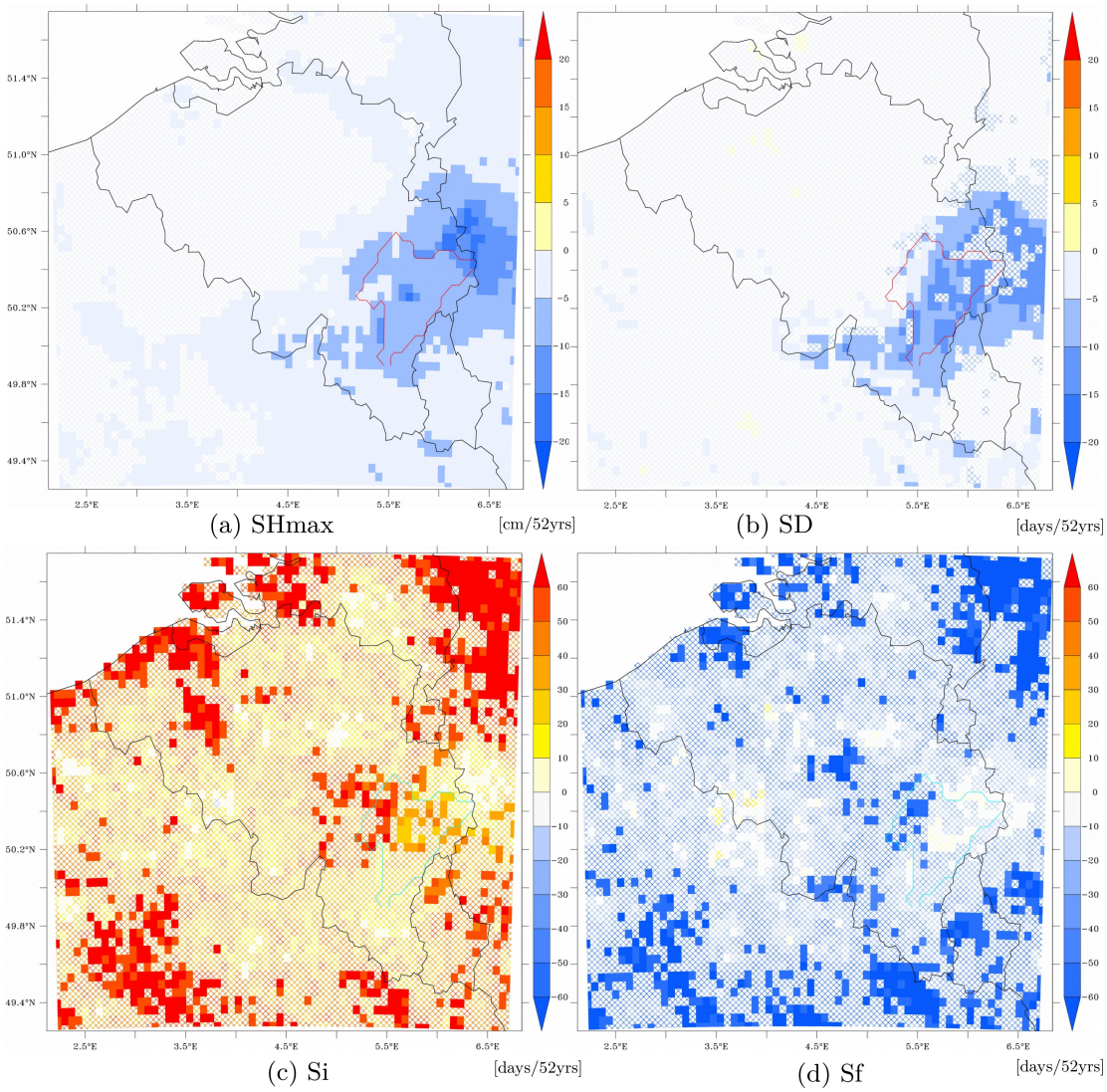

Figure A.5: Trends computed from MAR-NCEP1 over 1959–2010 in **(a)** the maximum daily snow depth (SD) in winter (DJF), **(b)** the number of days per winter with a snow cover of at least 5 cm of thickness (SD), **(c)** the first day of the year with a snow depth of at least 1cm (Si), and **(d)** the last day of the year with snow depth of at least 1 cm (Sf).

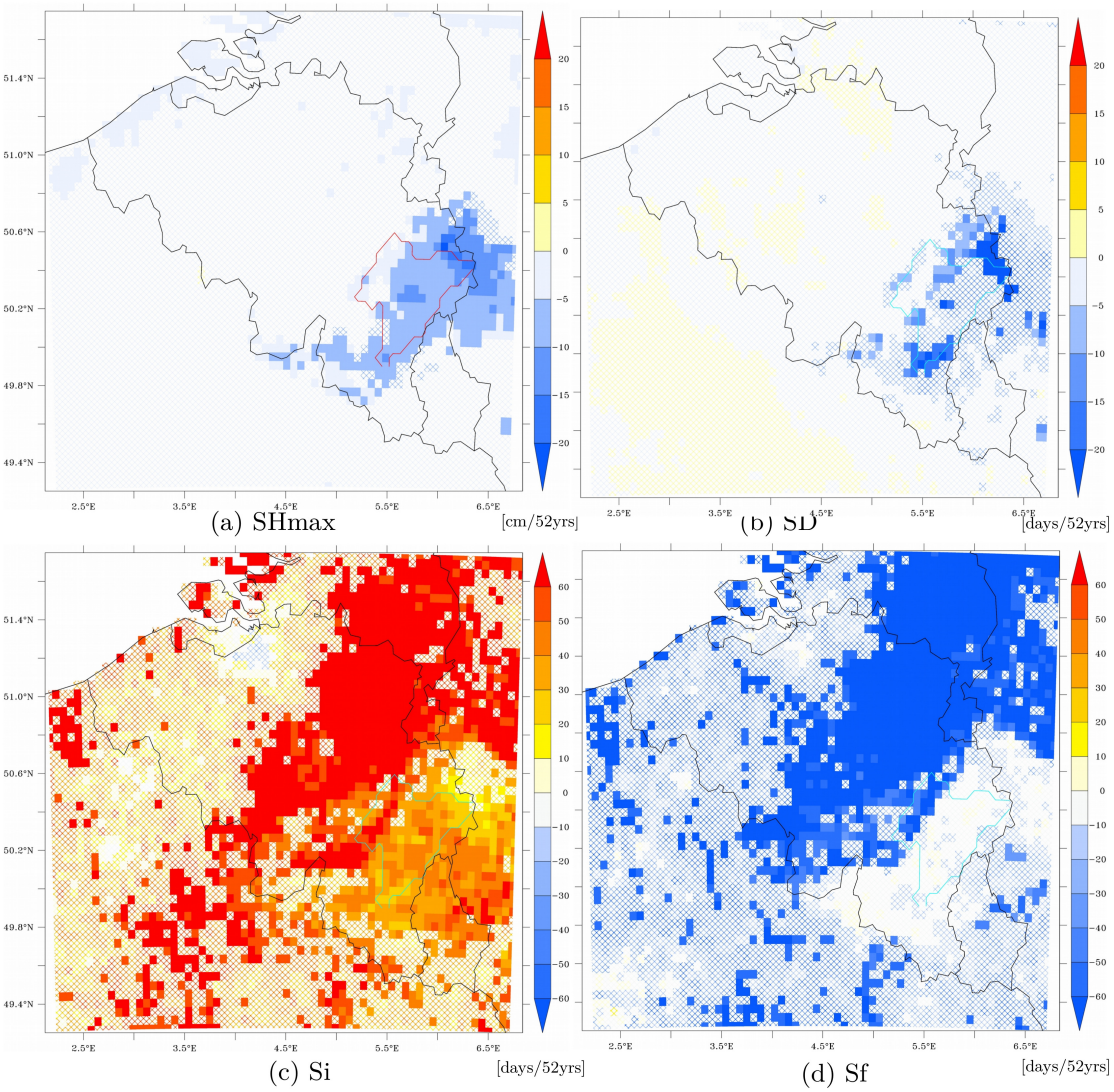

Figure A.6: Trends computed from MAR-ERA-20C over 1959–2010 in **(a)** the maximum daily snow depth (SD) in winter (DJF), **(b)** the number of days per winter with a snow cover of at least 5 cm of thickness (SD), **(c)** the first day of the year with a snow depth of at least 1cm (Si), and **(d)** the last day of the year with snow depth of at least 1 cm (Sf).

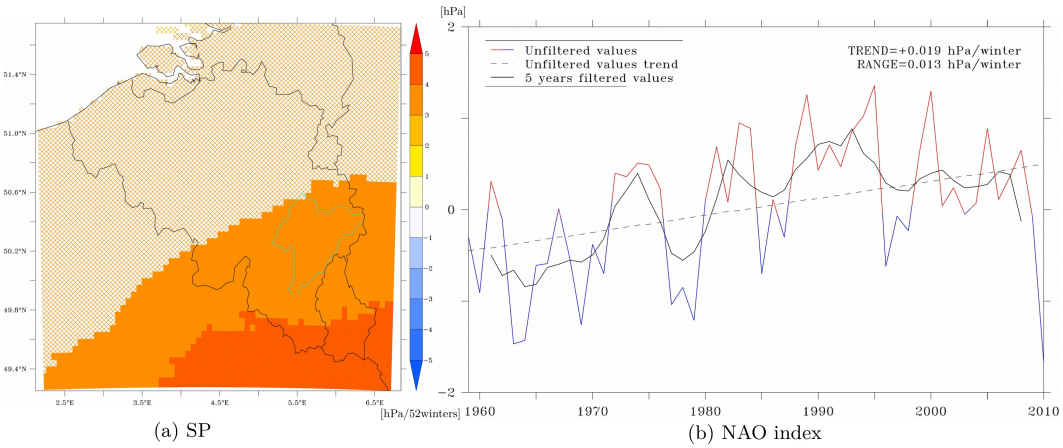

(a) SP (b) NAO index

Figure A.7: Trends over 1959–2010 of **(a)** the mean surface pressure in winter (DJF) computed from MAR-NCEP1, and **(b)** the mean NAO index recorded in winter. Filled pixels indicate the places where the trends are statistically significant

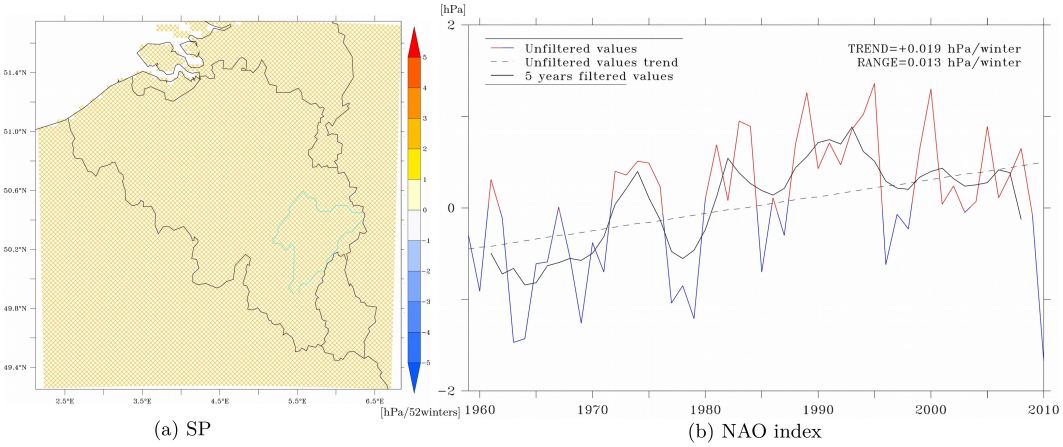

(a) SP (b) NAO index

Figure A.8: Trends over 1959–2010 of **(a)** the mean surface pressure in winter (DJF) computed from MAR-ERA-20C, and **(b)** the mean NAO index recorded in winter. Filled pixels indicate the places where the trends are statistically significant

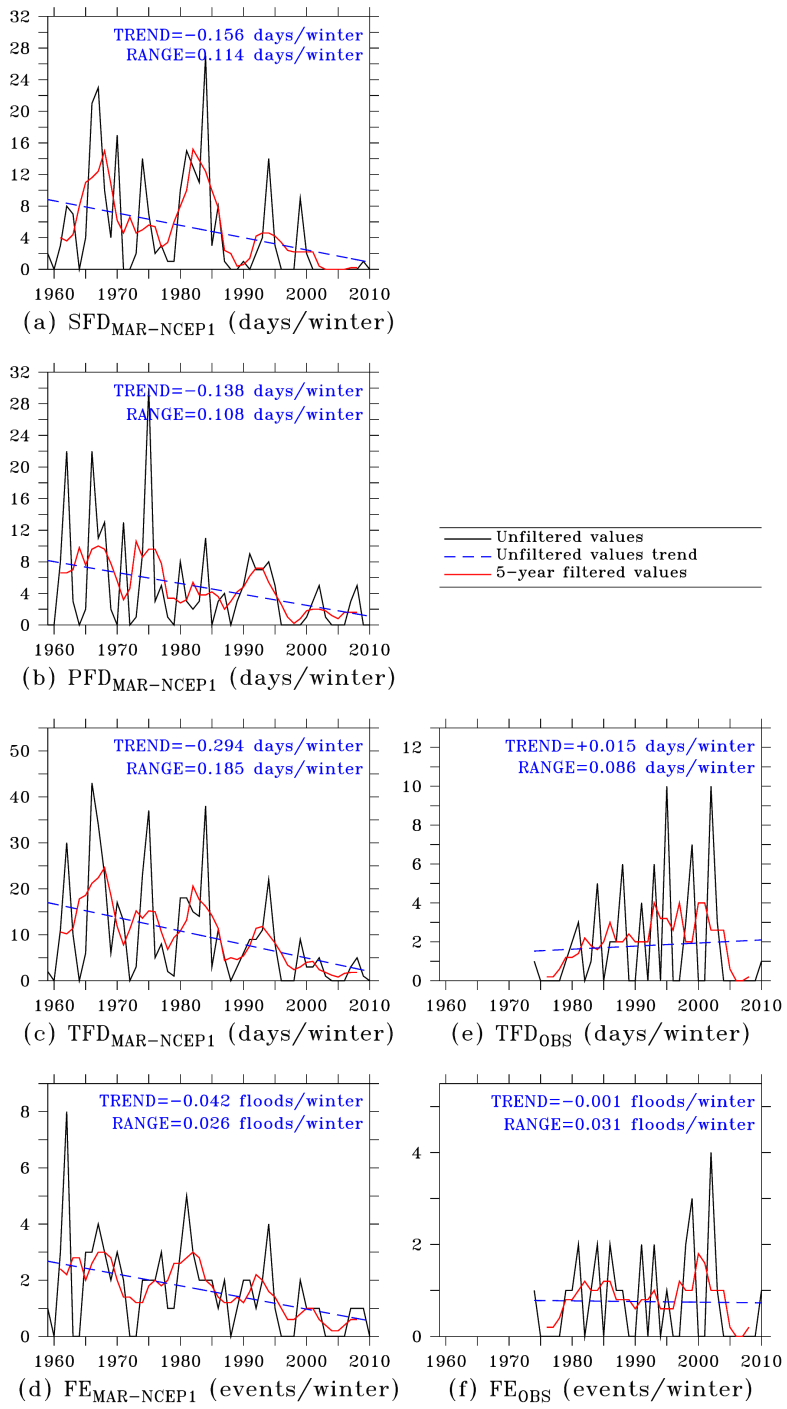

Figure A.9: Unfiltered values, 5-year filtered values and trends computed fromMAR-ERA over 1959–2010 of **(a)** the number of days per winter (DJF) favourable to floods due to snowpack melting combined with rainfall events (SFD$_{MAR-NCEP1}$), **(b)** the number of days per winter favourable to floods due to rainfall events alone (PFD$_{MAR-NCEP1}$), **(c)** the total number of days per winter favourable to floods (TFD$_{MAR-NCEP1}$), **(d)** the number of flood events favourable to floods per winter (FE$_{MAR-NCEP1}$). Unfiltered values, 5-year filtered values and trends computed from observations in Sauheid are also displayed with **(e)** the number of observed flood days per winter (TFD$_{OBS}$), and **(f)** the number of observed flood events per winter (FE$_{OBS}$).

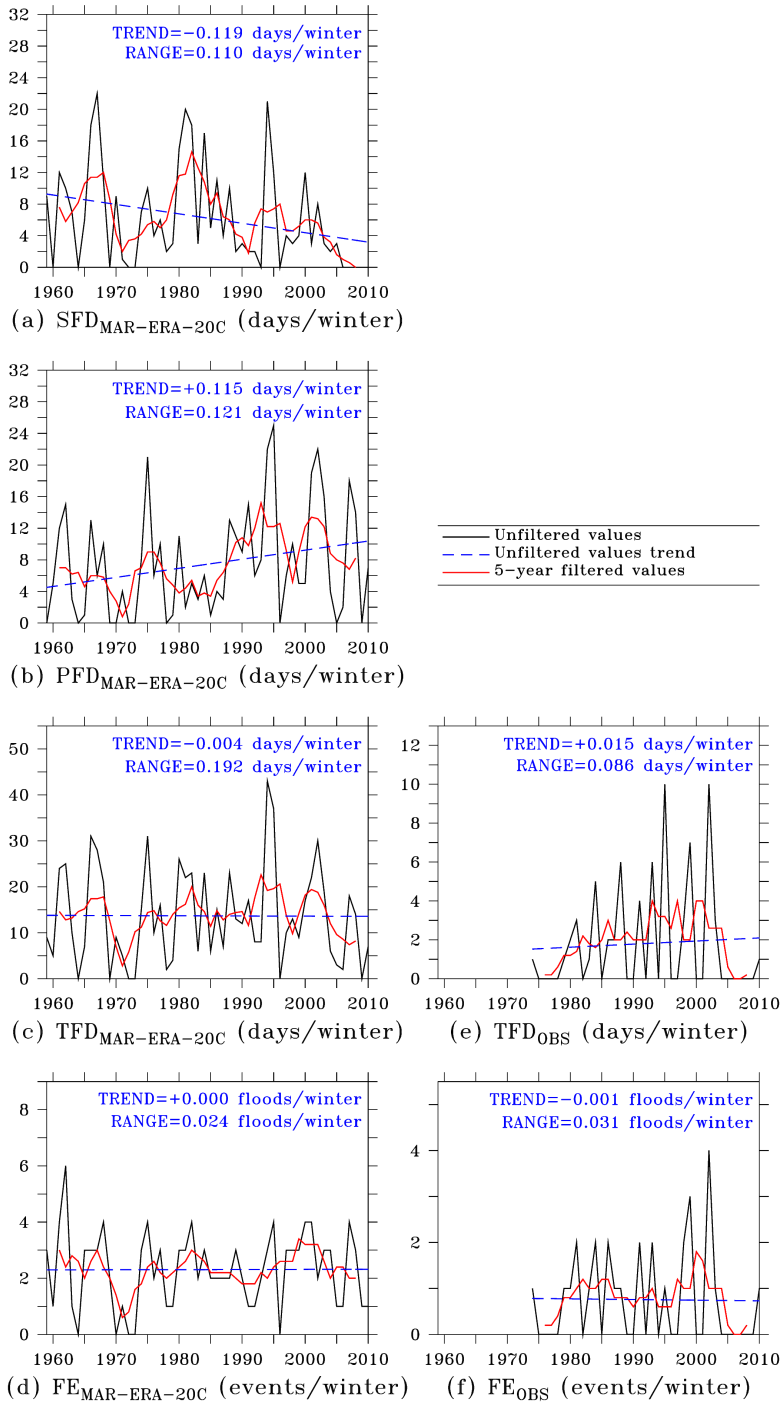

Figure A.10: Unfiltered values, 5-year filtered values and trends computed fromMAR-ERA over 1959–2010 of **(a)** the number of days per winter (DJF) favourable to floods due to snowpack melting combined with rainfall events (SFD$_{MAR-ERA20C}$), **(b)** the number of days per winter favourable to floods due to rainfall events alone (PFD$_{MAR-ERA20C}$), **(c)** the total number of days per winter favourable to floods (TFD$_{MAR-ERA20C}$), **(d)** the number of flood events favourable to floods per winter (FE$_{MAR-ERA20C}$). Unfiltered values, 5-year filtered values and trends computed from observations in Sauheid are also displayed with **(e)** the number of observed flood days per winter (TFD$_{OBS}$), and **(f)** the number of observed flood events per winter (FE$_{OBS}$).

B Additional figures for Chapter 4

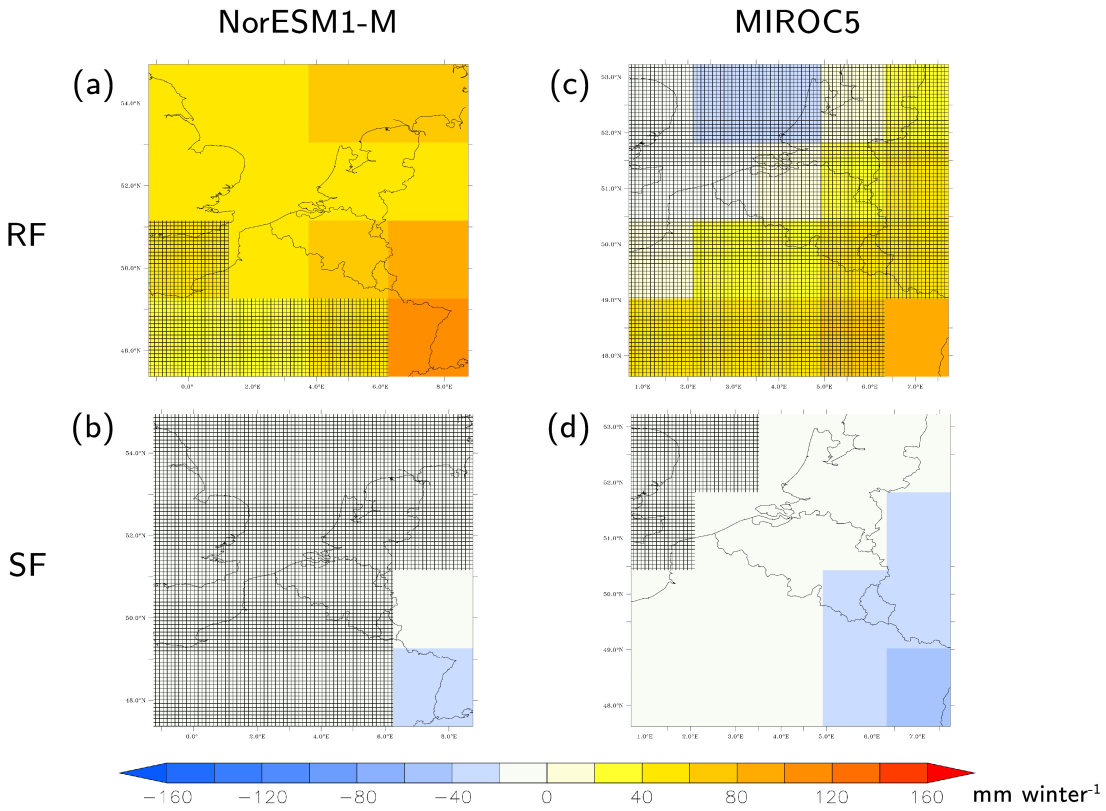

Figure B.1: Change in winter (DJF) of NorESM1M and MIROC5 for the period 2071–2100 with respect to 1976–2005 regarding **(a)-(c)** the amount of rainfalls (RF), **(b)-(d)** the amount of snowfalls (SF). Filled pixels indicate the places where the changes are statistically significant with respect to the NorESM1M and MIROC5 interannual varibility over 1976–2005. Hashed pixels indicate the places where the trends are statistically non-significant.

C Additional figures for Chapter 5

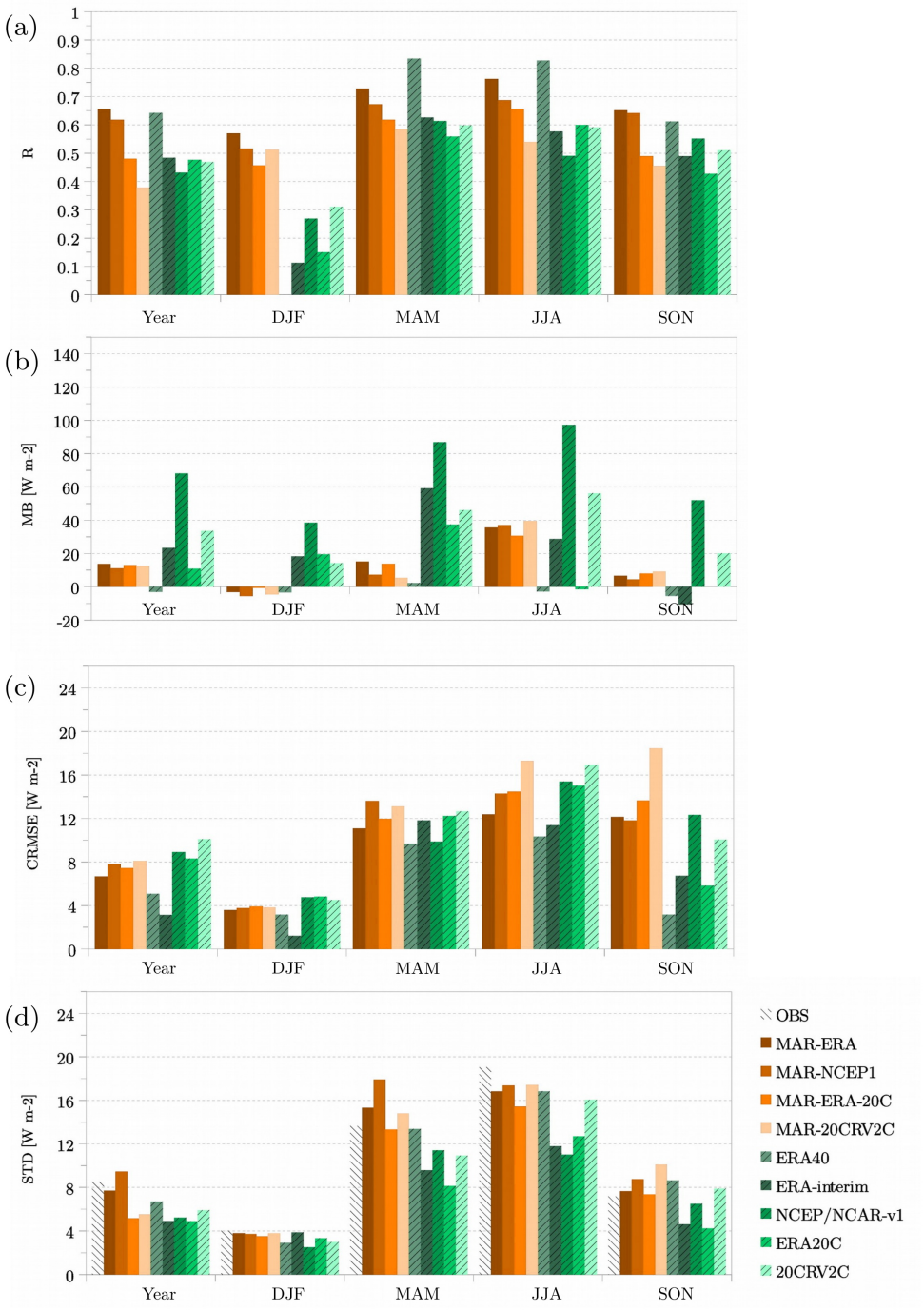

Figure C.1: Modelled $E_{g\downarrow}$ vs observed $E_{g\downarrow}$ at Melle for 1967-2010 : **(a)** annual and seasonal correlation (R), **(b)** mean bias (MB), **(c)** centred root mean square error (CMRSE) and **(d)** standard deviation (STD). It should be noted that ERA40 covers 1967-1978 while ERA-interim covers 1979-2010.

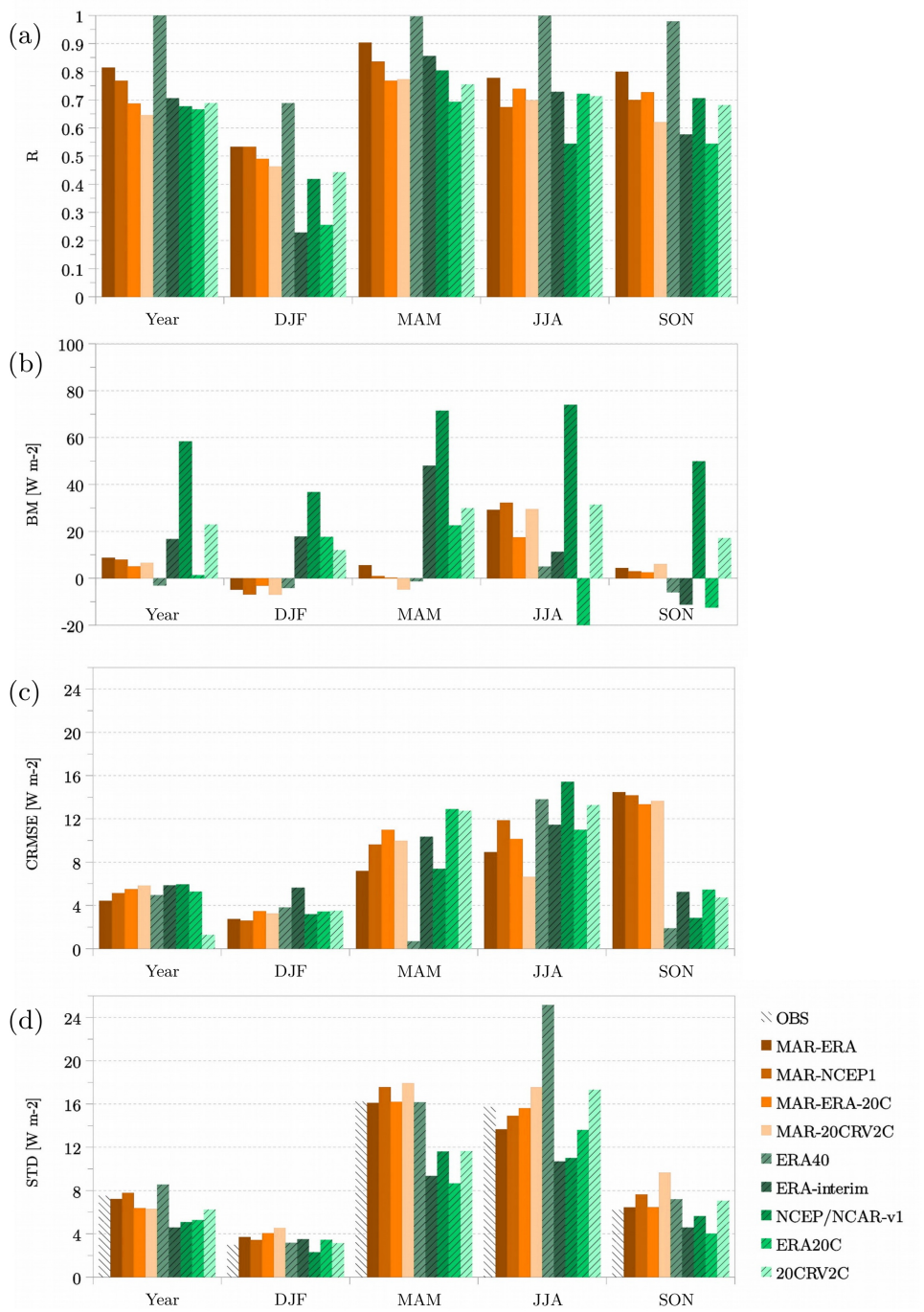

Figure C.2: Modelled $E_{g\downarrow}$ vs observed $E_{g\downarrow}$ at Oostende for 1975-2010: **(a)** annual and seasonal correlation (R), **(b)** mean bias (MB), **(c)** centred root mean square error (CMRSE) and **(d)** standard deviation (STD). It should be noted that ERA40 covers 1975-1978 while ERA-interim covers 1979-2010.

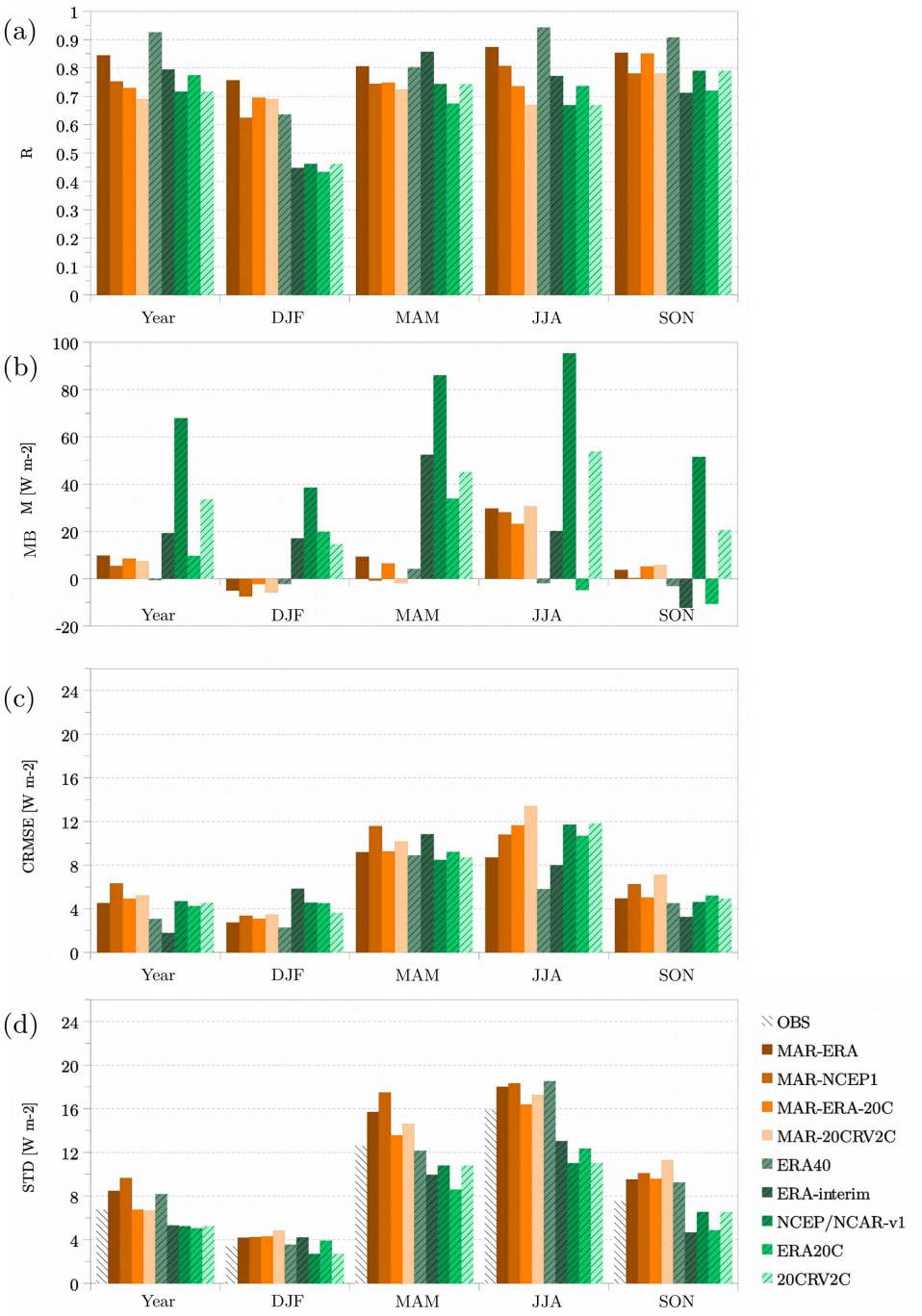

Figure C.3: Modelled $E_{g\downarrow}$ vs observed $E_{g\downarrow}$ at Uccle for 1959-2010: **(a)** annual and seasonal correlation (R), **(b)** mean bias (MB), **(c)** centred root mean square error (CMRSE) and **(d)** standard deviation (STD). It should be noted that ERA40 covers 1959-1978 while ERA-interim covers 1979-2010.

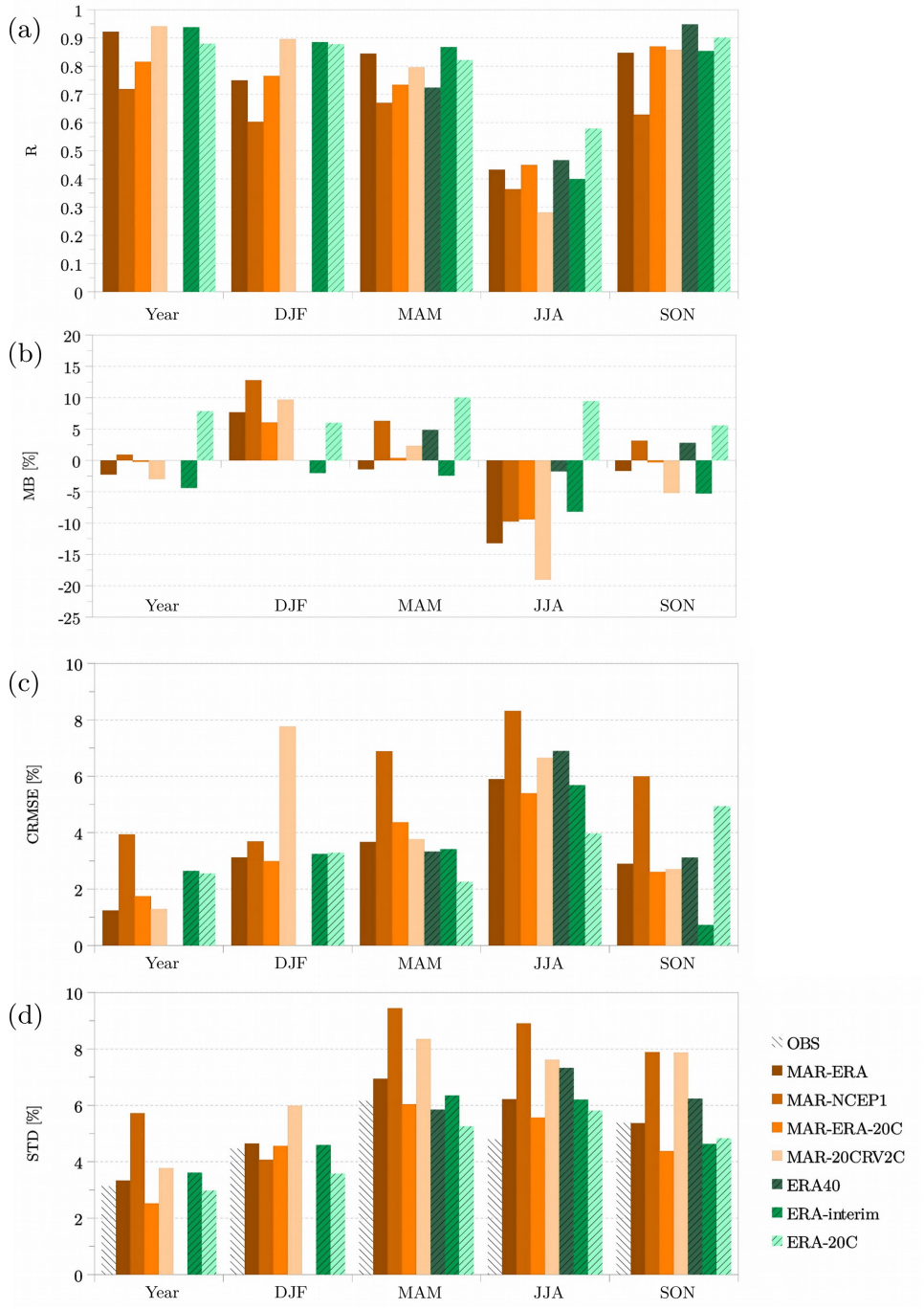

Figure C.4: Modelled TCC vs observed TCC at Oostende/Middlekerk for 1966-2010: **(a)** annual and seasonal correlation (R), **(b)** mean bias (MB), **(c)** centred root mean square error (CMRSE) and **(d)** standard deviation (STD). It should be noted that ERA40 covers 1966-1978 while ERA-interim covers 1979-2010. (TCC data from NCEP/NCAR-v1 and 20CRV2C were not available).

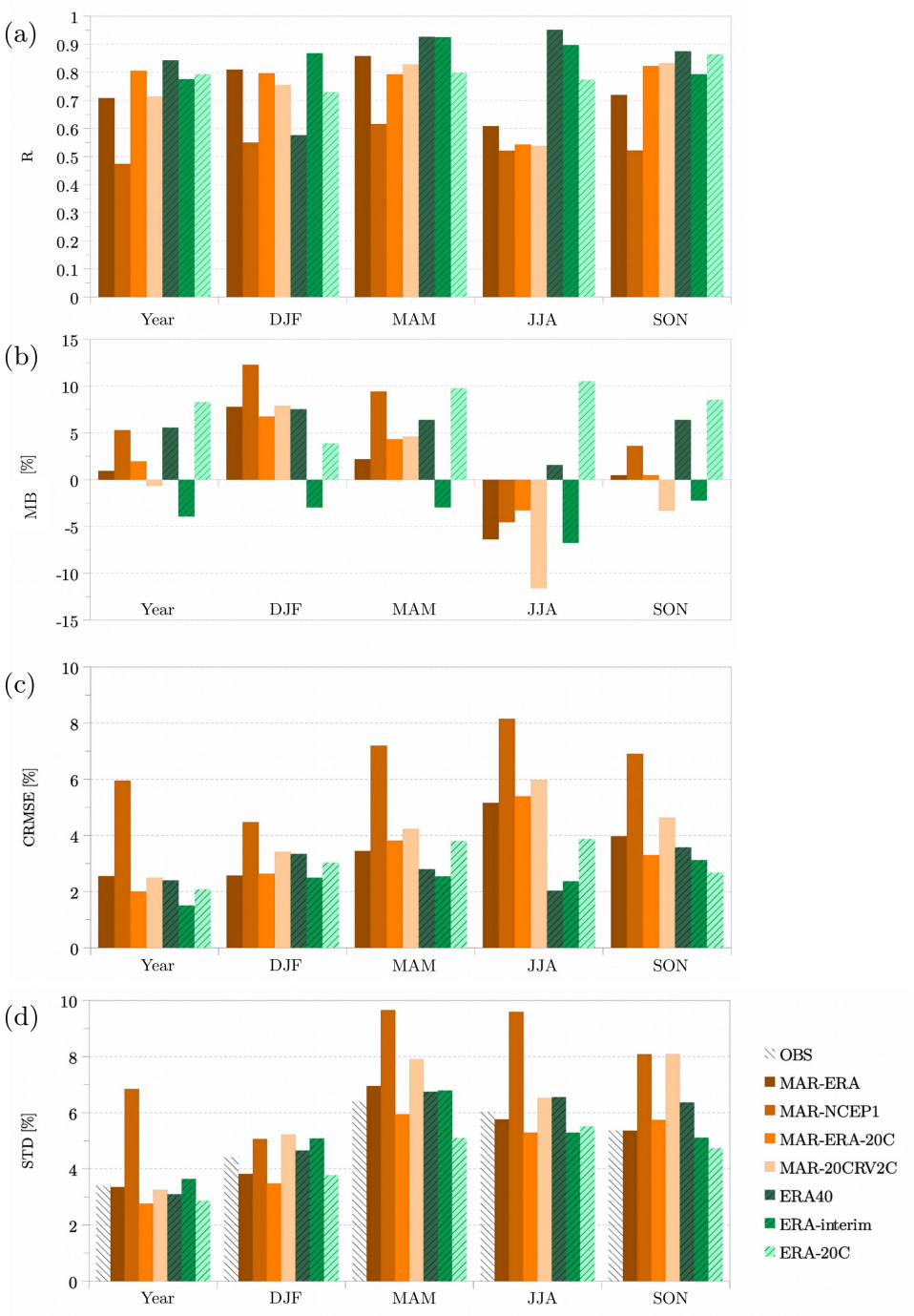

Figure C.5: Modelled TCC vs observed TCC at Bierset for 1966-2010: **(a)** annual and seasonal correlation (R), **(b)** mean bias (MB), **(c)** centred root mean square error (CMRSE) and **(d)** standard deviation (STD). It should be noted that ERA40 covers 1966-1978 while ERA-interim covers 1979-2010. (TCC data from NCEP1/NCAR-v1 and 20CRV2C were not available).

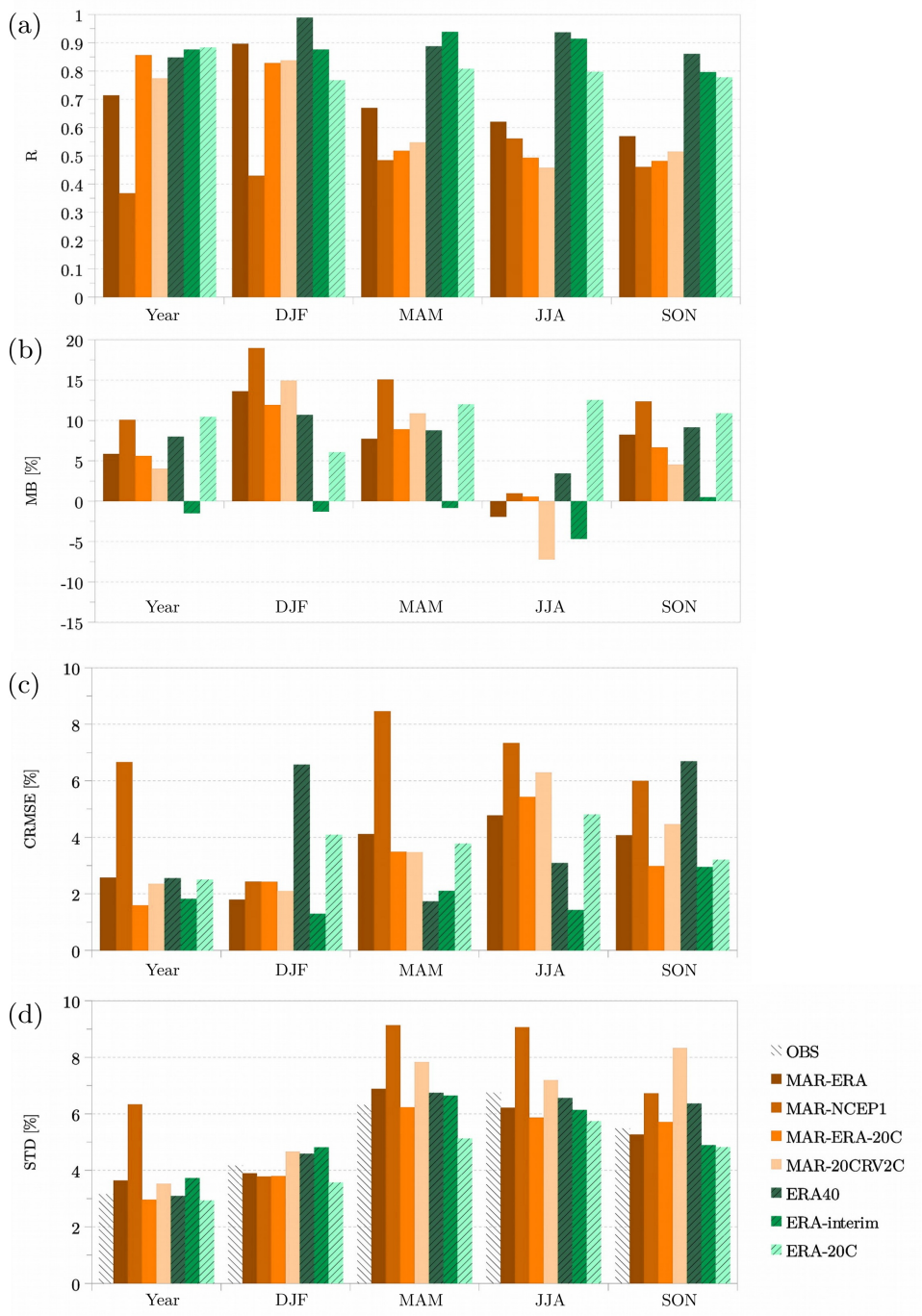

Figure C.6: Modelled TCC vs observed TCC at Uccle for 1966-2010: **(a)** annual and seasonal correlation (R), **(b)** mean bias (MB), **(c)** centred root mean square error (CMRSE) and **(d)** standard deviation (STD). It should be noted that ERA40 covers 1966-1978 while ERA-interim covers 1979-2010. (TCC data from NCEP/NCAR-v1 and 20CRV2C were not available).

Table C.1: Seasonal trends and their uncertainty range of Snedecor for the 95% confidence level, computed from measurements performed at Saint-Hubert. The values between brackets indicate that they are computed for 1966–1979.

Table C.2: Seasonal trends and their uncertainty range of Snedecor for the 95% confidence level, computed from measurements performed at Saint-Hubert. The values between brackets indicate that they are computed for 1966–1979.

	$\mathbf{E}_{g\downarrow}$ [W m^{-2}]				**TCC** [%]			
	1959–1979		**1980–2010**		**1959–1979**		**1980–2010**	
	Trend [decade^{-1}]	**Range** [decade^{-1}]	**Trend** [decade^{-1}]	**Range** [decade^{-1}]	**Trend** [decade^{-1}]	**Range** [decade^{-1}]	**Trend** [decade^{-1}]	**Range** [decade^{-1}]
Winter (DJF)	(-0.2)[1]	(7.9)	+1.4	2.5	(+6.5)	(10.5)	+2.5	2.5
Spring (MAM)	(-1.3)	13.2	**+10.7**[2]	6.1	(-1.3)	(9.8)	+1.9	3.7
Summer (JJA)	(+1.0)	(14.0)	**+12.0**	6.1	(-0.1)	(10.5)	+2.3	3.3
Autumn (SON)	(+3.4)	(10.0)	+4.3	4.4	(+0.6)	(10.0)	+3.3	2.9

[1] The values between brackets indicate that they are computed for 1966–1979.
[2] The values in bold indicate that the trends are statistically significant at the 95 % confidence level, namely that they are larger than the associated uncertainty range.